THE UNIVERSITY OF QUEENSLAND

AUSTRALIA

Fundamental studies on the chemical aspects of freeze linings

Tijl Crivits

M.Sc.

A thesis submitted for the degree of Doctor of Philosophy at the University of Queensland in 2016

School of Chemical Engineering

Abstract

The application of freeze lining technologies has been shown to be highly effective in extending the working lives of pyrometallurgical furnaces operating under aggressive process conditions and corrosive liquid melts. Freeze linings are obtained by cooling the outer furnace walls, resulting in the formation of solid protective deposits on the inner walls of the furnace linings. Of particular interest to process operators are the freeze lining thickness and the heat loss through the furnace walls, both of which are directly related to the bath-freeze lining interface temperature.

In most of the predictions for thermal steady state conditions, the assumption has been made that the temperature at the freeze lining/liquid interface is equal to the liquidus temperature of the bulk slag, and that the primary phase forms a dense sealing layer at this deposit/liquid interface. As a result of recent research on these systems, there is now extensive experimental evidence to demonstrate that the interface temperature can be below the liquidus and that the primary phase is not necessarily present at the deposit/liquid interface at thermal steady state conditions. These observations clearly indicate that other factors, in addition to thermal parameters of the system, need to be taken into account in the design of freeze lining systems.

In the present study, heat and mass transfer and elementary reaction steps, and the associated thermal, physical, and chemical factors that can influence freeze lining behaviour are identified.

From experiments undertaken using $CaCl_2$-H_2O solutions, accurate measurements have been made of deposit growth and microstructural changes taking place in the deposit over time were directly observed. These experiments have demonstrated the importance of nucleation rate of the primary phase and the thermal history of the freeze lining.

High-temperature experiments in the 'Cu_2O'-'Fe_2O_3'-MgO-SiO_2 system in equilibrium with metallic copper have clearly demonstrated that at thermal steady state, bath/freeze lining interface temperatures are lower than the liquidus temperatures, and the possibility of operating processes at subliquidus bath temperatures. These experiments also indicated that an increase in bath temperatures results in an increase of the steady state interface temperature.

High-temperature experiments in the Al_2O_3-CaO-SiO_2 system were designed to study the effect of slag viscosity. Differences in the characteristics of the deposit/liquid interface were observed, however, it was unclear whether the observed differences in freeze lining behaviour were caused by the changes in viscosity, or the differences in morphology of the primary phase. The spontaneous decrepitation of freeze linings containing the dicalcium silicate phase on cooling clearly illustrated

the need for caution when designing freeze lining systems that may form compounds undergoing significant changes in volume due to polymorphic transformations.

The research supports the view that deposit/liquid interface temperatures in freeze lining systems are determined by a complex combination of heat transfer, mass transfer and chemical processes, and that thermal steady state conditions of freeze linings are best described in a more general dynamic steady state framework.

.

Declaration by Author

This thesis is composed of my original work, and contains no material previously published or written by another person except where due reference has been made in the text. I have clearly stated the contribution by others to jointly-authored works that I have included in my thesis.

I have clearly stated the contribution of others to my thesis as a whole, including statistical assistance, survey design, data analysis, significant technical procedures, professional editorial advice, and any other original research work used or reported in my thesis. The content of my thesis is the result of work I have carried out since the commencement of my research higher degree candidature and does not include a substantial part of work that has been submitted to qualify for the award of any other degree or diploma in any university or other tertiary institution. I have clearly stated which parts of my thesis, if any, have been submitted to qualify for another award.

I acknowledge that an electronic copy of my thesis must be lodged with the University Library and, subject to the General Award Rules of the University of Queensland, immediately made available for research and study in accordance with the Copyright Act 1968.

I acknowledge that copyright of all material contained in my thesis resides with the copyright holder(s) of that material. Where appropriate I have obtained copyright permission from the copyright holder to reproduce material in this thesis.

Publications during candidature

Published Journal Papers

1. T. Crivits, P.C. Hayes and E. Jak (2015) "Influence of MgO on the phase equilibria in the CuO_x–FeO_y–MgO–SiO_2 system in equilibrium with copper alloy – Part I: methodology and liquidus in the tridymite primary phase field.", Int. J. Mater. Res., 106(5), 454-463

2. T. Crivits, P.C. Hayes and E. Jak (2015) "Influence of MgO on the phase equilibria in the CuO_x–FeO_y–MgO–SiO_2 system in equilibrium with copper alloy – Part II: results and discussion.", Int. J. Mater. Res., 106(6), 587-599

3. E. Haccuria, T. Crivits, P. C. Hayes, E. Jak (2015) "Selected phase equilibria studies in the Al_2O_3-CaO-SiO_2 system.", J. Am. Ceram. Soc., Online, doi. 10.1111/jace.13991

Conference Papers

1. T. Crivits, P.C. Hayes and E. Jak (2014) "Solubility of MgO in high Cu_2O slags in equilibrium with Cu metal.", COM 2014, Vancouver, CIM, Montreal, Canada, 2014.
2. T. Crivits, P.C. Hayes and E. Jak (2015) "Investigation of freeze linings in magnesia-containing copper slags", COM 2015, Toronto, DIM, Montreal, Canada, 2015.

Conference abstracts

1. T. Crivits, P.C. Hayes and E. Jak (2013) "Protecting the future – Investigation of phase equilibria and freeze linings in novel high temperature recycling processes.", HTP Symposium, Swinburne University, Melbourne, Australia

2. T. Crivits and E. Jak (2012) "Investigation of phase equilibria in the Cu-Fe-Si-Mg-O system at low MgO concentrations in equilibrium with copper metal", HTP Symposium, Swinburne University, Melbourne, Australia

Conference posters

1. T. Crivits, P.C. Hayes and E. Jak (2015) "Study of phase equilibria and freeze linings in novel high temperature processes", EMC 2015, Düsseldorf, Germany, 1100-1101

2. T. Crivits, P.C. Hayes and E. Jak (2015) “Study of phase equilibria and freeze linings in novel high temperature processes”, COM 2015, Toronto, Canada

Publications included in this thesis

T. Crivits, P.C. Hayes and E. Jak (2015). “Influence of MgO on the phase equilibria in the CuO_x–FeO_y–MgO–SiO_2 system in equilibrium with copper alloy – Part I: methodology and liquidus in the tridymite primary phase field.”, Int. J. Mater. Res., 106(5), 454-463. doi: 10.3139/146.111201

Parameters (%)	Contributors		
	T.C.	P.C.H.	E.J.
Experiment design	90	-	10
Data analysis	90	-	10
Interpretation of the results	60	10	30
Writing/Editing	60	20	20

T. Crivits, P.C. Hayes and E. Jak (2015). “Influence of MgO on the phase equilibria in the CuO_x–FeO_y–MgO–SiO_2 system in equilibrium with copper alloy – Part II: results and discussion.”, Int. J. Mater. Res., 106(6), 587-599. doi: 10.3139/146.111234

Parameters (%)	Contributors		
	T.C.	P.C.H.	E.J.
Experiment design	90	-	10
Data analysis	90	-	10
Interpretation of the results	60	10	30
Writing/Editing	60	30	10

Contributions by others to the thesis

The experimental design, data analysis, interpretation of the results and writing in this thesis are a result of meetings and discussions between my supervisors, Evgueni Jak and Peter Hayes, and myself.

Part of the data collection for the experiments in the $CaCl_2$-H_2O system was performed by Benjamin Trubshaw and Camille Lehmann.

Statement of parts of the thesis submitted to qualify for the award of another degree

None.

Acknowledgements

This thesis couldn't have completed without the help of a LOT of people.

First of all to Jeci, who made the years we were together so much more than they would've been without.

To my parents, for raising me to be the man I am today, and to 'Opa Jabbeke', for the memories I'll always cherish.

To my supervisors, Eugene and Peter, always ready to help, always having comments on my research and writing, always helping to improve my work.

To the present and past people at the Pyrometallurgy Rersearch Laboratory, in particular Taufiq, Ata, Denis, Lennart and Gloria, for the many professional discussions and chit-chat conversations, and Ben and Camille for their assistance with the collection of data from the cold experiments.

To Elien, the person I could always vent my frustrations to without anyone else understanding what I was talking about, and for keeping my Dutch relatively up to date.

To the people of the Australian Microscopy & Microanalysis Research Facility at the Centre for Microscopy and Microanalysis at the University of Queensland. (CMM), in particular Ron, Ying and Kim, for the interesting discussions about and assistance with electron microscopy.

To the Australian Research Council ARC Discovery program and Umicore for the financial support for this thesis, and to the UQ International Scholarship (UQI) program for providing a scholarship.

To the finance and administration people at UQ, particularly Siu Bit, for always being there when once again I was struggling to fill out a form correctly.

To 'my' students, who provided me with a welcome distraction from research in the form of tutoring.

And finally to all my friends, wherever they live. Through the many conversations I had with you, I somehow managed to keep the majority of my sanity during my 3.5 year-long Australian adventure.

Tijl Crivits

December 2015

Keywords

Freeze lining; Phase equilibria; Slag; Cu_2O–Fe_2O_3–MgO–SiO_2; Al_2O_3–CaO–SiO_2; H_2O–$CaCl_2$;

Australian and New Zealand Standard Research Classifications (ANZSRC)

ANZSRC code: 091407, Pyrometallurgy: 100%

Fields of Research (FoR) Classification

FoR code: 0914, Resources Engineering and Extractive Metallurgy: 100%

Table of contents

Figures and tables

Figures

Tables

Abbreviations and symbols

Symbols are ordered according to:

1) lowercase letter – capital letter – greek symbols
2) alphabetical

$c_{p,air}$	Specific heat capacity of the air
g	Gravitational acceleration constant
h	Convective heat transfer coefficient
h_{air}	Convective heat transfer coefficient between the air and the cooled probe
$h_{coolant}$	Convective heat transfer coefficient between the coolant and the cooling blocks
h_{bath}	Convective heat transfer coefficient between the bath and the freeze lining
$h_{bath,1}$	Convective heat transfer coefficient between the bath and the freeze lining at $t_1 < t_2$
$h_{bath,2}$	Convective heat transfer coefficient between the bath and the freeze lining at $t_2 > t_1$
k	Thermal conductivity
$k_{cooling}$	Thermal conductivity of the cooling blocks/cooling circuit
k_{FL}	Thermal conductivity of the freeze lining
k_i	Thermal conductivity of layer i
$\dot{m}_{air}$	Flow rate of the air through the cooled probe
$q_{bath,FL}$	Heat flux at the bath-freeze lining interface = $(Q_{bath,FL}/A_{bath,FL})$
$r_{FL,1}$	Distance from the centre of the cooled probe at position 1
$r_{FL,2}$	Distance from the centre of the cooled probe at position 2
t	Time

t_1	Time 1
t_2	Time 2
t_0	Time at which the liquid moving towards the freeze lining crosses the point where T = $T_{liquidus}$
t_f	Time at which the liquid moving towards the freeze lining reaches the freeze lining
v	Velocity of the bulk fluid
x	Distance from the freeze lining cold face
A	Surface area
$A_{bath,FL}$	Surface area of the bath-freeze lining interface
Gr	Grashof number (= $\frac{g\beta(T_s-T_\infty)}{(\mu/\rho)^2}$)
H_{latent}	Latent heat
L	Submerged depth of the cooled probe
M_{A0}	Number of moles of A in the bulk bath liquid
M_{B0}	Number of moles of B in the bulk bath liquid
Nu	Nusselt number (= $\frac{hX}{k}$)
Pr	Prandtl number (= $\frac{\mu}{\rho\alpha}$)
$Q_{bath,FL}$	Rate of heat transfer from the bath to the freeze lining
Q_{latent}	Rate of latent heat transfer
Q_{FL}	Rate of heat transfer through the freeze lining
$Q_{FL}^{hotface}$	Rate of heat transfer through the bath-freeze lining interface (the hotface)
$R(t)$	Crystallization rate onto the detached crystals at time t
Ra	Rayleigh number (= $Gr.Pr$)
Re	Reynolds number (= $\frac{\rho vX}{\mu}$)

Sc	Schmidt number (= $\frac{\mu}{\rho D}$)
Sh	Sherwood number (= $\frac{K}{D/X}$)
T	Temperature
T_{∞}	Bulk temperature
$T_{air,in}$	Temperature of the air at the inlet
$T_{air,out}$	Temperature of the air at the outlet
T_{bath}	Bulk bath temperature
$T_{bath,1}$	Bulk bath temperature at $t_1 < t_2$
$T_{bath,2}$	Bulk bath temperature at $t_2 > t_1$
$T_{bath,FL}$	Temperature at the bath-freeze lining interface
$T_{bath,FL,1}$	Temperature at the bath-freeze lining interface at $t_1 < t_2$
$T_{bath,FL,2}$	Temperature at the bath-freeze lining interface at $t_2 > t_1$
$T_{coldface}$	Temperature at the cooling circuit-freeze lining interface
$T_{coolant}$	Temperature of the coolant
$T_{FL,1}$	Temperature in the freeze lining at position $r_{FL,1}$
$T_{FL,2}$	Temperature in the freeze lining at position $r_{FL,2}$
X	Characteristic length
X_f	Composition of the liquid at time t_f
α	Thermal diffusivity
α_{FL}	Thermal diffusivity of the freeze lining
β	Thermal volume expansion coefficient
$\Delta M_{A,f}$	Extent of crystallization of the precipitating component, A, on the detached crystals in the subliquidus boundary layer
$\Delta x_{cooling}$	Thickness of the cooling blocks/cooling circuit
Δx_{FL}	Thickness of the freeze lining

$\Delta x_{FL,ss}$	Steady state thickness of the freeze lining
Δx_i	Thickness of layer i
ρ_{air}	Density of the air
ρ_{bath}	Density of the bulk bath liquid
μ	Dynamic viscosity

Part I

Introduction

“The only true wisdom is in knowing you know nothing. [Socrates]”

1 General introduction

The production of most metals – iron, steel, aluminium, copper, … – involves the use of pyrometallurgical or electro-metallurgical furnaces. To prevent furnace failure, the furnace shell needs to be protected from the materials inside the furnace bath: molten salts, slags, mattes or alloys. Traditionally, this is done through implementation of a refractory lining on the inner side of the furnace shell, preventing interaction between the shell and the bath material. Due to physical, thermal and chemical interaction between the refractory lining and the bath, the refractory lining slowly degrades over time, eventually leading to a furnace shutdown in order to reline the furnace. The tendency of pyrometallurgical furnaces to be operated at higher temperatures and increased levels of agitation of the bath increases the degradation rate of the refractory, making this option less profitable.

An alternative can be found in freeze linings – a layer of solidified bath material between the furnace shell and the liquid bath, an approach which has been used successfully in several processes including the Hall-Héroult process – which would not be sustainable without freeze linings as failure would occur within 6 months [1] –, zinc fuming and the lance of ISA- and AUSMELT furnaces (Table 1-1). These linings are a result of a thermal balance between heat transfer from the bath to the lining and heat transfer through the lining (see Figure 1-1). Any disruption of this balance, such as local mechanical failure or a change in bath composition, results in either solidification or dissolution of the freeze lining until the thermal balance is restored. As such, the freeze lining repairs itself and no relining of the furnace is required, reducing the downtime of the furnace and allowing for greater flexibility in operating conditions.

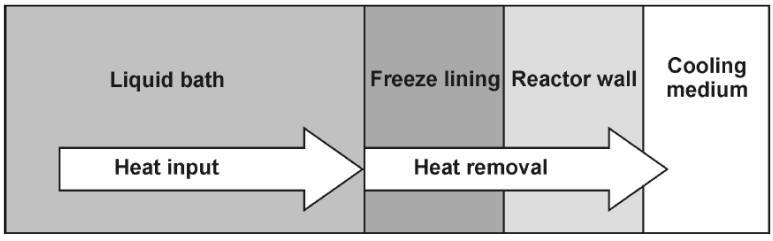

Figure 1-1: Schematic representation of the freeze lining concept [2].

Though freeze lining technology has been used for a long time, there are still uncertainties regarding some fundamental aspects of freeze lining behaviour. Take, for example, the steady state temperature at the bath-freeze lining interface. Most mathematical models describing the heat flux through the reactor wall assume that this temperature is equal to the liquidus temperature of the bulk slag. Recent research (see sections 2.3 and 2.4) has demonstrated that, even at thermal steady state, the freeze lining does not necessarily form a sealing crystal layer consisting of the primary phase in equilibrium

with the slag bath. As a result, the assumption of the interface being at the liquidus temperature is, at least in some cases, incorrect.

Table 1-1: Applications of freeze linings in industry.

Process		System	Reference
Hall-Héroult		Cryolite	[3-9]
Ilmenite smelting		Fe-Ti-O	[10-14]
Zinc fuming		Ca-Fe-Si-Zn-O	[15-19]
Iron blast furnace		Fe-C	[20, 21]
Copper smelting		Fe-Si-O	[22]
Copper converting		Fe-Si-O	[22]
Battery smelting		Al-Ca-Li-Si-O	[23]
Electric arc furnace	Cu blister slag cleaning	Al-Ca-Fe-Mg-Si-O	[24]
	Ferronickel processing	Fe-Mg-Si-O	[24, 25]
	Ferromanganese processing	Al-Ca-Mn-Si-O	[26, 27]
	Ferrocobalt processing	Al-Ca-Mg-Si-O	[28]
	Steel scrap recycling	Fe-C	[29]
ISASMELT/ AUSMELT lance	Cu smelting	Cu-Fe-Si-O	[30-32]
	Cu converting	Cu-Fe-Si-O	
	Pb smelting	Ca-Fe-Pb-Zn-Si-O	
	Pb converting	Ca-Fe-Zn-Si-O	
	e-scrap recycling	Al-Ca-Fe-Pb-Si-O	
Coal gasification		Al-Ca-Fe-Si-O	[33]

This has important consequences for the most common concerns when it comes to freeze linings: stability, thickness and heat losses. However, it also creates the opportunity for different approaches when it comes to pyrometallurgical processes. Usually it is assumed that a process should be operated above the liquidus temperature of the slag to avoid the formation of solid deposits in the furnace. The more recently proposed dynamic steady state model, on the other hand, suggests that a furnace could,

under certain conditions, be run at subliquidus temperatures. Adapting the composition of the slag to meet these conditions could thus result in a more efficient process.

At the present time, insufficient information is available on the dynamic steady state model to accurately predict freeze lining behaviour, preventing optimization of the operating conditions. The goal of this research is to experimentally determine the effect of key process variables, such as bath temperature and viscosity, on freeze lining behaviour in general and the bath-freeze lining interface temperature in particular to provide a better fundamental understanding of freeze linings.

Part II

Literature review

“I kind of lost track of time …

For two hours?

There were books involved.”

[Mistborn trilogy, Brandon Sanderson]

2 Freeze linings

2.1 Introduction

Freeze linings are used in industry as a replacement for refractory linings. Their purpose as such is to protect the furnace shell from degradation due to contact with the material inside the furnace. In the current work, a freeze lining is defined as a protective layer of solid material, created by cooling down the furnace shell and solidifying part of the bulk bath liquid onto the shell.

In a typical freeze lining experiment, when hot liquid slag is initially contacted with the cooled probe, the cooling rate is high and solidification of the slag occurs quickly. In later stages, as the thickness of the solidified slag increases, the rate of cooling and the solidification rate decrease. In this transient condition, the thermal profile in the freeze lining, as illustrated in Figure 2-1, differs at each stage of the freeze lining growth, with the thermal gradient decreasing as the freeze lining grows until thermal steady state conditions are established. In industrial applications, the formation of a freeze lining may occur in a much different manner, including, for example, interactions with the initial refractory, or with recently added cold charge material.

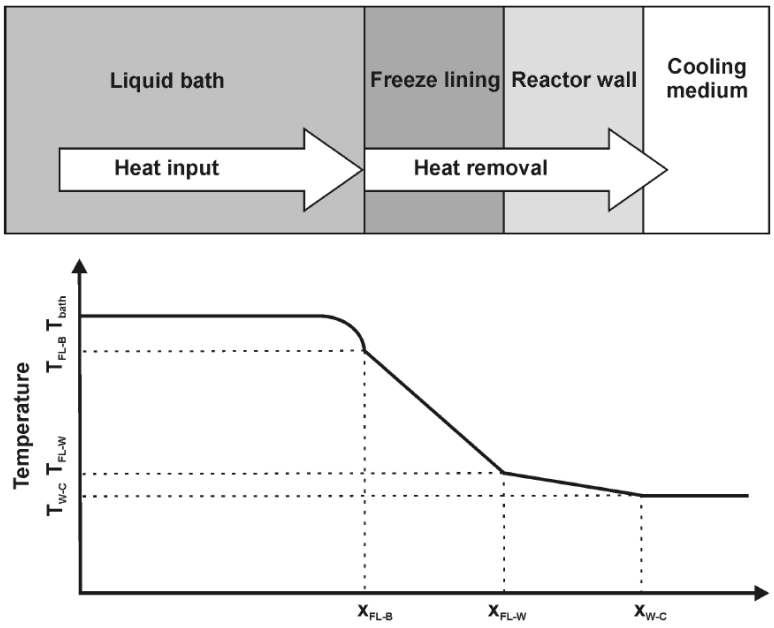

Figure 2-1 Schematic representation of the freeze lining concept [2]. T: temperature; x: position in the freeze lining; FL-B: freeze lining-bath interface; FL-W: freeze lining-reactor wall interface; W-C: reactor wall-cooling medium interface.

By maintaining a constant temperature in the bath and at the cold face (the cooling medium), a steady state is reached assuming constant operating conditions. Any damage caused, e.g. by mechanical

failure of the freeze lining, will be repaired until steady state is reached again: the freeze lining 'heals' itself, re-establishing a protective layer.

2.2 Modelling of freeze lining behaviour

2.2.1 Previous research

Haupin [34] reported a 1-D thermal steady state model of freeze linings and commented that the physical properties, such as thermal conductivity and the convective heat transfer coefficient, were generally hard to find. Several correlations for these properties in the cryolite system were provided based on earlier research.

Solheim et al. [3, 4] investigated the convective heat transfer coefficient between the bath and side ledge in aluminium cells using a physical molten biphenyl model. A full scale transverse section of an aluminium cell was modelled with gas-induced flow. Although horizontal flow induced by magnetic fields was not simulated, a method to calculate the convective heat transfer coefficient was proposed, resulting in values of the convective heat transfer coefficient in industrial cells between 250-600 W/m^2K.

Taylor et al. [7, 35, 36] created a mathematical model of an aluminium production cell including heat and mass transfer to predict the dynamic behaviour of the freeze lining. The variation of the freeze lining thickness, the liquidus temperature and the bath temperature due to alumina feeding and anode effects was determined. It was shown that the freeze lining thickness drastically decreases during and after an anode effect, and that the subsequent growth rate of the freeze lining is significantly smaller than the initial melting rate, making the process vulnerable to transient thermal disturbances.

The convective heat transfer coefficient between the bath and freeze lining in aluminium reduction cells was also investigated in laboratory experiments [6, 35]. A rotating steel tube, cooled by nitrogen gas, with a heat exchanger attached to the tip of the tube was used for this purpose. Convective heat transfer coefficients in the cryolite system were found to be between 600-830 W/m^2K.

Pfundt et al. [8] created a transient thermal model for aluminium reduction cells. A 2-D finite element method was used. Convection in the bath was modelled through use of an effective heat conductivity, dependent on the distance from the freeze lining. Similar steady state models were used by Bruggeman et al. [37], Ahmed et al. [38] and Valles et al. [39] to estimate the freeze lining profile in different types of reduction cells.

Fraser et al. [40] calculated the effect of bubble driven circulation in the bath on the convective heat transfer coefficient and used this information to estimate the steady state freeze lining profile through use of a 2-D, steady state, finite element thermal model. It was concluded that the most turbulent area was the metal-electrolyte interface, resulting in a thinner freeze lining at this position.

Wei et al. [41] created a 1-D transient moving finite difference model to predict dynamic ledge behaviour. Process disturbances caused by alumina feeding and the cell anode effect were found to result in a periodic freezing and melting of the freeze lining.

Solheim et al. [42, 43] created a 1-D freeze lining growth model combining heat and mass transfer. The assumption was made that the interface temperature is equal to the local liquidus temperature of the liquid at the bath-freeze lining interface, instead of the liquidus of the bulk bath liquid. The model demonstrated lower freeze lining growth rates than the conventional, purely thermal, treatment. It was found that the model worked for calculation of the freeze lining thickness, although the alumina concentration in the solid was not very well reproduced.

Solnordal et al. [32] experimentally studied freeze lining formation on a Sirosmelt lance in a pilot furnace. Several experiments were conducted using different slag compositions in the Al-Ca-Fe-Mg-Si-O system. The convective heat transfer coefficient was determined to be between 80-150 W/m^2K. Three explanations were provided for this relatively low value compared to previous research: As opposed to other furnaces, extremely large combustion gas bubbles are present in the Sirosmelt furnace, which can periodically shroud the lance, decreasing the overall heat transfer coefficient; A slight gap might be present between the freeze lining and the lance due to contraction of the lance; The model used to calculate the thermal parameters assumed a bath-freeze lining interface equal to the solidus temperature. It is acknowledged by the authors that a mushy zone consisting of a solid matrix surrounded by liquid might be present and that the interface temperature will be between the liquidus and the solidus temperature in reality. The thermal conductivity of the freeze lining was found to be between 0.5 and 1.1 W/m.K.

Robertson et al. [44] created a wax model to study the heat transfer and flow in slag cleaning furnaces, including freeze lining formation. The main conclusion was that more intense process conditions need more intense wall cooling.

Pistorius and Zietsman [10-12] modelled freeze lining growth through a combination of thermal modelling and phase equilibria considerations as part of a thermal model for an ilmenite smelting DC arc furnace [13]. The assumption was made that all formed solids were deposited onto the freeze lining. This dynamic model was used to investigate freeze linings in the ilmenite smelting process. It

was concluded that the freeze lining mechanism cannot force the liquid composition to the eutectic groove [10] and that changes in reductant and energy input need to be carefully balanced to avoid destabilization of the furnace and the freeze lining [11].

Guevara et al. [45] created a model to calculate freeze lining growth incorporating heat and mass transfer, fluid flow and phase equilibria. Based on experiments in the $CaCl_2$-H_2O system, precipitated solid particles were assumed to circulate with the fluid and not be deposited onto the freeze lining. The model was found to agree with earlier experiments [46] in cavities filled with air, water and tin and with the experimental research performed in the study.

Verscheure et al. [15] developed a process model for the analysis of zinc fuming processes, including the formation and behaviour of a freeze lining. The model was subsequently used to study the effect of operating conditions on the zinc fuming process. It was concluded that high liquidus temperatures limited the heat losses through the freeze lining and resulted in a stable operation of the process.

2.2.2 Transient

In the following sections, the thermal equations governing freeze linings in transient conditions and at steady state will be explained. The equations in these sections are based mainly on the work presented by Verscheure et al. [16, 47].

The change in local temperature in the bulk solid or liquid depends on the sensible heat, the temperature gradients in the system and the thermal conductivity.

$$\alpha . \Delta^2 T = \frac{\delta T}{\delta t} \quad \textbf{(2-1)}$$

where α and T are the local thermal diffusivity and temperature, and t the time. The tracking of the position of the deposit/liquid interface can be undertaken either explicitly or implicitly. Explicit tracking is done by calculating the change in temperature in the freeze lining and the bulk bath separately, and determining the position through an additional (set of) equations. An example of this approach is given below:

$$Q_{bath,FL} + Q_{latent} = Q_{FL}^{hotface} \quad \textbf{(2-2)}$$

With

$$Q_{bath,FL} = A . h_{bath} . (T_{bath} - T_{bath,FL}) \quad \textbf{(2-3)}$$

$$Q_{latent} = \rho_{bath}.A.H_{latent}.\frac{d\Delta x_{FL}}{dt} \quad \textbf{(2-4)}$$

$$Q_{FL}^{hotface} = A.k_{FL}.\frac{dT}{dx}\Big|_{hotface} \quad \textbf{(2-5)}$$

where $Q_{bath,FL}$is the rate of heat transfer from the bath to the freeze lining, $Q_{FL}^{hotface}$ is the rate of conductive heat transfer through the freeze lining at the hotface, Q_{latent} the rate of latent heat production, A the surface area of the freeze lining, h_{bath} the convective heat transfer coefficient of the bath, T_{bath} and $T_{bath,FL}$ the temperature of the bulk bath and at the bath-freeze lining interface, ρ_{bath} the density of the bulk bath, H_{latent} the latent heat of the slag, Δx_{FL} the thickness of the freeze lining, x the position in the freeze lining and k_{FL} the thermal conductivity of the freeze lining.

It is also possible to find an analytical solution for this problem when assuming constant values for the thermal parameter and negligible heat accumulation in the wall [47]. In doing this a quasi-steady state between the heat input in the wall through convection and solidification/melting and the heat output through the wall is assumed at all times. Though this analytical solution gives a basic insight in the growth process of a freeze lining, it has been found to overestimate the growth speed of freeze linings in real-life applications by a large amount [48]. For a more accurate calculation that does not neglect heat accumulation, numerical models have to be used. Examples of these are given in [12, 35, 48].

In models using implicit tracking of the interface, equation (2-1) is solved in the freeze lining and liquid simultaneously. The thermal conductivity of the liquid is increased to simulate convective heat transfer in the bulk bath. The heat capacity is increased in the solidification range to simulate the latent heat. The position of the interface is determined based on the percentage of solids present in the grid cells. These models are easier to implement in multi-component systems, and in 2-D and 3-D simulations

The results of these heat transfer models show that a higher latent heat or a higher heat capacity decreases the growth speed of a freeze lining, but does not influence the steady state thickness. A higher thermal conductivity of the freeze lining or lower convective heat transfer coefficient increases both the growth rate and the final thickness of the freeze lining. A higher bath temperature slows down the rate of growth of the freeze lining and results in a lower final thickness [48].

More complete freeze lining growth models need to include crystallization behaviour. Several such models have been made earlier. Zietsman [12] and Guevara et al. [45] both assumed equilibrium solidification. Whereas Zietsman assumed all formed solids would precipitate on the freeze lining,

Guevara assumed the solids would precipitate in the liquid and form a subliquidus layer, containing detached crystals. Solheim [49] calculated freeze lining growth through a combination of heat and mass transfer.

A mathematical model describing the formation of detached crystals has been made as part of this thesis and can be found in Appendix E.

2.2.3 Steady state

When cooling the furnace wall to temperatures below the liquidus temperature of a slag, part of the slag will start to solidify. The solidified slag will be deposited onto the wall of the furnace and create a layer of solid slag, which then protects the furnace wall from further chemical attack by the slag.

This process of solidifying slag will continue until thermal equilibrium is reached between the rate of heat transfer from the bath to the freeze lining $Q_{bath,FL}$ and the rate of heat transfer through the freeze lining and wall Q_{FL}. At steady state [47]:

$$Q_{bath,FL} = Q_{FL} \tag{2-6}$$

At steady state, for a plane wall, $Q_{bath,FL}$ and Q_{FL} are respectively given by equation (2-3) [47] and

$$Q_{FL} = \frac{A.(T_{bath,FL} - T_{coolant})}{R_{contact} + \sum \frac{\Delta x_i}{k_i} + \frac{1}{h_{coolant}}} \tag{2-7}$$

Where $h_{coolant}$ is the convective heat transfer coefficient of the cooling fluid, Δx_i and k_i the thicknesses and thermal conductivities of the several layers of the wall – the freeze lining and reactor wall in Figure 2-1, but usually also including a layer of refractory –, $T_{bath,FL}$ and $T_{coolant}$ are respectively the temperatures of the bath-freeze lining interface – also called the hotface – and of the coolant used as the cooling medium and $R_{contact}$ the contact resistance between the cooling blocks and the freeze lining.

From these equations, the steady state thickness of the freeze lining $\Delta x_{FL,ss}$ can be calculated. If it is assumed that the thermal heat resistance between the cooling fluid and cooling blocks, the thermal heat resistance between the cooling blocks and the cooland, the heat resistance of the cooling blocks and refractory layer and the contact resistance are negligible, and the thermal conductivity of the freeze lining is constant with temperature then from equation **(2-7)** [47]:

$$\Delta x_{FL,ss} = \frac{k_{FL}.(T_{bath,FL} - T_{coolant})}{h_{bath}.(T_{bath} - T_{bath,FL})} \tag{2-8}$$

Alternatively, when the thermal heat resistance between the cooling fluid and cooling blocks, and the thermal heat resistance of the cooling blocks and refractory are not negligible, the steady state thickness can be calculated as:

$$\Delta x_{FL,ss} = \frac{k_{FL}.(T_{bath,FL} - T_{coldface})}{h_{bath}.(T_{bath} - T_{bath,FL})} \quad \textbf{(2-9)}$$

Where $T_{coldface}$ is the temperature in the freeze lining at a position closest to the cooling system.

The final thickness of the freeze lining is thus dependent on the superheat ($T_{bath} - T_{bath,FL}$), the thermal conductivity of the freeze lining, the convective heat transfer coefficient of the bath, the temperature of the cooling water and the temperature at the bath-freeze lining interface. Although the exact equation for freeze linings in a cylindrical geometry differs in detail from equations (2-8) and (2-9), the behaviour is similar.

From equations (2-3) and (2-8), it is clear that the interface temperature is one of the key factors determining the heat flow through and thickness of the freeze lining. This so-called hotface temperature has long been assumed to equal the liquidus temperature of the slag, based on observations in molten salt systems [36, 50]. More recent research (see sections 2.3 and 2.4) though has shown that this is not necessarily the case [51]. Currently, insufficient information is available to predict the interface temperature of freeze lining, resulting in a high uncertainty on changes of the heat flux through and thickness of freeze linings under changing operating conditions. An improved fundamental understanding on the effect of operating conditions on the interface temperature is thus of the essence to allow for accurate predictions of freeze lining behaviour.

2.2.4 Summary of current models

Table 2-1 provides a summary of the developed models reported in the literature, identifying whether the model calculates transient or steady state conditions, whether heat transfer, mass transfer, fluid flow and phase equilibria are modelled, and the bath-freeze lining interface temperature assumed or calculated in the model.

Table 2-1: Summary of freeze lining models.

Ref.	Transient (T) Steady state (S)	Heat transfer (H) Mass transfer (M) Fluid flow (F) Phase equilibria (PE) Physical model (PM)	Tracking of interface: Implicit (I) Explicit (E)	$T_{bath,FL}$
[34]	S	H	E	$T_{liquidus}$
[3, 4]	/	PM	/	/
[7, 35, 36]	T	H, M	E	Variable ($T_{liquidus}$ at steady state)
[8]	T	H	I	$T_{liquidus}$
[37]	S	H	I	$T_{liquidus}$
[38]	S	H	I	$T_{liquidus}$
[39]	S	H	I	$T_{liquidus}$
[40]	S	H, F		
[41]	T	H, M	E	
[42, 43]	T	H, M	/	Variable
[44]	T + /	H + PM	E + /	$T_{liquidus}$ + /
[10-12]	T	H, M, PE	E	Variable ($T_{liquidus}$ at steady state)
[15]	quasi-SS	H, PE	E	$T_{liquidus}$
[45]	T	H, M, F, PE	E	$T_{solidus}$

2.3 Freeze lining compositions and microstructures

Thonstad et al. [5] studied the microstructure of freeze linings in Cryolite-based molten salts both through laboratory experiments using a laboratory cell with one cooled wall, and through ledge samples from industrial cells. Industrial samples were carefully selected to avoid areas contaminated by carbon dust and aluminium. The microstructure of the laboratory freeze linings was found to depend on the cooling rate. High cooling rates resulted in a porous, white, polycrystalline appearance,

while low cooling rates resulted in a layered structure consisting of large, clear, columnar crystals, similar to the industrial samples. This structured layer reflects the consecutive periods of melting and freezing. Based on chemical analysis of the subsequent layers, it was concluded that a pure cryolite ledge is only formed at low growth rates.

Solheim et al. [42] studied the microstructure of deposits formed from molten salts through use of a U-shaped, air-cooled steel probe in a laboratory setting. Depending on the bath composition, either an amorphous, somewhat porous structure (Na_3AlF_6-Al_2O_3), or distinct columnar crystals oriented parallel to the heat flow (Na_3AlF_6-AlF_3) were formed. Freeze linings in the (Na_3AlF_6-AlF_3-Al_2O_3) system consisted of two distinct zones: a zone similar to that of the (Na_3AlF_6-Al_2O_3) freeze linings at the bottom, and a zone similar to the (Na_3AlF_6-AlF_3) freeze linings at the top.

Verscheure et al. [17] studied the microstructure of zinc fuming slags (Al-Ca-Fe-Si-Zn-O) through laboratory experiments using a water-cooled probe consisting of two concentric steel tubes. The main focus was on development of the technique. It was demonstrated that the cooled-probe experiments allowed for production, observation and analysis of freeze linings in laboratory conditions. The difficulty of measuring the freeze lining thickness in-situ was considered the biggest disadvantage. The freeze linings were found to have a layered structure, consisting of an amorphous zone closest to the cooled probe and crystalline material further towards the bath, becoming coarser with increasing distance from the probe. The deposit layer closest to the bath was found to consist of both primary phase spinel crystals and melilite crystals, indicating that either the freeze lining had not reached steady state, or the steady state bath-freeze lining temperature was below the liquidus.

Campforts et al. [2, 52-56] used the cooled probe technique to study mass transfer, thermal history and microstructure formation in silica-containing lead slag freeze linings (Al-Ca-Fe-Pb-Si-O). The technique was modified in later studies to use air instead of water as a coolant to limit the steady state thickness of the freeze lining. In [56], the furnace power and the rotational speed of the crucible were varied. Due to the changing solidification rate, a layered structure was found to be present. Closest to the probe, an amorphous matrix with small crystals was found. At further distances from the probe, a zone with equiaxial crystals and later a zone with columnar crystals was observed. Crystal size was found to increase with increasing distance from the probe. Increased furnace power resulted in the same morphologies, but thinner layers, while an increase in rotational speed was found to favour the formation of columnar crystals. Depending on experiment, either melilite or olivine columnar crystals formed, using the same bath composition.

The mass transport and crystal growth in the freeze lining was studied in [55]. It was found that in the amorphous zone and the zone with equiaxial crystals, only short-range mass transport took place, and growth was dominated by heat transfer. In the columnar crystals zone, mass transport was found to influence the growth of the freeze lining. When a closed structure is formed, crystals exchange components with the liquid bath. When columnar crystals from in a liquid matrix, mass exchange takes place between the crystals and the liquid matrix. It was also concluded that minor elements can have a significant influence on freeze lining growth due to segregation effects.

The microstructure formation of lead slags was further studied in [52]. The layered microstructure was divided into 5 distinct layers: the glass layer, the glass layer with crystals, the crystalline layer, the crystals in liquid layer and the sealing crystals layer (Figure 2-2). A layer of entrained bulk bath liquid was also found to be present furthest from the probe. It was suggested that *"the solidification properties of the slag are important for rapid freeze lining formation"*. Rapid freeze lining formation was suggested to be favoured by rapidly forming interlocking crystals.

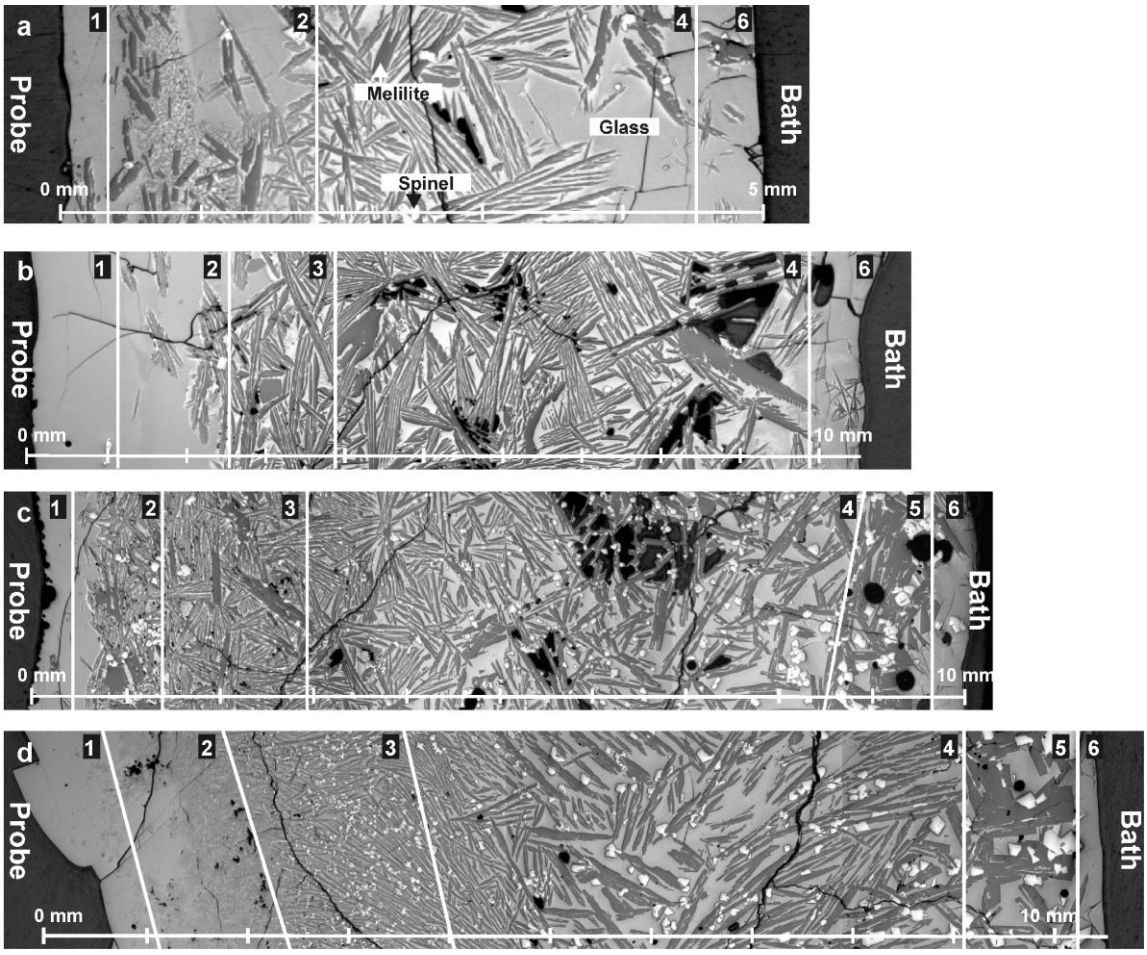

Figure 2-2: Cross-section of a freeze lining created in PbO-ZnO-FeO-Fe_2O_3-CaO-SiO slag using a cold probe. LOM images of the microstructure for a) 1 min, b) 5 min, c) 15 min and d) 120 min submergence times. Six layers are indicated: (1) glass layer, (2) glass with crystals layer, (3) crystalline layer, (4) crystals in liquid layer, (5) sealing crystals layer and (6) entrained slag bath layer. [52]

It was demonstrated in [53] that the thermal history and steady state temperature profile of a freeze lining can be estimated through comparison of the measured phase compositions with the phase equilibria of the system. Uncertainties on the estimate for the investigated freeze lining were found to be ±50 °C at the probe side and ±25 °C on the bath side of the freeze lining.

Figure 2-3 schematically represents the sequence of growth of freeze lining layers on the cold probe, as presented by Campforts et al. in [54]. When a freeze lining is formed on a cooled wall, the formed freeze lining will serve as an insulator, reducing the cooling rate of the subsequently formed portions of the freeze lining. This reduction in cooling rate as the freeze lining is growing results in the formation of several layers with distinctive microstructures in the freeze lining. Generally speaking, each subsequent layer has fewer, but larger solid crystals.

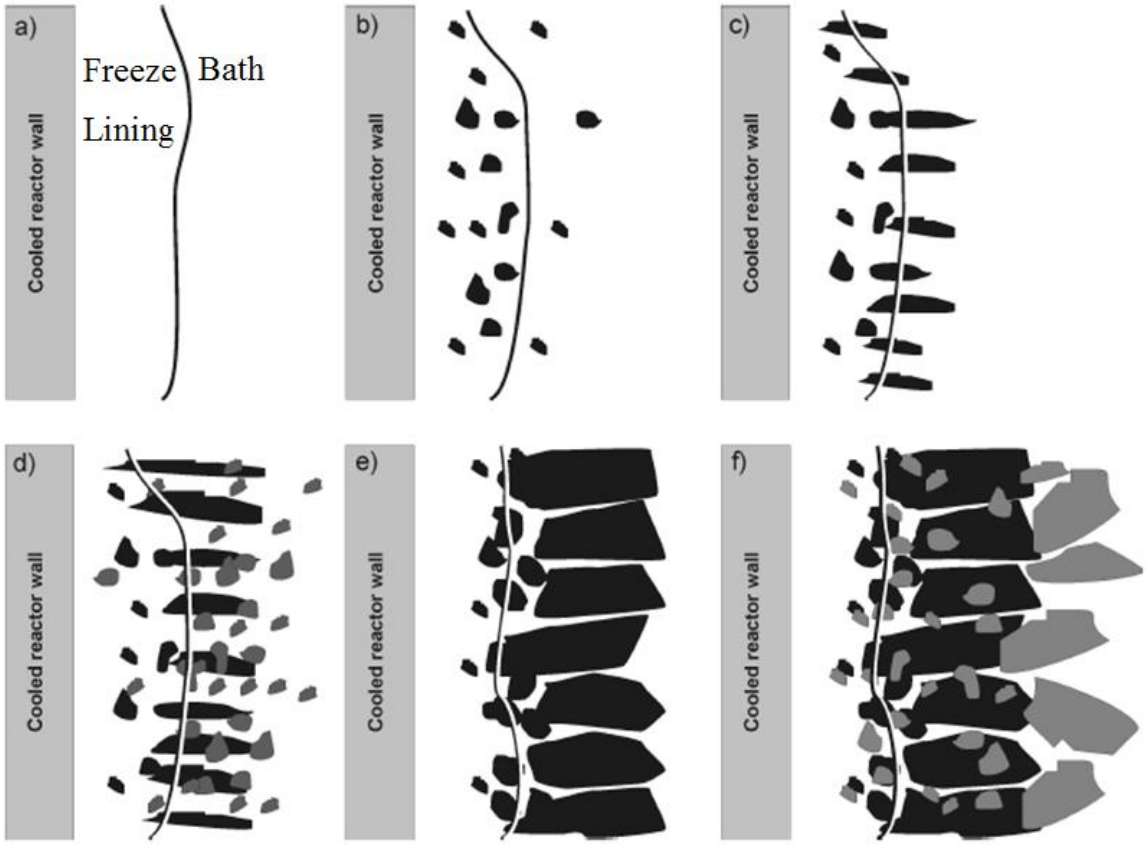

Figure 2-3: A schematic representation of different stages in freeze lining growth on a cooled probe in PbO-ZnO-FeO-Fe_2O_3-CaO-SiO slag: a) a glass/high-viscosity layer, b) non-interlocking crystals in the glass/high-viscosity layer, c) interlocking crystals in the glass/high-viscosity layer resulting in the formation of a crystals in liquid layer, d) crystals in liquid layer containing low-melting interlocking crystals and high-melting non-interlocking crystals, e) the sealing crystal layer of a high-melting interlocking phase and f) a high-melting phase layer formed after the crystals in liquid layer is formed which interlocking crystals differ from the high-melting phase [54]

Campforts et al. [54] then demonstrated the importance of engineering the slag composition to obtain an optimal freeze lining. For example, for high-viscous slags, containing a high percentage of SiO_2, it was found that only a glassy, fully amorphous, layer was formed, leading to a thin freeze lining and

high heat losses. It was concluded that operational demands – rapid formation and sufficient stability – are met when a freeze lining is formed in which the growth of the initial layer is dominated by the presence of interlocking crystals, and subsequently a high-melting crystalline sealing layer is formed.

Mehrjardi et al. [51, 57] studied freeze linings in several slag systems using the gas-cooled cold probe technique. The technique was slightly modified by introducing multiple, thin thermocouples in the bath and freeze lining, allowing for the accurate determination of the temperature profile and interface temperature.

In [51, 57, 58], freeze linings were studied in the Al-Cu-Fe-Si-O. Preliminary experiments were performed to determine the liquidus temperature and phase equilibria of the system [57]. The preliminary freeze lining experiments indicated that no sealing crystal layer was formed in the system. Instead, the interface was found to consist of a mix of cuprite and delaffosite crystals and a highly viscous high-silica liquid. The entrained bulk bath liquid was found to contain primary phase delafossite crystals at steady state, indicating that the steady state bath-freeze lining interface temperature was below the liquidus (see Figure 2-4).

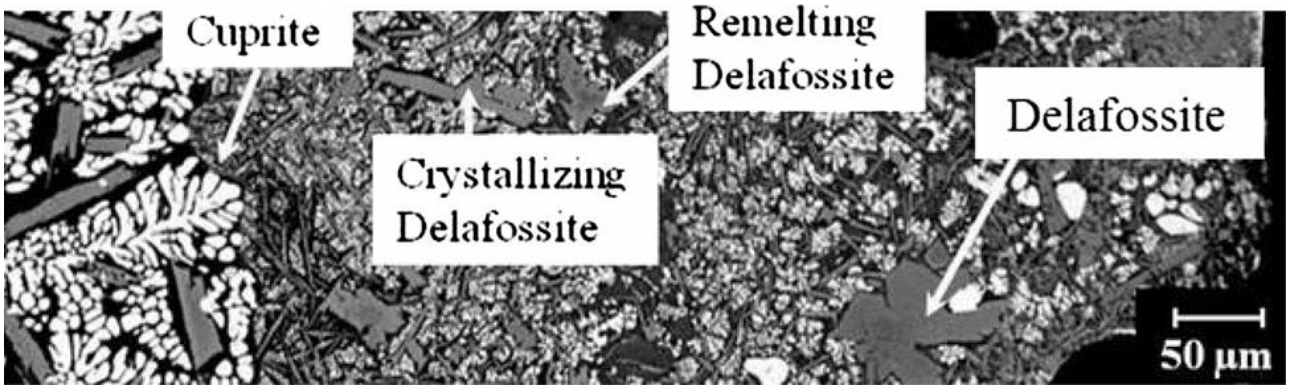

Figure 2-4: Microstructure of the deposit/bath interface. Slag composition, 6.5 wt.% Al_2O_3, 15.4 wt.% SiO_2, 15.8 wt.% Fe_2O_3, 62.3 wt.% Cu_2O; bath temperature: 1165 °C; air flow rate: 100 l/min; rotational speed of crucible: 20 RPM; immersion time, 1 h. [59]

These observations were confirmed in later experiments [51]. In order to explain the observed phenomena, a dynamic steady state mechanism was proposed in which crystals continuously grow while traveling towards the freeze lining and dissolve while traveling back to the bulk bath in a subliquidus boundary layer. This mechanism is illustrated schematically in Figure 2-5 and will be further explained in section 2.4.

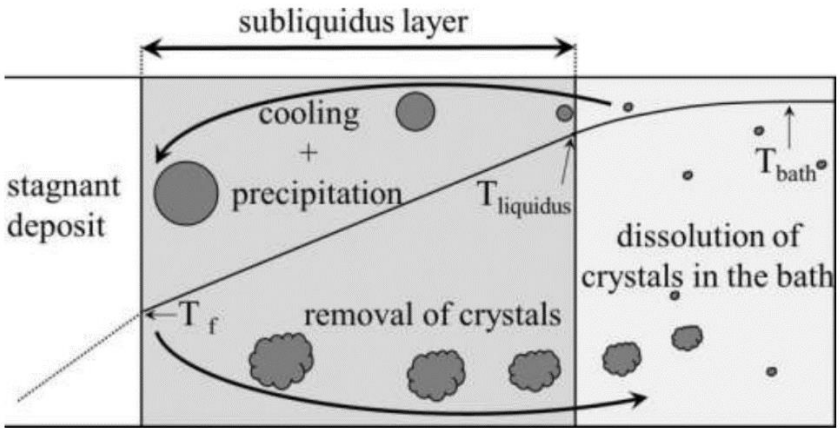

Figure 2-5 Proposed dynamic model illustrating mechanisms taking place within the boundary layer between freeze lining and bath at steady state conditions [51]

The subliquidus boundary layer was added to the microstructural layers observed by Campforts et al. [52], completing the list of microstructural layers used to date. The following description of the layers is taken from Mehrjardi et al. [51].

1) *"The Glassy Layer: In contact with and close to the cold finger is a layer of homogeneous glass. This is the first phase formed on contact of the probe with the melt and, as such, experiences a high initial cooling rate. The composition of the material is uniform and is identical to that of the bulk liquid. Since the material remains in contact with the probe throughout the experiment, it is retained below the glass transition temperature.*
2) *Glass with Microcrystals: Immediately adjacent to the fully glassy layer is material that consists of a matrix of glassy or highly viscous liquid and varying proportions of precipitated crystalline solids. This layer appears to have formed initially as a glass or highly viscous liquid: The fine crystalline phases forming at some later time as the overall frozen deposit thickness increased. The bulk composition of this layer is the same as the bulk bath composition.*
3) *The Closed Crystalline Layer: The material in this layer consists of predominantly crystalline solids. Residual liquid is present between the crystalline structures. The crystals in this next layer appear to have formed directly from the liquid phase, originally above the glass transition temperature. Extent of crystallisation in this layer is such that effectively there is no exchange of material with the bulk bath liquid.*
4) *The Open Crystalline Layer: The next layer of the deposit consists of widely-spaced, relatively large crystals with a significant liquid phase fraction. EPMA measurements have shown that the liquid composition in this layer varies significantly with distance from the bulk liquid and appears to be open to the liquid bulk composition.*

4').Subliquidus Boundary Layer: the temperature is below the liquidus of the bulk bath in this layer, implying the potential for phase precipitation. This layer is an intermediate layer between stagnant deposit and liquid bath.

5) *The Sealing Primary Phase: Theoretically at thermal steady-state and chemical equilibrium conditions the deposit material in direct contact with the liquid bath should consist entirely of the primary phase crystals. It might reasonably be expected that a continuous dense sealing layer of the primary phase would be present under all conditions."* This sealing primary phase layer was not observed in the study of silicate slags during Mehrjardi et al.'s research [60], but was observed in freeze lining formed from molten cryolite salts [60].

Nicol [61] and Scheiwe [62] were able to determine the growth mechanism of freeze linings during the first few seconds/minutes by dipping a copper rod in liquid slag, and immediately quenching the rod and the attached freeze lining on removal from the bath. Both were working in the Cu-Fe-Si-O system. Though the use of crucible differed (Al_2O_3 vs. MgO), the general conclusions were the same.

Layers 1 and 2 (glassy layer and glassy layer with crystals) only take a matter of seconds to form in this particular system. Once larger crystals – delafossite in the above-mentioned research – start to form, they grow rapidly in the form of dendrites and the residual liquid is retained in between the crystals. Depending on the subsequent thermal history, this remaining liquid can then crystallize later on or keep an amorphous structure depending on the crystallization kinetics. As with all freeze lining experiments, a layer of entrained bath slag is present at the bath-side of the freeze lining as the liquid sticks to the freeze lining when taking it out of the bath. The resulting microstructure can be seen in Figure 2-6.

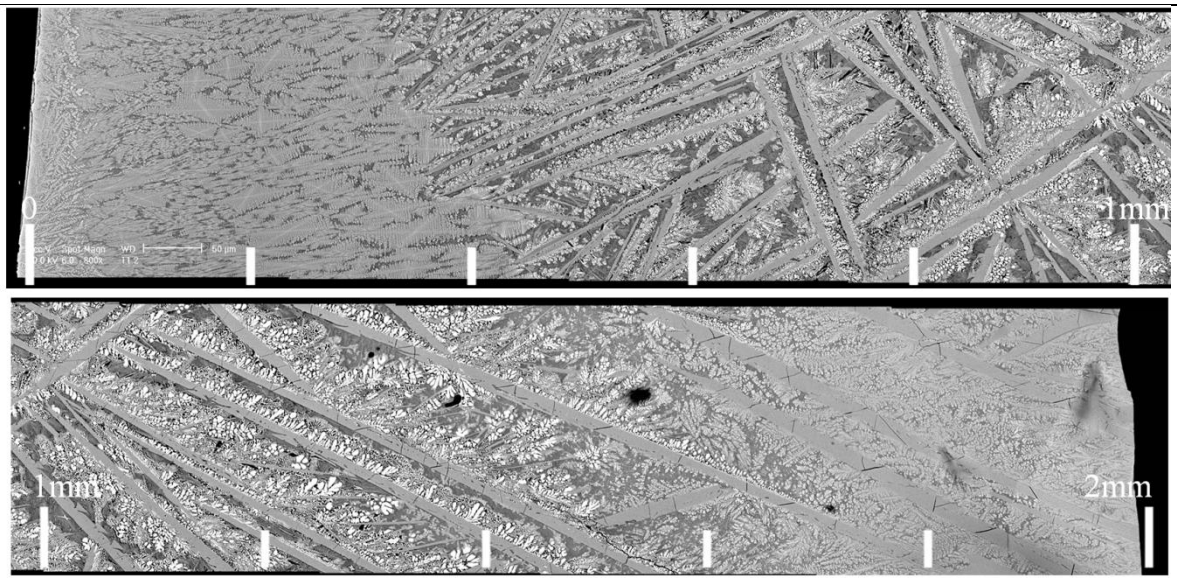

Figure 2-6 Microstructure of freeze lining after 5s [62]. Experiment was performed in the Cu-Fe-Si-Oxide system in a MgO crucible.

Fallah-Mehrjardi et al. [9] also studied freeze linings in the NaF-CaF_2-AlF_3 system using the cooled probe technique. A sealing layer of cryolite solid solution was observed at the bath-freeze lining interface, with the interface temperature at steady state equalling the liquidus temperature.

Freeze linings in an industrial copper converting calcium-ferrite slag [63] created through the cooled probe technique were observed to form a sealing layer of primary spinel phase. Based on the microstructure, it was concluded that detached spinel particles were also present in a subliquidus boundary layer and that the interface temperature at steady state was thus below the liquidus temperature. Based on the macro-images provided and the low viscosity of the system, it is also possible that these spinel particles were in fact attached to the freeze lining and that the interface temperature was approximately the liquidus temperature.

Fallah-Mehrjardi et al. [64] studied freeze linings in a non-ferrous industrial slag through use of the gas-cooled probe technique, both in industrial and laboratory environments. The interface in the freeze lining created in industrial setting was found to consist mainly of an inhomogeneous melilite matrix containing other phases such as wustite and spinel. This type of structure containing of a melilite matrix and other phases was also found in the bath, together with equiaxial spinel crystals. Although in a laboratory setting, the microstructure of the phases differed, similar phase assemblages were present both at the interface (melilite, spinel) and in the subliquidus boundary layer/bath (melilite spinel). Based on the presence of solid crystals in the bath, it was concluded that stable freeze linings can be obtained in pyrometallurgical furnaces when operating below the liquidus temperature.

Jansson et al. [65, 66] studied freeze linings in continuous converting calcium ferrite slags. The freeze linings were found to be fully crystalline throughout the freeze lining, consisting of a complex mix

of phases. At the interface, a mixture of calcium sulphate crystals, calcium arsenate crystals and barite crystals was observed. It was mentioned that part of these crystals might have formed after quenching.

Blancher et al. [26] studied the microstructure of a freeze lining created in a ferromanganese pilot furnace. It was shown that the observed layered microstructure could be linked to the thermal and chemical history of the furnace. Trapped slag droplets were found in the areas of the freeze lining created at low temperatures, or when part of the freeze lining begins to melt. It is mentioned that these droplets are zones of weakness and can cause parts of the freeze lining to fall into the furnace.

2.4 Dynamic steady state mechanism

In industry and in the majority of the previous research, the interface temperature between the bath and the freeze lining is assumed to be the liquidus temperature. Fallah-Mehrjardi et al. [51, 57] experimentally observed interface temperatures between the solidus and liquidus temperature, thus challenging the generally accepted view, and proposed the existence of a subliquidus boundary layer to explain the observed interface temperatures.

The existence of a subliquidus boundary layer was further confirmed through observations in calcium ferrite slags and a non-ferrous industrial slag by Fallah-Mehrjardi et al. [63, 64]. This layer consisting of detached crystals in liquid was also observed in cold modelling experiments performed by Guevara et al. [46].

2.4.1 Conceptual framework subliquidus boundary layer

In a significant departure from the conventional steady state model for freeze lining formation a new conceptual framework was proposed [60]. This new framework argues that at steady state there is a dynamic equilibrium between solidification of material on crystals moving towards the freeze lining and melting of material moving away from the freeze lining (figure 2-5). The proposed mechanism by which the liquid and detached crystals would be moving to and away from the interface are the well-known eddies created by turbulence. This area where part of the slag is continuously solidifying and melting is the 4’ layer described in section 2.3.

When the convective mass transfer to the freeze lining is slow compared to the solidification kinetics, the system might already have reached equilibrium upon reaching the freeze lining interface. When this is the case, no more material is available for solidification onto the freeze lining and the freeze lining will stop growing.

Based on this, the formation of freeze lining is a complex system that depends on many slag and furnace parameters; these parameters would include: viscosity, mass diffusivity, nucleation, crystallisation, dissolution kinetics, liquidus shape and mass transfer in the liquid phase.

Mehrjardi et al. [59] subsequently proposed a single parameter, the total quantity of material deposited on the detached crystals over the time interval t_f it takes a particle to travel through the subliquidus layer, $\Delta M_{A,f}$ (the extent of crystallisation), to determine the steady state bath-freeze lining interface temperature:

$$\Delta M_{A,f} = \int_{t_0}^{t_f} R(t)dt \quad \textbf{(2-10)}$$

Where R(t) is the rate of deposition of A on the detached crystals at time t and t_0 equals the time at which a particle is at the interface between the subliquidus layer and the bath.

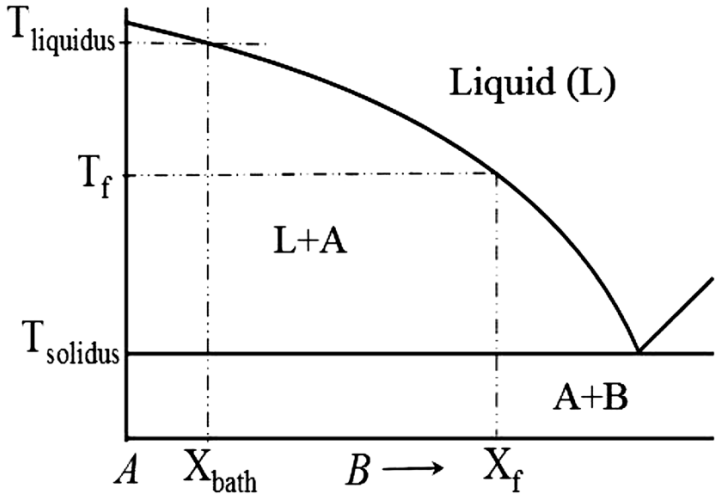

Figure 2-7: Hypothetical binary eutectic phase diagram for the system A-B [59]

It was proposed that the interface temperature can be calculated as the liquidus temperature corresponding to the composition of the liquid at the bath-freeze lining interface, X_f (Figure 2-7), determined by the initial number of moles of A and B in solution, M_{A0} and M_{B0}, and $\Delta M_{A,f}$ according to the following equation:

$$X_f = M_{B0}/\left(M_{B0} + M_{A0} - \Delta M_{A,f}\right) \quad \textbf{(2-11)}$$

As such, high rates of crystallization (R(t)), or high values for t_f would result in a higher extent of crystallization ($\Delta M_{A,f}$), a higher value for X_f, and a lower interface temperature (Figure 2-7).

It should be clear that this framework is only applicable when detached crystals are formed. Fully amorphous freeze linings, as observed by Campforts et al. [54] and discussed earlier in this chapter, are formed in systems with extremely low nucleation and growth rates. For these cases, $\Delta M_{A,f}$ would be close to zero, and the predicted interface temperature according to the framework proposed by

Fallah-Mehrjardi et al. [59] would be equal to the liquidus temperature of the bulk bath, which clearly is not the case.

2.4.2 Effect of fluid flow

Guevara and Irons [45, 46] investigated freeze linings in the $CaCl_2$-H_2O system. The system was chosen for its low liquidus temperatures, ranging from -60 up to 85 °C and for its Prandtl number (50), which is close to that of their selected slag. This choice of system allowed for determination of freeze lining thickness and fluid velocity in real time, which provides some interesting insights in freeze lining growth.

All experiments were performed in an isolated cavity with one hot and one cold side. This resulted in a fluid flow up from the hot side, away from the hot side via the upper side of the cavity, down on the cold side – along the freeze lining – and back towards the hot side via the bottom part of the cavity. This caused the liquid passing the upper section of the cold side to be hotter than the liquid at the lower section. Consequently, the upper part of the freeze lining was thinner than the bottom part.

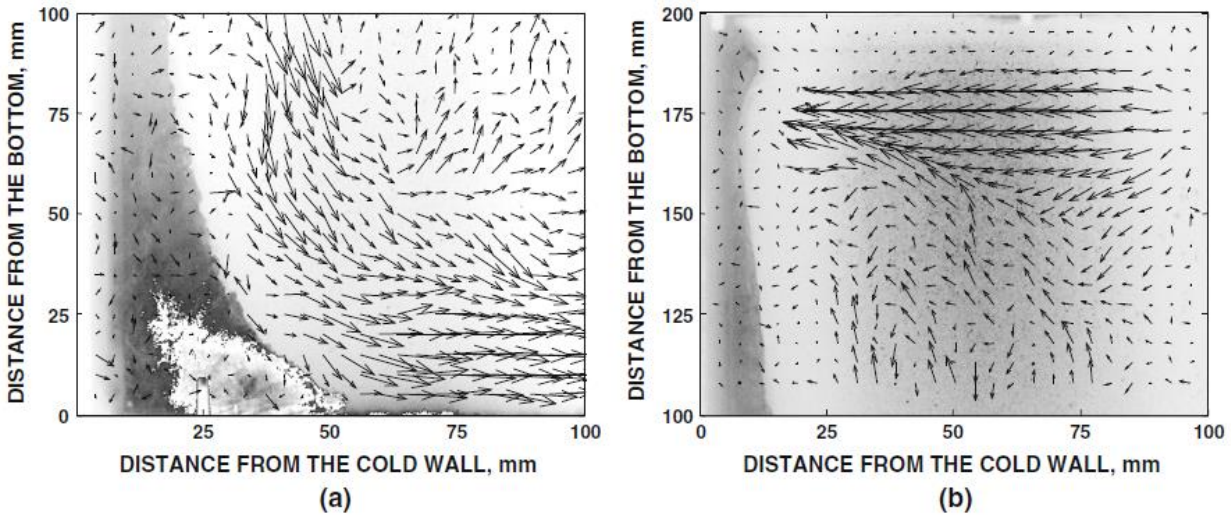

Figure 2-8 Fluid velocity field distribution after 15h of solidification at (a) the bottom and (b) the top quarter of the cavity in a 53 wt.% $CaCl_2/H_2O$ solution [46]

Consistent with the proposed mechanism by Mehrjardi et al. [51], the bath contained solid 300-500 µm large particles beyond the freeze lining, the quantity of which increases with decreasing local temperature. Though in this particular experiment, these particles were observed over the largest part of the cavity, it is mentioned that in real furnaces, the superheat is much larger, which will cause this area to be much thinner.

Mehrjardi et al. [58] investigated the effect of convective flow on the freeze lining microstructure in the Al-Cu-Fe-Si-O system. For this, a series of cold-finger probe experiments with different rotation speeds of the crucible was performed. It was found that higher rotation speeds resulted in thinner

freeze linings, with interface temperatures closer to the liquidus and caused the microstructure at the interface to be more dense.

2.4.3 Effect of viscosity

Based on a series of two experiments in the Al-Cu-Fe-Si-O system (high-SiO_2, low SiO_2), and experiments in the cryolite system, it was concluded that lower viscosity results in higher interface temperatures [9].

2.5 Summary of previous experiments

For comparison of experimental settings and observations, a summary has been proposed of observations in the previous experiments. The system used, bath temperature, rotation speed of the crucible, formation temperature of the solid compounds, crystal morphology, etc. are listed for ease of comparison in later chapters. Morphology of the phases at the interface has been indicated as follows: equiaxed (E), columnar (C), dendritic (D), faceted (F), non-faceted (NF).

Table 2-2: Summary of experiments in the Al-Ca-Fe-Si-Zn-O system [17].

Verscheure et al. [17]							
System	**Al-Ca-Fe-Si-Zn-O**						
Composition (wt.%)		**CaO**	**MgO**	**FeO**	**Al_2O_3**	**SiO_2**	**ZnO**
	Slag A	20.9	0.9	42.4	11.9	19.9	0.0
	Slag B	24.3	1.5	32.6	8.1	27.3	2.8
	Slag A			**Slag B**			
Bath temperature	1350 °C			1335 °C			
Crucible rotation speed	12 rpm			12 rpm			
Steady state?	No (decreasing heat flow)			No (decreasing heat flow)			
Formation temperatures	Wustite: 1270 °C Melilite: 1158 °C Spinel: 1138 °C Olivine: 1080 °C			Wustite: 1209 °C Melilite: 1158 °C Spinel: 1108 °C Olivine: 1080 °C			
p.p. stable during cooling?	Yes			Yes			
Interface temperature	/			/			
Phases at interface	Wustite (E, NF) Melilite (E, NF)			Wustite (E, NF) Melilite (E, F)			

Table 2-3: Summary of experiments in the Al-Ca-Fe-Mg-Si-Zn-O system [55, 56].

Campforts et al. [55, 56]						
System	**Al-Ca-Fe-Mg-Si-Zn-O**					
Composition (wt.%)	**SiO_2**	**CaO**	**Fe**	**ZnO**	**MgO**	**Al_2O_3**
	25.6	18.2	26.0	5.4	1.4	6.4
Bath temperature	1365-1375 (before experiment, then furnace power constant)					
Crucible rotation speed	5.7 rpm					
Steady state?	No (increasing thickness)					
Formation temperatures	Wustite: 1232 °C Melilite: 1198 °C Spinel: 1135 °C Olivine: 1111 °C (for target slag, not actual bath composition)					
p.p. stable during cooling?	Yes					
Interface temperature	/					
Phases at interface	Spinel (E,F) + Olivine (C,F) OR Spinel (E,F) + Melilite (C,F)					

Table 2-4: Summary of experiments in the Al-Ca-Fe-Pb-Si-Zn-O system [52, 53].

Campforts et al. [52, 53]					
System	**Al-Ca-Fe-Pb-Si-Zn-O**				
Composition (wt.%)	**CaO**	**SiO_2**	**PbO**	**ZnO**	**Fe_2O_3**
	11.7	16.3	50.5	8.3	13.2
	120 min experiment				
Bath temperature	1240 °C				
Crucible rotation speed	28.5 rpm				
Steady state?	Yes (no change in measured temperatures)				
Formation temperatures	Spinel: 1228 °C (disappears 950 °C, forms again at 818 °C) Melilite: 1160 °C Hematite: 1022 PCSi: 864 °C $P_2F_2S_2$: 786 °C CAS_2: 786 °C (for final bath composition)				
p.p. stable during cooling?	No				
Interface temperature	1100-1150 °C				
Phases at interface	Spinel (E,F) Melilite (C, F)				

Table 2-5: Summary of experiments in the Al-Ca-Fe-Pb-Si-Zn-O system [54].

Campforts et al. [54]						
System	**Al-Ca-Fe-Pb-Si-Zn-O**					
	M1					
Composition (wt.%)	**CaO**	**SiO_2**	**PbO**	**ZnO**	**Fe_2O_3**	**Al_2O_3**
	12.0	11.0	48.0	4.0	22.0	3.0
Bath temperature	1240 °C					
Crucible rotation speed	28.5 rpm					
Steady state?	No (Decreasing measured temperatures)					
Formation temperatures	Spinel: 1210 °C Melilite: 1180 °C Hematite 1150 °C PCSi: 860 °C $PbFe_{10}O_{16}$: 820 °C (estimated based on graph for initial bath composition)					
p.p. stable during cooling?	No					
Interface temperature	/					
Phases at interface	Melilite (C,F) Spinel (E,F)					
System	**Al-Ca-Fe-Pb-Si-Zn-O**					
	M3 (M2, see Table 2-4)					
Composition (wt.%)	**CaO**	**SiO_2**	**PbO**	**ZnO**	**Fe_2O_3**	**Al_2O_3**
	17.0	26.0	39.0	5.5	10.5	2.0
Bath temperature	1240 °C					
Crucible rotation speed	28.5 rpm					
Steady state?	No (Decreasing measured temperatures)					
Formation temperatures	Spinel: 1220 °C Melilite: 1160 °C Hematite 1160 °C PCSi: 920 °C CAS_2: 840 °C $P_2F_2S_2$: 800 °C (estimated based on graph for initial bath composition)					
p.p. stable during cooling?	No					
Interface temperature	/					
Phases at interface	Melilite (D,NF)					

System	**Al-Ca-Fe-Pb-Si-Zn-O**					
	S1					
Composition (wt.%)	**CaO**	**SiO_2**	**PbO**	**ZnO**	**Fe_2O_3**	**Al_2O_3**
	4.0	11.0	58.5	3.5	20.5	2.5
Bath temperature	1240 °C					
Crucible rotation speed	28.5 rpm					
Steady state?	Yes (changes in measured temperatures similar to changes in bath)					
Formation temperatures	Spinel: 1280 °C Hematite: 1090 °C Melilite: 1070 °C $PbFe_{10}O_{16}$: 810 °C PCSi: 790 °C (estimated based on graph for initial bath composition)					
p.p. stable during cooling?	Yes					
Interface temperature	/					
Phases at interface	Spinel (E,F)					
System	**Al-Ca-Fe-Pb-Si-Zn-O**					
	S2					
Composition (wt.%)	**CaO**	**SiO_2**	**PbO**	**ZnO**	**Fe_2O_3**	**Al_2O_3**
	13.3	22.4	44.8	5.7	11.3	2.5
Bath temperature	1240 °C					
Crucible rotation speed	28.5 rpm					
Steady state?	Yes (no change in measured temperatures)					
Formation temperatures	Spinel: 1280 °C Melilite: 1170 °C Hematite: 1090 °C PCSi: 800 °C $P_2F_2S_2$: 800 °C CAS_2: 780 °C (estimated based on graph for initial bath composition)					
p.p. stable during cooling?	No					
Interface temperature	/					
Phases at interface	Spinel (D?,F) Melilite (C,F)					

System	**Al-Ca-Fe-Pb-Si-Zn-O**					
	S3					
Composition (wt.%)	**CaO**	**SiO_2**	**PbO**	**ZnO**	**Fe_2O_3**	**Al_2O_3**
	8.0	25.3	50.5	4.1	9.5	2.5
Bath temperature	1240 °C					
Crucible rotation speed	28.5 rpm					
Steady state?	Yes (no change in measured temperatures)					
Formation temperatures	Spinel: 1300 °C Hematite: 1260 °C Melilite: 940 °C PCSi: 780 °C CAS_2: 780 °C $P_2F_2S_2$: 770 °C (estimated based on graph for initial bath composition)					
p.p. stable during cooling?	No					
Interface temperature	/					
Phases at interface	fully amorphous freeze lining					

Table 2-6: summary of experiments in the Al-Cu-Fe-Si-O system [57].

Fallah-Mehrjardi et al. [57]				
System	**Al-Cu-Fe-Si-O**			
Composition (wt.%)	**Al_2O_3**	**SiO_2**	**'Fe_2O_3'**	**Cu_2O**
	6.5	15.4	15.8	62.3
Bath temperature	1165 °C			
Crucible rotation speed	20 rpm			
Steady state?	Yes (no change in measured temperatures)			
Formation temperatures	Delafossite: 1140 °C Cuprite: >1100 °C			
p.p. stable during cooling?	Yes			
Interface temperature	1110 °C			
Phases at interface	Delafossite (E,F) Cuprite (D, NF)			
Comments	Detached delafossite crystals in subliquidus boundary layer			

Table 2-7: summary of experiments in the Al-Cu-Fe-Si-O system [51].

Fallah-Mehrjardi et al. [51]				
System	**Al-Cu-Fe-Si-O**			
	2.5 h experiment (≈ 9 h experiment)			
Composition (wt.%)	**Al_2O_3**	**SiO_2**	**'Fe_2O_3'**	**Cu_2O**
	7.6	14.4	15.9	62.1
Bath temperature	1165 °C			
Crucible rotation speed	20 rpm			
Steady state?	Yes (no change in measured temperatures)			
Formation temperatures	Delafossite: 1140 (experiment) / 1150 °C (calculated) Cuprite: 1100 °C (calculated) Tridymite: 1075 °C (calculated) solidus: < 1050 °C (experiment) / 1065 °C (calculated)			
p.p. stable during cooling?	Yes			
Interface temperature	1113 °C			
Phases at interface	Delafossite (E,F) Cuprite (D, NF)			
Comments	Detached delafossite crystals in subliquidus boundary layer			
Fallah-Mehrjardi et al. [51]				
	low-SiO_2 experiment			
Composition (wt.%)	**Al_2O_3**	**SiO_2**	**'Fe_2O_3'**	**Cu_2O**
	5.2	9.2	9.6	76.0
Bath temperature	1190 °C			
Crucible rotation speed	20 rpm			
Steady state?	Yes (no change in measured temperatures, confirmed through communication with author)			
Formation temperatures	Delafossite: / Cuprite: / Tridymite: / solidus: /			
p.p. stable during cooling?	Yes			
Interface temperature	1168 °C			
Phases at interface	Delafossite (E,F)			

Table 2-8: summary of experiments in [58].

Fallah-Mehrjardi et al. [58]				
System	**Al-Cu-Fe-Si-O**			
	0 rpm experiment			
Composition (wt.%)	**Al_2O_3**	**SiO_2**	**'Fe_2O_3'**	**Cu_2O**
	5.8	14.9	15.7	63.6
Bath temperature	1165 °C			
Crucible rotation speed	0 rpm			
Steady state?	Yes (no change in measured temperatures)			
Formation temperatures	Delafossite: 1140 (experiment) / 1150 °C (calculated) Cuprite: 1100 °C (calculated) Tridymite: 1075 °C (calculated) solidus: < 1050 °C (experiment) / 1065 °C (calculated)			
p.p. stable during cooling?	Yes			
Interface temperature	1110 °C			
Phases at interface	Delafossite (C,F) Cuprite (D, NF)			
Comments	Detached delafossite crystals in subliquidus boundary layer			
System	**Al-Cu-Fe-Si-O**			
	60 rpm experiment (for 20 rpm experiment, see high-SiO_2 experiment previous table)			
Composition (wt.%)	**Al_2O_3**	**SiO_2**	**'Fe_2O_3'**	**Cu_2O**
	6.1	15.9	16.1	61.9
Bath temperature	1165 °C			
Crucible rotation speed	60 rpm			
Steady state?	Yes (no change in measured temperatures)			
Formation temperatures	Delafossite: 1140 (experiment) / 1150 °C (calculated) Cuprite: 1100 °C (calculated) Tridymite: 1075 °C (calculated) solidus: < 1050 °C (experiment) / 1065 °C (calculated)			
p.p. stable during cooling?	Yes			
Interface temperature	1127 °C			
Phases at interface	Delafossite (E,F)			
Comments	Detached delafossite crystals in subliquidus boundary layer			

Table 2-9: summary of experiments in the Na-Ca-Al-F system [9]

Fallah-Mehrjardi et al. [9]		
System	**Na-Ca-Al-F**	
	90 min, water quenched experiment	
Composition (wt.%)	**Na_3AlF_6**	**$NaCaAlF_6$**
	85	15
Bath temperature	975 °C	
Crucible rotation speed	0 rpm	
Steady state?	Yes (no change in measured temperatures)	
Formation temperatures	Cryolite: 990 °C (calculated) / 965 °C based on freeze lining experiment CaF_2: 940 °C solidus: 930 °C $NaCaAlF_6$: 620 °C	
p.p. stable during cooling?	Yes	
Interface temperature	965 °C	
Phases at interface	Cryolite (C,F)	
Comments	Estimated liquidus temperature seems to be based on temperature measurements in the freeze lining and the assumption that the interface temperature equals the liquidus temperature. Conclusion that the interface temperature equals the liquidus temperature can only be based on the microstructural characteristics (phase assemblages and compositions)	

Table 2-10: summary of experiments in the Al-Ca-Fe-Mg-Si-Zn-O system [64]

Fallah-Mehrjardi et al. [64]						
System	**Al-Ca-Fe-Mg-Si-Zn-O**					
	in-situ experiment					
Composition (wt.%)	**SiO_2**	**CaO**	**Al_2O_3**	**Fe**	**ZnO**	**MgO**
	27.3	21.5	5.9	22.6	7.3	1.7
Bath temperature	1200 °C					
Crucible rotation speed	0 rpm					
Steady state?	No (changes in measured temperatures)					
Formation temperatures	/					
p.p. stable during cooling?	Yes					
Interface temperature	/					
Phases at interface	Melilite (E,F, contains other crystals) Wustite (rod-like, in melilite matrix) Spinel (E,F)					
Comments	Detached melilite and spinel crystals in subliquidus boundary layer. Melilite contains wustite crystals, similar to interface structure.					

Fallah-Mehrjardi et al. [64]						
System	**Al-Ca-Fe-Mg-Si-Zn-O**					
	lab experiment					
Composition (wt.%)	**SiO_2**	**CaO**	**Al_2O_3**	**Fe**	**ZnO**	**MgO**
	27.5	22.7	6.4	23.7	7.8	1.8
Bath temperature	1230 °C					
Crucible rotation speed	0 rpm					
Steady state?	Yes (no change in measured temperatures)					
Formation temperatures	/					
p.p. stable during cooling?	Yes					
Interface temperature	1201 °C					
Phases at interface	Melilite (E,F) Spinel (E,F)					
Comments	Detached melilite and spinel crystals in subliquidus boundary layer, spinel crystals throughout the bath					

Table 2-11: summary of experiments in the As-Cu-Ca-Fe-Pb-Si-O system [63]

Fallah-Mehrjardi et al. [63]							
System	**As-Cu-Ca-Fe-Pb-Si-O**						
	120 min. experiment						
Composition (wt.%)	**Cu**	**Fe**	**CaO**	**SiO_2**	**MgO**	**PbO**	**As_2O_5**
	22.6	38.9	12.7	1.1	0.6	1.5	1.0
Bath temperature	1300 °C						
Crucible rotation speed	10 rpm						
Steady state?	Yes (no changes in measured temperatures)						
Formation temperatures	Spinel: 1250 °C (calculated from simplified composition)						
p.p. stable during cooling?	Yes						
Interface temperature	1205 °C (or 1250 °C, see comments)						
Phases at interface	Spinel (F)						
Comments	Detached spinel crystals in subliquidus boundary layer. Based on the macrostructure of the freeze lining, viscosity of the slag and microstructure of the freeze lining, it seems possible that these spinel crystals are in fact attached to the freeze lining.						

Table 2-12: summary of experiments in the As-Cu-Ca-Fe-Pb-Si-O system [65, 66]

Jansson et al. [65, 66]								
System	**As-Cu-Ca-Fe-Pb-Si-O**							
	Cu	**Fe**	**CaO**	**MgO**	**As_2O_3**	**BaO**	**PbO**	**SiO_2**
	17.5	30.5	16.3	0.3	3.8	1.4	1.3	1.4
Bath temperature	1325 °C							
Crucible rotation speed	10 rpm							
Steady state?	Yes (thickness constant over time)							
Formation temperatures	Spinel: 1245 °C (calculated using Mtox 7.1 using simplified composition) Ca_2SiO_4: 1160 °C Delafossite: 1080 °C C4WF4: 1080 °C							
p.p. stable during cooling?	Yes							
Interface temperature	/							
Phases at interface	$Ca_4As_2O_9$ Ca_2SiO_4 $CaSO_4$							

Table 2-13: summary of experiments in the CaCl2-H2O system [45, 46]

Guevara and Irons [45, 46]		
System	**$CaCl_2$-H_2O**	
Composition (wt.%)	**$CaCl_2$**	**H_2O**
	53	47
Bath temperature	40-48 °C	
Horizontal velocity liquid	0.4 mm/s (experiment performed in cavity, no rotating crucible)	
Steady state?	Yes (thickness constant over time)	
Formation temperatures	$CaCl_2.4H_2O$ 39 °C $CaCl_2.6H_2O$: 29.9 °C (= solidus)	
p.p. stable during cooling?	Yes	
Interface temperature	30 °C	
Phases at interface	/ (no microstructural analysis)	
Comments	Detached crystals floating around in the liquid in the majority of the bath	

2.6 Current state of the research

During the past decade, knowledge of the microstructure of freeze linings and the mechanisms behind the formation of this microstructure has gradually improved. The gas-cooled probe technique was first used to study the heat transfer characteristics of freeze linings [6]. Subsequently, this approach

was adapted through the use of the water- or air-cooled probes to study freeze lining microstructures by Verscheure et al. [17] and subsequently improved by Campforts et al. [2] and Mehrjardi et al. [60]. This approach has provided important insights into the formation and microstructure of freeze linings.

The latest observations indicate that the bath-freeze lining interface is not necessarily the liquidus temperature of the slag in contact with the freeze lining [51], as was earlier assumed. In fact, freeze linings have been studied with interface temperatures ranging from the solidus temperature to the liquidus temperature of the slag and freeze linings and more extreme interface temperatures have been suggested [60].

To address the multitude of parameters that could have an influence on this interface temperature, a conceptual framework was proposed by Mehrjardi et al. [60]. This framework includes the formation and dissolution of detached crystals in a subliquidus boundary layer adjacent to the freeze lining.

A more mathematical approach was developed, involving the use of the extent of crystallization '$\Delta M_{A,f}$'.

$$\Delta M_{A,f} = \int_{t_0}^{t_f} R(t)dt \qquad \textbf{(2-12)}$$

This term depicts the extent of crystallization over the time it takes the slag to travel through the subliquidus layer. It is intended that this term simplifies the estimation of the effect of certain variables on the formation of a sealing crystal layer.

It has been shown experimentally that, in line with the proposed framework, an increase in bath agitation results in an increase of the bath-freeze lining interface temperature at steady state conditions. It has further been suggested that a decrease in viscosity results in a higher interface temperature and that freeze linings can be formed at subliquidus bath conditions.

At this stage, however, there is insufficient information to provide a true quantitative description of the freeze lining steady-state hotface temperature. Nor have all phenomena that have been observed during freeze lining formation been adequately explained.

3 Objective & scope of the present study

In the current study, the effect of selected key process parameters on the dynamic steady state freeze lining behaviour will be further investigated and quantified where possible by carrying out experimental studies in controlled lab conditions. Particular attention will be paid to the interface temperature of the deposit at thermal steady state conditions, which has been shown to significantly influence both the heat losses and the steady state thickness.

In contrast to previous studies, the freeze lining investigation will be accompanied by a thorough phase equilibria study of the systems being used. The knowledge gained during the phase equilibria experiments will then be used to interpret the results from the cold-finger probe freeze lining experiments.

To accomplish this, a combination of room-temperature experiments and high-temperature experiments will be used. Cold-model experiments will be performed in the $CaCl_2$-H_2O system (Chapter 6). Earlier research [45, 46] suggests that crystallisation in this system is relatively rapid, making it ideal to study the dynamic steady state mechanism proposed by Fallah-Mehrjardi et al. [60].

High-temperature experiments will be undertaken in the 'Cu_2O'-'Fe_2O_3'-MgO-SiO_2 system (Chapter 7) and the Al_2O_3-CaO-SiO_2 system (Chapter 8). The 'Cu_2O'-'Fe_2O_3'-MgO-SiO_2 system was chosen for its application in copper processing combined with its relatively low liquidus temperatures. A thorough phase equilibria study on this system (Chapters 4 and 5) will be performed. The results of this study will be used to assist in the interpretation of phenomena observed in the freeze linings created in this system.

The Al_2O_3-CaO-SiO_2 system was chosen for its application in several industrial processes, including iron making and several recycling processes. A recent phase equilibria study [67] on this system was conducted in parallel with this study, and will be used during the interpretation of freeze lining data in this system (Chapter 8).

In both high-temperature studies, a single parameter influencing freeze lining behaviour is selected for further investigation. In the 'Cu_2O'-'Fe_2O_3'-MgO-SiO_2 system, the bath temperature will be varied, while in the Al_2O_3-CaO-SiO_2 system, several compositions in the gehlenite primary phase field were selected to investigate the effect of slag viscosity.

In conclusion, the following issues will be investigated:

- Phase equilibria of the 'Cu_2O'–'Fe_2O_3'–MgO–SiO_2 system at copper metal saturation, using the standard PYROSEARCH methodology [68].
- Freeze linings in the $CaCl_2$–H_2O system, with particular attention being paid to the effect of solidification kinetics on freeze lining behaviour.
- Freeze linings in the 'Cu_2O'–'Fe_2O_3'–MgO–SiO_2 system, with particular attention being paid to the effect of bath temperature on freeze lining behaviour.
- Freeze linings in the Al_2O_3–CaO–SiO_2 system, with particular attention being paid to the effect of viscosity on freeze lining behaviour. (A phase equilibria study on this system was performed [67], but is not part of this thesis.)

Part III

Phase equilibria

“Imagination is more important than knowledge.” [Albert Einstein]

4 Influence of MgO on the phase equilibria in the CuO_x–FeO_y–MgO–SiO_2 system in equilibrium with copper alloy – part I: methodology and liquidus in the tridymite primary phase field

4.1 Introduction

Magnesia (MgO) is commonly present dissolved in copper smelting, converting and refining slags. The sources of this component are minerals present in concentrates and fluxes, and the dissolution of MgO-containing refractories. Previous studies of copper-free systems [69-73] have shown that the presence of magnesia can significantly influence the liquidus temperatures of slags and the phases that form. Relatively little information is available on the effect of magnesia on copper-containing slags. The current study focuses on the SiO_2–'Cu_2O'–'Fe_2O_3'–MgO system in equilibrium with copper alloy. This information will be used in the interpretation of the subsequent freeze lining experiments reported in this thesis.

Several studies have been performed on the 'Cu_2O'–'Fe_2O_3'–SiO_2 and the 'Cu_2O'–MgO–SiO_2 subsystems in equilibrium with copper. Ruddle et al. [74] investigated the solubility of copper oxide in copper and silica-saturated iron silicate slags for a range of oxygen partial pressures between 1300 and 1400 °C. Oishi et al. [75] measured the oxygen partial pressures of 'Cu_2O'–'Fe_2O_3'–SiO_2 slags at silica saturation in equilibrium with liquid copper between 1217 and 1307 °C using a solid electrolyte galvanic cell technique. Nikolic et al. [76] and Hidayat et al. [77, 78] determined phase equilibria and liquidus temperatures in the 'Cu_2O'–'Fe_2O_3' [76], the 'Cu_2O'–SiO_2 [77], the 'Cu_2O'–MgO–SiO_2 [77] and the 'Cu_2O'–'Fe_2O_3'–SiO_2 [78]] systems in equilibrium with metallic copper using high-temperature equilibration/quenching/electron-probe X-ray microanalysis (EPMA) techniques.

The focus of the present study is on the determination of liquidus temperatures in the tridymite, pyroxene and olivine primary phase fields at temperatures between 1100 and 1300 °C since this is the temperature range of interest to many copper smelting systems. The present paper in this series of 2 papers discusses the modifications made to the standard high-temperature equilibration/quenching/EPMA methodology used for the phase equilibria experiments and the steps

that were undertaken to ensure the achievement of equilibrium. New experimental data are provided on the effect of MgO on the liquidus in the tridymite primary phase field. Paper 2 will provide experimental data on the liquidus in the olivine and pyroxene primary phase fields and the associated solid solutions. This information will subsequently be used in the interpretation of the observed phenomena in the freeze lining experiments performed in this system (see Chapter 7).

4.2 Experimental technique and procedure

The experimental techniques and procedures followed in the present study are based on the methodology developed by PYROSEARCH at the University of Queensland and used in a number of previous studies [68, 76-80]; this approach has been modified for application in the current slag system. First, the general procedure will be described, after which a more detailed description will be given of some of the issues encountered in this particular chemical system and the procedure followed to maximise the accuracy of the results

4.2.1 Preparation of initial Mixtures

Initial sample mixtures, presented in Table 5.1, were prepared using high purity (>99.9 wt.%) powders of Cu_2O, MgO, Fe_2O_3, SiO_2 and Cu, supplied by Alfa Aesar (MA, USA). The oxide powders were weighed within ±1 % of the required amount and ground in an agate mortar until a homogeneous colour was obtained. An extra 20 wt.% metallic copper powder was then added separately and the mixture again ground until homogeneous dispersion of the components was achieved.

For each experiment approximately 0.25 g of the mixture was selected and pelletized into discs with approximately 12 mm diameter and 2 mm thickness using a tool steel die.

Table 4-1: Initial slag compositions for experiments.

Number	SiO_2 (wt.%)	'Cu_2O' (wt.%)	'Fe_2O_3' (wt.%)	MgO (wt.%)
1	3.5	25.0	40.0	35.0
2	2.0	20.0	65.0	15.0
3	4.0	25.0	50.0	25.0
4	4.0	25.0	40.0	35.0
5	2.0	20.0	65.0	15.0

Number	SiO_2 (wt.%)	'Cu_2O' (wt.%)	'Fe_2O_3' (wt.%)	MgO (wt.%)
6	2.5	25.0	55.0	20.0
7	5.0	45.0	10.0	45.0
8	2.5	35.0	55.0	10.0
9	5.0	40.0	40.0	20.0
10	5.0	40.0	48.0	12.0
11	2.5	35.0	40.0	25.0
12	5.0	45.0	10.0	45.0
13	10.0	50.0	5.0	45.0
14	10.0	60.0	20.0	20.0
15	5.0	60.0	20.0	20.0
16	5.0	40.0	48.0	12.0
17	10.0	50.0	5.0	45.0

4.2.2 Selection of containment materials

Experiments in the tridymite primary phase field were performed using SiO_2 crucibles with a diameter of 13 mm and 5 mm depth, made from fused high-purity silica-rod. Platinum wire was attached to the substrates to enable them to be suspended in the vertical tube furnace and alumina rods were attached to the platinum wire to prevent contact of the crucible with the furnace walls (see Figure 4-1a).

Experiments in high-MgO containing phase fields, which will be reported in Part II of this series of two papers, were performed using cylindrical MgO crucibles (99.6 wt.% MgO, 0.17 wt.% ZrO_2, 0.15 wt.% CaO and 0.06 wt.% SiO_2, Nikkato corporation, Japan) cut up in 6 pieces. This resulted in substrates with a final shape illustrated schematically in Figure 4-1b.

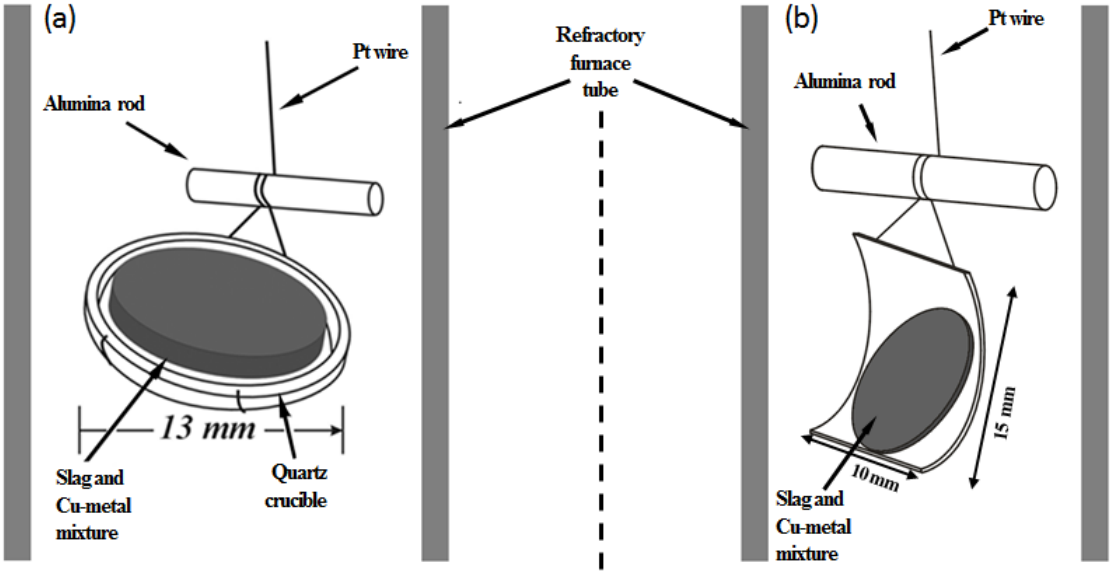

Figure 4-1: Shape of (a) SiO_2 substrate [77] and (b) MgO substrates used in the present study.

4.2.3 Equilibration technique

Substrates were attached to platinum wires and raised into the lower, cold zone of a vertical reaction tube (impervious recrystallized alumina (Alsint), 38 mm OD, 30 mm ID, 1000 mm length, MTC Haldenwanger, Germany) within an electrical resistance lanthanum chromite heated furnace (Figure 4-2).

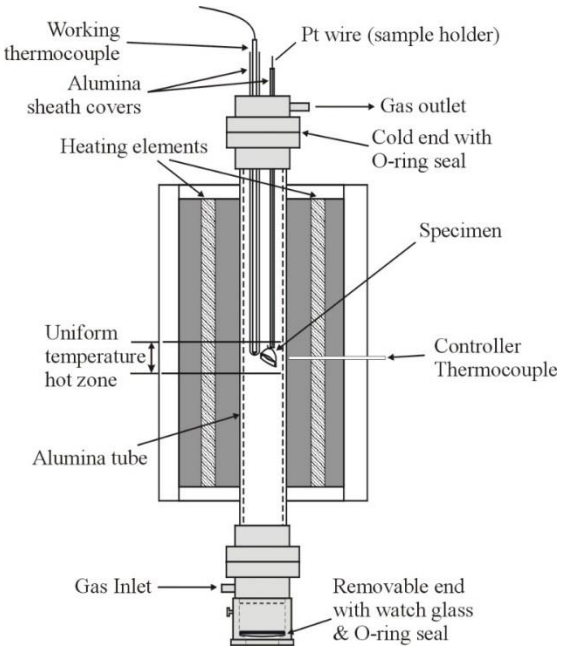

Figure 4-2: Furnace design for equilibrium experiments [77]

With the samples still suspended in the cold region, the reaction tube was sealed and flushed with an inert high-purity argon gas (99.999 % purity, supplied by Coregas, NSW, Australia) for 30 minutes

at a flow rate of approximately 200 ml/min to remove the air present in the furnace. During the remainder of the experiment, argon gas was continuously supplied to the furnace to both remove any ingress air and any gases formed during equilibration.

After the inert gas flushing the samples were raised into the uniform temperature hot zone where they were premelted at 40 °C above the equilibration temperature for a further 30 minutes. The temperature of the hot zone was then lowered to the equilibration temperature. During the experiment, the temperature was controlled to within ±1 °C.

After a predetermined time, the samples were quenched by dropping them directly into NaCl-saturated water. After quenching, the samples were rinsed in tap water and dried on a hot plate. The samples were then mounted in epoxy resin. These mounted samples were ground and polished using conventional metallographic methods.

In order to accurately measure the temperature of the sample, a working type R thermocouple (Pt/Pt-13Rh) inside a recrystallized alumina sheath was placed inside the furnace, immediately adjacent to the sample. This thermocouple was regularly calibrated against a standard thermocouple supplied by the National Measurement Institute of Australia (NSW, Australia). The overall absolute temperature accuracy of the experiment was estimated to be within ±5 °C.

4.2.4 Electron Probe X-ray Micro-Analysis (EPMA)

The microstructures of the samples were investigated by examination of the polished cross-sections using optical microscopy. The samples were subsequently carbon-coated and the compositions of the phases present were measured using an EPMA (electron probe X-ray micro-analyzer JEOL 8200L with wavelength dispersive detectors (WDD), Japan Electron Optics Ltd., Tokyo, Japan) using a 15 kV accelerating voltage and a 15 nA probe current. The standard Duncumb–Philibert ZAF correction supplied with the probe was applied to the raw data obtained from the EPMA measurements.

EPMA–ZAF corrections were made for differences in atomic number, absorption and fluorescence. Corrections are made under the assumption that the sample is both homogeneous in composition and has a flat surface [81].

Fe_2O_3, MgO and $CaSiO_3$ standards supplied by Charles M. Taylor Co. (Stanford, PA) and a Cu_2O standard supplied by Structure Probe Inc. (SPI) Supplies (West Chester, PA) were used to calibrate the EPMA. The amount of oxygen in the samples was not measured, but calculated based on the relative concentrations of Fe, Mg, Si and Cu in the sample and the selected valencies of these metals.

The proportions of cations with different possible oxidation states (i.e. Fe^{2+}/Fe^{3+} and $Cu^{0}/Cu^{+}/Cu^{2+}$) were not measured. For presentation purposes, all iron is presented as Fe_2O_3 and all copper as Cu_2O.

4.3 Discussion of microstructure

As a first step in the analysis of the EPMA results, the microstructure of the final samples was investigated. At the equilibration temperature, the material consists of the liquid slag matrix and the primary phases; on cooling the intention is to retain the liquid slag and alloy as an amorphous or glassy phase and to retain the solids at the respective composition present at the equilibration temperature.

Examples of backscattered electron (BSE) images of the SiO_2–'Cu_2O'–'Fe_2O_3'–MgO slag sample cross sections are given in Figure 4-3. Hexagonal-shaped pyroxene ($MgSiO_3$) crystals and rectangular-shaped tridymite (SiO_2) crystals can be seen to be distributed in the matrix.

Near the outer sample surface, the quenched matrix is present as an amorphous or glassy phase. At further distances from the surface, the matrix consists of glass containing a large amount of submicron copper particles (SCP) (<1 µm) (Figure 4-3a) or 1–10 µm, irregular crystals (CR) (Figure 4-3b). The size of the submicron copper particles in Figure 4-3a increases with increasing distance from the free surface, however, no submicron copper particles are observed in the areas surrounding the large copper droplets (10–300 µm) and in some areas adjacent to the pyroxene crystals.

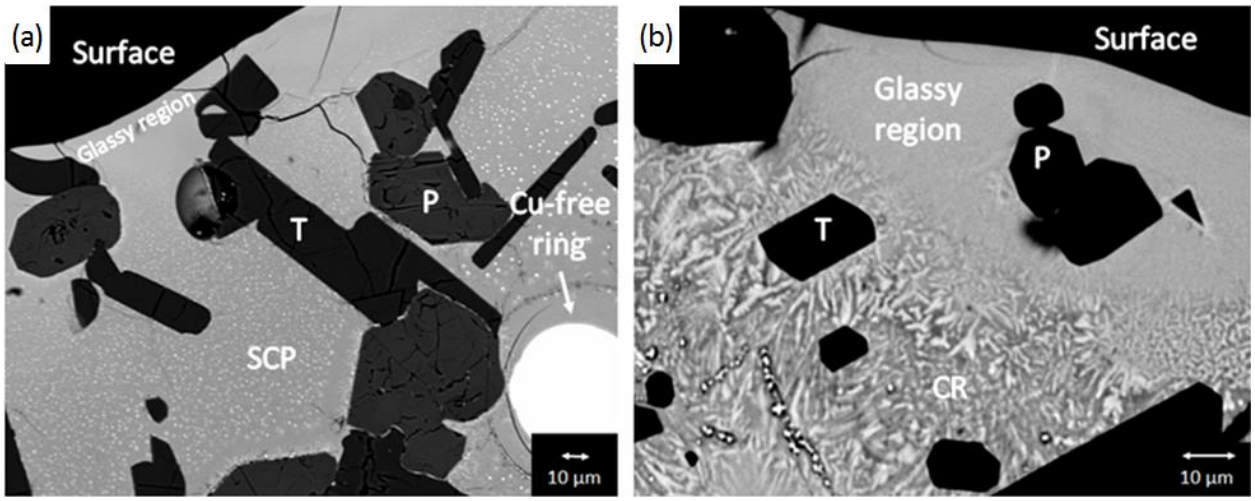

Figure 4-3: BSE images illustrating the different features in the microstructure: glassy region, submicron copper particles (SCP), crystallized region (CR) and copper-free ring around copper droplets. The contrast in (b) has been increased to enhance the visibility of the crystallized material. Phases present are Cu alloy (Cu), Tridymite (T) and Pyroxene (P).

Possible mechanisms of the formation of the submicron copper particles are the precipitation of Cu from the slag during cooling due to a change in solubility in slag with temperature, or the disproportion reaction proposed by Jalkanen et al. [82].

$$Fe^{2+}{}_{sl} + Cu^{+}{}_{sl} = Fe^{3+}{}_{sl} + Cu^{0} \qquad \textbf{(4-1)}$$

The copper concentration in slag in the "ring" and the regions between the submicron copper particles was measured to be significantly lower than in the glassy region (Table 5.2). The absence of submicron copper particles in a ring surrounding the larger copper droplets and areas around the pyroxene crystals could then be explained by preferential precipitation of the copper from the slag onto the existing copper droplets.

Table 4-2: Comparison of mean concentrations of matrix in between submicron copper particles and in a well-quenched area.

	wt.% MgO	wt.% SiO_2	wt.% 'Cu_2O'	wt.% 'Fe_2O_3'	wt.% SiO_2/ wt.% 'Fe_2O_3'
In well-quenched area	4.8	34.5	19.8	40.9	0.84
Between submicron copper particles	4.9	36.0	17.2	41.9	0.86

As can be seen in Table 5.2, the SiO_2/Fe_2O_3 ratio of the liquid slag in between the submicron copper particles does not equal that of the well-quenched liquid slag. Additionally, Figure 4-4 shows that the submicron copper particles are associated with other microcrystals. As the SiO_2/Fe_2O_3 ratio of the well quenched area is lower than that in between submicron copper particles, the observed

microcrystals most likely consists of a phase rich in Fe, such as delafossite or spinel, which are anticipated to form at lower temperatures.

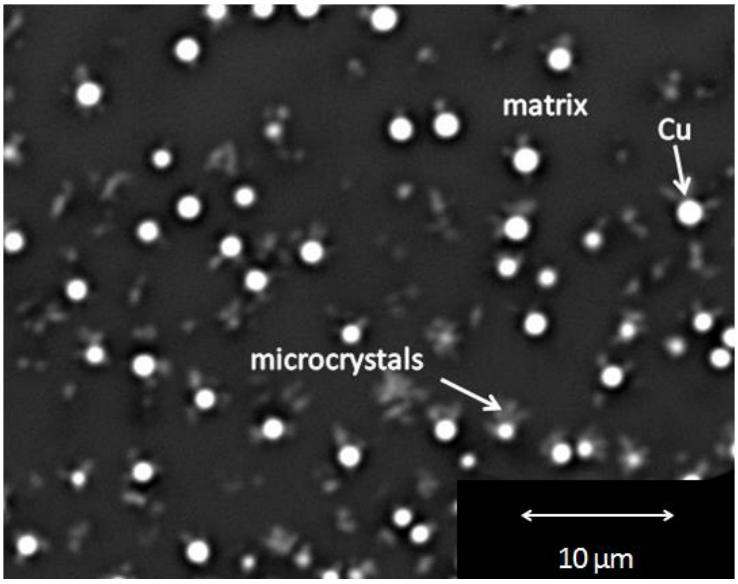

Figure 4-4: Close-up of submicron copper particles (white spots) in the liquid slag phase, showing other microcrystals surrounding the copper particles. Microstructure is similar to the one observed by Jalkanen et al. [15] in iron silicate copper smelter slags.

To avoid uncertainties associated with copper precipitation, measurements of liquid slag were taken only in the homogeneously-looking, well quenched areas as these will provide the most accurate values of the liquid slag composition. To ensure that this represents the true equilibrium value the area analysed should also be immediately adjacent to the primary phases present at equilibration temperature. Measurement of the slag composition as a function of distance from the solids in this well-quenched region also ensures that these compositions are representative of the equilibrium liquid slag phase.

Even in homogeneously-looking areas, submicron copper particles might be present beneath the polished surface that is being analysed – the take-off volume of the EPMA is in the range of 1 μm^3 [81], while some copper particles and crystallites are clearly smaller than this in size.

Multiple measurements – e.g. 10 point analyses – are necessary to ensure the composition of the well quenched area is accurately measured. These 10 measurements were taken parallel to the outer surface of the slag. A standard deviation of less than 0.6 wt.% has been shown to be achievable in the present study (see Figure 4-5). This approach is similar to that previously described by Nikolic et al. [76].

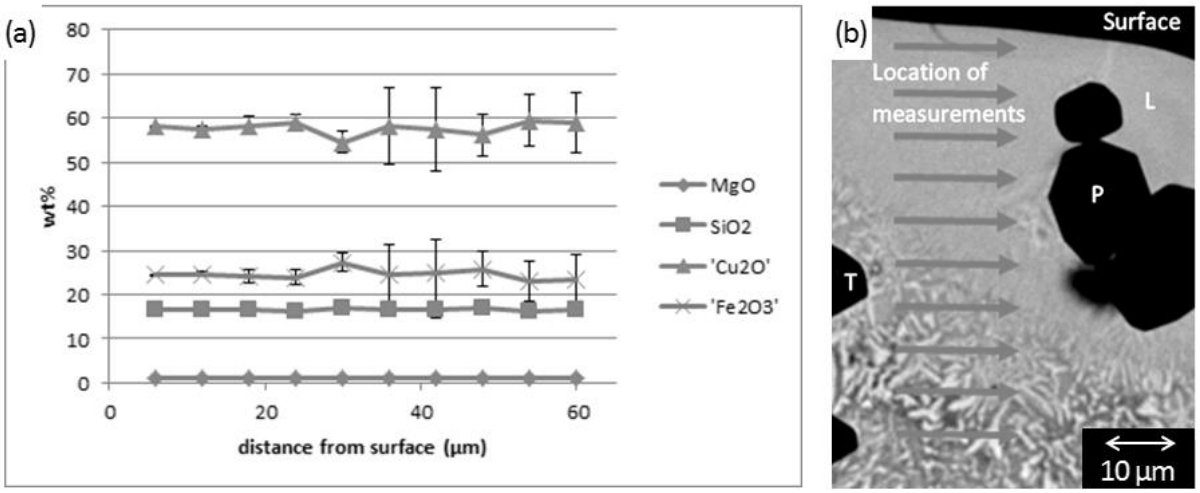

Figure 4-5: Example of EPMA composition analysis of quenched slag. Average values and standard deviations of 10 x 10 measurements on a straight line parallel to the surface. The standard deviations increase with increasing distance from the surface. Experiment was undertaken in equilibrium with tridymite, pyroxene and metallic copper phases at 1100 °C.

Figure 4-5 shows an example of measurements as a function of distance from the free surface. It can be seen that the standard deviation of the measurement of each component increases with increasing distance from the free surface; this coincides with a transition from the glassy, well-quenched region to increasingly coarser crystals that have been formed in the matrix material. The maximum and minimum values reflect increasing proportions of one or other of the crystalline material in the take-off volume. In the limit the compositions will be those of the crystalline phases formed. The mean value of concentrations obtained in the crystallized regions do not necessarily reflect the mean value of the original liquid slag, but rather approach it as the proportion of crystalline solids decreases.

The standard error, or uncertainty, due to inhomogeneity of the quench can be calculated as the standard deviation divided by the root of the number of measurements, in this case 10. On top of this, there is the standard uncertainty associated with EPMA, which is estimated as 1 % of the measured compositions based on measurement of standards after calibration and measurements of stoichiometric compounds present in the investigated samples. For simplicity's sake, a single absolute uncertainty of ±0.6 wt.% will be reported, based on the addition of the absolute and relative errors for the highest measured concentration in liquid slag in the entire study, which was around 80 wt.% (see Chapter 5).

4.4 Confirmation of achievement of equilibrium

In order to be able to confirm the achievement of equilibrium, four conditions have to be fulfilled:

1) No more changes in chemical composition of individual phases occurring over time.

2) Phases are uniform in composition.
3) Same results are obtained when approaching equilibrium from different starting compositions
4) No reactions are occurring that prevent the sample from reaching equilibrium.

Several experiments were performed to confirm these conditions were met. All measurements were taken in areas where the quenching was sufficiently fast so as to prevent the precipitation of submicron copper particles and microcrystals. These areas are located near the surface, where direct contact with the cooling medium results in the highest achievable cooling rates.

4.4.1 Changes over time

A series of experiments was performed using the same starting composition of powders with equilibration times ranging from 6 to 48 hours at 1200 °C, at tridymite saturation in equilibrium with metallic copper (Table 5.3). It was observed that in the 6 hour sample, variations in composition of the rapidly quenched material were measured, indicating that reactions were still taking place at the moment of quenching. In the 24 and 48 hour samples, these inhomogeneities had disappeared and the compositions of the phases within these samples were within the standard deviation of 0.6 wt.%. As a result of these experiments, all samples in the phase equilibrium studies were held at the equilibration temperature for 24 hours.

Table 4-3: Measured liquid slag compositions in wt% of the 6h, 24h and 48h experiment with an initial powder composition of 5 wt% MgO, 40 wt% SiO_2, 40 wt% Cu_2O and 20 wt% Fe_2O_3, experiments were performed at 1200 °C under Cu-metal and tridymite saturation.

Equilibration time	MgO (wt.%)	SiO_2 (wt.%)	'Cu_2O' (wt.%)	'Fe_2O_3' (wt.%)
6 h	4.1	27.7	42.4	25.9
24 h	4.7	30.1	38.7	26.6
48 h	4.8	30.0	38.4	26.9

4.4.2 Uniform composition

In those cases where a relatively large area (>10 by 10 µm) of well-quenched liquid slag was obtained, a uniform composition was measured over the whole area.

In the solid phases, measured compositions were uniform. For example, 10 measurements on a straight line in the tridymite phase showed less than 0.1 % standard deviation for SiO_2.

4.4.3 Direction of approach to equilibrium

Experiments were carried out with bulk oxide compositions in both the tridymite and pyroxene primary phase fields.

When working in the tridymite primary phase field, experiments were performed using both an excess and a shortage of SiO_2 in the original powder mixture relative to the final bulk slag composition. The approaches to equilibrium in these cases are quite different. In the former, solid silica is present already in the mixture, while in the latter the dissolution of the tridymite substrate into the liquid slag takes place. In all of these experiments the resulting composition of the liquid slag was the same (Table 5.4).

Table 4-4: Measured compositions in wt.% of the liquid slag in the experiments using an excess and a shortage of SiO_2 in the initial oxide mixture, at 1200 °C in equilibrium with tridymite and metallic copper.

Initial condition	MgO (wt.%)	SiO_2 (wt.%)	"Cu_2O" (wt.%)	"Fe_2O_3" (wt.%)
SiO_2 surplus	3.6	26.0	51.7	18.8
SiO_2 shortage	3.7	26.2	51.9	18.2

4.4.4 Analysis of reactions

The final step in the confirmation of the achievement of equilibrium is the analysis of possible reactions. In order to make sure that no reactions were overlooked, a general method for the systematic analysis of reactions and countermeasures to ensure equilibrium is achieved was developed.

First, the experiment was divided into three stages: a) heating + premelt, b) equilibration and c) quenching.

For each stage, all possible reactions were classified in one of 5 categories: a) solid–solid, b) solid–liquid, c) solid–gas, d) liquid–liquid and e) liquid–gas.

When applying this method to the oxide/metal system currently under study, the following reactions were identified:

Table 4-5: List of possible reactions taking place during an equilibration experiment above the solidus temperature.

Step/ type of reaction	Reaction	Countermeasures
Heating + premelt		
Solid–solid	Formation of compounds	Ensure equilibrium of peritectic reactions by avoiding reactions that require solid state diffusion.

Step/ type of reaction	Reaction	Countermeasures
Solid–liquid	Dissolution of substrate in slag	Desirable. This supersaturates the liquid slag with substrate component.
	Melting of components in powders	If remnants of powders are observed, increase premelt time/temperature. Choose premelt temperature above a binary eutectic.
	Dissolution of components in melt	Intended
Solid – gas	Decomposition of unstable oxides (Fe_2O_3, …)	Include experiments with equilibrium solid oxides in the initial mixture
Equilibration		
Solid – liquid	Formation of (metastable) phases	Approach equilibrium from different starting compositions. Ensure sufficient residence time for uniform phase compositions.
	Dissolution of oxide components in phases/substrate	Decrease particle/substrate size.
Liquid – liquid	Dissolution of slag components in alloy	Start from estimated equilibrium alloy composition to test reaction pathways and avoid large changes in slag composition.
	Dissolution of alloy components in slag	
Liquid–gas	Oxidation of alloy	Inert gas atmosphere. When working under fixed p_{O2}, start from estimated equilibrium slag composition
	Vaporization of slag components.	Work in closed system or lower equilibration time and increase sample size.
		Check composition profiles in sample.
Quenching		
Solid–liquid	Precipitation of micro-crystals from melt	Faster quench (open substrate, NaCl saturated water), smaller sample size.
Liquid–liquid	Dissolution of slag components in alloy	Faster quench, smaller sample size.

For each of these reactions, compositional profile measurements of micron scale were performed using EPMA close to the phase boundaries of phases involved in the reaction, to verify that no compositional gradients are present; differences in phase composition indicate that local equilibrium has not been achieved.

An example of this is given in Figure 4-6, where the liquid slag compositions measured near a tridymite crystal are shown. If the tridymite crystal was still being formed at the moment of quenching, a compositional gradient of SiO_2 in the liquid slag close to the crystal should be observed. As SiO_2 in the liquid slag would be consumed during the formation of tridymite, a lower SiO_2 concentration would be expected near the crystal. However, it is clear from measurements in the well-quenched area immediately adjacent to the tridymite crystal (Figure 4-6) that this is not the case.

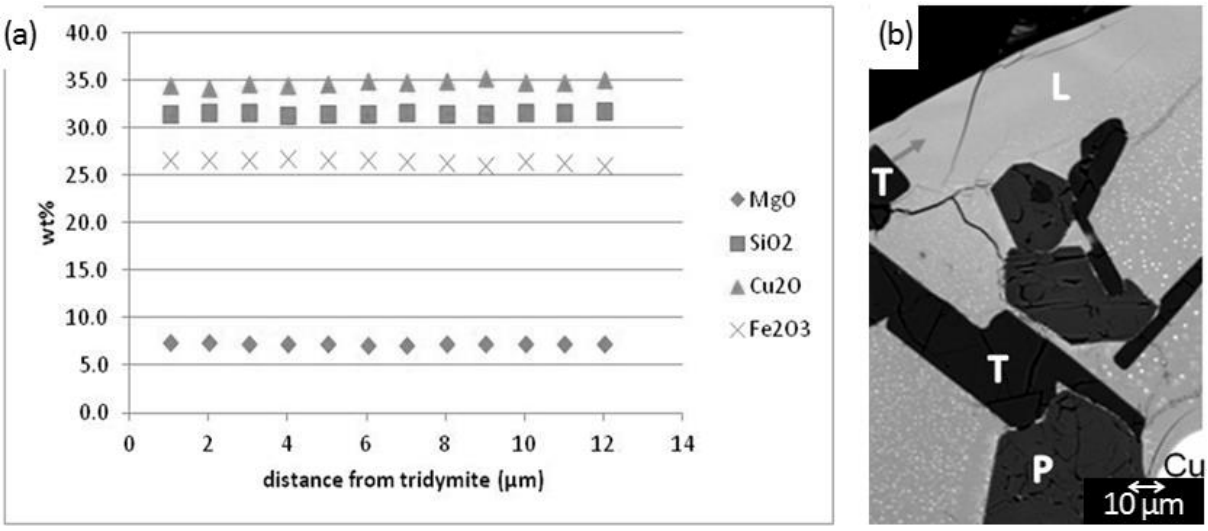

Figure 4-6: Compositions of the liquid slag phase measured on a straight line perpendicular to the tridymite/slag interface (arrow, (b)) in the well-quenched area. Experiment was performed in equilibrium with tridymite and metallic copper at 1200 °C. Phases visible in the micrograph are tridymite (T), pyroxene (P), copper metal (Cu) and liquid slag (L).

Dissolution of Fe in Cu

The composition of the alloy powder in the initial mixture is 99.9 wt.% copper. Following equilibration with the slag, measurements of the copper droplets (10–300 µm diameter) indicated they contain 0.0 and 1.5 wt.% Fe. No clear correlation between the slag composition and the concentration of dissolved Fe was discernible.

Further analysis of the copper droplets showed that the measured composition varied systematically inside each droplet. The regions closer to the slag–copper interface contained (0.7–1.5 wt.% Fe), while the alloy in the inner region was found to be low in iron (<0.1 wt.% Fe).

The exact reason for the phenomenon has yet to be determined and will be the subject of further examination. Because of this, no alloy compositions will be reported.

4.5 Results and discussion

Table 5.6 shows the measured compositions of liquid slag and solids for samples equilibrated in the tridymite primary phase field, including the tridymite–pyroxene, tridymite–spinel and tridymite–pyroxene–spinel phase boundary conditions, of the 'Cu_2O'–'Fe_2O_3'–MgO–SiO_2 system in equilibrium with metallic copper. The concentrations of oxide components were calculated based on measured cation-concentrations, normalized and reported as Cu_2O, Fe_2O_3, MgO and SiO_2. The estimated uncertainties in compositions are within ±0.6 wt.%.

Elemental data can be obtained by recalculating the reported wt.% of all oxides to the total before normalization ('Measured total') and multiplying by the wt.% of the metal in each oxide. Note that the measured totals should not be used to calculate the ratios of Fe^{2+}/Fe^{3+} and/or Cu^0/Cu^{1+}.

Table 4-6: Experimentally determined phase compositions for the 'Cu_2O'–'Fe_2O_3'–MgO–SiO_2 system in equilibrium with Cu-metal. Equilibration time was 24h (48h for the sample indicated with '*')

Temperature (°C)	Initial composition	Phase	SiO_2 (wt.%)	'Cu_2O' (wt.%)	'Fe_2O_3' (wt.%)	MgO (wt.%)	Measured total (wt.%)
1100	1	Liquid	16.5	58.0	24.4	1.1	100.3
		Tridymite	98.3	0.9	0.7	0.0	100.7
		Pyroxene	55.9	2.4	9.2	32.5	103.9
		Spinel	0.2	5.1	91.2	3.5	102.9
1100	2	Liquid	15.9	66.0	17.1	1.0	100.9
		Tridymite	98.8	1.0	0.2	0.0	100.4
		Pyroxene	55.8	3.3	6.8	34.1	103.2
1150	6	Liquid	20.2	59.9	17.9	2.0	100.7
		Tridymite	98.6	1.1	0.3	0.0	100.0
		Pyroxene	56.5	2.4	6.3	34.8	102.4
1150	5	Liquid	21.1	54.9	21.9	2.2	101.5
		Tridymite	98.5	1.2	0.4	0.0	101.0

Temperature (°C)	Initial composition	Phase	SiO_2 (wt.%)	'Cu_2O' (wt.%)	'Fe_2O_3' (wt.%)	MgO (wt.%)	Measured total (wt.%)
		Pyroxene	55.7	2.2	8.8	33.3	101.9
1150	5	Liquid	20.9	55.1	21.8	2.2	101.9
		Tridymite	98.3	1.2	0.5	0.0	100.6
		Pyroxene	55.6	2.6	8.8	33.1	103.6
1150	4	Liquid	21.6	48.3	27.9	2.3	101.4
		Tridymite	98.6	0.9	0.5	0.0	100.4
		Pyroxene	55.5	1.9	10.8	31.8	102.5
1150	3	Liquid	22.1	45.8	29.6	2.6	100.6
		Tridymite	98.8	0.7	0.5	0.0	100.5
		Spinel	0.1	3.1	93.4	3.3	104.2
1150	3	Liquid	22.1	45.2	30.1	2.6	101.1
		Tridymite	98.8	0.7	0.5	0.0	101.8
		Pyroxene	55.3	1.7	11.7	31.4	102.9
		Spinel	0.1	3.3	93.2	3.4	103.4
1200	11	Liquid	25.5	42.4	29.1	3.0	101.2
		Tridymite	98.6	0.8	0.5	0.0	100.8
1200	9	Liquid	30.1	38.7	26.6	4.7	102.5
		Tridymite	98.8	0.7	0.5	0.0	101..2
		Pyroxene	55.6	2.4	10.0	32.0	102.0
1200*	9	Liquid	30.0	38.4	26.9	4.8	102.2
		Tridymite	97.6	1.7	0.8	0.0	99.8
		Pyroxene	54.3	4.8	10.2	30.7	101.2
1200	8	Liquid	25.2	55.6	15.8	3.4	100.5
		Tridymite	98.5	1.3	0.2	0.0	101.3

Temperature (°C)	Initial composition	Phase	SiO_2 (wt.%)	'Cu_2O' (wt.%)	'Fe_2O_3' (wt.%)	MgO (wt.%)	Measured total (wt.%)
		Pyroxene	56.6	2.1	5.9	35.5	100.8
1200	8	Liquid	24.8	56.7	15.1	3.4	100.7
		Tridymite	98.9	0.9	0.2	0.0	100.3
		Pyroxene	56.2	2.0	6.8	35.1	101.5
1200	10	Liquid	25.4	52.0	19.1	3.5	99.4
		Tridymite	98.8	0.8	0.3	0.0	98.9
		Pyroxene	56.6	2.2	7.0	34.2	100.2
1200	10	Liquid	26.0	51.7	18.8	3.6	99.3
		Tridymite	98.8	0.9	0.3	0.0	100.6
		Pyroxene	56.9	1.7	7.7	33.7	102.1
1200	7	Liquid	31.3	26.9	36.7	5.1	102.0
		Tridymite	99.0	0.2	0.8	0.0	101.3
		Pyroxene	54.0	1.5	16.3	28.1	103.7
		Spinel	0.2	1.7	95.2	2.9	103.5
1250	12	Liquid	34.0	20.1	40.9	5.0	104.0
		Tridymite	98.7	0.6	0.7	0.0	100.8
1250	13	Liquid	36.9	15.9	39.5	7.6	102.8
		Tridymite	98.8	0.4	0.7	0.0	99.9
		Pyroxene	53.9	0.7	18.6	26.8	102.9
1250	14	Liquid	36.6	32.8	23.9	6.7	101.6
		Tridymite	98.6	0.9	0.6	0.0	100.4
		Pyroxene	55.5	1.7	12.4	30.5	102.9
1250	15	Liquid	36.9	23.7	32.5	6.9	100.5
		Tridymite	98.8	0.7	0.5	0.0	100.5

Temperature (°C)	Initial composition	Phase	SiO_2 (wt.%)	'Cu_2O' (wt.%)	'Fe_2O_3' (wt.%)	MgO (wt.%)	Measured total (wt.%)
		Pyroxene	55.2	1.5	14.7	28.7	101.3
1250	17	Liquid	38.4	9.9	44.5	7.3	104.1
		Tridymite	98.9	0.3	0.8	0.0	102.4
		Pyroxene	50.7	0.3	29.9	19.1	104.6
1300	16	Liquid	40.5	30.9	19.5	9.1	99.8
		Tridymite	99.0	0.6	0.3	0.0	100.7

The measured compositions were projected onto the 'Cu_2O'–'Fe_2O_3'–SiO_2 plane by normalizing the sum of the weight percentages of 'Cu_2O', 'Fe_2O_3' and SiO_2 to 100 wt.%, as is illustrated in Figure 4-7.

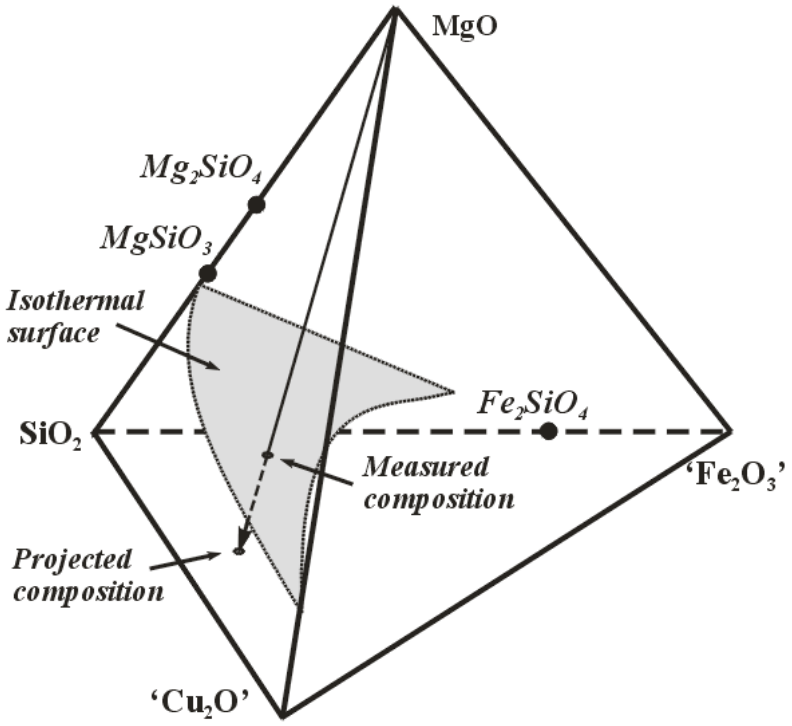

Figure 4-7: Projection of the measured liquidus compositions onto the 'Cu_2O'–'Fe_2O_3'–SiO_2 plane.

The results from the current study were combined with measurements obtained by Hidayat et al. [77, 78] and are represented on Figure 4-8. Liquidus isotherms were manually fitted to the points.

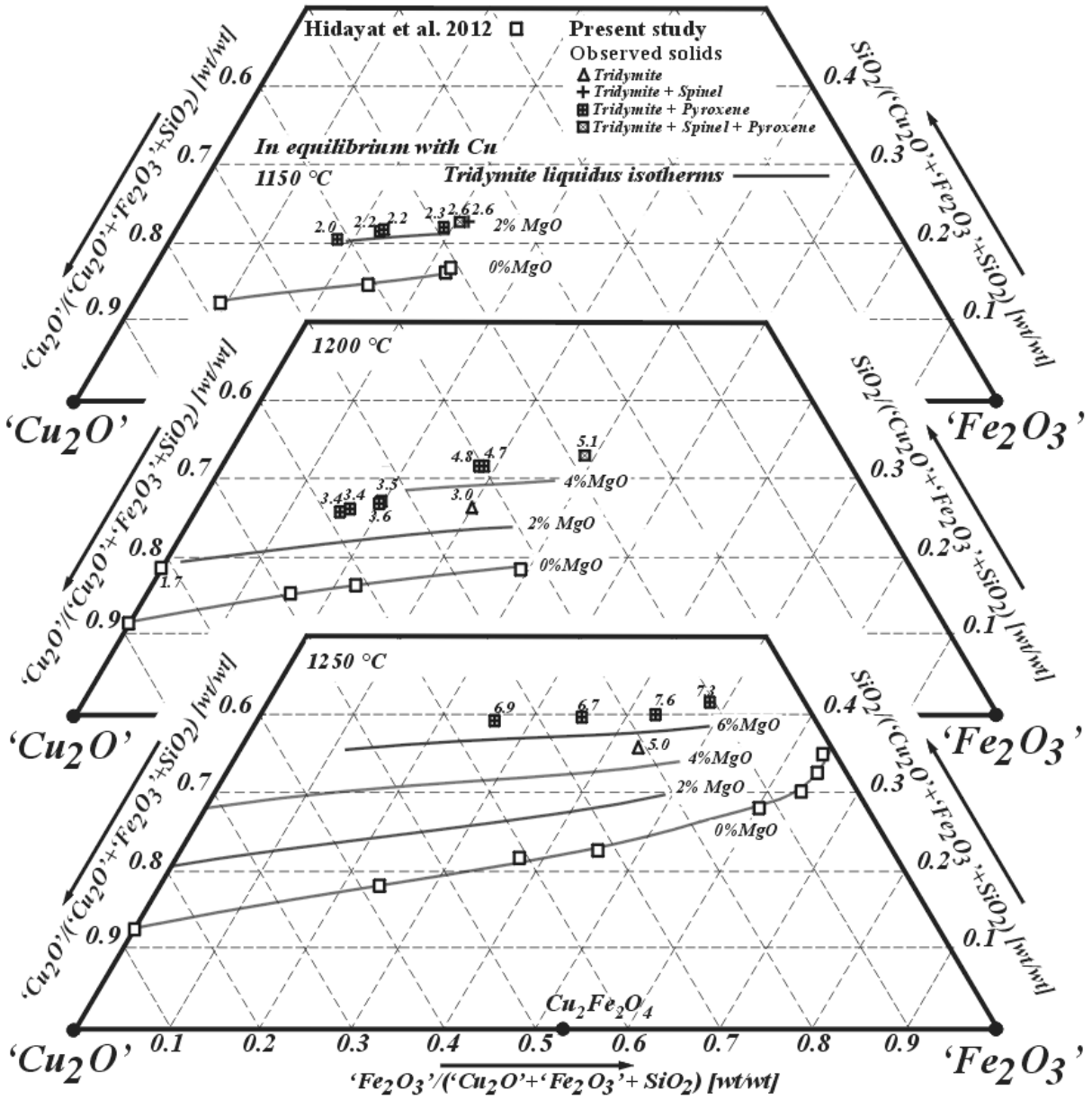

Figure 4-8: Projection of the tridymite liquidus in the 'Cu₂O'–'Fe₂O₃'–MgO–SiO₂ phase diagram in equilibrium with Cu-metal on the 'Cu₂O'–'Fe₂O₃'–SiO₂ plane at 1150, 1200 and 1250 °C. Measured MgO concentrations are given for each experimental point.

The liquidus isotherms in the tridymite primary phase field in this system are principally a function of silica concentration and relatively insensitive to 'Cu₂O'/'Fe₂O₃' ratio.

It can be observed that a relatively small addition of 2 wt.% MgO causes the liquidus isotherm to be 4–5 wt.% closer to the SiO_2 apex of the diagram and the tridymite liquidus temperatures decrease with increasing MgO concentrations. For example, the projected composition of 50 wt.% 'Cu₂O', 30 wt.% 'Fe₂O₃' and 20 wt.% SiO_2 has a liquidus temperature of 1250 °C without added MgO, while having a liquidus temperature of 1150 °C when approximately 1.8 wt.% MgO is present in the slag.

As a result, adding 2 wt.% MgO to a mixture of 'Cu_2O', 'Fe_2O_3' and SiO_2 in the tridymite primary phase field can decrease the liquidus temperature by as much as 200 °C.

The maximum solubility of MgO in the liquid increases with increasing temperature. At 1150 °C, the maximum solubility is 2.6 wt.% for a projected composition of approximately 47 wt.% 'Cu_2O', 31 wt.% 'Fe_2O_3' and 22 wt.% SiO_2, while at 1200 °C the maximum solubility is 5.1 wt.% at a composition of 28 wt.% 'Cu_2O', 39 wt.% 'Fe_2O_3' and 33 wt.% SiO_2. The maximum solubility of MgO for constant 'Cu_2O'/'Fe_2O_3'/SiO_2 ratios also increases with temperature.

A more thorough analysis of the results, including the results in the pyroxene and olivine primary phase fields will be given in Part II of this series of two papers.

4.6 Conclusions

After a careful analysis of the achievement of equilibrium and reactions occurring in the 'Cu_2O'–'Fe_2O_3'–MgO–SiO_2 system, a methodology has been developed to accurately determine high temperature phase equilibria in this system. The uncertainty on the reported phase compositions is estimated to be within ±0.6 wt.%.

Phase equilibria measurements and liquidus in the tridymite primary phase field of the 'Cu_2O'–'Fe_2O_3'–MgO–SiO_2 at temperatures between 1100 and 1250 °C in equilibrium with metallic copper are reported. It was found that for each 2 wt.% MgO added to the system, the liquidus lies 4–5 wt.% closer to the SiO_2 apex of the phase diagram. The MgO solubility in the slag increases with increasing temperature.

5 Influence of MgO on the phase equilibria in the Cu_xO-FeO_y-MgO-SiO_2 system in equilibrium with copper alloy – Part II: Results and discussion

5.1 Introduction

In Chapter 4 [83], the research methodology for the study of phase equilibria in the 'Cu_2O'–'Fe_2O_3'–MgO–SiO_2 system in equilibrium with copper metal and the materials used were established. This involves the use of the high-temperature equilibration/quenching/electron-probe X-ray micro-analysis (EPMA) techniques. This approach was applied to determine the liquidus temperatures in the tridymite (SiO_2) primary phase field in this system. Further experimental results are now reported for liquidus temperatures in the pyroxene ($(Mg,Fe,Cu)SiO_3$) and olivine ($(Mg,Fe,Cu)_2SiO_4$) primary phase fields. In Chapter 7, these liquidus temperatures are then compared to the estimated steady state interface temperatures of the freeze lining experiments performed in this system.

5.2 Methodology

The high-temperature/equilibration/quenching technique in this study has been described in Chapter 4 [83]. A discussion on the formation of pyroxene and olivine when working in contact with a MgO substrate can be found in [84].

In brief, synthetic slag samples were prepared from high-purity oxide and metal powders. The samples were equilibrated for 24 h in an inert argon gas atmosphere and then rapidly quenched to room temperature. Oxygen partial pressures are determined by the condensed system through a series of reactions such as '$Fe^{3+} \leftrightarrow Fe^{2+}$' based on the assumption of limited interaction with the gas phase as the condensed system approaches equilibrium significantly faster. This has been described in detail in previous papers [85, 86]. The resulting oxygen partial pressures were not measured.

Each equilibrated sample was examined using optical microscopy and scanning electron microscopy (SEM). The compositions of the present phases were measured using EPMA. For each reported liquid composition, an average was taken of 10 measurements on a straight line in a well-quenched area; points were only accepted when the standard deviation between measurements was less than 0.6 wt.%.

The phase compositions were calculated based on measured cation-concentrations, normalized to 100 wt.% and reported as Cu_2O, Fe_2O_3, MgO and SiO_2. The $Cu^{2+}/Cu1^{+}/Cu^{0}$ and Fe^{3+}/Fe^{2+} ratios were not determined. The estimated uncertainty in compositions is ±0.6 wt.% (see Chapter 4 [83]).

5.3 Results

5.3.1 Microstructures

Backscattered electron (BSE) images of typical microstructures observed in the study are shown in Figure 5-1.

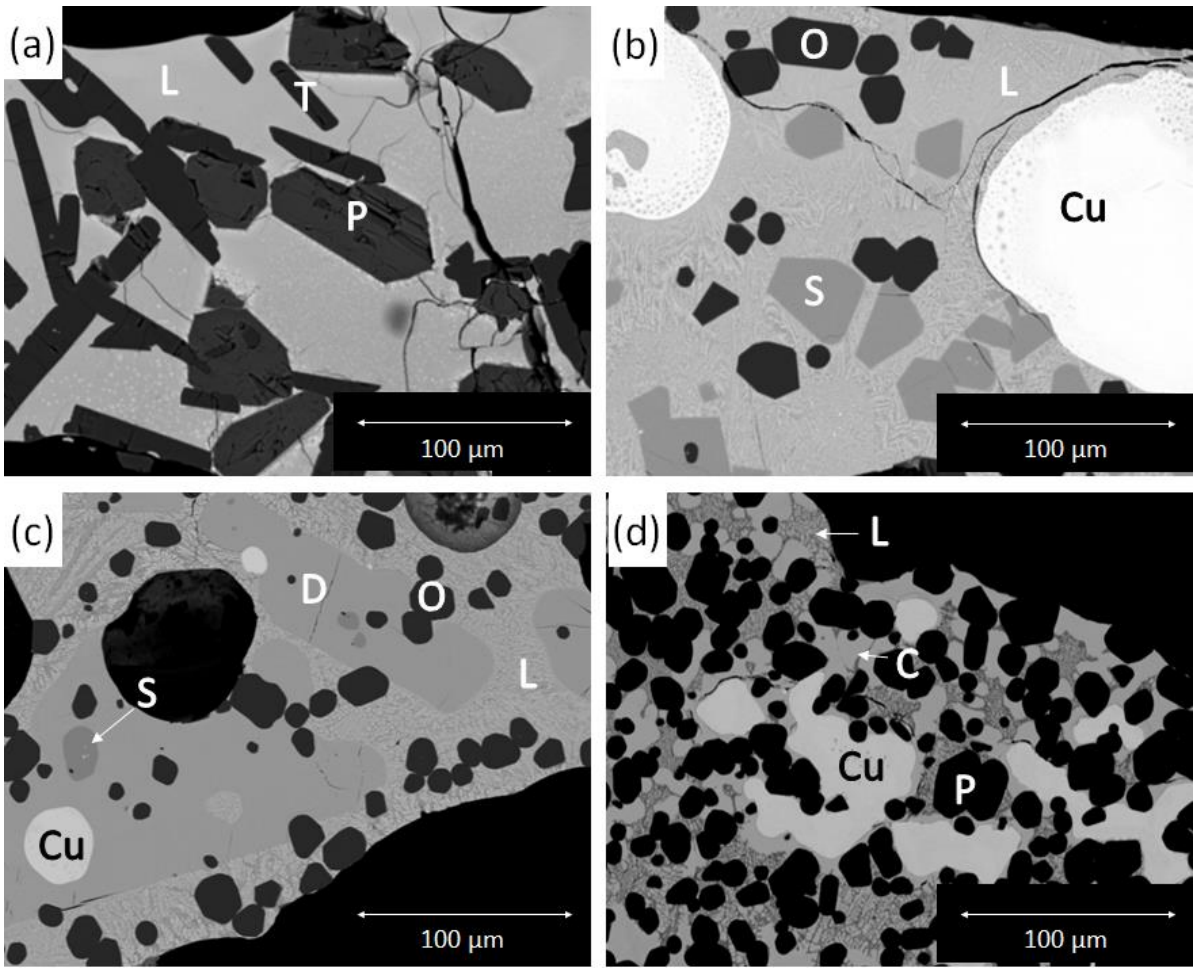

Figure 5-1: Backscattered electron images illustrating typical microstructures of 'Cu_2O'–'Fe_2O_3'–MgO–SiO_2 slags in equilibrium with copper metal (Cu). Liquid (L), tridymite (T), pyroxene (P), olivine (O), cuprite (C), spinel (S) and delafossite (D).

All of the microstructures obtained in the study consisted of a liquid-glassy phase, copper metal and one or more solid oxide phases. As discussed in Chapter 4 [83], submicron copper particles or

microcrystals are often observed in the liquid phase; it was determined that these precipitated during quenching.

The observed solid phases were tridymite (SiO_2), pyroxene ($(Mg,Fe,Cu)SiO_3$), olivine ($(Mg,Fe,Cu)_2SiO_4$), spinel ($(Fe,Mg,Cu)O.Fe_2O_3$), delafossite ($CuFeO_2$) and cuprite (Cu_2O). As can be seen in Figure 5-1a, tridymite forms plate-like crystals and spinel has an irregular angular morphology. Figure 5-1b shows the coexistence of olivine and spinel solids.

As shown in Figure 5-1c, delafossite forms large, rectangular crystals, sometimes containing a completely enclosed spinel core when the transformation of spinel to delafossite has not yet been completed. These enclosed spinel cores are not part of the equilibrium structure.

Pyroxene and olivine crystals have similar angular structures and similar mean atomic number, making it difficult to distinguish them using BSE images. The most noticeable difference is that pyroxene crystals tend to contain cracks, which may be caused by a transformation from proto- to orthopyroxene on quenching the sample.

Cuprite crystals are rounded, without particular shape or symmetry (Figure 5-1d).

5.3.2 Phase equilibria

The measured compositions of the oxide-containing phases formed during equilibration are listed in Table 5-1.

In some cases, it was not possible to obtain well-quenched amorphous liquid due to nucleation and growth of microcrystals on cooling. In these cases, the standard deviation of the measurements was higher than 0.6 wt.%. These data have been included for the sake of completeness and are indicated with '*' in Table 5-1. Copper alloy compositions are not reported due to the difficulties in obtaining accurate measurements in this phase (see Chapter 4 [83]).

The measured compositions in the tridymite, pyroxene and olivine primary phase fields for the different phases formed during equilibration are listed in Table 5-1. The phase compositions were calculated based on measured cation-concentrations, normalized to 100 wt.% and reported as Cu_2O, Fe_2O_3, MgO and SiO_2. The $Cu^{2+}/Cu1^{+}/Cu^{0}$ and Fe^{3+}/Fe^{2+} ratios were not determined. The estimated uncertainty in compositions is ±0.6 wt.% (see Chapter 4 [83]).

Table 5-1: Experimentally determined phase compositions for the 'Cu_2O'–'Fe_2O_3'–MgO–SiO_2 system in equilibrium with Cu-metal. The copper and iron oxide concentrations in the slag, spinel, olivine and pyroxene phases are reported as 'Cu_2O' and 'Fe_2O_3'. The actual oxidation states of copper and iron in these solids will depend on process conditions and slag composition.

Temp. (°C)	Phase	SiO_2 (wt.%)	'Cu_2O' (wt.%)	'Fe_2O_3' (wt.%)	MgO (wt.%)	Measured total (wt.%)
1100*	Liquid	11.3	65.6	22.3	0.8	104.4
	Pyroxene	56.7	1.7	7.2	34.5	103.1
1100*	Liquid	8.1	70.2	21.2	0.5	103.3
	Olivine	38.8	2.2	10.6	48.4	104.9
	Delafossite	0.1	46.5	53.4	0.1	102.3
1150	Liquid	10.6	67.6	20.9	0.9	102.6
	Olivine	39.7	1.6	9.9	48.8	103.3
1150*	Liquid	11.6	66.2	21.2	1.1	103.6
	Olivine	39.4	2.2	9.5	49.0	105.6
1150	Liquid	13.1	64.3	21.4	1.3	104.1
	Pyroxene	56.1	2.3	6.6	35.0	104.8
	Olivine	39.0	1.9	10.5	48.6	104.1
1150*	Liquid	2.8	75.5	21.3	0.4	97.9
	Olivine	40.5	2.3	4.4	52.9	106.2
	Cuprite	0.0	98.7	1.3	0.0	100.7
1150*	Liquid	10.8	63.9	24.4	0.8	103.7
	Olivine	38.9	2.2	12.6	46.3	106.6
	Spinel	0.1	4.4	90.5	5.0	105.0
1150	Liquid	11.4	61.1	26.3	1.2	104.9
	Olivine	38.4	2.1	12.7	46.8	105.0
	Spinel	0.1	3.8	91.1	5.0	103.9
1200	Liquid	17.7	69.9	10.4	2.0	100.9
	Pyroxene	57.9	2.4	1.9	37.8	102.9
1200	Liquid	19.3	61.5	16.5	2.6	101.0
	Pyroxene	57.6	2.0	5.0	35.4	100.9
1200*	Liquid	21.4	44.7	30.5	3.3	102.0

Temp. (°C)	Phase	SiO_2 (wt.%)	'Cu_2O' (wt.%)	'Fe_2O_3' (wt.%)	MgO (wt.%)	Measured total (wt.%)
	Pyroxene	55.9	1.8	9.4	32.8	103.4
1200	Liquid	25.7	38.8	31.7	3.8	104.3
	Pyroxene	55.8	1.6	9.5	33.1	100.2
1200*	Liquid	3.0	78.4	18.2	0.4	101.7
	Olivine	-	-	-	-	-
1200	Liquid	7.9	72.6	18.7	0.8	101.9
	Olivine	40.2	2.1	5.3	52.4	102.5
1200	Liquid	8.3	61.8	29.0	0.9	102.7
	Olivine	39.3	1.4	11.7	47.6	104.9
1200*	Liquid	10.0	67.2	21.8	1.1	101.0
	Olivine	39.2	1.6	8.9	50.3	102.7
1200	Liquid	16.8	52.2	28.7	2.3	99.7
	Olivine	38.4	1.2	15.8	44.6	104.0
1200	Liquid	22.2	40.7	33.1	3.9	103.1
	Pyroxene	54.9	1.2	13.1	30.8	101.0
	Olivine	37.6	1.3	18.1	42.9	103.5
1200*	Liquid	18.0	46.9	32.3	2.8	101.1
	Olivine	38.2	1.6	16.2	44.0	103.5
	Spinel	0.1	2.9	92.4	4.6	102.7
1250	Liquid	33.9	40.8	18.2	7.1	103.4
	Pyroxene	56.8	1.8	5.7	35.7	100.7
1250	Liquid	9.6	59.1	29.9	1.3	102.2
	Olivine	39.6	1.5	8.6	50.2	105.4
1250	Liquid	15.9	48.5	32.8	2.8	103.1
	Olivine	38.6	1.4	14.9	45.2	107.3
1250	Liquid	26.0	49.9	18.9	5.1	102.3
	Olivine	39.4	2.5	8.9	49.2	103.0
1250*	Liquid	13.7	39.2	44.7	2.4	103.5

Temp. (°C)	Phase	SiO_2 (wt.%)	'Cu_2O' (wt.%)	'Fe_2O_3' (wt.%)	MgO (wt.%)	Measured total (wt.%)
	Olivine	38.4	1.3	15.6	44.7	106.8
	Spinel	0.2	1.9	92.7	5.2	105.0

5.3.3 Presentation of phase equilibria

To enable convenient representation of the chemical compositions in the 'Cu_2O'–'Fe_2O_3'–MgO–SiO_2 system, several operations are undertaken on the experimental data. Firstly, all copper and iron in the sample is presented as Cu^{1+} and Fe^{3+} respectively. This can be visualised as the projection of the phase compositions in the direction of the O apex for the Cu–Fe–Si–O system, onto the Cu_2O–Fe_2O_3–SiO_2 plane (Figure 5-2).

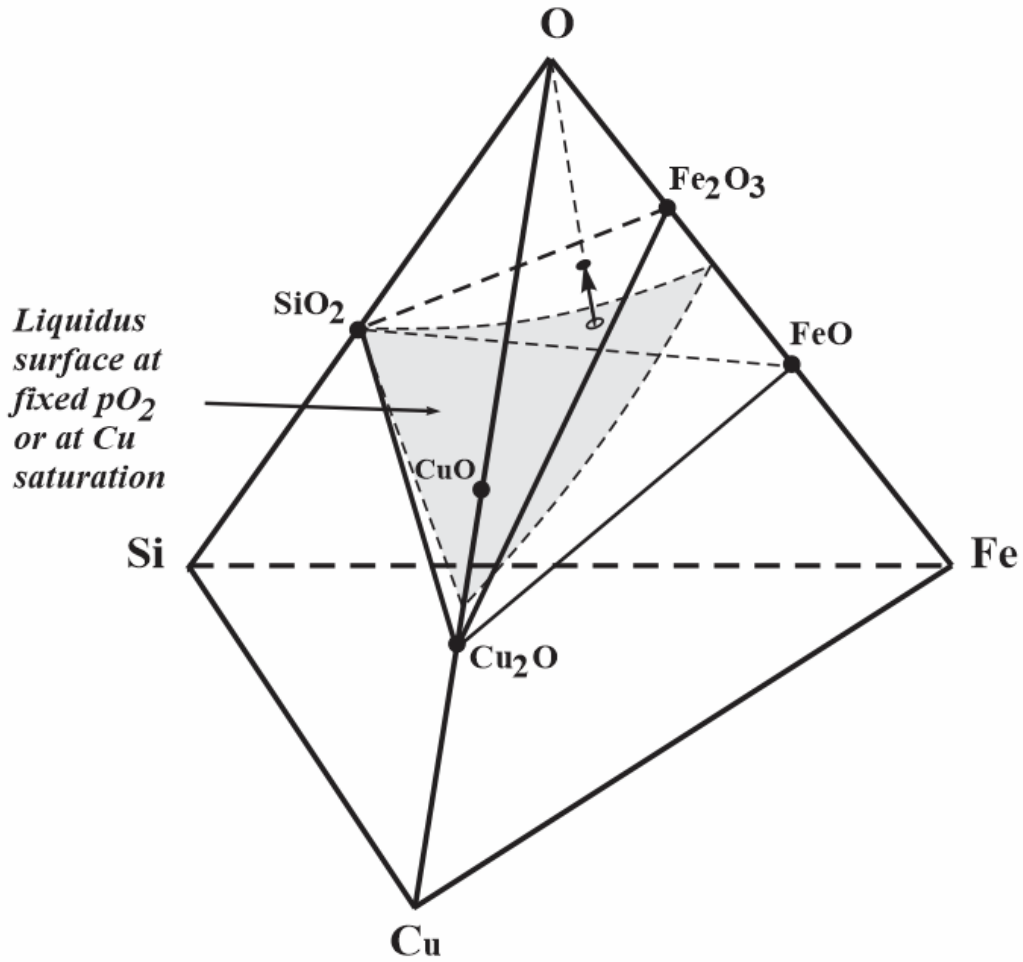

Figure 5-2: Projection of measured iron and copper oxide concentrations onto the Cu_2O–Fe_2O_3–SiO_2 plane [78].

As measurements were taken in the quaternary oxide system, it was necessary to fix an additional parameter to be able to unambiguously represent the results. Two options were selected. In Figure 5-3a, the MgO concentration is chosen to be constant, effectively taking a cross-section of the quaternary diagram parallel to the Cu_2O–Fe_2O_3–SiO_2 plane at selected MgO concentrations. This method of representation is used in Figure 5-4–5-6. Figure 5-3b shows an example of the construction of the diagrams at constant temperature with measured MgO concentrations in the liquid marked on the diagram. This type of projection is used in Figure 5-7–5-9. In both cases, compositions are projected onto the Cu_2O–Fe_2O_3–SiO_2 plane.

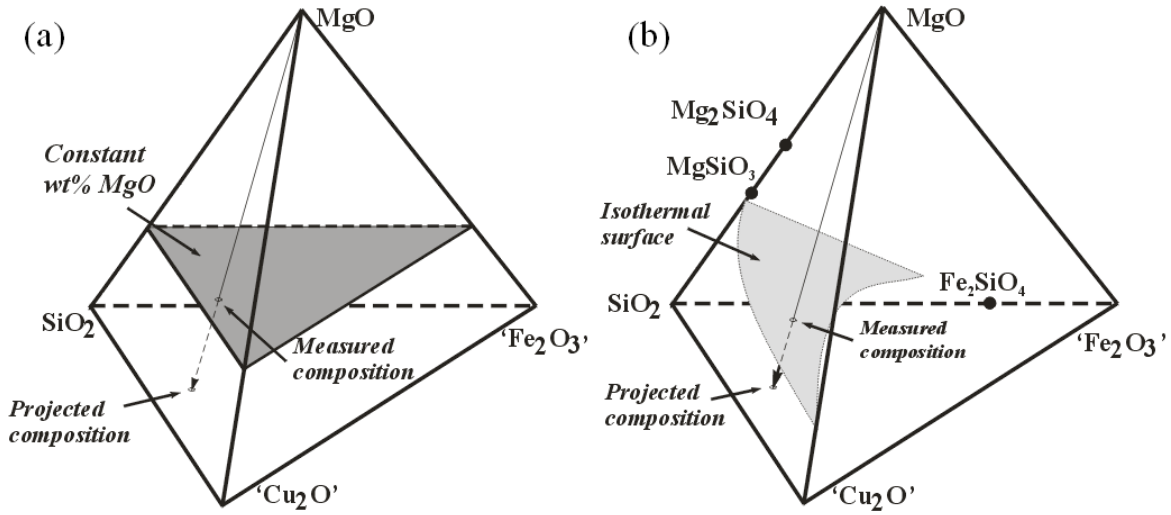

Figure 5-3: Representation of measured phase compositions at (a) constant MgO-concentration in liquid or (b) isothermal surface projected onto the Cu_2O–Fe_2O_3–SiO_2 plane.

5.3.4 Construction of diagrams

Liquidus diagrams in the 'Cu_2O'–'Fe_2O_3'–MgO–SiO_2 system were constructed as follows: All data from the present study in the olivine and pyroxene primary phase fields, the data from the silica primary phase field [83] and data for the 'Cu_2O'–'Fe_2O_3'–SiO_2 system by Hidayat et al. [78], at a particular temperature were projected onto the 'Cu_2O'–'Fe_2O_3'–SiO_2 plane. Liquidus isotherms at constant MgO concentrations were manually fitted to the plotted compositions, creating the projections at constant temperature in Figure 5-7–5-9.

The obtained liquidus lines for a given MgO concentration at 1150, 1200 and 1250 °C were then plotted on a single diagram, creating the projections at constant MgO concentrations in Figure 5-5 and Figure 5-6. Particular attention was paid to the consistency of the liquidus lines with the experimental data and each other.

Trends on the 'Cu_2O'–'Fe_2O_3'–MgO plane were determined using the FToxid database in FactSage 6.2 [87]. Measured MgO concentrations are reported next to the plotted points. At low 'Cu_2O' concentrations in the liquid slag, there is a drastic change in partial oxygen pressure. Because of this, the present primary phase fields change drastically in this area (Figure 5-4). As no experimental data were obtained in this area, these primary phase fields are not shown on the diagrams constructed in the present study.

5.3.5 Sections at constant MgO concentration

The phase diagrams at 0, 2 and 4 wt.% MgO in liquid are shown in Figure 5-4, Figure 5-5 and Figure 5-6 respectively. In the 'Cu_2O'–'Fe_2O_3'–SiO_2 system, 4 primary phase fields are observed within the investigated region of temperatures between 1100 and 1250 °C and high 'Cu_2O' concentrations: a cuprite primary phase field in the 'Cu_2O' apex of the diagram, a tridymite primary phase field at higher SiO_2 concentrations, a spinel primary phase field at high 'Fe_2O_3' concentrations and a delafossite primary phase field in between the cuprite and spinel primary phase fields. The phase boundaries are marked with thick lines and the isotherms in thin lines. Estimated phase boundaries and isotherms are marked with dashed lines.

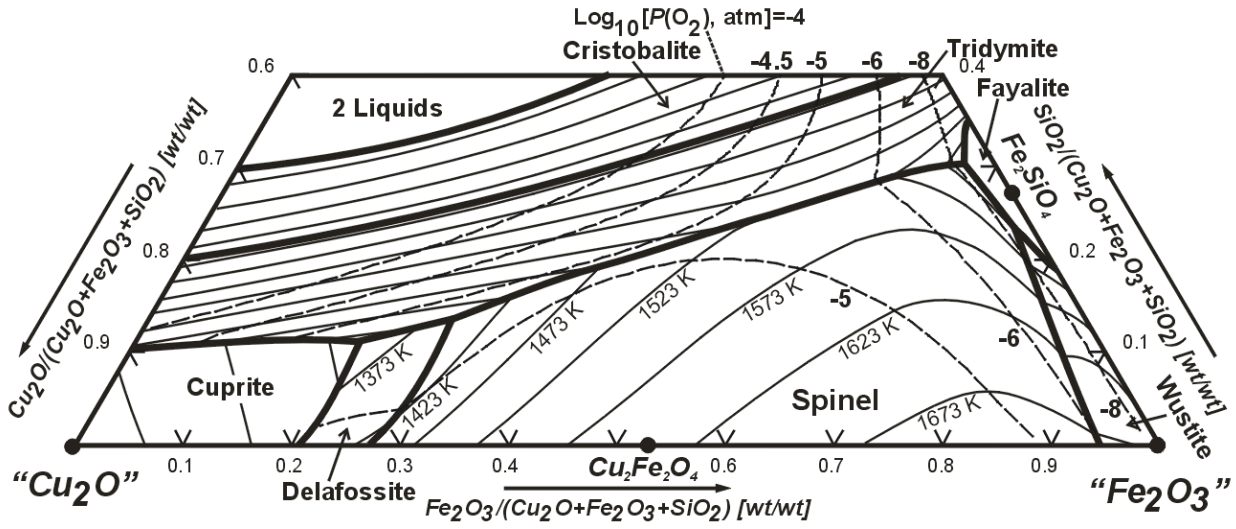

Figure 5-4: Calculated liquidus isotherms, oxygen isobars on the liquidus surface and univariant lines in the 'Cu_2O'–'Fe_2O_3'–SiO_2 system in equilibrium with metallic copper [88].

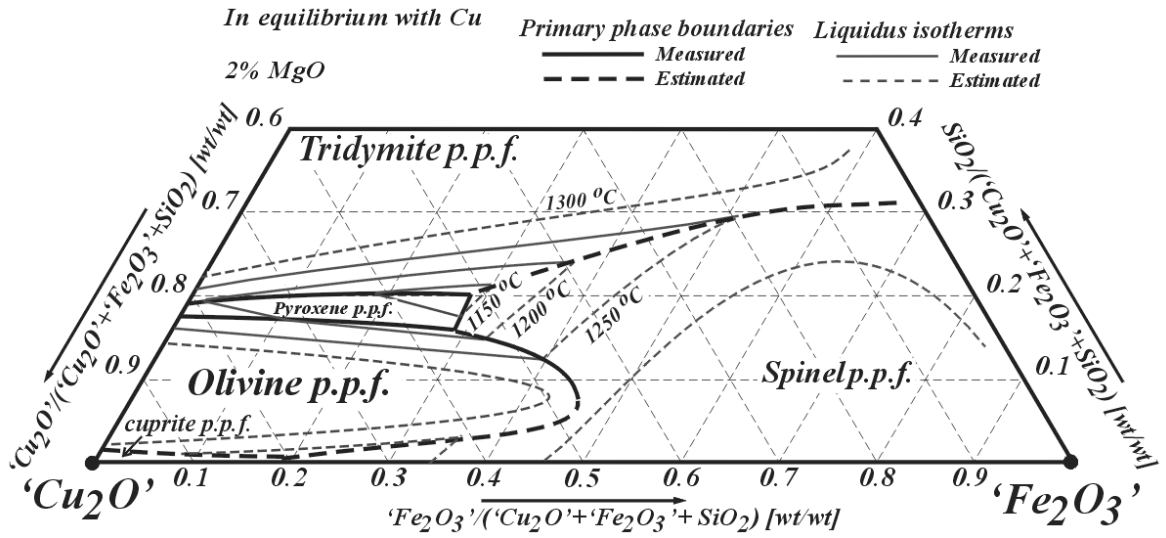

Figure 5-5: Estimated cross-section of the 'Cu_2O'–'Fe_2O_3'–MgO–SiO_2 phase diagram at 2 wt.% MgO in liquid in equilibrium with Cu-metal projected on to the 'Cu_2O'–'Fe_2O_3'–SiO_2 plane.

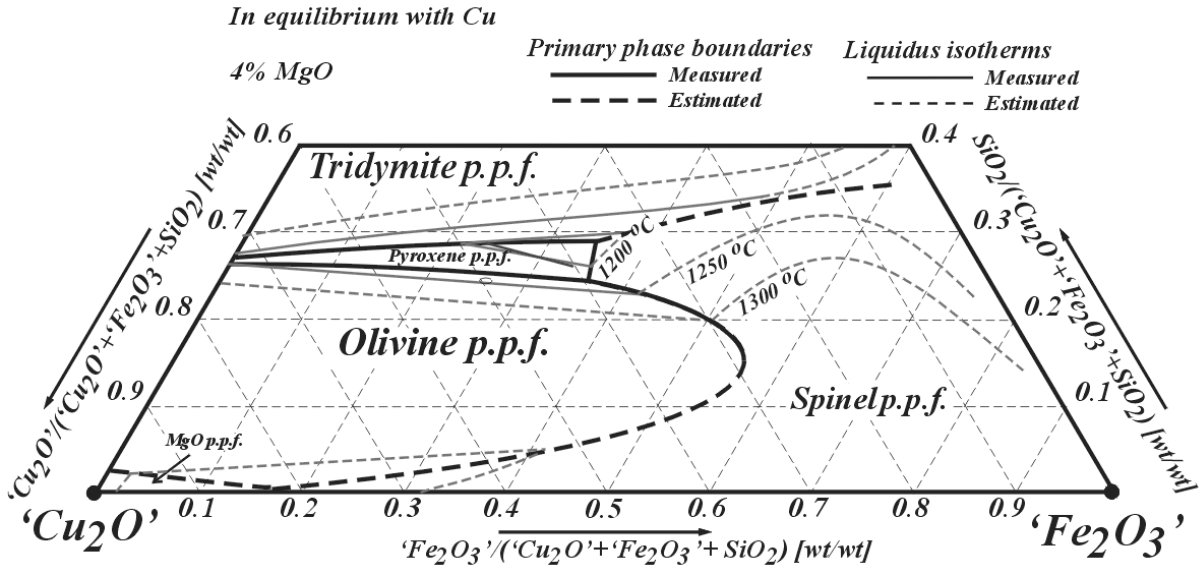

Figure 5-6: Estimated cross-section of the 'Cu_2O'–'Fe_2O_3'–MgO–SiO_2 phase diagram at 4 wt.% MgO in liquid in equilibrium with Cu-metal projected on to the 'Cu_2O'–'Fe_2O_3'–SiO_2 plane.

Figure 5-5 and Figure 5-6 show that, at higher MgO concentrations, the cuprite and delafossite primary phase fields almost completely disappear as pyroxene and olivine are more stable. Instead, an olivine and a pyroxene primary phase field appear near the 'Cu_2O' apex of the diagram. In the measured regions of the phase diagram, liquidus temperatures in the olivine and pyroxene primary phase fields increase with decreasing SiO_2 concentrations. However, with further decreasing SiO_2 concentrations, liquidus temperatures will decrease as the Cu_2O apex is approached.

With increasing wt.% MgO in the liquid phase, the liquidus temperatures in the tridymite primary phase field decrease; as a result, the join between the silica and spinel primary phase fields moves to

higher SiO_2 concentrations. Changes in liquidus temperature in the spinel primary phase field are relatively minor, however, with increasing MgO concentration, the olivine–spinel phase boundary occurs at increasingly higher 'Fe_2O_3' concentrations.

The calculated 'Cu_2O'–MgO–SiO_2 diagram [88] indicates that at very low MgO and SiO_2 concentrations, the cuprite primary phase field would still be present, as is indicated in Figure 5-5 and shown by one of the experiments at 1150 °C in Table 1. At higher MgO concentrations, the magnesiowustite primary phase field is stable in the region of the Cu_2O apex, as is indicated in Figure 5-6.

Of special interest for the direct to blister copper production process is the boundary line between tridymite and spinel, which determines the lowest liquidus temperature that can be reached by adding silica flux. When comparing Figure 5-5 and Figure 5-6 with results from Hidayat et al. [78] on the system at 0 wt.% MgO, it can be concluded that this boundary line lies 3–4 wt.% closer towards the SiO_2 apex of the phase diagram for each 2 wt.% MgO added. The liquidus temperatures on this boundary line stay approximately constant.

5.3.6 Diagrams at constant temperature

The effects of varying the MgO concentration in the slag can be seen by inspection of Figure 5-7, Figure 5-8 and Figure 5-9, which show the projections of the isothermal 'Cu_2O'–'Fe_2O_3'–MgO–SiO_2 liquidus surfaces at 1250, 1200 and 1150 °C onto the 'Cu_2O'–'Fe_2O_3'–SiO_2 section. It should be noted that the liquidus isotherms on these projections are the same as those in Figure 5-4, Figure 5-5 and Figure 5-6, although the grouping of isotherms is different. Unlike the sections at constant MgO concentration, the projection of the isothermal liquidus surface allows the representation of the experimentally-measured compositions. The measured MgO concentrations in the liquid are shown next to the projected compositions.

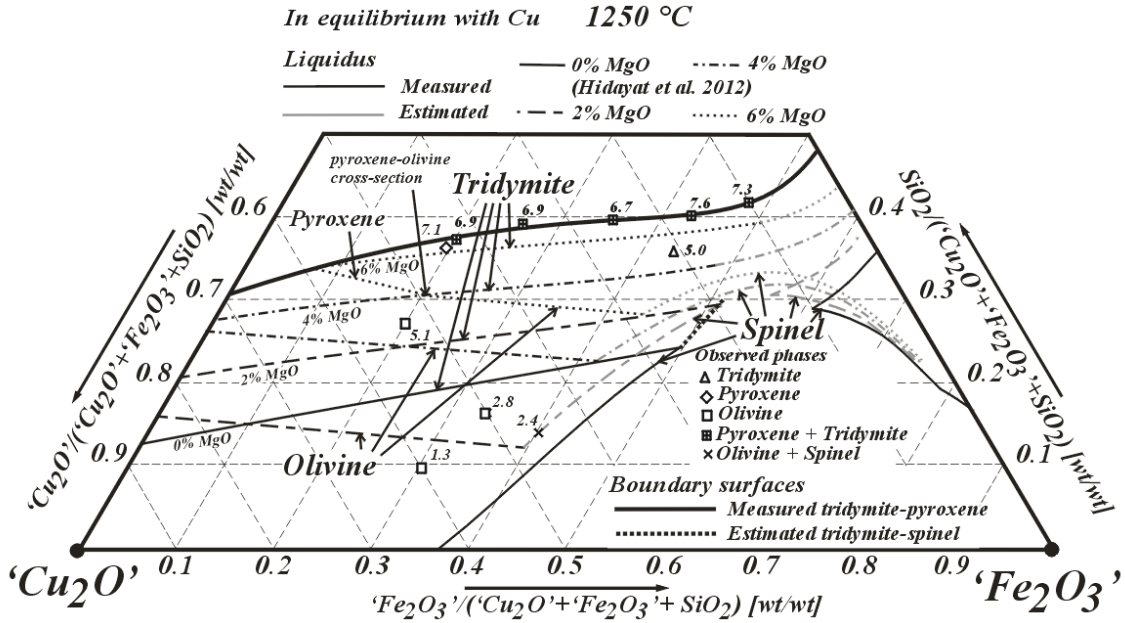

Figure 5-7: Projection of the 'Cu_2O'–'Fe_2O_3'–MgO–SiO_2 phase diagram in equilibrium with Cu-metal at 1250 °C onto the 'Cu_2O'–'Fe_2O_3'–SiO_2 section showing the liquidus at 0, 2, 4 and 6 wt.% MgO.

This constant temperature representation also enables the extent of the fully liquid region at fixed temperatures and MgO wt.% to be readily identified. The fully liquid area is determined by the area enclosed by the isothermal liquidus lines at constant MgO concentration in the tridymite, pyroxene, olivine and spinel primary phase fields. It can be observed on Figure 5-4 and Figure 5-7 that at 0 wt.% MgO, two separate fully liquid areas are present below 1250 °C, one at high Cu_2O concentrations and one at low Cu_2O concentrations. These two regions are separated by the presence of the tridymite and spinel primary phase fields. The experimental results indicate that at MgO concentrations between approximately 2.5–5 wt.% MgO there is a continuous liquid area from 0 wt.% 'Cu_2O' to 0 wt.% 'Fe_2O_3' at 1250 °C.

In the high 'Cu_2O' region of the phase diagram, the position of the tridymite liquidus moves to higher SiO_2 concentrations as the MgO concentration is increased. It should be noted, however, that the range of compositions that are fully liquid decreases with increasing MgO concentration with the appearance and expansion of the pyroxene and olivine primary phase fields. The fully liquid area decreases in size with decreasing temperature. As can be seen in Figure 5-8, at 1200 °C it is not possible to obtain fully liquid slag at concentrations greater than approximately 5 wt.% MgO. At 1150 °C (Figure 5-9), the slag cannot be fully liquid if it contains more than approximately 2.6 wt.% MgO.

Using these diagrams, it is possible to determine the maximum solubility of MgO in liquid slag in contact with an MgO substrate/crucible/refractory (Figure 5-10). When an undersaturated slag is contacted with MgO, the MgO will initially dissolve in the liquid phase. The phase diagrams indicate

that an MgO-rich phase will be formed at the slag–MgO interface, preventing direct contact between slag and crucible/substrate [84].

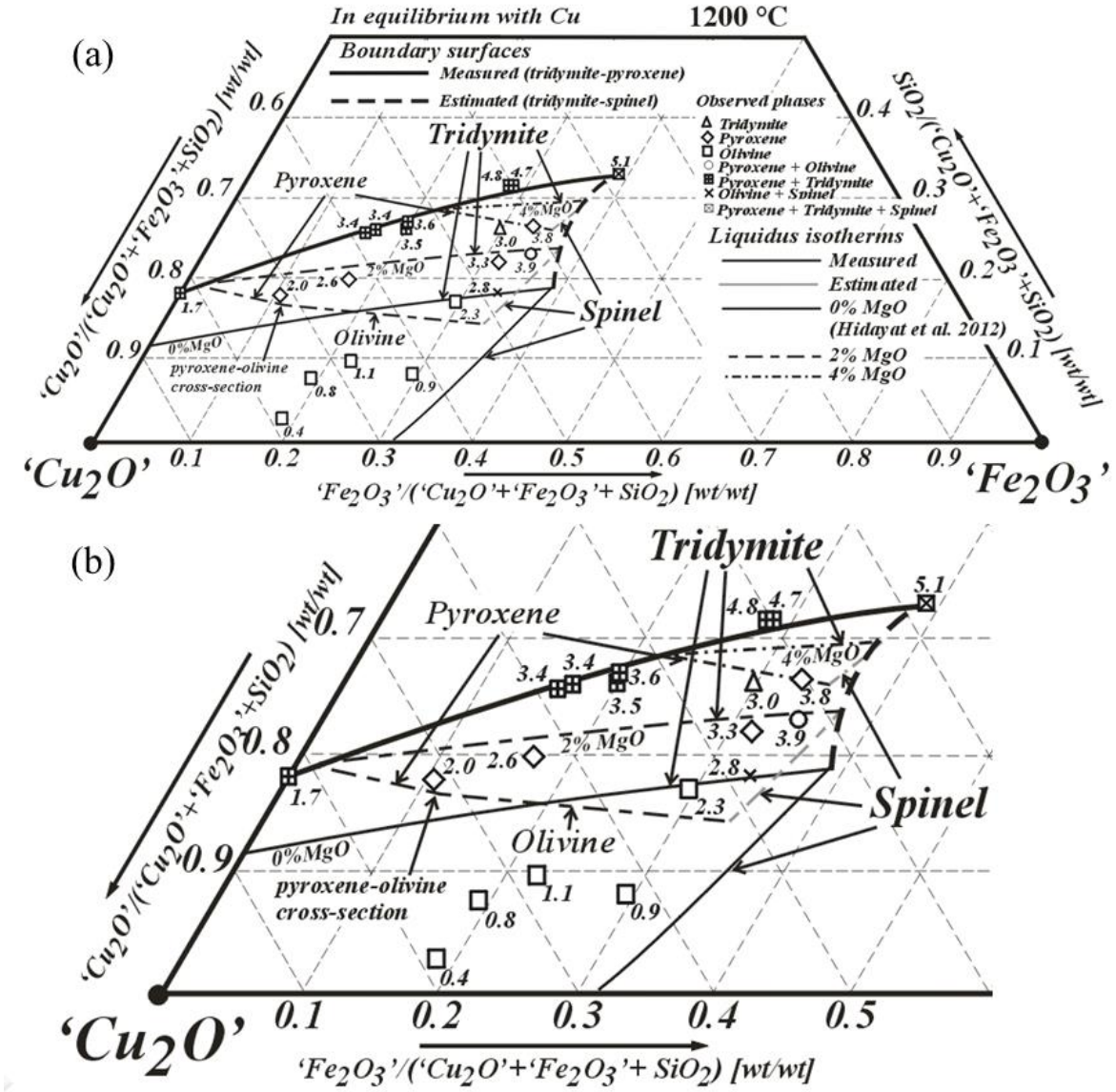

Figure 5-8: (a) Projection of the 'Cu_2O'–'Fe_2O_3'–MgO–SiO_2 phase diagram in equilibrium with Cu-metal at 1200 °C onto the 'Cu_2O'–'Fe_2O_3'–SiO_2 section showing the liquidus at 0, 2 and 4 wt.% MgO and (b) detail of the Cu_2O corner.

For Cu_2O-rich slags containing no MgO or low MgO concentrations, MgO will dissolve into the slag until the liquid slag is in equilibrium with either olivine or pyroxene. Hence, the MgO concentration in the liquid will increase until it reaches the isothermal liquidus surface of the pyroxene or olivine primary phase field. Note that during reaction the ratios of the principal components in the slag may change due to the formation of the olivine or pyroxene phases.

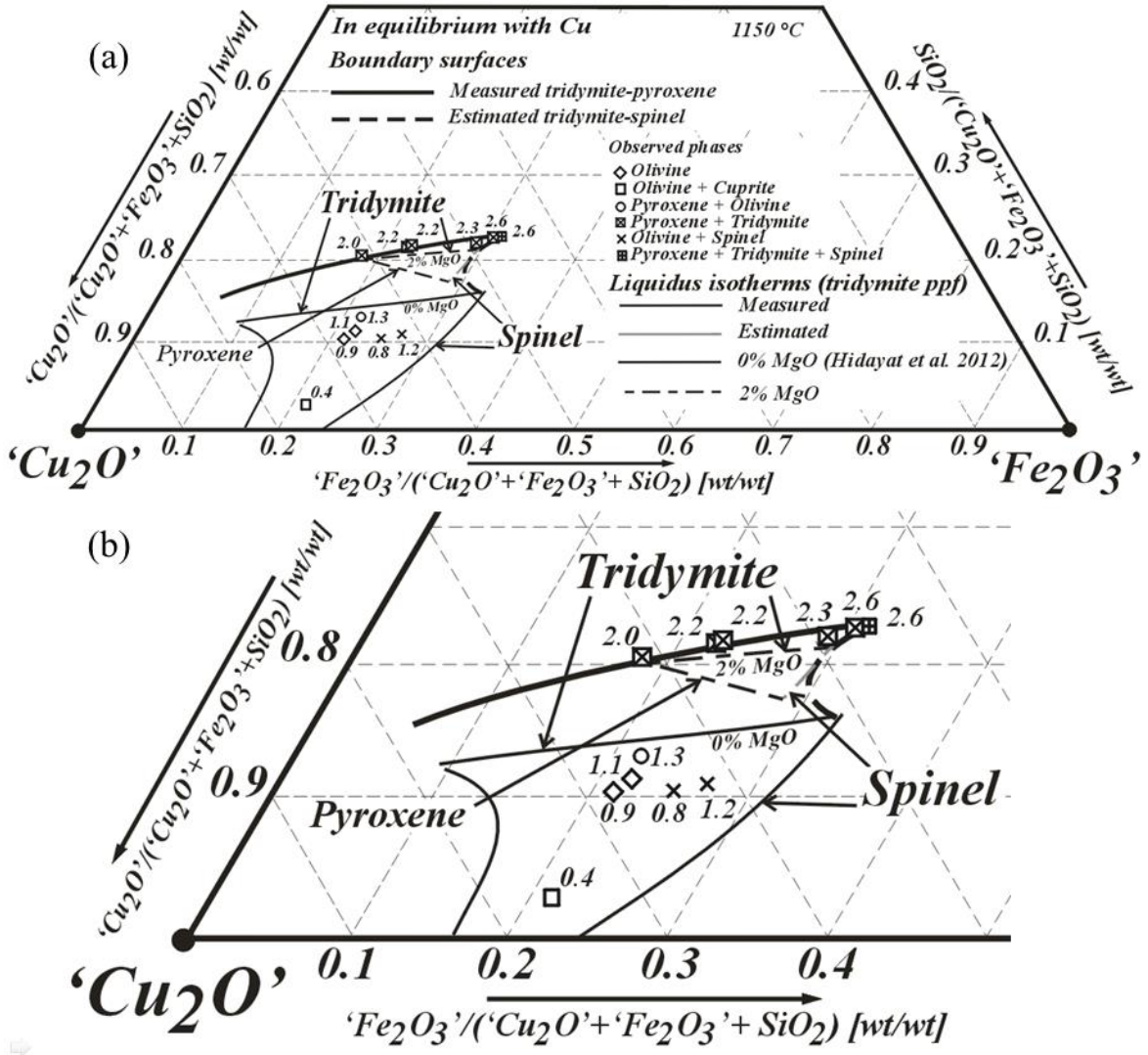

Figure 5-9: (a) Projection of the 'Cu₂O'–'Fe₂O₃'–MgO–SiO₂ phase diagram in equilibrium with Cu-metal at 1150 °C onto the 'Cu₂O'–'Fe₂O₃'–SiO₂ section showing the liquidus at 0 and 2 wt.% MgO and (b) detail of the Cu₂O corner.

For example, a slag of the composition marked with (⊞) on Figure 5-10 in contact with an MgO substrate would dissolve up to 2.5 wt.% of MgO. Any further dissolution of MgO will result in the formation of pyroxene, forming a pyroxene layer between the MgO substrate and the slag. As the precipitated pyroxene mainly consists of MgO and SiO_2 (Table 1), the SiO_2/'Fe_2O_3' and SiO_2/'Cu_2O' ratios would decrease.

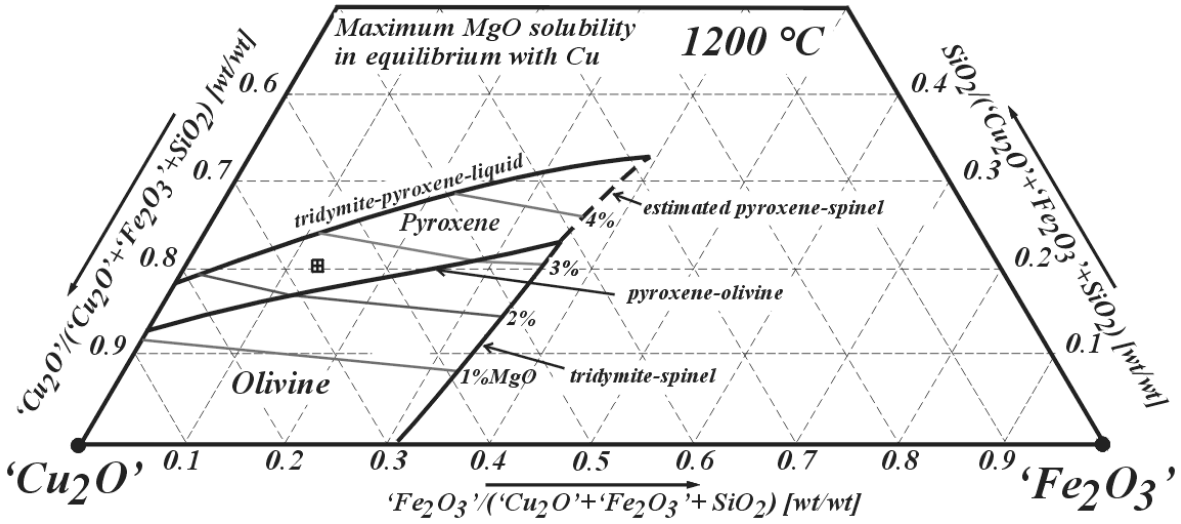

Figure 5-10: Maximum solubilities of MgO in liquid 'Cu_2O'–'Fe_2O_3'–MgO–SiO_2 slag at 1200 °C [84].

5.4 Solid solutions

As stoichiometry is an important factor in solid solutions, all solid solution diagrams are presented using mole percentages or mole fractions of the measured oxides.

5.4.1 Tridymite solid solution

As can be seen in Table 1, the measured MgO concentrations in the tridymite solid solutions are negligible for all conditions investigated. For this reason, the measured compositions were projected on the CuO_x–FeO_x–SiO_2 plane (Figure 5-11).

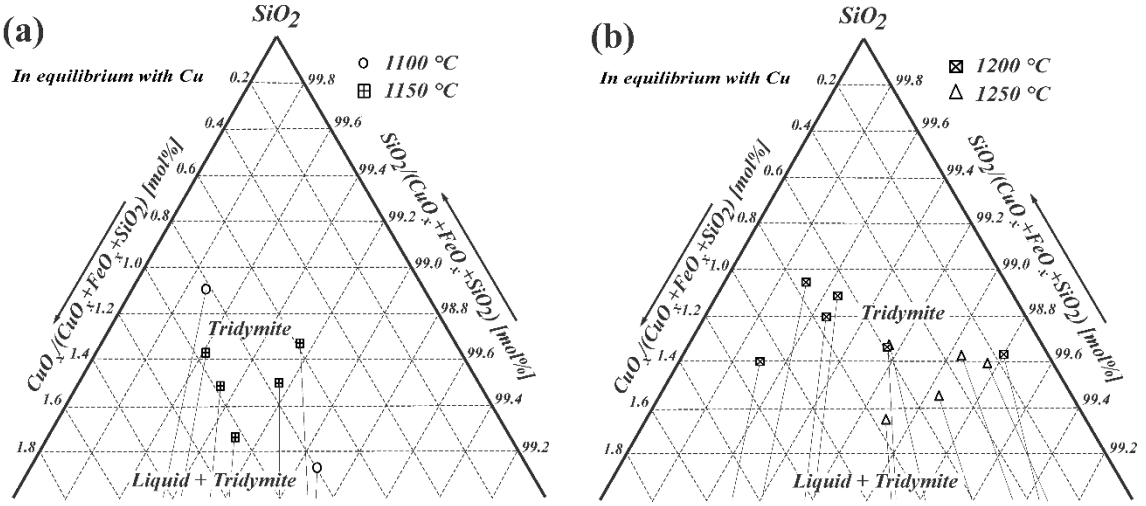

Figure 5-11: Extent of Fe and Cu solubility in tridymite at Cu metal saturation in the Cu_2O'–'Fe_2O_3'–MgO–SiO_2 system at (a) 1100, 1150, (b) 1200 and 1250 °C.

When comparing these results to the results obtained by Hidayat et al. [77, 78] it can be seen that the obtained values for the solubility of iron and copper oxide in tridymite are similar. However, due to

the spread of the results in the current study, it was not possible to confirm the trend of the CuO_x vs. the FeO_x solubility.

5.4.2 Pyroxene solid solution

To represent the extent of the pyroxene solid solutions, the measured compositions were projected onto the MgO–CuO_x–FeO_x composition plane (Figure 5-12) as the concentration of SiO_2 in pyroxene stays approximately constant at 50 mol.%. Data on the CuO_x–MgO–SiO_2 plane were taken from Hidayat et al. [77].

Copper oxide has a solubility between 0.3 and 3.6 mol.% CuO_x in the pyroxene under the experimental conditions, decreasing with increasing temperatures and iron oxide concentration in slag.

Iron oxide has a large solubility in pyroxene. The maximum solubility of iron oxide in pyroxene at a set temperature is obtained in contact with the liquid slag on the tridymite–pyroxene–spinel boundary line. This slag has the highest possible iron oxide concentration in the fully liquid area. Iron oxide solubility in pyroxene in contact with this slag ranges from 6.1 mol.% FeO_x at 1100 °C to 11.2 mol.% FeO_x at 1200 °C. At 1250 °C, the highest observed solubility of FeO_x in pyroxene was 22.1 mol.%. However, as the fully liquid area at this temperature extends all the way from 0 mol.% FeO_x to 0 mol.% CuO_x (Figure 5-7), higher FeO_x solubilities in pyroxene could be obtained by using slag with a higher concentration of FeO_x.

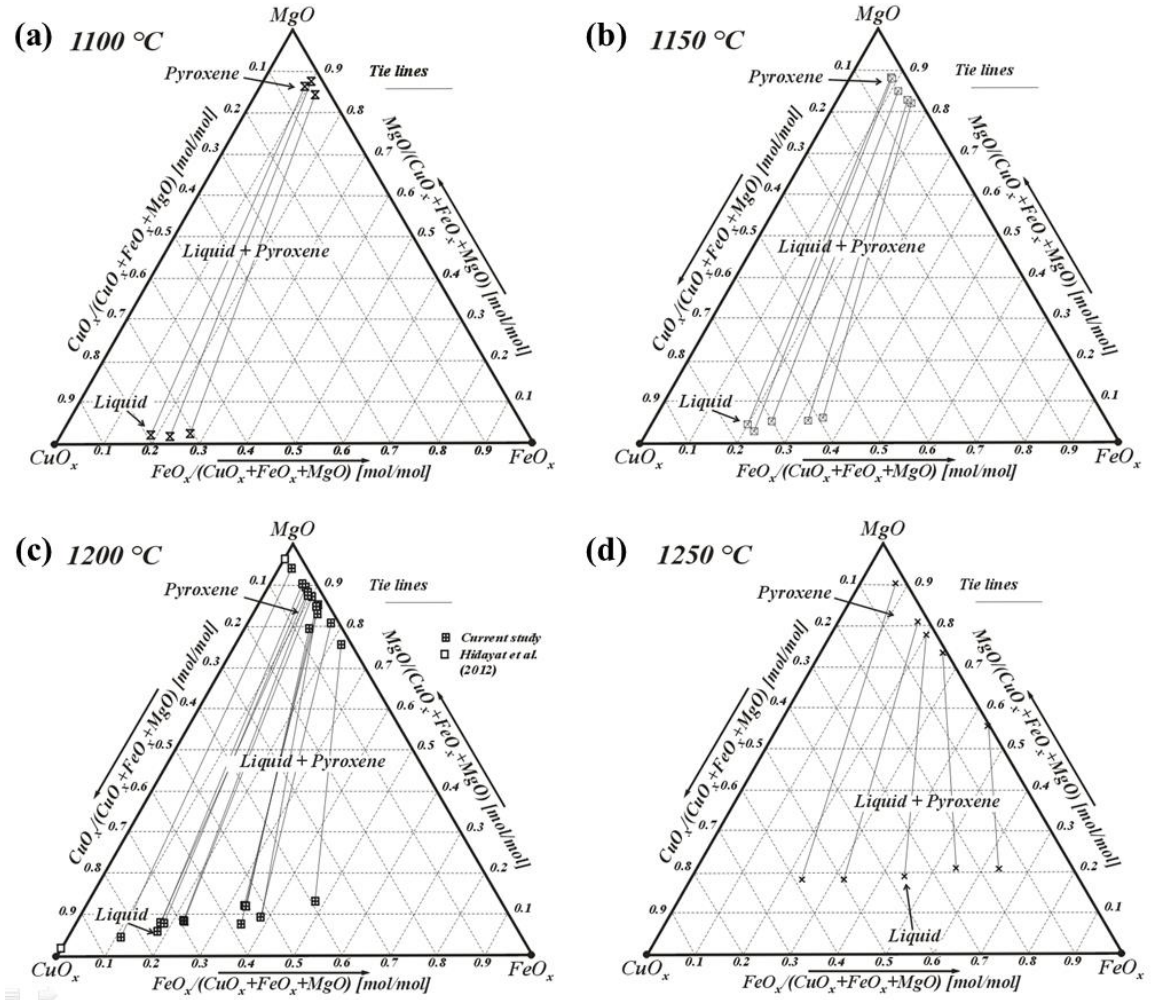

Figure 5-12: Pyroxene solid solutions at (a) 1100, (b) 1150, (c) 1200 and (d) 1250 °C in equilibrium with Cu-metal (50 mol.% SiO_2) in the 'Cu_2O'–'Fe_2O_3'–MgO–SiO_2 system.

It was expected that higher MgO concentration in the liquid would increase the Mg^{2+}/Fe^{2+} ratio in pyroxene. However, The MgO concentration in pyroxene appears to be primarily related to the iron concentration in slag as the variation in MgO concentration in slag at a given temperature is small.

5.4.3 Olivine solid solution

To represent the extent of the olivine solid solutions, the measured compositions were projected onto the MgO–CuO_x–FeO_x (Figure 5-13). The concentration of SiO_2 in olivine stays approximately constant at 33 mol.%.

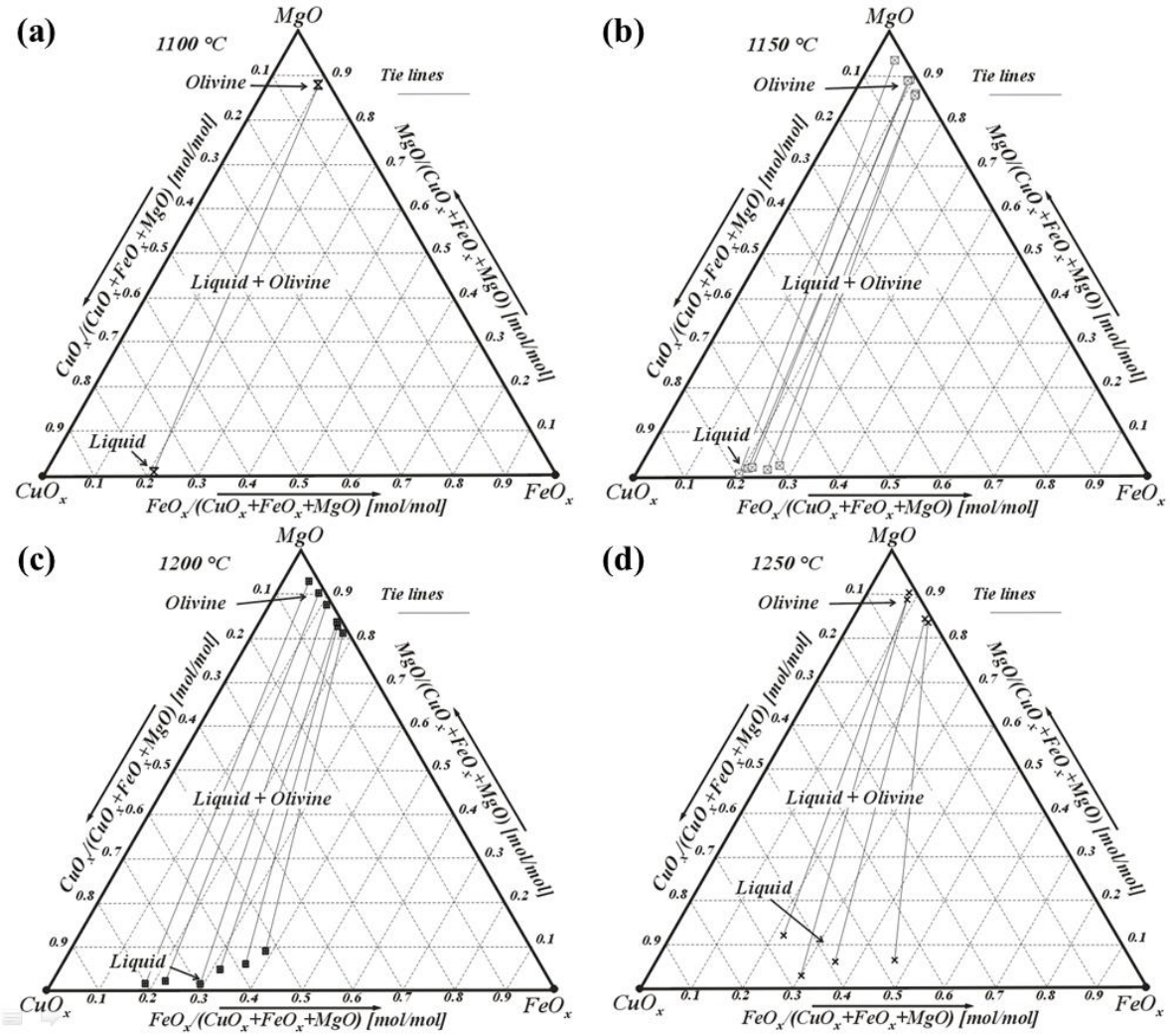

Figure 5-13: Olivine solid solutions at (a) 1100, (b) 1150, (c) 1200 and (d) 1250 °C in equilibrium with Cu-metal (50 mol.% SiO_2) in the 'Cu_2O'–'Fe_2O_3'–MgO–SiO_2 system.

Similar to the pyroxene solid solution, Cu^{2+} has a limited solubility in olivine under the experimental conditions with copper oxide concentrations ranging from 0.9 to 1.7 mol.% CuO_x. Increasing Fe^{2+} concentration in olivine slightly reduces the solubility of Cu^{2+}. No clear trends were observed between Cu^{2+} concentrations in olivine and temperature.

Iron oxide has a large solubility in olivine. Contrary to the pyroxene solid solution, no maximum solubility of Fe^{2+} was determined as no experiments with a maximum concentration of FeO_x in liquid were performed. In fact, fayalite (Fe_2SiO_4 olivine) is a stable compound and Fe_2SiO_4–Mg_2SiO_4 is a continuous solution at Fe-saturation [89], which is the condition at 0 mol.% CuO_x (Figure 5-4). Measured concentrations of iron oxide in olivine ranged from 2.6 to 11.7 mol.% FeO_x.

No trend was observed between the MgO concentration in the liquid and the Mg^{2+} concentration in olivine.

5.4.4 Spinel solid solution

Figure 5-14 shows the compositions of spinel solid solution in equilibrium with liquid 'Cu_2O'–'Fe_2O_3'–MgO–SiO_2 slag and copper metal. As the solubility of SiO_2 in spinel was negligible, all measured compositions were projected onto the MgO–CuO_x–FeO_x plane. These spinel compositions represent solid solution of Fe_3O_4, $MgFe_2O_4$ and $CuFe_2O_4$ [85, 90].

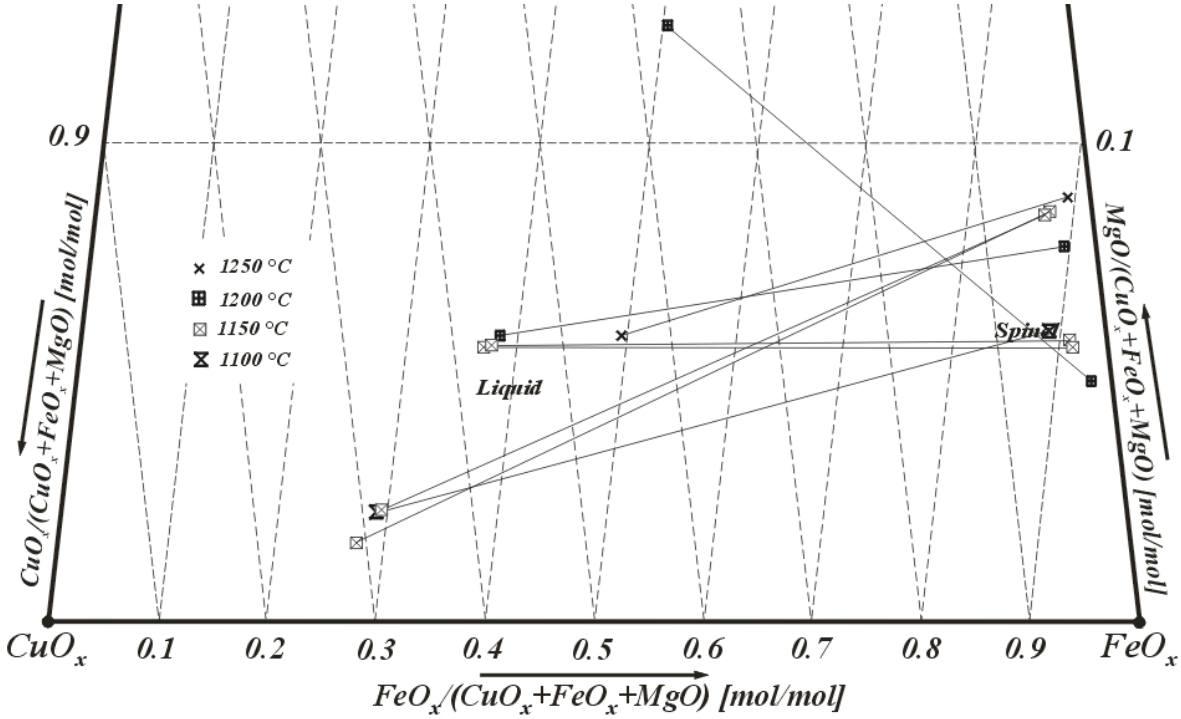

Figure 5-14: Compositions of liquids and spinel solid solutions in equilibrium with Cu-metal in the 'Cu_2O'–'Fe_2O_3'–MgO–SiO_2 system projected onto the 'Cu_2O'–'Fe_2O_3'–MgO plane.

When the concentration of a certain species in one phase increases, the expected result is an increase in concentration of the same species in the other phases present in the system. Figure 5-15a demonstrates this for the CuO_x concentration in the slag and spinel phases. However, the concentration of MgO in slag and spinel shows the exact opposite relation (Figure 5-15b).

This is explained as follows: As the CuO_x/FeO_x ratio in slag decreases so does the oxygen partial pressure. As a result, the Fe^{2+}/Fe^{3+} ratio increases, resulting in a higher activity of FeO. As FeO and MgO occupy the same atom positions in the spinel structure, an increase in FeO concentration could result in a decrease in MgO concentration.

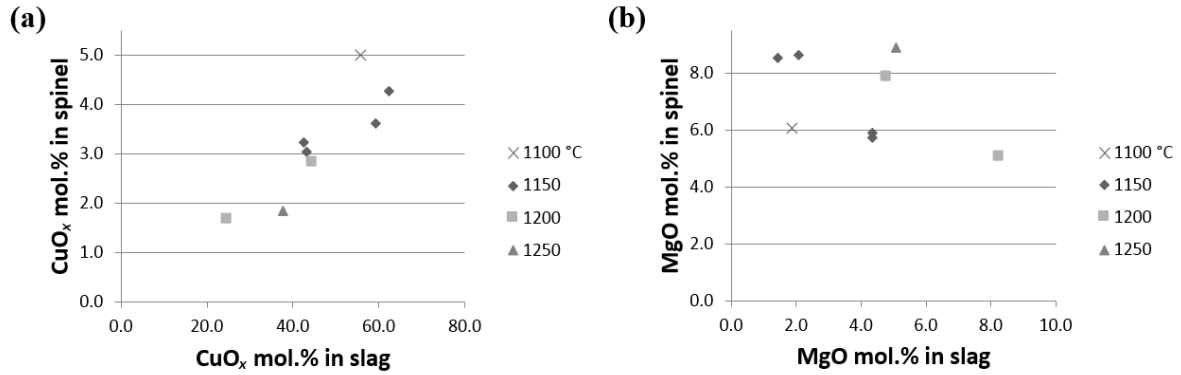

Figure 5-15: Comparison of (a) CuO_x and (b) MgO concentrations in slag and spinel.

For the investigated compositions, the concentration of 'Cu_2O' in spinel decreases with increasing temperature, while the concentration of MgO in spinel increases with increasing temperatures.

5.4.5 Determination of solidus

In addition to the experiments shown above, experiments in equilibrium with copper were carried out to determine the tridymite–pyroxene–delafossite–cuprite eutectic temperature and the temperature at which spinel transforms into delafossite on the tridymite–pyroxene–spinel boundary. These temperatures are of particular importance to the freeze lining studies described in Chapter 7, where they can be used to estimate the temperature in the freeze linings at the positions where these transformations occur.

Two series of experiments were performed. In series I, the samples were premelted at 1150 °C to ensure a fully liquid sample was obtained. The samples were subsequently cooled down to, and equilibrated at, temperatures in between 1050 and 1100 °C. In series II, the premelt step was omitted and the solid components of the powder samples were heated directly to their equilibration temperature.

Upper and lower limits for the tridymite–pyroxene–delafossite–cuprite eutectic temperature were determined as follows: As the series I samples were being cooled down after the premelt, a certain unknown undercooling is needed to provide the driving force for nucleation and precipitation of the final solid phase. Hence, the highest temperature at which this solid is observed lies below the eutectic temperature and provides the lower limit for the eutectic temperature.

As the series II samples are being heated up, some superheat is needed to start forming a liquid phase. As a result, the lowest temperature at which a liquid phase is observed in this series provides the upper limit for the eutectic temperature.

Similarly, the temperature at which the first delafossite appeared in the series I experiments provided the lower limit for the spinel–delafossite transformation temperature, while the temperature at which the first spinel appeared provided the upper limit.

Table 5-2: Oxide phases observed during cooling and heating experiments. Liquid (L), Cuprite (C), Delafossite (D), Tridymite (T), Spinel (S), Pyroxene (P) all samples contained copper metal

Temperature (°C)	**Final phases when cooling down (series I)**						**Final phases when heating up (series II)**					
	L	C	D	S	T	P	L	C	D	S	T	P
1075	X	X	X		X	X		X	X		X	X
1080	X		X		X	X	X	X	X		X	X
1085	X		X		X	X	X		X		X	X
1090	X		X	X	X	X	X			X	X	X
1095	X			X	X	X	X			X	X	X

Table 5-2 shows that, upon cooling down, spinel starts transforming into delafossite at a temperature in between 1095 and 1090 °C. Cuprite appears at a temperature between 1080 and 1075 °C. Upon heating up, liquid appears between 1075 and 1080 °C and delafossite transforms to spinel at approximately 1090 °C.

It was concluded that the tridymite–pyroxene–delafossite–cuprite eutectic temperature lies between 1075 and 1080 ± 5 °C and the delafossite–spinel transformation temperature on the tridymite–pyroxene–spinel boundary is approximately 1090 ± 5 °C.

5.5 Summary

Phase equilibria data on the 'Cu_2O'–'Fe_2O_3'–MgO–SiO_2 system in equilibrium with copper alloy were obtained. The results were used to determine liquidus temperatures and primary phase fields of pyroxene and olivine. Also, solid solutions of tridymite, pyroxene, olivine and spinel were reported.

Several phase diagram sections at constant wt.% MgO and at constant temperatures have been developed. It was found that at MgO concentrations as low as 1 wt.%, the pyroxene and olivine primary phase fields appear in the system. As MgO concentrations increase, liquidus temperatures in the olivine and pyroxene primary phase fields increase causing the primary phase fields to expand further into the spinel and tridymite primary phase fields. The maximum solubility of MgO in the system was determined to be 2.6 wt.% at 1150 °C and 5.1 wt.% at 1200 °C.

The cuprite–delafossite–tridymite–pyroxene eutectic temperature of the quaternary system was determined to be between 1075 and 1080 ± 5 °C. The spinel–delafossite transformation temperature on the spinel–tridymite–pyroxene boundary was found to be 1090 ± 5 °C.

These results can be used to improve existing phase equilibria databases.

Part IV

Freeze linings

“Always something new, always something I didn’t expect, and sometimes it isn’t horrible. [The Wheel of Time, Robert Jordan]”

6 Cold modelling of freeze lining behaviour

6.1 Introduction

6.1.1 Freeze linings

The conventional approach to the containment of aggressive molten slags in pyrometallurgical processes is to use high-density, high-melting temperature refractory materials that are in direct contact with the liquid. Under these hot-face conditions, in which containment material is at the same temperature as the bulk bath, the refractories progressively degrade and must be periodically replaced. The usable refractory life time is dependent on the rates of interactions between refractory and slag, which include the mechanisms of direct dissolution of refractory grains into the liquid slag or their removal through selective dissolution of the binding phase.

An alternative approach is the use of freeze linings in which a layer of solid bath material is deliberately formed on the surfaces and inner walls of high temperature reactors to provide protection from these corrosive liquid slags. The technology involves extracting heat through the lining through cooling of one face of the lining. The freeze lining approach has been applied to the design of lances and to fixed walls in particularly aggressive environments to enable the processes to be successfully undertaken at an industrial scale [9, 24, 26, 63]. In these systems, the heat is transferred from the bulk slag to the deposit liquid interface, then through the thickness of the freeze lining and the outer wall of the reactor. The rate of heat transfer, Q_{FL}, from the bulk bath to the deposit liquid interface can be described by an equation of the form

$$Q_{FL} = h_{bath} A_{bath,FL} (T_{bath} - T_{bath,FL}) \quad \textbf{(6-1)}$$

where $T_{bath,FL}$ is the bath-freeze lining interface temperature, T_{bath} the bulk bath temperature, and h_{bath} the convective heat transfer coefficient of the bath [9]. As such, the heat loss through the freeze lining (Q) is determined by the difference between the bulk bath temperature and the bath-freeze lining interface temperature, the interface area ($A_{bath,FL}$) and the convective heat transfer coefficient of the bath.

The heat loss through a planar furnace wall at steady state can also be described by an equation of the form

$$Q_{FL} = \frac{\left(T_{bath,FL} - T_{coolant}\right)}{\frac{\Delta x_{FL,ss}}{A_{bath,FL}k_{FL}} + \frac{\Delta x_{cooling}}{A_{bath,FL}k_{cooling}} + \frac{1}{A_{bath,FL}h_{coolant}} + A_{bath,FL}R_{contact}} \quad \textbf{(6-2)}$$

where k_{FL} represents the thermal conductivity of the freeze lining, $T_{bath,FL}$ the bath-freeze lining interface temperature, $T_{coolant}$ the temperature of the coolant, T_{bath} the bulk bath temperature, $\Delta x_{cooling}$ the thickness of the cooling blocks, $k_{cooling}$ the thermal conductivity of the cooling blocks, $h_{coolant}$ the convective heat transfer coefficient between the coolant and the cooling blocks and $R_{contact}$ the contact resistance between the cooling blocks and the freeze lining.

It is difficult to accurately predict from first principles the temperature profiles in these systems since the interface temperature and the thermal parameters are not strictly independent variables [51, 57-59]. As a first approximation, a number of simplifying assumptions can be made. For example, if under thermal steady state conditions the parameters are constant, the steady state thickness of the freeze lining ($\Delta x_{FL,ss}$) can be described by equation **(6-3)** [5, 16, 65].

$$\Delta x_{FL,ss} = k_{FL}\left(\frac{\left(T_{bath,FL} - T_{coolant}\right)}{h_{bath}\left(T_{bath} - T_{bath,FL}\right)} - \left(\frac{\Delta x_{cooling}}{k_{cooling}} + \frac{1}{h_{coolant}} + R_{contact}\right)\right) \quad \textbf{(6-3)}$$

Equations **(6-1)** and **(6-3)** show that both the steady state thickness of the lining and the heat loss through the lining are dependent on $T_{bath,FL}$. A number of approaches have been used to predict the growth and steady state thickness of freeze linings [6, 9, 10, 12, 16, 45]. In most of the previous predictions for thermal steady state conditions, the assumption has been made that the temperature at the bath-freeze lining interface equals the liquidus temperature of the bulk slag, and that the primary phase forms a dense sealing layer at this deposit/liquid interface. As a result of recent research on these systems, there is now extensive experimental evidence [51, 57, 58, 60, 63, 91] to demonstrate that the interface temperature can be below the liquidus and that the primary phase is not necessarily present at the deposit/liquid interface at thermal steady state conditions (see sections 2.3 and 2.4). These observations clearly indicate that to explain freeze lining behaviour, other factors, in addition to thermal parameters of the system, need to be considered.

Based on examination of freeze lining deposit/liquid interfaces and samples taken from slag baths prepared under a range of conditions, a general conceptual framework has been proposed by Fallah-Mehrjardi et al. [51] that can be used to explain the observed phenomena. The framework envisages dynamic steady state conditions in which crystallisation on detached crystals continuously takes place in the liquid as it moves towards the freeze lining deposit through a boundary layer below the liquidus temperature. The detached crystals approach local equilibrium with the liquid and, rather than

becoming attached to the deposit, are returned to the bulk liquid through the action of turbulent eddies formed at the cooled deposit/liquid interface. These detached crystals are subsequently fully or partially dissolved upon moving back towards the bulk bath, which is maintained above the liquidus temperature (Figure 6-1).

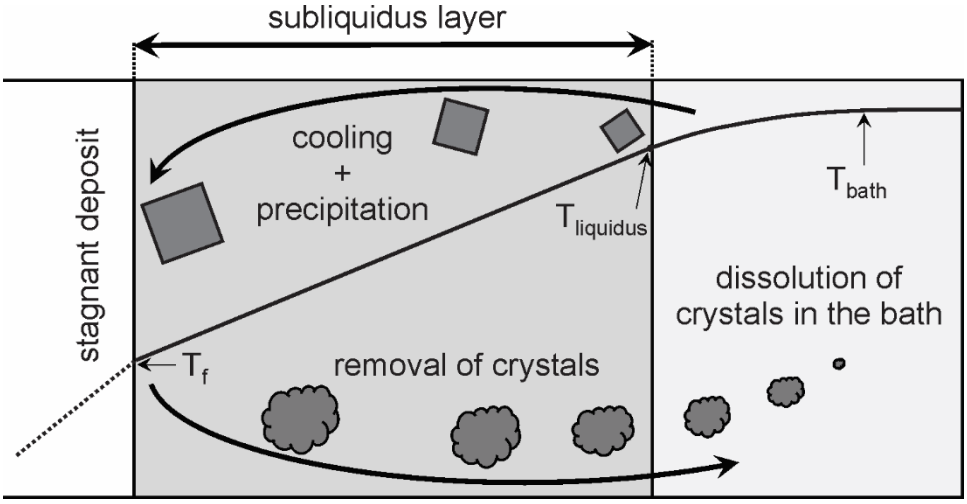

Figure 6-1: Schematic representation of the conceptual dynamic steady state framework for freeze lining formation proposed by Mehrjardi et al. [51].

Using this conceptual framework, it becomes clear that steady state freeze lining behaviour is determined by not only heat transfer and thermal factors, but also by the relative rates of mass transfer and elementary reaction steps, such as nucleation, crystallisation rate, crystallisation pathway, phase transformations and phase equilibria in the reaction system. These factors are summarised in Table 6-1. How they might influence the behaviour within different systems is briefly discussed in the following sections.

6.1.2 Heat transfer/thermal factors

The principal mechanisms of heat transfer are well established involving thermal diffusivity, natural convection and forced convection. These mechanisms all contribute to the overall heat transfer coefficient, h_{bath}, which is commonly described through the use of the dimensionless Nusselt number ($Nu = f(Re,Pr,Gr)$), where Re, Pr and Gr represent the Reynolds number, Prandtl number and Grashof number respectively. The relationships between physical properties of the fluids and heat transfer for simple geometries have been established [92]. Alternatively, computational fluid dynamic models are available to assist in estimating these values.

Whilst conduction and convection are the principal mechanisms of heat transfer in opaque systems, heat transfer can also take place through electromagnetic radiation through translucent materials [93].

From equation **(6-1)**, it can be seen that the heat flux to the lining from the bulk bath is directly proportional to the temperature difference (T_{bath}-$T_{bath,FL}$) between the bath and the liquid bath/freeze lining interface. Through equation **(6-3)**, it can be determined that an increasing bath temperature will result in a reduction of the freeze lining thickness.

All chemical reactions and phase transformations have enthalpy changes associated with them, either exothermic or endothermic. Locally, heat transfer mechanisms will take place in parallel with any chemical change.

6.1.3 Mass transfer/physical factors

Mass transfer takes place through analogous mechanisms to those described for heat transfer, involving contributions from mass diffusivity, natural convection and forced convection. The mass transfer coefficients are related to physical characteristics of the system through the Sherwood number (Sh = f(Re,Sc,Gr)) whith Re, Sc and Gr representing the Reynolds number, Schmidt number and Grashof number respectively [92].

Flow mechanisms, such as laminar and turbulent flow are also influenced by the relative movements of solids and fluid phases, as well as local geometry.

In the context of the influence on freeze lining formation, these mass transfer mechanisms have the potential to influence, e.g. the rate of transfer of the fluid and detached crystals to and from the bulk liquid and the deposit liquid interface, the time of passage through the subliquidus region, and local mass transfer of solute to and from these detached crystals.

6.1.4 Elementary reaction steps/chemical factors

Having established that the deposit liquid interface can be less than the equilibrium liquidus temperature for the system, the relative rates of a number of different reaction steps must be considered. Some of these arise directly from consideration of the conceptual framework that has been described in Figure 6-1.

It is envisaged that primary phase crystals can form in the subliquidus layer ahead of the steady state interface. These crystals can form through homogeneous or heterogeneous nucleation mechanisms. The rate of nucleation depends on a number of factors, including the thermodynamic driving force (also expressed as local undercooling of the melt), solids composition and interfacial energy. In the

case of heterogeneous nucleation, additional factors, such as pre-existing solids, % solids, and the composition and crystal structure of these solids can be important.

The rates of growth and dissolution of these crystals as they pass through the subliquidus layer should also be considered. The rate of crystal growth will be influenced by local undercooling and concentrations of the components in the solid and liquid phases.

As the crystals approach the deposit interface, the local temperature will decrease and the relative stabilities of solid phases that could be formed in the system will change. The crystallization path and the sequence of changes at the crystal surface depend on the shape of the liquidus, the shape of the solidus, maximum% of solids above the solidus, the extent of solid solutions and the change in composition of the liquid and solid phases with temperature.

There are different reasons why there may be no crystals that are formed ahead of the deposit interface, associated with slow nucleation and/or growth rates. In extreme conditions, the deposit interface may even be at or below the glass transition temperature T_g, in which case the deposit interface would consist of an amorphous or glassy phase.

In the deposit itself, phase transformations and secondary reactions may take place; in these cases the reaction will depend on the phases present, the phase compositions and the proportion of phases. The microstructures and associations of these new phases can influence physico-chemical properties of the deposit, such as the local thermal conductivity. The shapes of the phases, e.g. faceted/non-faceted crystals, can also have an effect on the microstructures formed and the resulting physico-chemical properties.

At subsolidus temperatures, some materials undergo polymorphic transformation or other transitions that can influence chemical or physical properties, e.g. release of gases from solution and changes in molar volume.

It will be clear from the many elementary reaction steps that can take place in these systems that many of the factors listed (Table 6-1) influence more than one process or reaction step.

Table 6-1: Potential elementary reaction steps and factors that influence steady state freeze lining behaviour.

	Heat transfer/ thermal factors	**Elementary reaction steps/ chemical factors**	**Mass transfer/ physical factors**
Bath	*Bulk heat transfer* Nu = f(Ra,Re,Pr,Gr) (T_{bath}-$T_{bath,FL}$) - Natural convection - Forced convection - h_{bath} - $c_{p,bath}$ - k_{bath} • k_{phonon} • $k_{radiation}$ • $k_{electronic}$ - ρ_{bath} - Geometry	*Homogeneous nucleation rate* - Solids composition - Undercooling - Interfacial energy *Heterogeneous nucleation rate* - Pre-existing solids - % solids - Crystal structure *Crystallization rate* - Undercooling - Mass diffusivity - Natural convection - Forced convection *Crystallization path* - Shape of liquidus - Shape of solidus - Max% of solids above solidus - Solid solutions *Glass transition temperature, T_g*	*Bulk flow* - Sh = f(Re,Sc) - Mass diffusivity - Natural convection - Forced convection *Local flow* - Geometry
Freeze lining	k_{FL} - porosity - phases present - phase proportions - microstructure	*Phase transformations/reactions* - phases present - phase compositions - phase proportions - microstructure, faceted/non-faceted crystals - phase transition temperature - change in molar volume - chemical reactions	

	Heat transfer/ thermal factors	**Elementary reaction steps/ chemical factors**	**Mass transfer/ physical factors**
Cooling blocks	$k_{cooling}$ Geometry		
Coolant	$T_{coolant}$ $h_{coolant}$ - $c_{p,coolant}$ - $k_{coolant}$ - $\rho_{coolant}$		

Only some of these factors have been investigated to date

Heat transfer

The effect of heat transfer on the steady state freeze lining behaviour is well established by previous research [3-6, 16, 32, 37, 39, 41, 43, 44, 49, 94, 95], as has been discussed in Chapter 2.

Mass transfer

Mehrjardi et al. [58] studied the effect of bath agitation on freeze lining behaviour. Increasing bath agitation was found to increase the liquid bath/deposit interface temperature and result in a denser interface structure, containing a higher proportion of solids. The steady state thickness decreased and the steady state heat flux increased with increasing bath agitation.

Guevara and Irons [46] demonstrated the effect of the bulk fluid flow. The freeze lining is thinnest at the position at which the fluid arrives from the bulk bath at the freeze lining interface. The longer the fluid travels across the freeze lining interface, the thicker the freeze lining becomes. This change in thickness can be attributed to two causes. Firstly, the temperature of the liquid is higher at the top than at the bottom due to thermal stratification. Secondly, the natural convective boundary layer grows thicker the longer the liquid travels along the freeze lining.

Liquidus temperature

Thonstad et al. [50] studied the effect of changes in liquidus temperature, using a solution of stearic acid and myristic acid, as well as plant observations in aluminium processing. It was found that, as the liquidus temperature of the bath is changed, the bath temperatures shifts in the same direction.

This was attributed to the achievement of thermal balance. As long as the heat input stays constant, the heat loss through the freeze lining has to stay constant as well. Equation **(6-1)** demonstrates that this requires the superheat ($T_{bath} - T_{bath,FL}$) to stay constant. As the bath-freeze lining interface equalled the liquidus temperature in the investigated systems, the bath temperature has to shift in the same direction as the liquidus temperature to achieve a constant superheat.

Chemical composition

Campforts et al. [54] investigated the microstructure of six synthetic lead slags to demonstrate the importance of slag engineering in the optimization of freeze lining behaviour. While most slag systems formed freeze linings consisting of several (partially) crystalline layers, the slag system containing the highest concentration of silica was found to form a glassy freeze lining, containing only a few microcrystals.

Fallah-Mehrjardi et al. [9, 51, 57, 58, 60, 63, 91] studied freeze linings in the Al_2O_3-'Cu_2O'-'Fe_2O_3'-SiO_2, calcium ferrite, cryolite and industrial lead slag systems. Depending on the system, the interface temperature ranged from the solidus temperature to the liquidus temperature. In one particular study [51], it was shown that slightly decreasing the silica content of a slag could cause a transition of the interface temperature from below the liquidus to the liquidus temperature.

Superheat, undercooling

Guevara and Irons [46] studied the effect of changing superheat on freeze lining behaviour in the $CaCl_2$-H_2O system. The steady state thickness of the freeze lining was found to decrease with increasing superheat. The liquid bath/deposit interface was found to be equal to the solidus temperature in all experiments.

Fallah-Mehrjardi et al. [64] observed the presence of solids in the bulk bath liquid during freeze lining experiments in a non-ferrous industrial slag. Based on this, it was suggested that freeze linings could possibly be created while operating at subliquidus bath temperatures.

6.2 Methodology

6.2.1 Experimental apparatus

Undertaking experimental studies at high temperature using metallurgical slag systems is difficult and time consuming, and it is not possible to observe the phenomena taking place at the deposit/liquid

interface. In the present study, the approach used by Guevara and Irons [46] of using a cold model to investigate the effects of different factors on freeze lining formation has been adopted. The detailed design of the apparatus used in the present study differs slightly from that reported in [46]. Figure 6-2 shows the experimental apparatus in which aqueous solution containing $CaCl_2$ flows over a water-cooled copper plate. The freeze lining deposit forms on the surface of the plate and the process is continuously observed through the transparent wall of the reactor. The reactor consists of a tank made from acrylic sheet (inside dimensions 30 cm length, 5 cm width, 10 cm height, 1 cm wall thickness) surrounded on three sides, the top and the bottom by 3 cm thick polystyrene foam insulation. The fourth side, along the length of the bath, was made of a double layer of acrylic sheet with a 1 cm air gap in between. A removable lid containing a 2 mm wide slit across the length of the lid allowed temperature measurements to be made using thermocouples without removal of the lid. A copper cooling plate with cooling circuit welded on the back, through which tap water at room temperature was run, was used on the cold side of the tank. To direct the solution flow to the surface of the copper plate, a 2 mm thick acrylic plate was positioned horizontally in the middle of the tank, leaving a 5 cm gap between the cooled copper circuit and the acrylic plate. The forced circulation of the aqueous solution along the tank above the acrylic dividing plate was achieved using an electrically driven peristaltic pump (Masterflex console drive + Masterflex Easyload head, model 7518-10, ColePalmer, USA) with Masterflex Norprene tubing (A60 G, L/S 18). The solution exited the tank at the opposite end to the water-cooled plate. The bulk solution was heated in a separate copper tank (10x10x10 cm, 1mm wall thickness) containing a spiral shaped titanium heating element (240V, 200 W, 40 mm OD, 75 mm height).

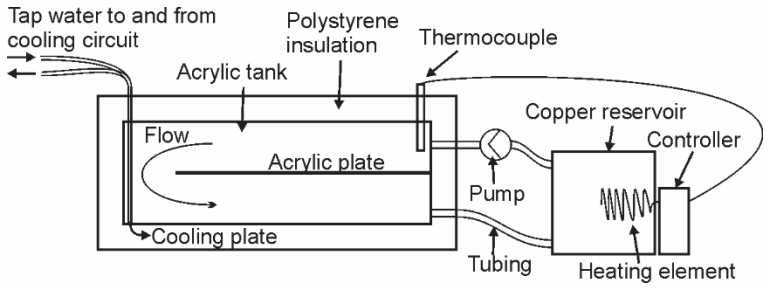

Figure 6-2: Schematic of the experimental apparatus

A 0 – 120 °C bulb/capillary type thermostat was used to control the bath temperature within ±0.5 °C. The temperatures in the bath were measured using thin K-type thermocouples (⌀ 1 mm, ECEFAST, Australia). A similar thermocouple was used to measure the interface temperature. To provide more accurate interface temperature measurements, the stainless steel protective sheath was stripped back from this thermocouple, exposing the thermocouple tip. All thermocouples were calibrated against

the controller thermocouple (Figure 6-2) before each measurement. The temperature of the tap water was found to be approximately 20 °C and varied within ±1 °C over the course of each experiment.

6.2.2 Experimental procedure

Distilled water and $CaCl_2.2H_2O$ (>99% purity, Sigma Aldrich) were mixed in the acrylic tank. The tank was closed and heated to 50 °C while applying a solution flow rate of 875 ml/min. The acrylic tank was left over night until all the $CaCl_2.2H_2O$ had dissolved. The bath was cooled until the desired bath temperature was reached and the solution flow rate was adjusted to the desired experimental value, after which the cooling water to the copper plate was turned on. Images of the thickness of the freeze lining deposit were recorded through the transparent side of the acrylic tank using a digital camera, positioned approximately 0.5 m from the acrylic tank. The thickness of the freeze lining was measured using the ImageJ software [96]. The same grid cell was chosen as scale on each image. The distance from the freeze lining interface to a set vertical grid line was measured. Subtracting this value from the distance of this vertical grid line to the cooling plate measured in the initial image yielded the freeze lining thickness.

Temperatures at the interface were measured at specific positions at specific times, with larger intervals between measurements as the experiment progressed and the freeze lining grew more slowly.

6.2.3 The $CaCl_2$-H_2O system

Figure 6-3 shows the phase diagram of the $CaCl_2$-H_2O system from -60 to +80 °C and 0 to 80 wt. % $CaCl_2$, reported by M Conde Engineering [97]. In this composition range, four solid compounds are present: congruently melting ice (H_2O), and incongruently melting $CaCl_2.6H_2O$ (50.7 wt.% $CaCl_2$), $CaCl_2.4H_2O$ (60.6 wt.% $CaCl_2$) and $CaCl_2.2H_2O$ (75.5 wt.% $CaCl_2$).

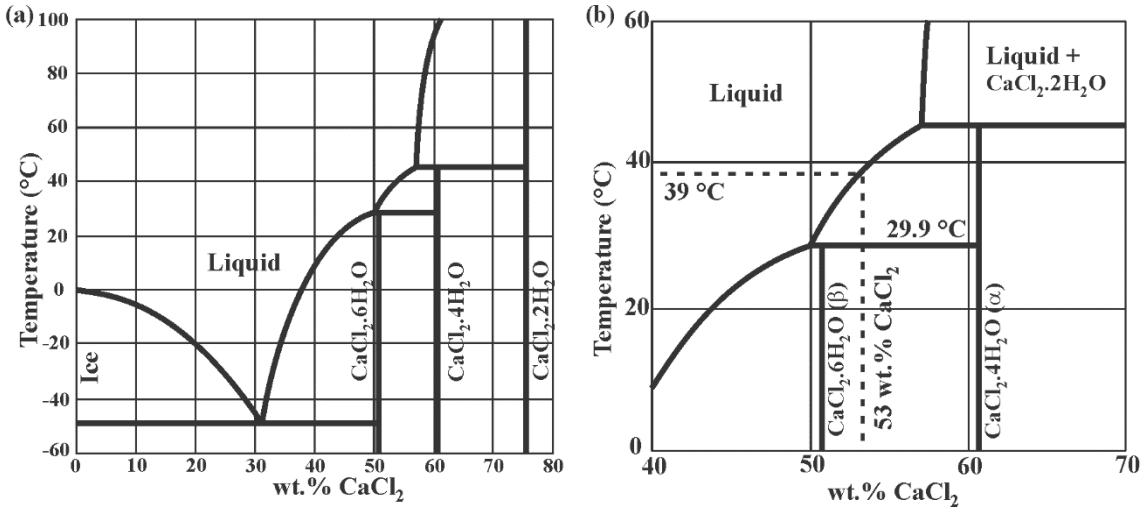

Figure 6-3: (a) Phase diagram of the $CaCl_2$-H_2O system; (b) Close-up of the conditions of interest for the current study

For experimental convenience, initially a 53 wt.% $CaCl_2$ solution was selected for the study, equal to the solution selected by Guevara et al. [46]. Upon equilibrium cooling of this solution, the $CaCl_2.4H_2O$ solid primary phase (α) precipitates out of the liquid at approximately 39 °C. Upon reaching the solidus temperature of 29.9 °C [98], a peritectic reaction between the liquid and the primary phase results in the formation of solid $CaCl_2.6H_2O$; this secondary phase will be referred to as (β) in the following figures.

To examine the effect of solution composition, the behaviour of a 52 wt.% $CaCl_2$ solution was also examined. The crystallization path of this solution is similar to that of the 53 wt.% $CaCl_2$ solution, but this solution has a liquidus temperature of approximately 35 °C according to the phase diagram presented in Figure 6-3.

6.3 Experimental results

6.3.1 Deposit structure

A number of experiments have been carried out using a range of operational conditions, examining the influence of solution composition, aqueous solution flow rate and bath temperature on freeze lining formation (see Table 6-2). A typical example of freeze lining growth in the current study is shown in Figure 6-4 (Experiment 1, Table 6-2). This experiment was carried out using a solution containing 53 wt.% $CaCl_2$, a bath temperature of 40 °C and a solution flow rate of 111 ml/min.

Table 6-2: List of experimental settings, times at which the white area was first observed, interface temperatures at the end of the experiments and solid phases present at the deposit/liquid interfaces. Experiments marked by

'*' indicate experiments where the gap between the cooling plate and the tank was closed off using Norprene tubing.

Exp.	wt.% $CaCl_2$ in solution	Solution flow rate (ml/min)	T_{bath} (°C)	Time at which white area was first observed	$T_{interface,end}$ (°C)	Phases at interface
1	53	111	40	840	35.3	α
2	53	328	40	180	37.0	α
3*	53	328	40	10560	29.8	β
4	53	854	40	1920	36.9	α
5*	53	328	50	7440	29.5	β
6*	53	854	50	3240	/	α
7*	52	111	40	8880	29.4	β
8*	52	111	40	5520	34.7	α
9	52	111	40	2100	35.9	α
10	52	854	40	1320	35.5	α

At time zero, there is no deposit on the cooled copper plate. The first layer of freeze lining formed (β + L) was grey in appearance and grew evenly over the height of the cooled plate (see 0.27 h). After 0.53 h, a white area has appeared in the deposit, growing from a position at the rear of the cooled copper plate and increasing in size, as can be seen from the images obtained at 0.53, 0.80 and 1.45 h. As the time progressed, the extent of this white region increased until it occupied the whole length of the deposit from top to bottom, and also reached the deposit/liquid interface. At those locations where the white area reached the deposit/liquid interface, facetted grey crystals (α) were formed during subsequent growth of the deposit (0.80 h, 1.45 h). The thickness of the deposit continued to grow until the experiment was terminated after 41.0 h. No steady state was achieved. During growth of the freeze lining, the interface is non-planar due to the columnar growth of the α crystals, with each crystal forming a 'bump' on the interface, as can be see at 2.5h (Figure 6-4). As can be seen in Figure 6-4, the lower section of freeze lining near the bottom of the tank formed a thicker deposit than on the upper part of the copper plate. The deposit/liquid interface temperature at the end of the experiment (41 h) was found to be 35.3°C. No detached crystals were observed in the liquid bath at any time during the experiment.

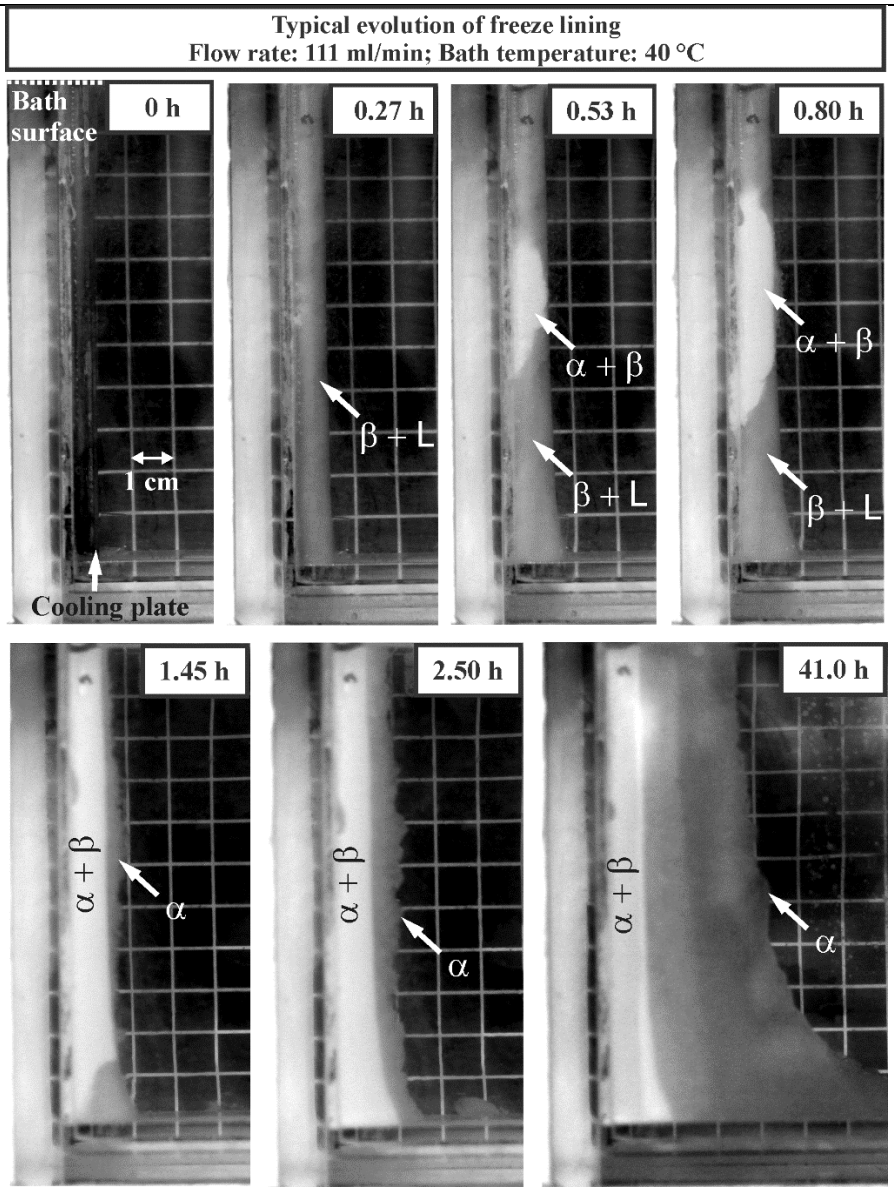

Figure 6-4: Freeze lining growth in a 53 wt.% $CaCl_2$/water solution. Experiment was carried using a bath temperature of 40 °C and a flow rate of 111ml/min.

Similar results were obtained for a 53 wt.% $CaCl_2$ solution, a bath temperature of 40 °C and fluid flow rates of 328 and 850 ml/min, and for a 52 wt.% $CaCl_2$ solution with a bath temperature of 40 °C and fluid flow rates of 111, 328 and 850 ml/min; the interface temperatures in all of these cases were in the range of 34.7 to 37.0 °C.

The time and position at which the white area was first observed in the deposit on the copper plate was different for each experiment; it was unclear what causes or facilitates the formation of this layer, however, it was found that isolating the back of the copper plate from the bulk solution decreased the rate at which the white phase spread to the freeze lining that was in contact with the bulk solution. In experiments 3*, 5*, 6*, 7* and 8*, the apparatus was modified by inclusion of a barrier in the form of a Norprene rubber strip between the copper plate and the bath sidewall to limit the spread of the

white area. In these experiments, thermal steady state was achieved in relatively short times (2 – 10 h, see Figure 6-5) and, in stark contrast to the other experiments, the temperature of the deposit/liquid interface of experiments 3*, 5* and 7* was found to be between 29.4 and 29.8 °C. Inspection of the phase diagram shown in Figure 6-3 shows that this corresponds to the upper limit of stability of the β $CaCl_2.6H_2O$ phase.

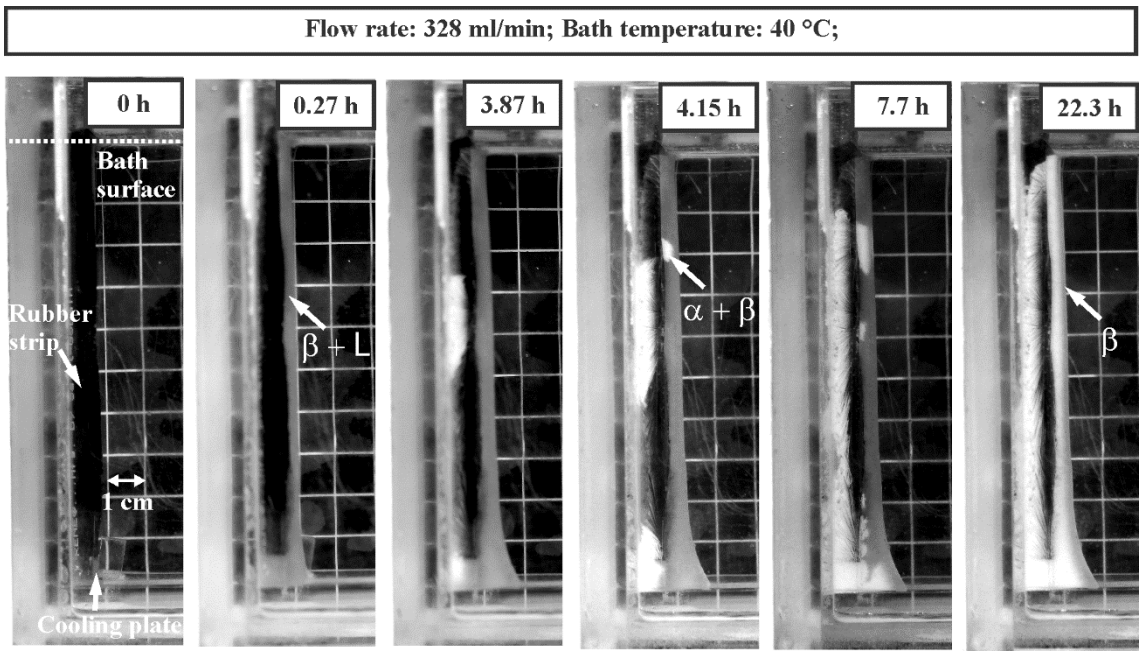

Figure 6-5: Freeze lining growth in a 53 wt.% $CaCl_2$/water solution. Experiment 3* was carried out using a bath temperature of 40 °C and a flow rate of 328 ml/min. No layer of α was formed at the deposit/liquid interface. Steady state interface temperature was found to be 29.8 °C.

Subsequently, samples of the deposit formed in experiment 9 were taken for thermo-gravimetric analysis (TGA) (see Appendix A). It was found that the sample from the white layer had a bulk composition of 51.2 wt.% $CaCl_2$, which approximately corresponds to the bulk bath composition of 52 wt.% $CaCl_2$ in this experiment. According to the phase diagram shown in Figure 6-3, this bulk composition below the solidus would result in a mixture of the β phase, $CaCl_2.6H_2O$, and α phase, $CaCl_2.4H_2O$, assuming chemical equilibrium is achieved. In the same experiment, the composition of the crystals in the grey layer formed after the white layer had reached the deposit/liquid interface was determined to be 59.0 wt.% $CaCl_2$, which closely approximates the composition of the primary $CaCl_2.4H_2O$ phase, α, (60.6 wt.% $CaCl_2$).

In experiments (Exp 3*, 5*, 7*), in which the white layer never reached the deposit/liquid interface, the layer consisting solely of α $CaCl_2.4H_2O$ was never formed. Due to interaction with the bulk bath, interconnectivity with the white area and hydration + melting when exposed to the atmosphere, no samples could be taken of the interface in these experiments.

Figure 6-6 shows a section of the deposit in which individual primary phase α, $CaCl_2.4H_2O$, crystals have nucleated and started to grow along the deposit/liquid interface. It can be seen that the α phase forms relatively large (0.3 cm diameter) facetted crystals and the interface is irregular in shape. In contrast, the first-formed β interface exhibits a macroscopically smooth and even structure, producing a deposit layer of uniform thickness.

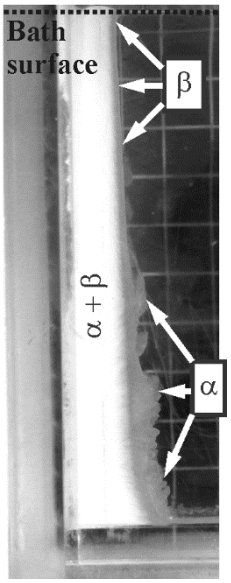

Figure 6-6: Deposit interface showing the formation and growth of primary phase α crystals across the original interface consisting of the β phase. Experiment was carried out in a 52 wt.% $CaCl_2$ in water solution, bath temperature of 40 °C and solution flow rate of 111 ml/min.

6.3.2 Deposit thickness

The thicknesses of the deposits as a function of time are shown in Figure 6-7 and Figure 6-8. The thicknesses of the deposits were measured at the mid-height of the cooling plate at the same level as the dividing plate. It can be seen that in all cases, the rate of growth of the deposits decreases as the thickness increases. From the results obtained in experiments 1, 2, 4, 8*, 9 and 10 (Figure 6-7), it can be seen that there is no significant effect of solution fluid flow rate on deposit growth rate. Inspection of the deposit structure of experiments 4 and 8* shows that in these cases, the nucleation of the primary phase was delayed relative to the other experiments. The dotted lines in these experiments represent estimated sections, based on the growth of the deposit in experiments with similar settings, where the primary phase was present at the interface. Whilst there are differences in the initial growth rates of the deposits, the steady state deposit thickness, approached at longer times for the solutions containing 52 wt.% $CaCl_2$ are, for these conditions, within the uncertainty of the experiments, independent of the fluid flow rate (Exp. 8*, 9, 10).

The steady state deposit thicknesses, in contrast, appear to be highly sensitive to solution concentration. In experiments 1, 2 and 4, the limiting values of deposit thickness for the solution containing 53 wt.% $CaCl_2$ appear to be approximately twice that of the solution containing 52 wt.% $CaCl_2$.

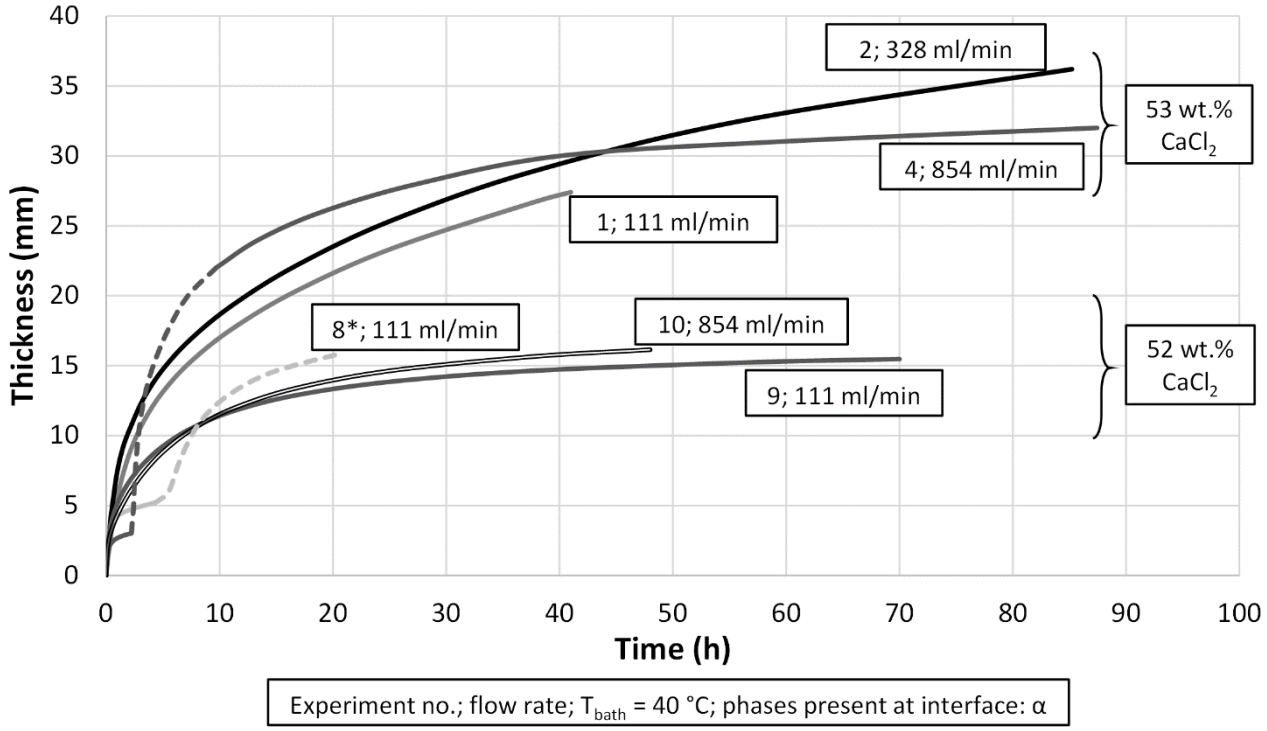

Figure 6-7: Deposit thickness as function of time for experiments 1, 2, 4, 8*, 9 and 10.

The thicknesses of the deposits as a function of time for experiments 3*, 5*, 6* and 7* are shown in Figure 6-8. It can be seen that for experiments 3* and 7*, the steady state deposit thicknesses for the 52 and 53 wt.% $CaCl_2$ solutions respectively, having the β phase at the deposit/liquid interface, are significantly less than for conditions where the primary α phase layer is formed, for comparable solution flow and bath temperature conditions (experiments 2, 9).

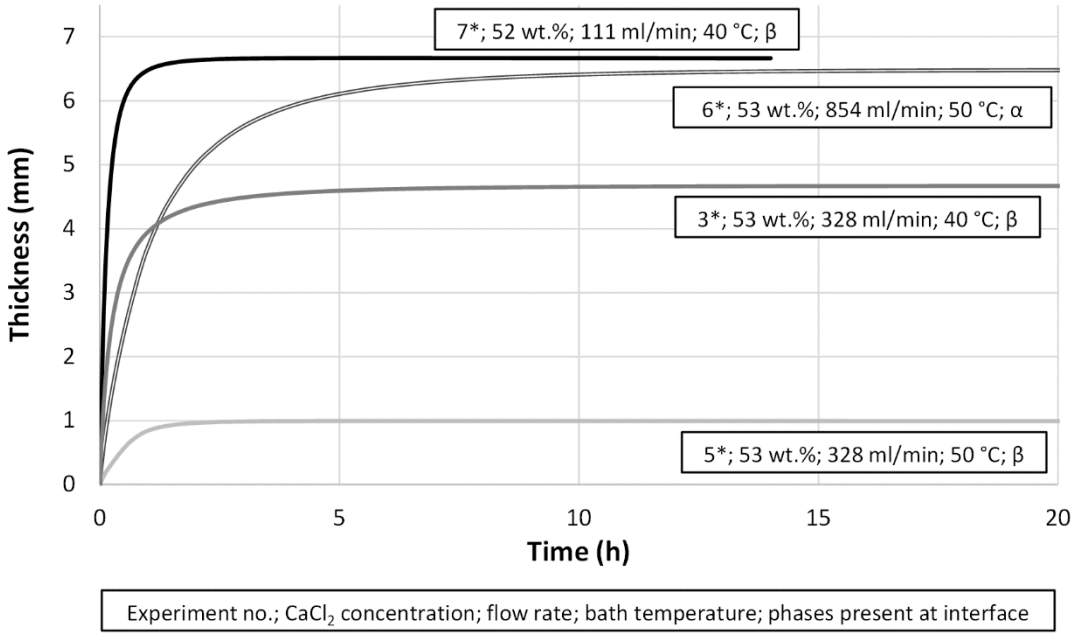

Figure 6-8: Deposit thickness as function of time for experiments 3*, 5*, 6* and 7*.

The effect of bath temperature can be seen from comparison of experiments 3* and 5* at 53 wt.% $CaCl_2$, having the β phase at the deposit/liquid interface, the deposit thickness for the higher bath temperature of 50 °C is significantly lower, than that for the bath at 40 °C.

The bath composition was not independently controlled at fixed composition. The total quantity of $CaCl_2$ in the system is fixed. As the deposit thickness increases, the $CaCl_2$ concentration in the aqueous solution changes. By undertaking a mass balance on the $CaCl_2$, the change in concentration can be calculated. Based on the total volume of solution (2.5 l) and the volume of the deposit when the deposit is 3.5 mm thick, the solution contains between 52.5 and 53.2 wt.% $CaCl_2$ for a starting composition of 53 wt.% $CaCl_2$, depending on the relative proportion of α and β in the deposit. This represents the worst case scenario where the thickest observed freeze lining consists of 100% α or β. As such, the actual changes in composition during the experiments will be lower and are not expected to significantly influence the freeze lining behaviour.

The level of the solution was found to stay constant through experiments, suggesting negligible evaporation of water took place during the course of each experiment.

6.4 Discussion

6.4.1 Comparison with previous study

The current study differs in several ways from the study by Guevara and Irons in the same system [45, 46]. As to the experimental apparatus, in the present study the geometry of the acrylic tank is different to that in [46], and a peristaltic pump was used to induce forced convection as opposed to the natural convection used by Guevara and Irons [46]. Also, in the present study the use of a separate tank containing the heating element significantly increased the time which the solution spent at temperatures above the liquidus compared to the previous design in [46].

These differences in experimental set-up resulted in some new observations: (i) the formation of a white, 2-phase area, within the deposit; (ii) the formation of an α, $CaCl_2.4H_2O$, layer at the interface in some experiments as opposed to a β, $CaCl_2.6H_2O$, layer; (iii) the lack of any detached crystals in the bulk liquid, even at temperatures below the liquidus.

The lack of detached crystals in the liquid close to the interface, at temperatures below the liquidus, can not be explained by the equilibrium solidification model proposed by Guevara and Irons [45].

6.4.2 Influence of phases present at the deposit/liquid interface

The results of the present study (see Table 6-2, Figure 6-7, Figure 6-8) indicate differences in the steady state interface temperature and deposit thickness depending on the phase that is in direct contact with the liquid bath. To demonstrate this, the bath temperature of the 7* experiment was adjusted after reaching steady state at 13 h. At this point in time, a β layer was present at the interface (Table 6-2). The deposit was then partially dissolved by increasing the bath temperature to 50 °C to reveal the underlying α + β layer before returning again to the original bath temperature of 40 °C. The measured thickness of the freeze lining over time and the measured interface temperature at the top, middle and bottom of the freeze lining are shown on Figure 6-9. The experiment was undertaken using the Norprene rubber seal to slow down the formation of the α + β layer (Figure 6-5).

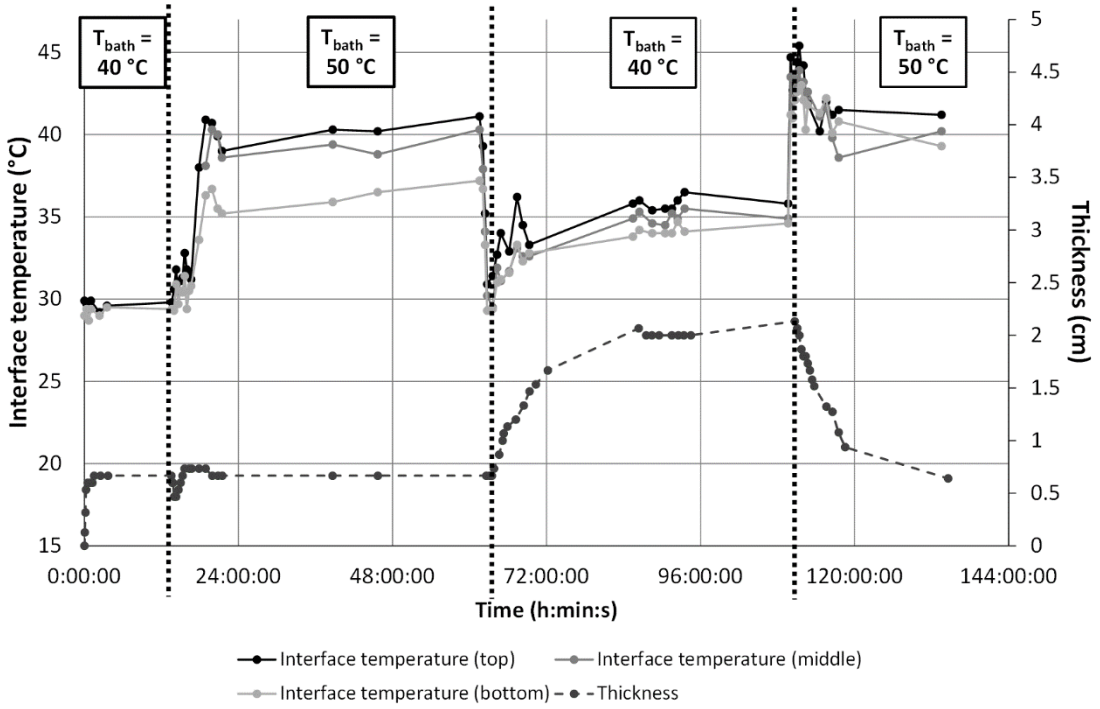

Figure 6-9: Measured interface temperatures at the top, middle and bottom of the freeze lining and the measured thickness of the freeze lining. The first 13 hours correspond to experiment 7*. Experiment was carried out in a 53 wt.% $CaCl_2/H_2O$ solution at a flow rate of 111 ml/min. Bath temperature was changed as indicated on the upper side of the graph.

During the initial stage of this experiment, the bath temperature was set at 40 °C. The freeze lining grew rapidly until it reached a thickness of approximately 7 mm (experiment 7*). No measurements of the interface temperature were performed until the freeze lining had reached a thickness of 5 mm (0.33 h). After this initial growth, interface temperatures at the top and at the bottom of the freeze lining were found to be 29.6 and 29.2 °C respectively. Interface temperatures at this stage remained constant with time.

After 13 h, the temperature of the bath was increased to 50 °C. After an initial decrease in the thickness of the freeze lining, the freeze lining thickness increases to approximately 7 mm (see Figure 6-9, Figure 6-10). Interface temperatures during this growth phase increase over time.

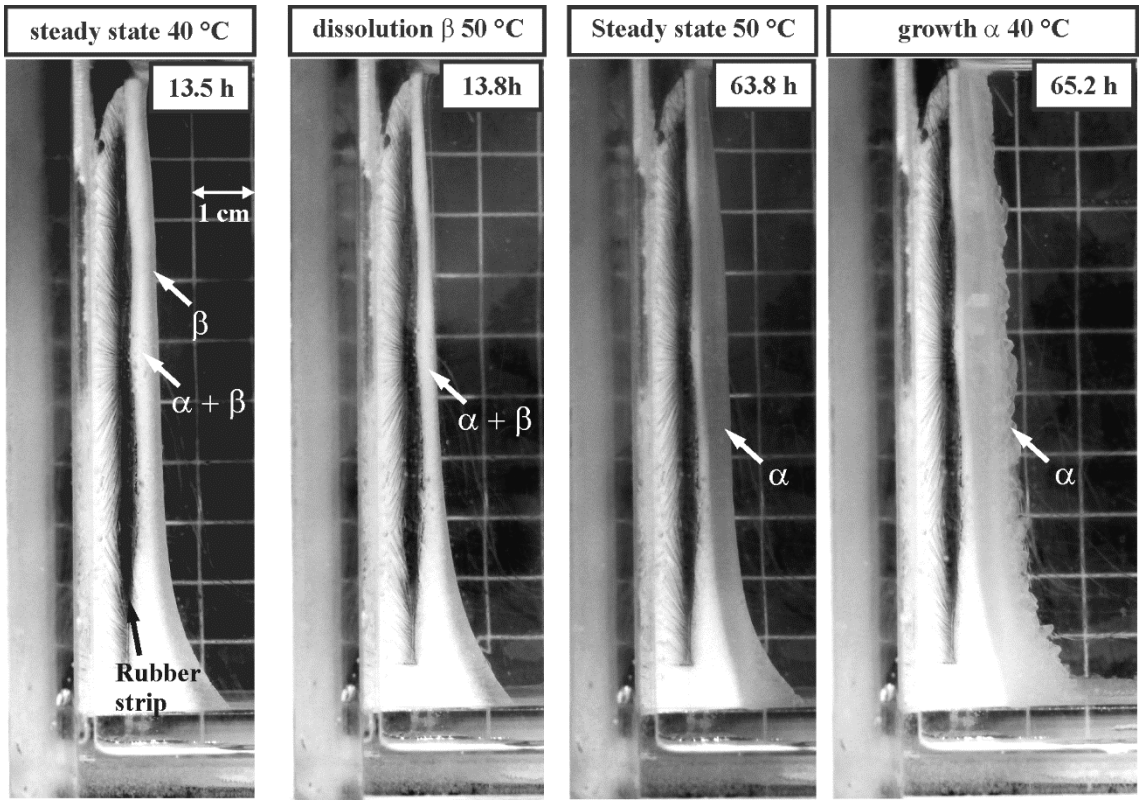

Figure 6-10: Evolution of freeze lining after increase and subsequent decrease in bath temperature. Experiment was carried out in a 53 wt.% $CaCl_2/H_2O$ solution at a flow rate of 111 ml/min. Bath temperature was changed as indicated on the upper side of the graph.

The subsequent decrease in temperature back to 40 °C after 60 h resulted in an increase in deposit thickness up to approximately 21 mm (see Figure 6-9, Figure 6-10). In the final step, the bath temperature was increased in temperature again to 50 °C after 108 h. The freeze lining partially dissolved back into the bath, decreasing the thickness to approximately 6 mm, which was within uncertainty of the thickness observed between 15 and 63 h. The measured interface temperatures after 108 h initially increased to values significantly above the steady state interface temperatures measured earlier at a bath temperature of 50 °C. Subsequently, interface temperatures dropped and reached values comparable to that observed between 20 and 63 h.

The results can be explained as follows: The β sealing layer formed initially at the deposit/liquid interface between 2 and 12 h was metastable. By changing the bath temperature from 40 °C to 50 °C, the metastable sealing layer was dissolved and replaced by a primary α phase sealing layer. When decreasing the bath temperature to 40 °C again, the primary phase sealing layer grew further, creating a much thicker freeze lining comparable to that observed in experiments 1, 2 and 4 in which the α phase was clearly identified.

The experiment indicates that once the initial metastable β layer has been dissolved, it does not reform when returning to the original conditions due to the formation of an α sealing layer.

6.4.3 Metastability of freeze linings

In a previous study by Guevara and Irons [46], detached crystals were observed in the liquid at subliquidus temperatures. Based on this observation, a numerical model was proposed assuming equilibrium solidification [45]. In the current study, no detached crystals were observed in the liquid adjacent to the freeze lining deposit, even when the interface temperature was well below the liquidus (Exp. 4*, 5*, 8*). As a result, the assumption of equilibrium solidification is not valid for the investigated conditions.

The results can be explained by considering a dynamic steady state, as proposed by Fallah-Mehrjardi et al. [51]. If, in the investigated system, the growth kinetics of the primary and secondary phases are such that the secondary β, $CaCl_2.6H_2O$, phase precipitates first (Figure 6-12b, c), and the subsequent nucleation/growth of the primary $CaCl_2.4H_2O$ phase (α) is slow compared to the mass transfer of material towards the deposit, the secondary β phase forms a sealing crystal layer before the primary α phase reaches the interface (Figure 6-12c). As no primary phase is present at the interface, the freeze lining stops growing when the interface temperature equals the temperature at which the secondary $CaCl_2.6H_2O$ phase becomes stable, that is, the liquidus temperature in the metastable system excluding the formation of $CaCl_2.4H_2O$ (Figure 6-11). It can be observed from Figure 6-11 that this temperature is approximately 29 °C, which is within the experimental uncertainty of the solidus temperature of 29.9 °C on the stable phase diagram (Figure 6-3).

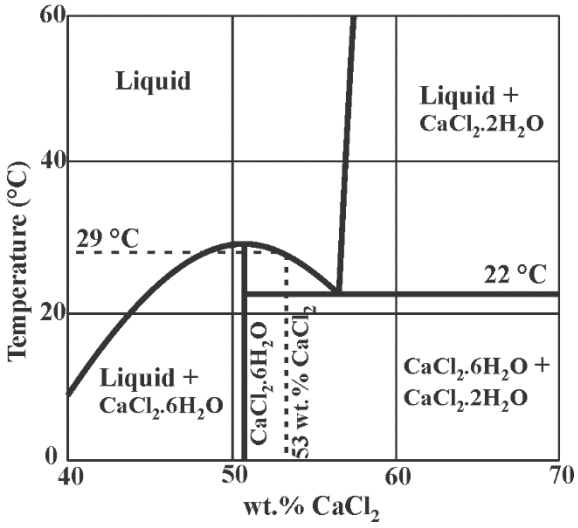

Figure 6-11: Estimated metastable phase diagram at the conditions of interest, excluding the formation of $CaCl_2.4H_2O$

Moreover, any primary $CaCl_2.4H_2O$ (α) crystals that do eventually nucleate in the liquid close to the deposit interface at subliquidus temperatures keep circulating in the bath, eventually dissolving back into the bulk bath liquid, at temperatures above the liquidus temperature.

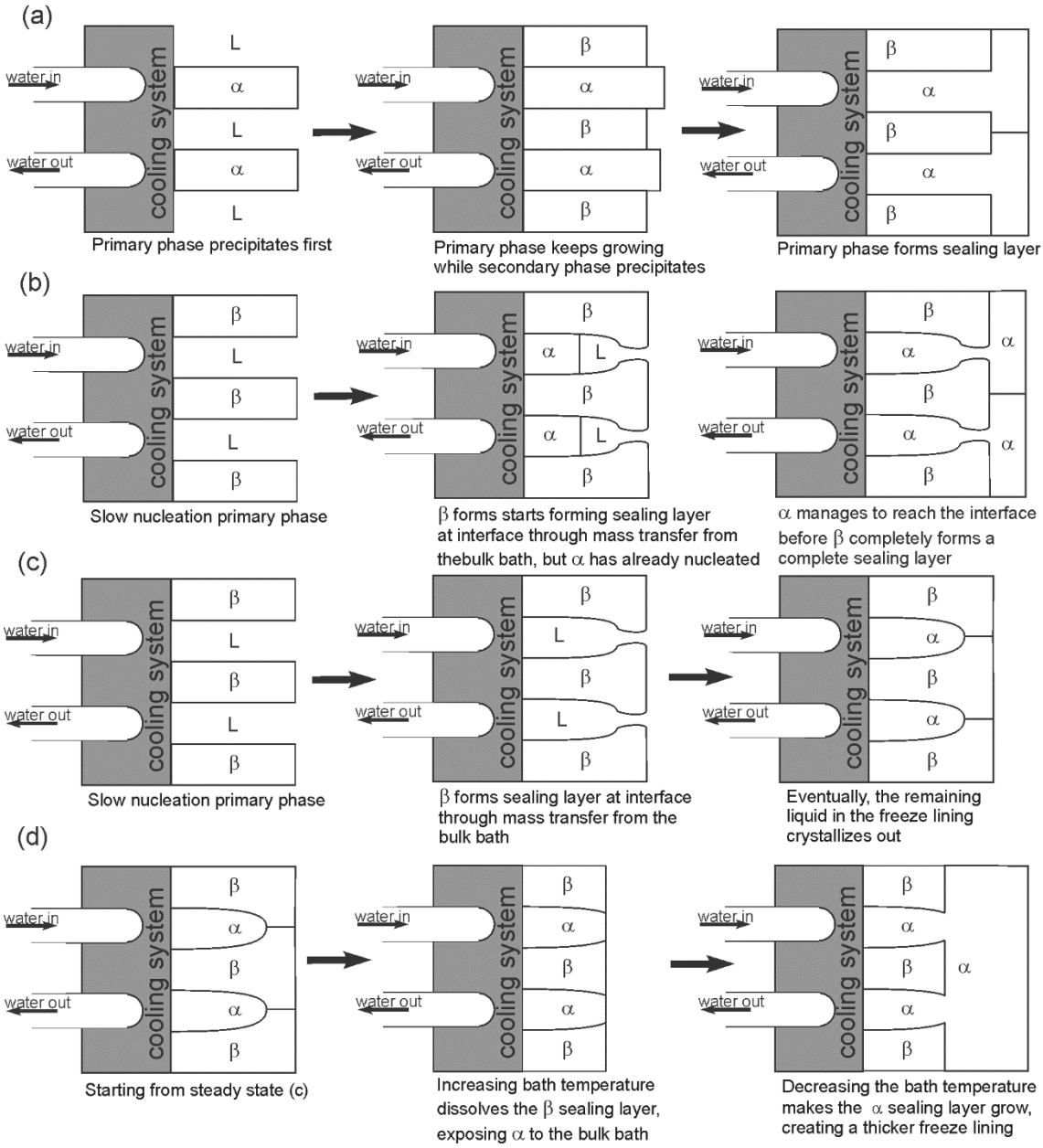

Figure 6-12: Potential microstructural changes during freeze lining formation. (a) Expected growth of the freeze lining, with the primary phase α precipitating first; (b) The formation of the primary α phase is slow, resulting in the partial closure of the β layer at the interface; (c) Dynamic steady state model where the formation of the primary α phase is inhibited. As a result, the secondary β phase forms a sealing layer; (d) Evolution of the freeze lining formed in (c) after an increase and subsequent decrease in bath temperature.

The detached crystals observed in earlier experiments by Guevara and Irons [46] can then be explained by considering the relatively short time detached crystals spent in the area with temperature above the liquidus. As such, these crystals, once nucleated, never dissolved completely and kept circulating in the bath.

As has been shown in the previous section (Figure 6-9, Figure 6-10), increasing the bath temperature after formation of the β sealing layer dissolves this sealing layer, exposing the primary α crystals to

the bulk bath. Subsequently, the primary α phase grows and forms a sealing layer (Figure 6-12d). Upon decreasing the bath temperature to its original value, this primary α sealing layer grows further, increasing the thickness of the freeze lining beyond its original thickness, to the same steady state thickness as in Figure 6-12a and b.

6.4.4 Liquification of intermediate layers

Inspection of Figure 6-13a shows that the local bulk composition in the freeze lining changes with increasing distance from the cooling system. It is interesting to consider what happens after increasing the bath temperature and/or agitation of the bath.

As mass transfer in the solid freeze lining is limited, the local bulk composition in the freeze lining will stay constant. As the agitation of the bath and/or the bath temperature increases, the thermal gradient inside the freeze lining will increase, evolving towards a new thermal steady state, according to the equation:

$$Q_{FL} = h_{bath} A_{bath,FL} \left(T_{bath} - T_{bath,FL}\right) = k_{FL} A_{bath,FL} \frac{dT}{dx} \qquad \textbf{(6-4)}$$

Assuming the temperature at the cold face stays constant, the local temperature in the freeze lining will thus increase.

If the increase in bath temperature/agitation is sufficiently high, part of the freeze lining containing the β phase can reach a local temperature higher than the local solidus temperature. As a result, this layer (partly) liquefies, as is demonstrated in Figure 6-13b, that is, the reaction β → α + L takes place.

This hypothesis was tested by increasing the bath temperature after conclusion of experiment 10 to 47 °C. It was found that a layer of the freeze lining liquefied, as is demonstrated in Figure 6-13c by inserting tweezers in the liquid gap.

The result of the liquification of this intermediate layer in the freeze lining is a reduction in the mechanical stability of the freeze lining. This is demonstrated in Figure 6-13c, where the impact of one of the 1mm diameter K-type thermocouples is enough to break off part of the freeze lining.

Assuming a constant coolant temperature, it can be shown that liquification occurs when the current temperature gradient is higher than the original temperature gradient in the freeze lining, that is:

$$\frac{h_{bath,2}\left(T_{bath,2}-T_{bath,FL,2}\right)}{h_{bath,1}\left(T_{bath,1}-T_{bath,FL,1}\right)}>1 \qquad \textbf{(6-5)}$$

Where $h_{bath,1}$ and $h_{bath,2}$, $T_{bath,1}$ and $T_{bath,2}$, $T_{bath,FL,1}$ and $T_{bath,FL,2}$ represent the initial and current convective heat transfer coefficient of the bath, temperature of the bath, and temperature at the bath-freeze lining interface.

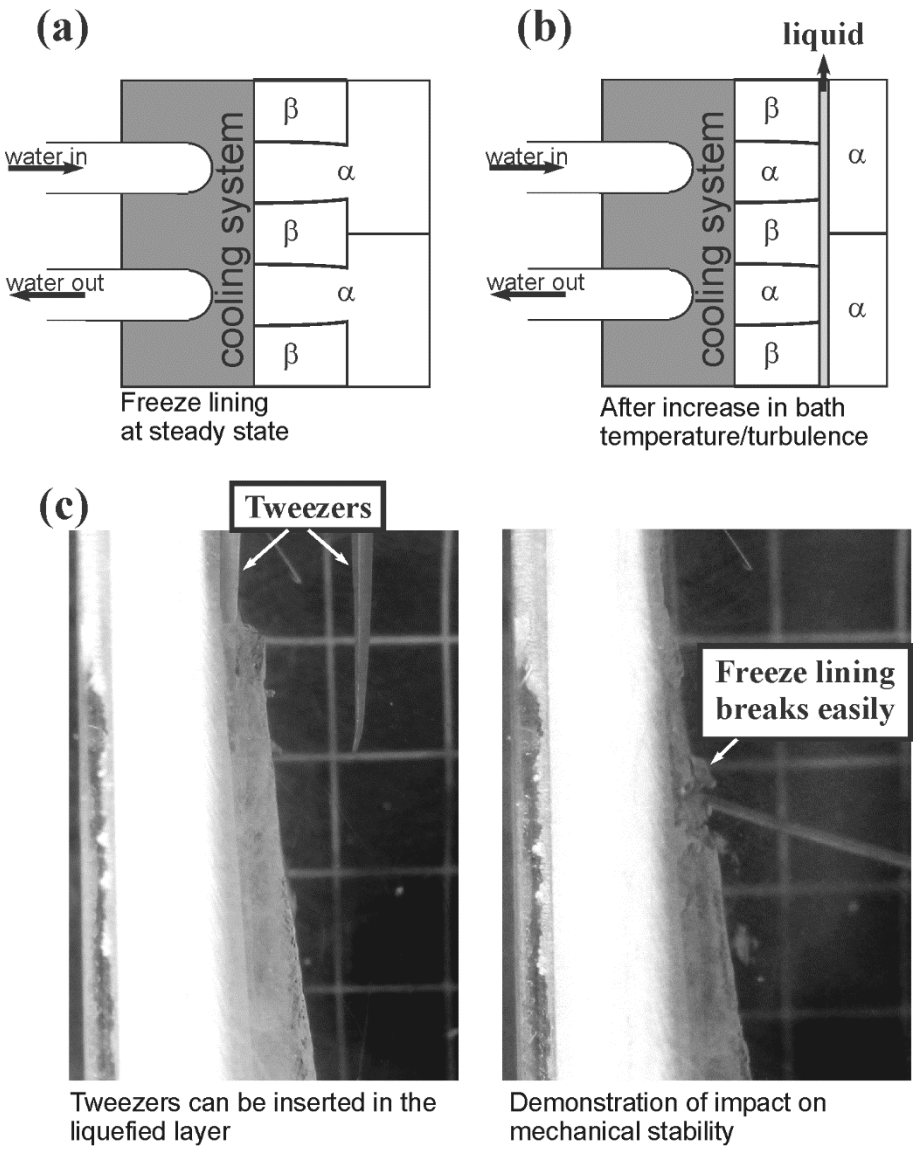

Figure 6-13: Liquification of intermediate freeze lining layers: (a) freeze lining at steady state, (b) freeze lining after an increase in bath temperature and/or turbulence (c) demonstration of the impact of liquification of the intermediate layer on the mechanical stability of the freeze lining

6.5 Conclusions

The present study of freeze lining formation confirms previous observations that the deposit/liquid interface temperatures in these systems can be below those anticipated from chemical equilibrium

considerations. This being the case, the formation of freeze linings can exhibit a range of behaviours from equilibrium to dynamic steady state. The departure from thermodynamic or chemical equilibrium means that steady state freeze lining behaviour is determined by not only heat transfer and thermal factors, but also by the relative rates of mass transfer and elementary reaction steps, such as nucleation, crystallisation rate, crystallisation pathway, phase transformations and phase equilibria in the reaction system.

In the present study, freeze lining behaviour in concentrated $CaCl_2$ containing solutions was studied through in-situ experimental observations. The influence of bath composition, bath temperature, fluid flow rate and thermal history have been investigated. The system behaviour was not noticeably influenced by differences in bulk fluid flow. It has been clearly shown, however, that the phases formed, the interface temperatures and the freeze lining thicknesses are highly sensitive to parameters that determine the chemical driving forces for change as reflected in the bath temperature, the bath composition and the thermal history of the deposit. These are significant findings since they are not predicted using conventional thermal treatment of freeze lining behaviour, and point to the need for further systematic examination of the influence of the various process parameters that influence the elementary reaction steps that may be active in these systems under dynamic steady state conditions.

7 Investigation of the effect of bath temperature on the bath-freeze lining interface temperature in the CuO_x–FeOy–MgO–SiO_2 system at copper metal saturation

7.1 Introduction

In Chapter 6, a range of potential factors that can influence freeze lining behaviour was discussed. It was shown in cold model studies that the steady state interface temperature could be lower than the liquidus temperature and that the phases present at the interface were not necessarily those predicted from phase equilibrium considerations. This indicates that freeze linings are formed not only under equilibrium conditions, but can exist in a dynamic steady state influenced by the relative rates of heat and mass transfer processes, chemical reactions and phase transformations.

In the cold model study in Chapter 6, it was shown that the bath composition and temperature, and the thermal history were important factors in determining freeze lining behaviour. The temperature of the freeze lining deposit interface appeared to be independent of fluid flow rate.

The phase equilibria and liquidus temperatures of slags present in industrial copper smelting and refining operations at copper metal saturation are described by the pseudo-ternary 'Cu_2O'-'Fe_2O_3'-SiO_2 system [77-79]. Experiments have been undertaken [58] to demonstrate the influence of bulk flow of the bath on freeze lining formation on the steady state bath-freeze lining interface temperature in this slag system. It was shown that increased convective flow in the bath lead to decreased thickness of the freeze lining and increased interface temperatures. The original intention of that research was to study the Al_2O_3-free pseudo-ternary 'Cu_2O'-'Fe_2O_3'-SiO_2 system. However, the slag was found to be contaminated with Al_2O_3, which was the direct result of the use of alumina crucibles to contain the slags. The Al_2O_3 was found to significantly change the resulting phase equilibria. It was also found that rather than a single sealing primary $Cu_2O.(Fe,Al)_2O_3$ delafossite phase, three phases – cuprite (Cu_2O), delafossite and metallic copper – were present at the deposit liquid interface at low levels of bath agitation, indicating clearly that the interface was below the liquidus temperature of the bulk liquid.

In many industrial copper smelting and refining operations, magnesia –containing refractories are used. As reported in Chapters 4-5, the presence of MgO in the slags has a significant influence on the phase equilibria and liquidus temperatures in this system. The focus of the current study is the effect of the bath temperature and composition on freeze lining formation and on the steady state bath-freeze lining interface temperature. A 'Cu_2O'-'Fe_2O_3'-MgO-SiO_2 slag at copper metal saturation was selected for the investigation, with the slag contained in a MgO crucible. In preparation for this study on freeze lining formation, phase equilibria and liquidus temperatures in this slag system at the compositions of interest were experimentally determined. The results of the study under equilibrium conditions are reported in Chapters 4-5 [83, 84, 99] and are utilised in this subsequent investigation.

7.2 Methodology

7.2.1 Cooled finger technique

The cooled finger technique [6], first used to study freeze lining microstructures by Verscheure et al. [17] and further improved by Campforts et al. [56, 100, 101] and Mehrjardi et al. [57], was used to create freeze linings under controlled conditions in a laboratory setting. This technique uses an air or water-cooled probe, which is submerged in a crucible containing liquid slag. After the desired immersion time, the probe and attached freeze lining are removed from the bath and quenched in water within approximately 10 s.

In the current study, an air-cooled probe was used. Compressed air (93-130 lpm at 25 °C) was passed through a stainless steel cold probe consisting of two concentric stainless steel (316 grade) tubes (6.3 and 12.7 mm OD, 1 mm wall thickness). The cold air enters the probe through the inner tube and exits through the annular space between the inner and outer tube. The probe was submerged in a liquid slag bath, initially containing 55 wt.% Cu_2O, 28 wt.% Fe_2O_3, 17 wt.% SiO_2 + 1% MgO. The slag was prepared using ≥99.5% pure SiO_2, Cu_2O (Alfa Aesar, USA), Fe_2O_3 and MgO (Strem Chemicals, USA) powders. The mixture was placed in a high-density MgO crucible (98.6 wt.% MgO +Y_2O_3 (up to 2 wt.%), Ozark Technical Ceramics, USA), which was placed in a graphite crucible (Graphite Australia LLC, USA). A 1 cm layer of high-MgO castable was applied at the bottom of the MgO crucible and MgO powder was placed underneath the MgO crucible. This practice has been found to avoid cracking of the crucible on heating. A 1 cm layer of copper shot (99.9%, Alfa Aesar, USA) was placed on the surface of the castable MgO in contact with the slag to ensure equilibrium with copper metal was attained in the charge. The crucible assembly was placed on a rotating platform in an electrical induction furnace (HEREUS, type MFU 105, 25 kW, 10 kHz) (Figure 7-1).

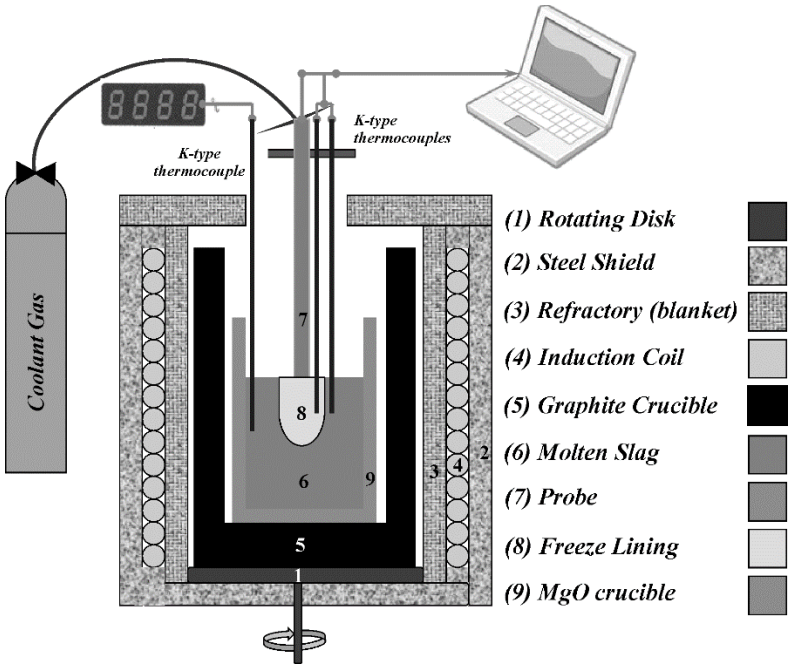

Figure 7-1: Schematic of the experimental apparatus for high-temperature experiments [57]

The crucible was heated at a rate of approximately 100 °C/h until the desired temperature was achieved. The experiments were performed using a constant generator power (12.5, 16, 19.5 kW) instead of a constant bath temperature due to difficulties of finding a suitable material for protection of the bath thermocouples in the temperature range of interest. The resulting bath temperatures were measured using an R-type thermocouple protected by a stainless steel tube with one closed end. The stainless steel tube was found to have a limited lifetime under the experimental conditions. As such, no continuous monitoring of the bath temperature could be performed.

The temperatures in the freeze lining were measured using 5, K-type thermocouples (ø 1 mm, ECEFAST, Australia). The positions of the thermocouples within the freeze lining were determined following completion of the experiment by cutting the freeze lining perpendicular to the probe at the position of the thermocouple tips and measuring the distance between the cooled probe and thermocouples in this cross-section. The first thermocouple ($T_{FL,1}$) was inserted in a 1 mm deep groove on the outer surface of the steel probe.

The temperatures of the in- and out-going air were measured using similar K-type thermocouples positioned in the inner inlet and outer outlet tube of the cooled probe at the estimated bath surface level.

7.2.2 Microstructural analysis

Following removal of the deposit from the cooled probe, sample cross-sections were prepared by sectioning of the obtained freeze linings using an MK-303 professional grade diamond blade (MK Diamond Products, Canada). The samples were mounted in epoxy resin and prepared for examination using conventional metallographic polishing techniques. An electron-probe X-ray micro-analyser (EPMA), Superprobe JEOL (Japan Electron Optics Ltd., Tokyo) 8200L operated at an accelerating voltage of 15 kV and probe current of 15nA was used to obtain backscattered electron images and to determine the compositions of the phases present in the freeze lining. $CaSiO_3$, Fe_2O_3, MgO (Charles M. Taylor Co., Stanford, CA), and Cu_2O standards (prepared in-house using 99.99 wt.% pure Cu_2O) were used for calibration. The standard Duncumb-Philibert atomic number, absorption and fluorescence correction (ZAF-correction) supplied with the probe was used. The concentrations of the oxide components were calculated based on measured cation-concentrations, normalized and reported as Cu_2O, Fe_2O_3, MgO and SiO_2. Fe^{3+}/Fe^{2+} and $Cu^{2+}/Cu^{1+}/Cu^0$ ratios were not determined. The estimated uncertainty on measurements was estimated to be within ±1 wt.%.

7.3 Results

7.3.1 Freeze lining temperature profile

The measured temperatures at the air in- and out-let ($T_{air,in}$; $T_{air,out}$), inside the freeze lining ($T_{FL,1}$ – $T_{FL,5}$), and in the bath (T_{bath}) are shown in Figure 7-2. The bath temperature in each experiment was measured after 1 h ± 10 min. The use of a constant furnace generator power instead of constant bath temperature resulted in changes of the bath temperature over time; the estimated temperature is marked as a dotted line in the figure. The temperature at the end of the experiment was estimated using the procedure outlined in Appendix I.

In the FL4 experiment, 2 of the thermocouples in the freeze lining ($T_{FL,2}$ and $T_{FL,3}$) failed after the 1 h period. Temperatures in the freeze lining at the positions of these thermocouples were estimated by assuming the changes in temperatures at these positions were equal to the change in temperature at the position of $T_{FL,1}$. This resulted in an additional uncertainty of -30°C for the bath temperature and bath-freeze lining interface temperature.

At each position, and in each of the four experiments, measured freeze lining temperatures show the same trend (Figure 7-2a,c,e,g). After reaching a maximum immediately after submergence of the probe, the temperatures decrease and reach minimum values after approximately 50 minutes. During

the remainder of the experiment, the measured temperatures slowly increase, as does the difference between the air inlet and outlet temperatures (Figure 7-2).

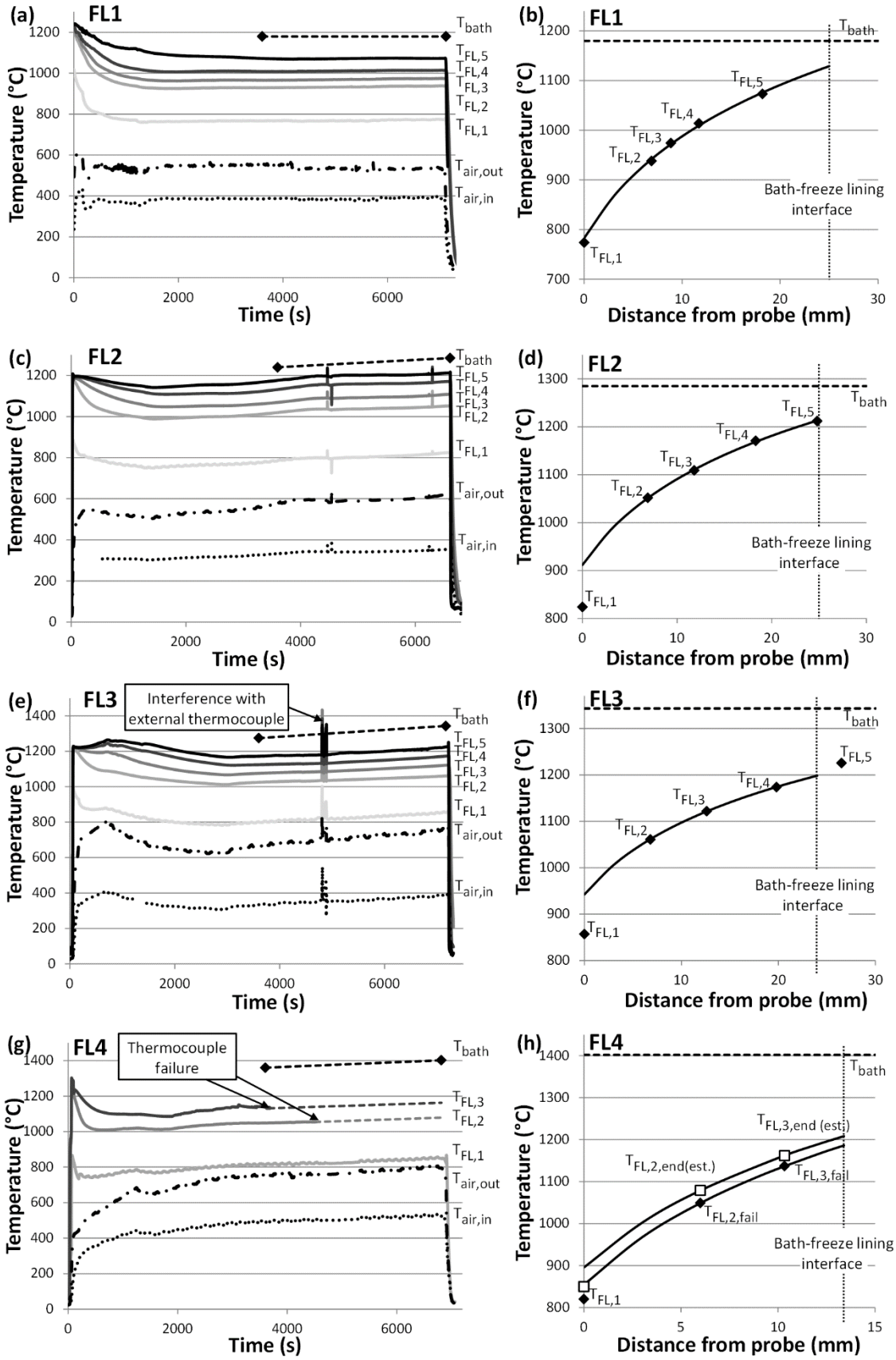

Figure 7-2: In-situ freeze lining temperatures. Experimental conditions for each of the experiments can be found in Table 7-1.

The preliminary experiments performed in an electrical resistance furnace, using control of the bath temperature instead of generator power (including FL1) [102], showed the same trend of slowly increasing temperatures, but far less pronounced (15 °C/h vs. 40-70 °C/h). This observation suggests that the main reason for the increase in temperatures is a change in bath temperature due to the use of fixed generator power. As determined in the preliminary experiments and as demonstrated by FL1, thermal steady state in this system at constant bath temperature is achieved after approximately 1 h [102]. Increases in temperatures after this point in time are considered to be caused by an increase in bath temperature.

All temperatures within the freeze lining except $T_{FL,1}$ closely follow the relationship given by equation **(B-3)** (Figure 7-2b,d,f,h). The temperature measured at the cold probe ($T_{FL,1}$) is always less than indicated by this trend, which might be caused by its positioning inside the 1mm groove in the cooled probe. It was therefore decided to exclude $T_{FL,1}$ from the determination of the temperature profiles using equation **(B-3)**.

7.3.2 Bath compositions

The bath compositions were measured before and after each experiment. Inside the dip samples taken for this purpose, measurements on the dip rod side of the dip samples contained a significantly higher concentration (1-5 wt.%) of iron oxide, which is thought to be caused by interaction with the stainless steel dip rod. All measurements of the liquid were taken at the furthest possible distance from the dip rod.

The FL1 experiment was performed using an electrical resistance furnace [102]. The FL3, 4 and 2 experiments were performed in this order in an induction furnace using the bulk slag from the previous experiment.

The dip sample after the FL4 experiment was taken after the bath had cooled down significantly – causing olivine to precipitate – due to furnace failure right after quenching of the freeze lining. As a result, the dip sample taken after the FL4 experiment contained olivine crystals. These crystals stayed present in the bulk slag throughout the FL2 experiment. The bulk composition of the bath after the FL4 experiment and before and after the FL2 experiment was determined as follows: the volume percentage of olivine was estimated by quantitative metallographic approach from polished sections of the samples. The relative proportions of olivine were determined through counting pixels of the corresponding grayscales of the compound using an in-house MATLAB 2013a code. Assuming the densities of the olivine compound and the liquid slag are similar, the bulk bath composition was

calculated as a weighted average of the measured liquid and olivine compositions. Attempts were made at conventional chemical bulk analysis through ICP-OES and through XRF. ICP-OES analysis could not be carried out as there was no suitable sample preparation method available to quantitatively dissolve the sample. Fusion was not successful as the metal content of the samples reacted with the platinum crucibles at high temperature, and acid digestion was not considered suitable as all silica would be lost during the digestion process as volatile silicon tetrafluoride (SiF_4). XRF analysis failed due to the small sample sizes.

The bath compositions are shown in Table 7-1. It can be seen that the MgO concentration in the slag increases as the study progressed (FL1, 3, 4, 2). The source of the increase in MgO concentration during the tests is the progressive dissolution of the magnesia crucible. Concentrations of the other components change during experiments due to interaction with the metallic copper alloy and the surrounding air, and precipitation of solid compounds on the freeze lining.

Table 7-1: Comparison between bath compositions before and after each experiment. Compositions are normalized such that SiO_2 + Cu_2O + Fe_2O_3 = 100 for ease of comparison to the phase equilibria data. (*) denotes compositions well outside the range of experimental phase equilibria data. (**) denotes experiment in electrical resistance furnace [102]

Experiment (time, RPM, air flow rate)		MgO (wt.%)	SiO_2 (wt.%)	Cu_2O (wt.%)	Fe_2O_3 (wt.%)	T_{liq} (°C)	$T_{bath,end}$ (±15 °C)	Primary phase	Interface phase	$T_{bath,FL}$ (°C)
Initial mixture		1.0	17.0	55.0	28.0	1125		Spinel		
FL1 (**), 2 h, 10 RPM, 130 lpm	before	3.1	19.5	50.6	29.9	1240	1180	Olivine	Pyroxene	
	after	3.6	21.5	51.3	27.3	1260	1180	Olivine	Pyroxene	1132
FL2 2 h, 0 RPM, 93 lpm	before	8.1	25.6	46.0	28.3	1680*	1285	Olivine	Pyroxene	
	after	9.1	25.1	46.5	28.4	1800*	1285	Olivine	Pyroxene	1205
FL3 2 h, 0 RPM, 93 lpm	before	4.7	25.8	43.0	31.3	1290	1343	Olivine	Pyroxene	
	after	5.4	26.3	44.9	28.8	1340	1343	Olivine	Pyroxene	1199
FL4 2 h, 0 RPM, 130 lpm	before	6.0	26.6	45.3	28.1	1420*	1402	Olivine	Pyroxene	
	after	7.4	22.8	46.9	30.3	1660*	1402	Olivine	Pyroxene	1203

Liquidus temperatures were estimated using phase equilibria data of the 'Cu_2O'–'Fe_2O_3'–MgO–SiO_2 system at copper metal saturation obtained in an earlier study [83, 99]. This was done as follows: the measured bulk bath compositions were projected onto the two cross-sections closest in MgO concentration to the MgO concentration measured in the bulk bath. The liquidus temperature of the olivine primary phase was determined for the projected composition on both cross-sections. The liquidus temperature of the bulk bath was then determined through interpolation or extrapolation of the estimated liquidus temperatures of the projected compositions.

The sections of the system at 1, 2, 3 and 4 wt.% MgO are shown in Figure 7-3-Figure 7-6. As demonstrated in the earlier study, the liquidus temperature is extremely sensitive to the MgO concentration with each 1 wt.% MgO increase causing an increase in liquidus temperature of approximately 120 °C [83, 99]. The projected bulk compositions of the slags for FL 1 (before) and FL3 (before) are marked on the figures. The slag compositions at the start of each experiment were in the olivine primary phase field. It can be seen (see Table 7-1) that the estimated liquidus temperatures increase in the order the experiments were executed (FL 1, 3, 4, 2) and increase during each experiment.

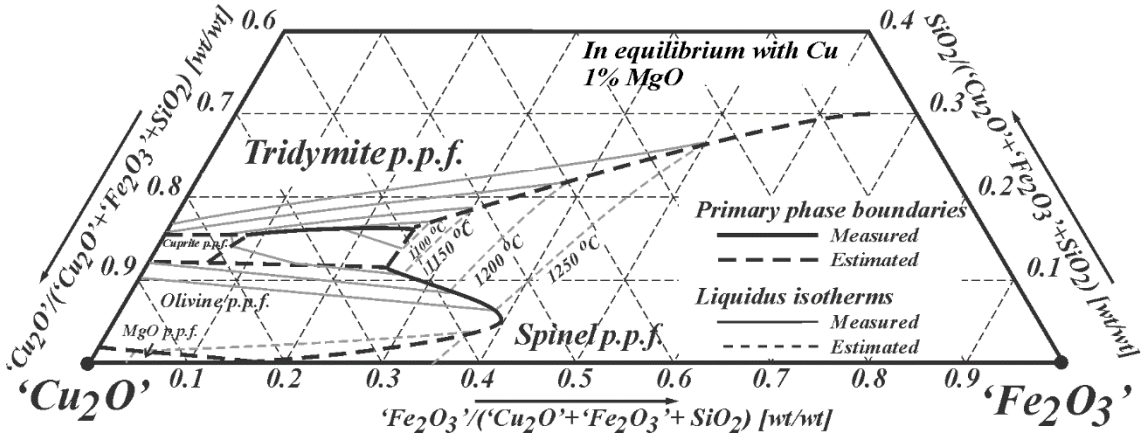

Figure 7-3: Estimated liquidus of the 'Cu₂O'–'Fe₂O₃'–MgO–SiO₂ phase diagram at 1 wt.% MgO in liquid in equilibrium with Cu-metal projected on to the 'Cu₂O'–'Fe₂O₃'–SiO₂ plane.

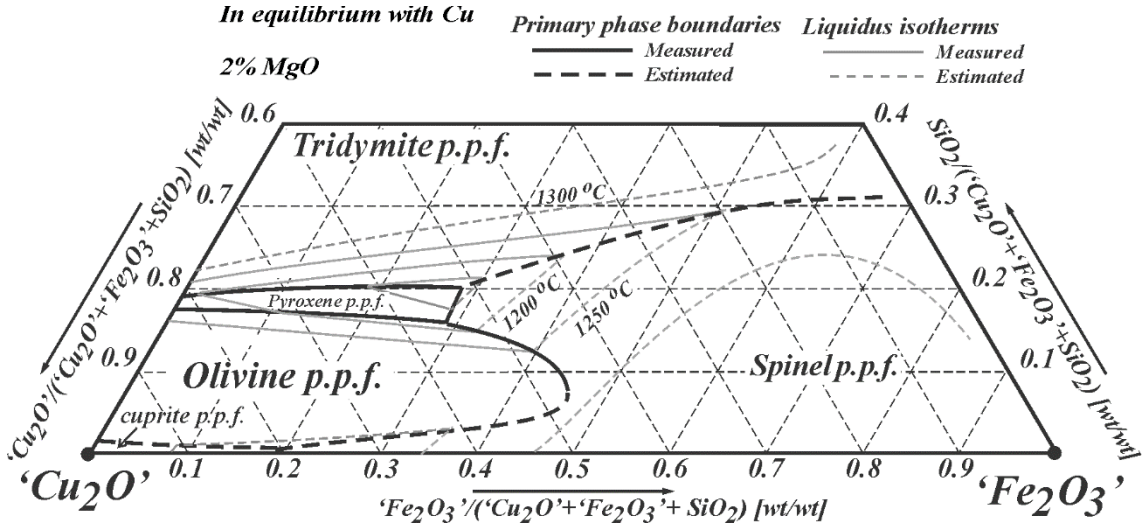

Figure 7-4: Estimated liquidus of the 'Cu₂O'–'Fe₂O₃'–MgO–SiO₂ phase diagram at 2 wt.% MgO in liquid in equilibrium with Cu-metal projected on to the 'Cu₂O'–'Fe₂O₃'–SiO₂ plane [99]

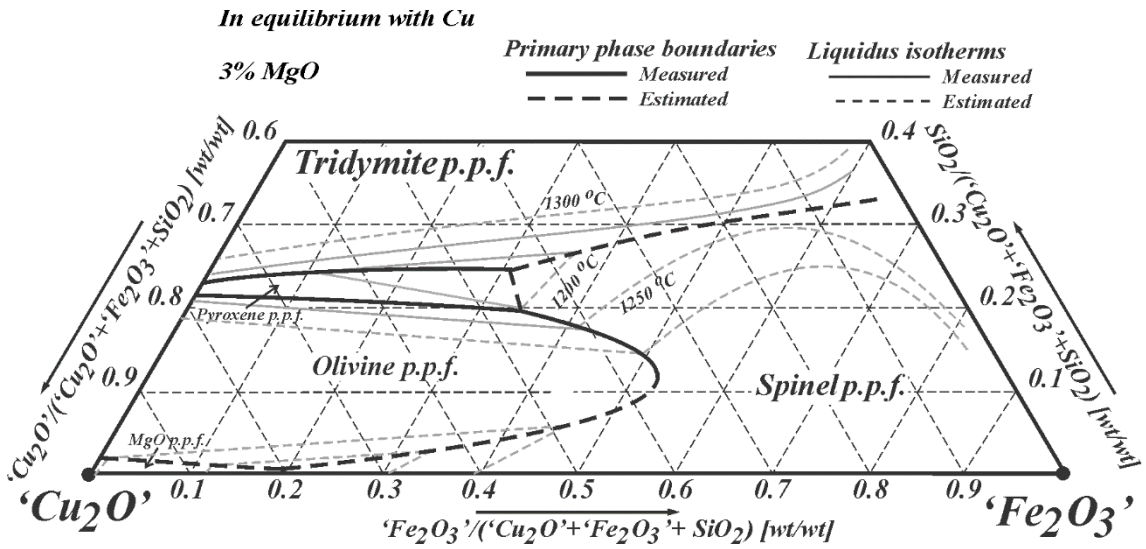

Figure 7-5: Estimated liquidus of the 'Cu_2O'–'Fe_2O_3'–MgO–SiO_2 phase diagram at 3 wt.% MgO in liquid in equilibrium with Cu-metal projected on to the 'Cu_2O'–'Fe_2O_3'–SiO_2 plane

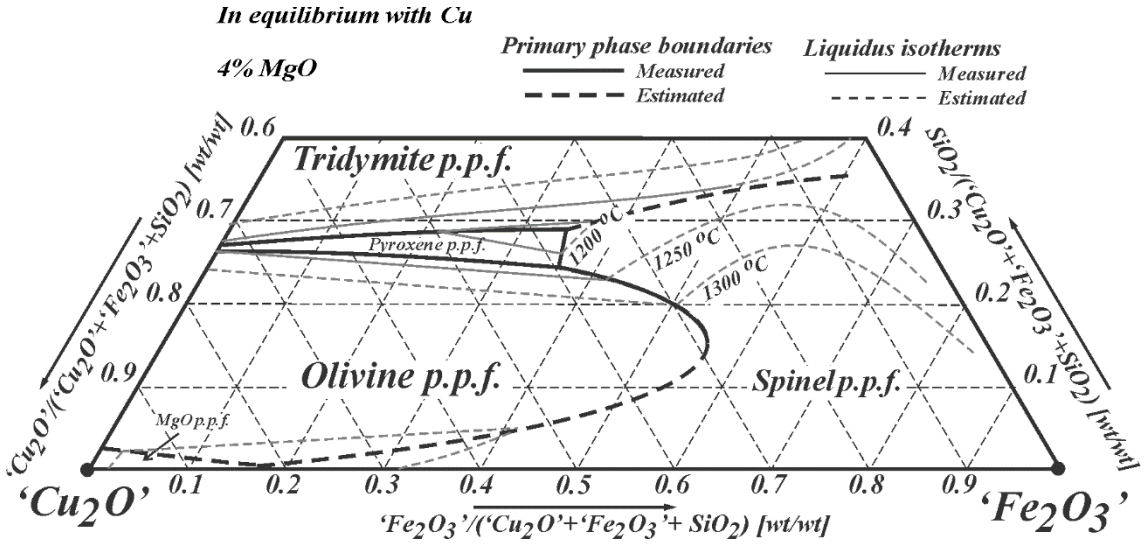

Figure 7-6: Estimated liquidus of the 'Cu_2O'–'Fe_2O_3'–MgO–SiO_2 phase diagram at 4 wt.% MgO in liquid in equilibrium with Cu-metal projected on to the 'Cu_2O'–'Fe_2O_3'–SiO_2 plane [99]

7.3.3 Macrostructure

Figure 7-7a, b and c show macro-images of the FL2, 3 and 4 freeze lining deposits formed at bath temperatures of 1285, 1343 and 1402 °C respectively. Protrusions can be seen on each of the surfaces, creating an uneven deposit-liquid interface.

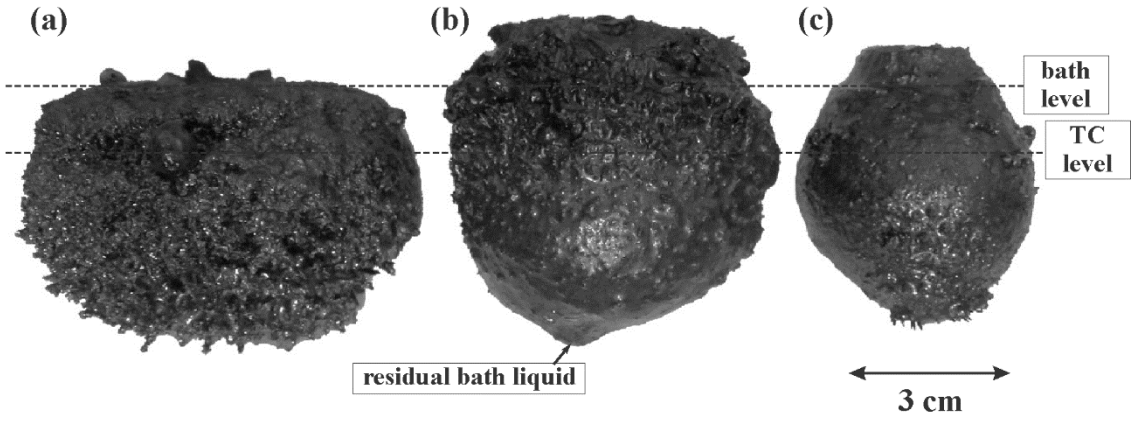

Figure 7-7: Macro-images of freeze linings formed at bath temperatures of (a) 1285 °C, (b) 1343 °C and (c) 1402 °C. Experiments were carried out over 2 h using an initial bath composition of 55 wt% Cu_2O, 28 wt% Fe_2O_3, 1 wt% MgO and 28 wt% SiO_2 and a rotational speed of 0 RPM.

In all experiments, liquid was observed to flow and detach from the sample as the freeze lining samples were removed from the bath. These macro-images suggest that liquid drained away from in between the protrusions as the probe was removed from the melt. Some residual bath liquid can be observed at the bottom of Figure 7-7b.

The thicknesses of the freeze lining deposits were measured at the level of the tips of the thermocouples inside the freeze lining. The range of thicknesses obtained for each of the freeze linings after 2h immersion are shown in Figure 7-8.

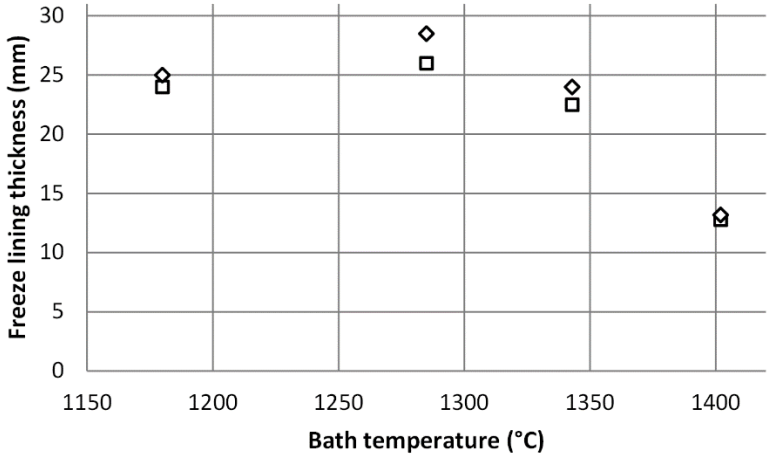

Figure 7-8: Upper (diamond) and lower (square) limits of the measured freeze lining thickness. Experiments were performed over 2 h using an air flow of 93 (1285, 1343 °C) or 130 (1402 °C) lpm, an initial bath composition of 55 wt% Cu_2O, 28 wt% Fe_2O_3, 1 wt% MgO and 28 wt% SiO_2 and a rotational speed of 0 RPM.

It can be see that the freeze lining thickness decreases with increasing bath temperatures due to the increase in temperature difference between the bath and the bath-freeze lining interface, while keeping the temperature of the air relatively constant through fluctuation of the air flow. It can also

be observed that the range of thicknesses decreases with increasing bath temperature. Note that the thickness of the freeze lining in the 1180 °C experiment does not follow this trend (Figure 7-8).

7.3.4 Microstructure

Fallah-Mehrjardi et al. [51, 57] defined 6 distinct freeze lining layers: (1) the glassy layer, (2) the glass-with microcrystals layer, (3) the closed crystalline layer, (4) the open crystalline layer, (4') the subliquidus boundary layer and (5) the primary phase sealing crystal layer.

Following examination of the freeze lining microstructures obtained in the present study (Figure 7-9-Figure 7-12), this classification has been modified for the following reasons:

1) No fully glassy or amorphous layer was observed. Instead, a layer of quenched material consisting of microcrystalline material was present. This layer exhibits the same properties as the (1) glassy layer proposed by Fallah-Mehrjardi et al. [51, 57]: fast cooling rates and low steady state temperatures, resulting in a local bulk composition equal to that of the bulk bath and no changes occurring over time

2) In structures exhibiting the open crystalline layer, the liquid phase present forms a continuous pathway from the junction of layers (3)/(4) to the subliquidus boundary layer (4'). Whilst these pathways remain connected, there will be diffusional transfer of solute species down the temperature gradient leading to continued but slow growth of the crystal phases stable at these layer's temperatures. Over the relatively short reaction times that can be observed in these laboratory studies, layer (4) is observed in the microstructures. Over long exposure, such as are expected in industrial applications, layer (4) evolves into a layer consisting of crystalline material that is effectively acting as a sealing crystalline layer. This sealing layer may consist of solely the primary phase, or of other phases that are stable at the interface temperature.

For clarity, the classification of the freeze lining layers has been modified to be: (1) the quenched layer, (2) the devitrified quenched layer, (3) the closed crystalline layer, (4) the open crystalline layer, (5) the sealing, (6) the subliquidus boundary layer and (7) entrained bulk bath liquid.

The following phases were found to be present in the deposits: cuprite (C), delafossite (D), olivine (O), pyroxene (P), spinel (S), tridymite (T), quenched liquid (L), copper metal (Cu) and a cuprite-delafossite-pyroxene-tridymite eutectic (Eu).

The microstructures present nearest the cold probe in the FL1, 3 and 4 deposits contained a layer of microcrystals rather than a fully homogeneous glassy layer. The crystals varied in dimensions between the samples and were generally less than 2 μm in diameter. In the FL2 experiment, the quenched layer (1) contained large olivine crystals surrounded by microcrystals. The olivine crystals were also found to be present in the bulk bath material. The smooth, well-defined interface indicates that these did not form during quenching.

Adjacent to the quenched layer (1), the devitrified quenched layer (2), consisted of 0.1-1 mm long plate-like delafossite crystals surrounded by a glassy/microcrystalline matrix. The closed crystalline layer (3) consisted principally of delafossite crystals 0.5-2 mm long, surrounded by angular pyroxene and fine delafossite-pyroxene-cuprite-tridymite eutectic structure. The proportion of pyroxene crystals increased with increasing distance from the probe.

Due to the gradual change of the microstructures of the FL1-4 freeze linings from the devitrified quenched layer (2) to the closed crystalline layer (3), no boundary between the two was drawn.

The open crystalline layer (4) consisted of pyroxene crystals surrounded by microcrystalline material, containing equiaxed spinel crystals in the majority of this layer. Given the fine microstructure of the microcrystalline material, it is argued that this was liquid at the experimental temperatures.

In experiments FL1, 3 and 4, the layer closest to the bath was found to consist of an open crystalline layer (4). In the FL2 experiment, which was conducted significantly below the liquidus temperature, a subliquidus boundary layer (6) was observed adjacent to the open crystalline layer (4). This layer consists of equiaxed olivine crystals in liquid. As olivine crystals were observed in the dip samples taken from the bulk bath, the whole bath was below the liquidus temperature and the subliquidus boundary layer essentially consisted of the complete bulk bath. The presence of relatively large spinel crystals in the majority of layer (4) in addition to the pyroxene plates indicates that the interface temperatures were close to the temperatures on the pyroxene-spinel boundary (see Figure 7-3-Figure 7-6).

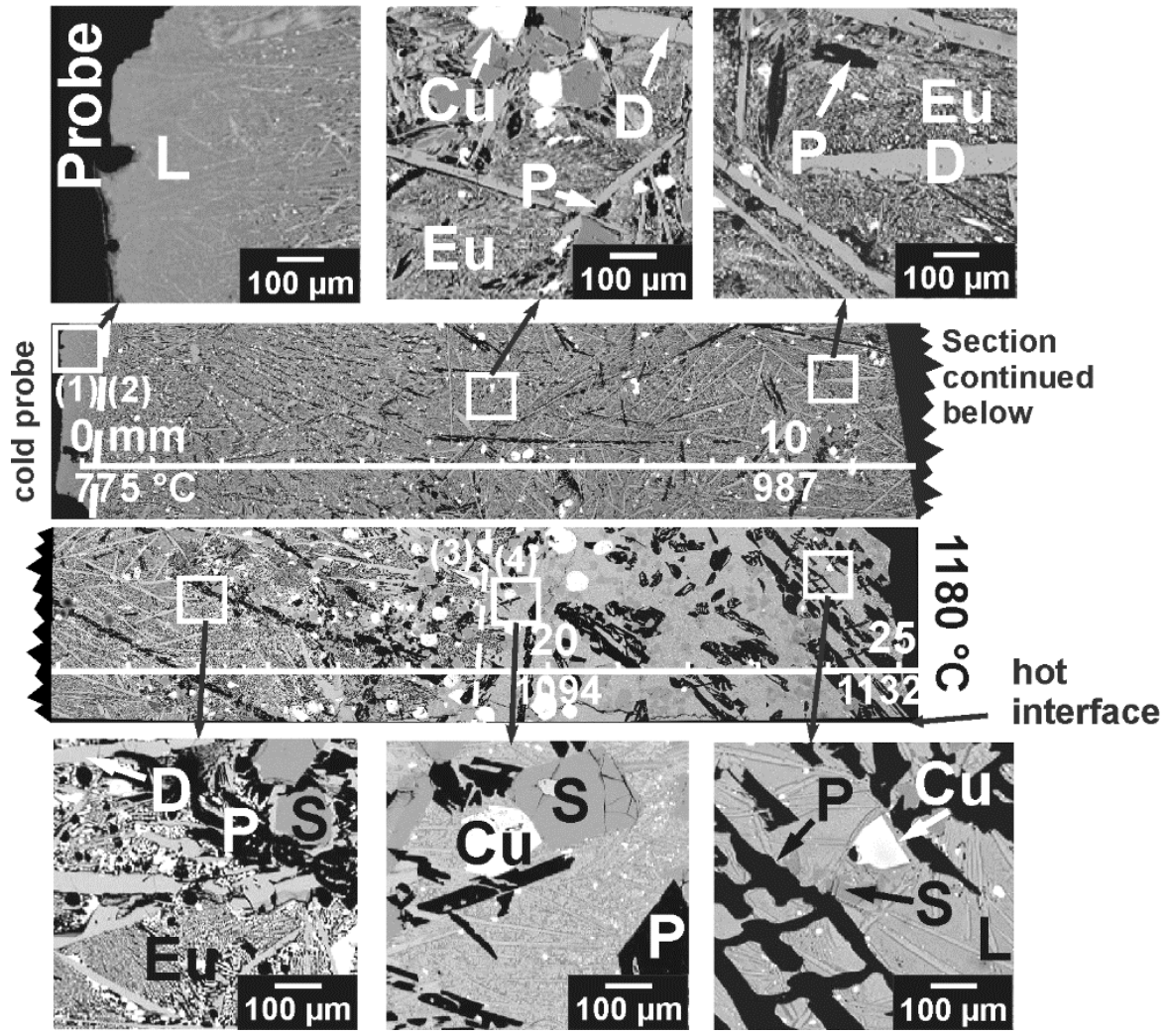

Figure 7-9: Microstructure of the deposit of the FL1 experiment. Experiment was carried out over 2 h using an initial bath composition of 55 wt% Cu_2O, 28 wt% Fe_2O_3, 1 wt% MgO and 18 wt% SiO_2, bath temperature of 1180 °C, air flow rate of 130 lpm and a rotational speed of 10 RPM. Phases present are: Olivine (O), Pyroxene (P), Delafossite (D), Spinel (S), Liquid (L) and a eutectic structure (Eu) consisting of cuprite, tridymite, delafossite and pyroxene.

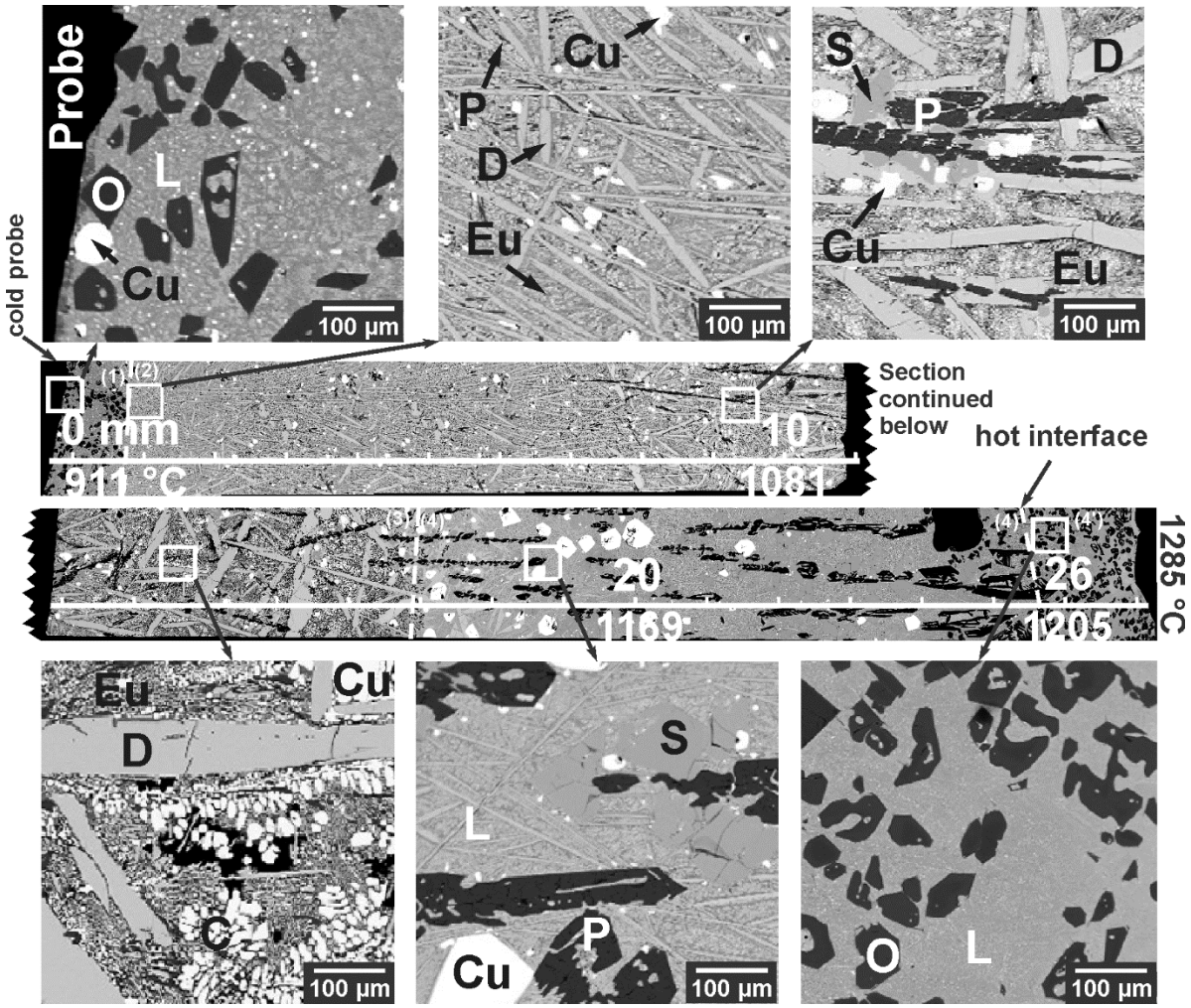

Figure 7-10: Microstructure of the deposit of the FL2 experiment. Experiment was carried out over 2 h using an initial bath composition of 55 wt% Cu_2O, 28 wt% Fe_2O_3, 1 wt% MgO and 18 wt% SiO_2, bath temperature of 1285 °C, air flow rate of 93 lpm and a rotational speed of 0 RPM. Phases present are: Olivine (O), Pyroxene (P), Delafossite (D), Spinel (S), Liquid (L) and a eutectic structure (Eu) consisting of cuprite, tridymite, delafossite and pyroxene.

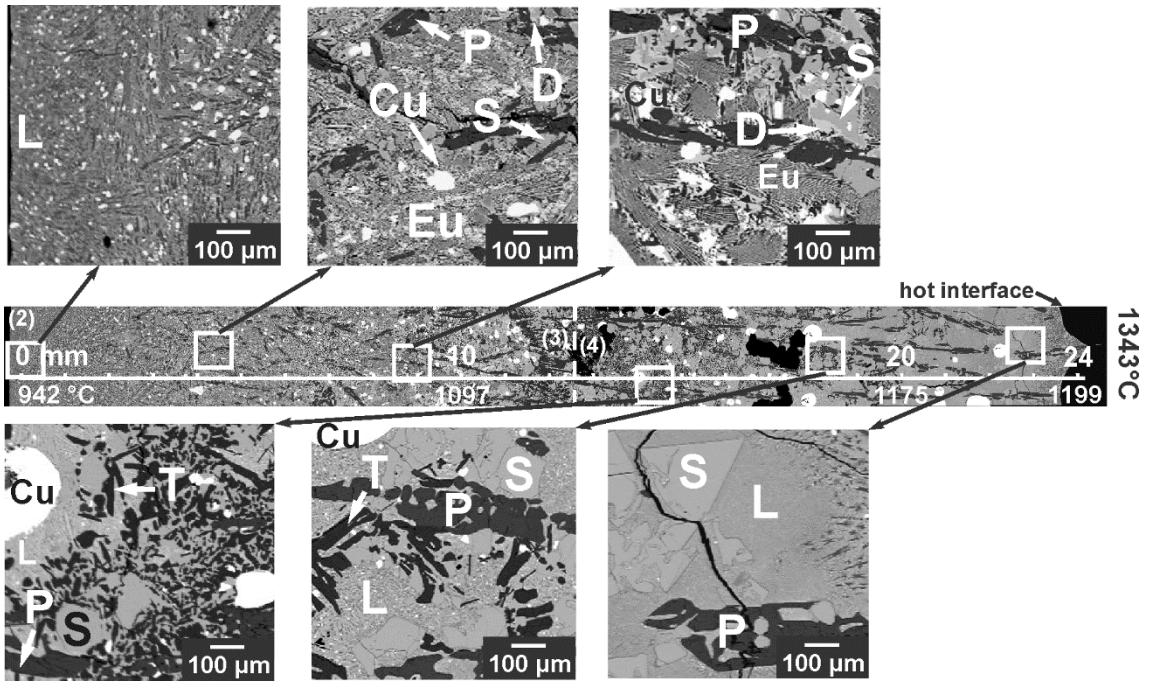

Figure 7-11: Microstructure of the deposit of the FL3 experiment. Experiment was carried out over 2 h using an initial bath composition of 55 wt% Cu_2O, 28 wt% Fe_2O_3, 1 wt% MgO and 18 wt% SiO_2, bath temperature of 1343 °C, air flow rate of 93 lpm and a rotational speed of 0 RPM. Phases present are: Olivine (O), Pyroxene (P), Delafossite (D), Spinel (S), Liquid (L) and a eutectic structure (Eu) consisting of cuprite, tridymite, delafossite and pyroxene.

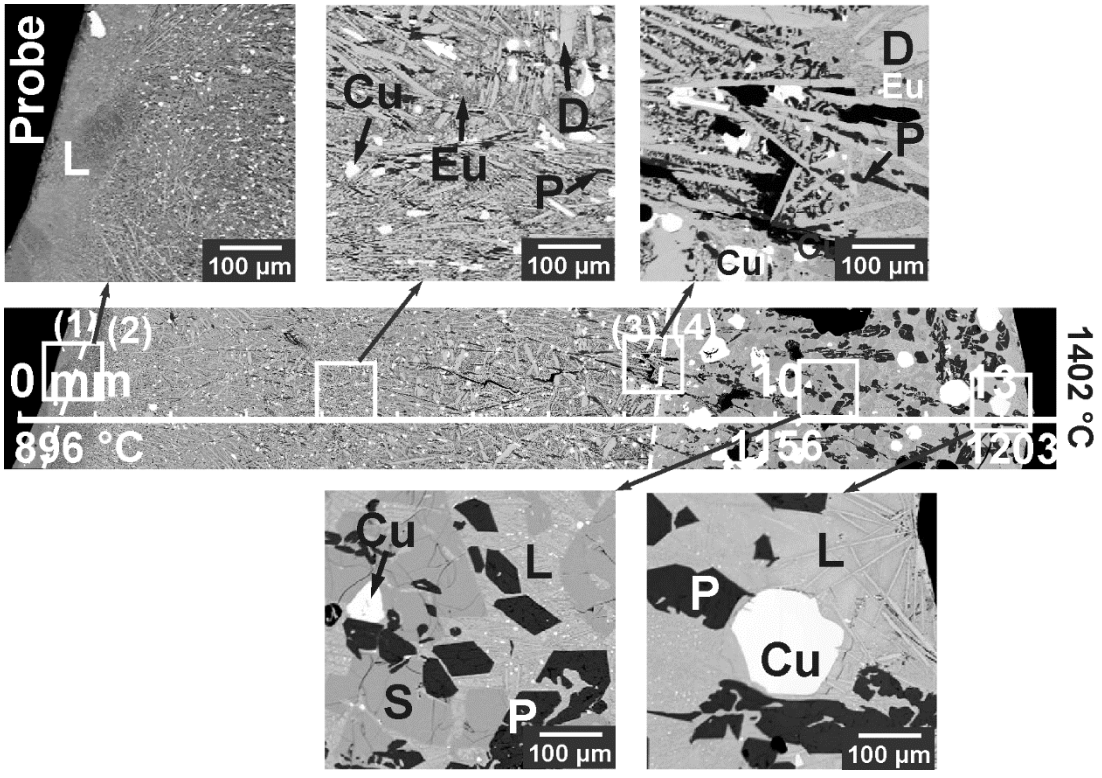

Figure 7-12: Microstructure of the deposit of the FL4 experiment. Experiment was carried out over 2 h using an initial bath composition of 55 wt% Cu_2O, 28 wt% Fe_2O_3, 1 wt% MgO and 18 wt% SiO_2 bath temperature of 1402 °C, air flow rate of 130 lpm and a rotational speed of 0 RPM. Phases present are: Olivine (O), Pyroxene (P), Delafossite (D), Spinel (S), Liquid (L) and a eutectic structure (Eu) consisting of cuprite, tridymite, delafossite and pyroxene.

Of particular interest in this study is the bath-freeze lining interface. The microstructures at the deposit interface of the FL1-4 experiments (Figure 7-9-Figure 7-12) are similar, consisting of plate-like pyroxene crystals directed towards the interface surrounded by quenched liquid.

The volume percentage of the pyroxene phase in the layer (4) microstructure was determined by counting the pixels of a certain grayscale representative of the pyroxene phase as a function of distance from the probe and dividing by the total number of pixels, excluding pores. This was done using an in-house Matlab code. The results are presented on Figure 7-13 as a function of the fractional distance between the layer (3)/(4) transition and the layer (4)/(6) transition (deposit interface). Each of the experiments shows the same trend where the vol.% of pyroxene clearly increases with increasing distance from the cold probe up to approximately 25 vol.%.

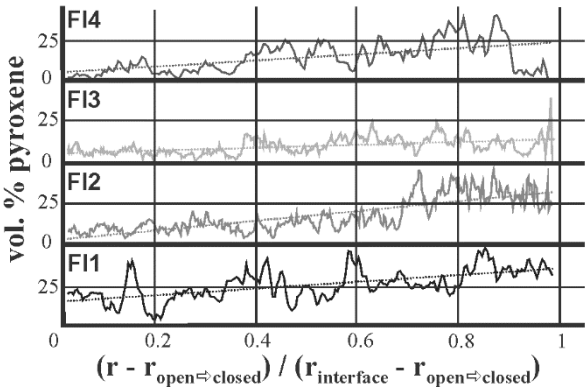

Figure 7-13: Volume percentage of pyroxene in the open crystalline layer in experiments FL1-4.

7.3.5 Phase compositions

Even though the cold probe and freeze lining were quenched into water, it was not possible to prevent crystallisation of the liquid taking place on cooling. It was therefore decided to measure approximately 200 points in the liquid spread throughout the freeze lining using a probe diameter of 50µm and choose a polynomial trend line fitted to these points through the least square method as 'average' concentration at each particular position in the freeze lining. This average concentration for the liquid is given along the composition of the phases forming a solid solution present in the freeze lining in Table 7-2.

Table 7-2: Stoichiometric phases – delafossite (D), tridymite (T) and cuprite (C) – and composition of solution phases – liquid (L), olivine (O), pyroxene (P) and spinel (S) – in the FL1-4 freeze linings. Experiments were carried out using an initial bath composition of 55 wt% Cu_2O, 18 wt% Fe_2O_3, 1 wt% MgO and 28 wt% SiO_2 and a rotational speed of 0 (FL2-4) or 10 (FL1) RPM and air flow of 93 (FL2,3) or 130 (FL1,4) lpm.

T_{bath} (±15 °C)	Distance from cold probe (mm)	T (°C) (stoichiometric phases present)	Phase	wt.% MgO	wt.% SiO_2	wt.% Cu_2O	wt.% Fe_2O_3
FL1	0	775	L	2.9	18.8	49.5	28.8
1180	5	905 (D, T, C)	P	32.0	57.3	2.5	11.5
	10	987 (D, T, C)	P	32.2	56.8	2.4	11.0
	15	1047 (D, T, C)	P	31.8	56.3	2.3	10.6
	20	1094	L	1.7	19.4	56.5	22.6
			P	32.0	56.0	2.1	10.1
			S	4.3	0.1	3.0	87.9
	25	1132	L	2.2	19.2	52.4	26.5
			P	33.4	56.5	1.4	8.9
			S	5.1	0.1	3.8	91.1
FL2	0	911	L	4.6	24.0	37.5	33.9
1285			O	49.8	41.5	1.8	10.7
	5	1015 (D, T, C)	P	32.5	57.8	3.0	10.7
	10	1081 (D, T, C)	P	33.2	58.3	2.9	9.9
	15	1130 (D, T, C)	P	33.8	58.6	2.5	9.5
	20	1169	L	2.2	21.5	53.0	23.5
			P	34.3	58.8	1.9	9.2
			S	4.4	0.1	4.0	93.6
	25	1201	L	4.2	23.7	41.6	30.7
			P	34.9	58.9	1.6	8.5
			S	5.4	0.1	3.4	90.3
	26	1207	L	3.9	23.6	41.4	31.1
			P	35.0	58.9	1.6	8.2
	27	1213	L	2.3	22.0	49.5	26.2
			O	50.1	41.3	1.6	11.3
FL3	0	942	L	9.4	41.5	10.1	43.5
1343	5	1037 (D, T, C)	P	29.1	55.3	2.1	15.0
	10	1097 (D, T, C)	P	31.0	55.8	1.8	12.2
	15	1141 (T)	L	2.5	23.2	49.9	24.6
			P	31.1	55.7	1.8	11.8
			S	3.5	0.1	4.1	94.7
	20	1175	L	4.1	27.3	38.2	30.5
			P	30.7	55.1	1.7	12.4
			S	3.3	0.1	3.1	95.6
	24	1198	L	6.1	30.3	28.2	35.5
			P	30.8	54.4	1.3	12.8
FL4	0	896	L	5.3	25.0	38.0	31.7
1402	5	1054 (D, T, C)	P	31.9	56.4	2.7	11.6
	10	1156	L	1.6	17.8	56.1	24.5
			P	33.4	56.6	2.0	9.1
			S	4.5	0.1	3.9	93.6
	13	1203	L	3.9	22.2	46.8	27.0
			P	34.4	56.8	1.8	8.5

7.4 Discussion

7.4.1 Freeze lining microstructure/temperature

Examining the microstructures, several important observations can be made:

1) Figure 7-9, 11 and 12 show that, when no detached crystals are observed, the primary olivine phase is not present at the bath-freeze lining interface, even though thermal steady state was reached.
2) Even when the bulk liquid contains detached olivine crystals, as in FL2, these are not deposited on the bath-freeze lining interface (Figure 7-10).
3) The measured bath-freeze lining interface temperatures are well below the estimated liquidus temperatures at thermal steady state in all of the conditions studied in this system (see Table 7-1).

All of the above observations indicate that the bath-freeze lining temperatures were below the liquidus temperature at thermal steady state. Moreover, the detached crystals observed in the FL2 glassy layer and bath indicate that stable freeze linings can be formed under subliquidus bath temperature conditions.

For comparison, the olivine to pyroxene transformation temperature ($T_{oli \rightarrow pyro}$), the bath temperature (T_{bath}) and the steady state bath-freeze lining interface temperature ($T_{bath,FL}$) for each experiment are shown in Figure 7-14.

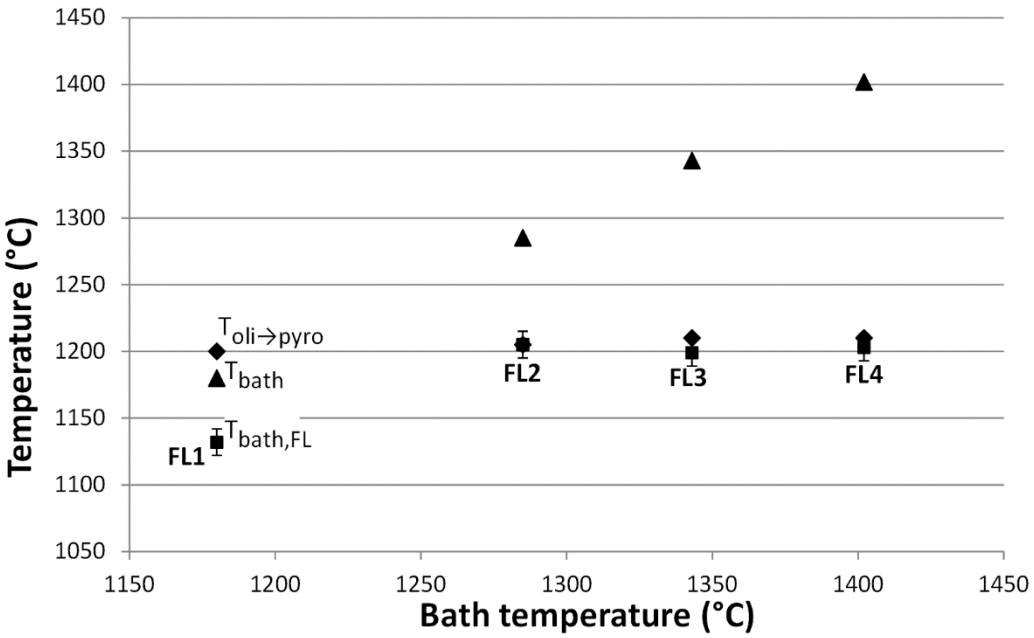

Figure 7-14: Influence of bath temperature on the bath-freeze lining interface temperature in the present study, FL1-4

It is clear that the bath temperature is always equal to or lower than the estimated liquidus temperature, indicating that all experiments were run at subliquidus conditions. It is unclear why no olivine crystals were observed in the dip samples of the FL1, 3 and 4 experiments. The undercooling might have been too small for the formation of olivine, or no olivine crystals might have been 'caught' in the dip samples as the expected percentage of olivine crystals at the measured bath temperatures was low.

As discussed earlier, the bath-freeze lining interface temperature is always lower than the estimated liquidus temperatures. Interestingly, the olivine to pyroxene transformation temperature and the steady state bath-freeze lining interface temperatures for the FL2, 3 and 4 experiments are equal within the range of uncertainty. For the one experiment where this is not the case (FL1), the bath temperature is lower than the olivine to pyroxene transformation temperature.

In a previous study by Fallah et al. [64] in a non-ferrous industrial slag, measurements were undertaken in an industrial setting by taking freeze lining samples from slag present in a ladle. Analysis of the deposits indicated that stable freeze linings can be created under subliquidus bath temperatures. This was in stark contrast to accepted theories of freeze lining formation at that time. The results of the present study at thermal steady state conditions support these earlier findings. The samples taken from experiment FL2 clearly show the presence of primary phase olivine crystals in the bulk bath, but these do not become incorporated into the freeze lining deposit.

These observations are consistent with the dynamic steady state mechanism proposed by Fallah-Mehrjardi et al. [51], as it allows for solid crystals to continuously form and dissolve in a subliquidus layer, as opposed to the conventional view on freeze linings where all precipitated solids are deposited onto the freeze lining. The subliquidus layer in the FL2 experiment essentially consists of the complete bath.

Similar to the cold modelling experiments in Chapter 6, the interface temperature was found to be within uncertainty of the formation temperature of a solid compound in the present study (pyroxene) in the FL 2, 3 and 4 experiments. The following explanation for this was hypothesized: The formation temperature of each compound marks a sudden change in chemical and physical parameters. The difference in nucleation rate, crystallization rate and mass transfer of the components present in different solid compounds could be such that certain compounds are more likely to be deposited on the freeze lining, while others are more likely to continuously form and dissolve in the subliquidus layer, or to not form at all.

7.4.2 Thermal parameters

In a cylindrical cold-probe geometry, the convective heat transfer coefficient of the bath (h_{bath}) and the thermal conductivity of the freeze lining (k_{FL}) can be calculated using the following equations:

$$Q_{FL} = \dot{m_{air}} \rho_{air} c_{p,air} \left(T_{air,out} - T_{air,in}\right) \quad \textbf{(7-1)}$$

$$Q_{FL} = h_{bath} A_{bath,FL} \left(T_{bath} - T_{bath,FL}\right) \quad \textbf{(7-2)}$$

$$Q_{FL} = \frac{2\pi L k_{FL} \left(T_{FL,2} - T_{FL,1}\right)}{\ln\left(r_{FL,2}/r_{FL,1}\right)} \quad \textbf{(7-3)}$$

Where Q_{FL} is the rate of heat transfer through the freeze lining, ($\dot{m_{air}}$) the air flow rate, ρ_{air} the density of the air, ($c_{p,air}$) the heat capacity of the air, ($T_{air,in}$ and $T_{air,out}$) the in- and outlet temperature of the air, (L) the submerged length of the probe, and ($T_{FL,1}$ and $T_{FL,2}$) two known temperatures at two known positions in the freeze lining ($r_{FL,1}$ and $r_{FL,2}$) and $A_{bath,FL}$ the surface area of the bath-freeze lining interface. The results of these calculations can be seen in Table 7-3.

In the actual calculations, the non-cylindrical shape of the freeze linings was taken into account and the heat capacity of air was taken as a function of temperature [103]. The Matlab code used for these calculations can be found in Appendix D.

Table 7-3: Calculated thermal conductivities and heat transfer coefficients from bath to deposit in the Al_2O_3-Cu_2O-Fe_2O_3-SiO_2 system.

Bath temperature (±15 °C)	k_{FL} (W/m.K)	h_{bath} (W/m^2.K)	$q_{bath,FL}$ (kW/m^2)
1180	7	610	31
1285	15	750	53
1343	23	530	76
1402	14	760	146

The calculated thermal conductivities of the freeze linings are in the range of 7-23 W/m.K, which are well above the value of 2.6 W/m.K calculated by Fallah-Mehrjardi et al. [58] for the Al_2O_3-'Cu_2O'-'Fe_2O_3'-SiO_2 system, and the effective heat transfer coefficients of the bath range from 530 to 760 W/m^2.K, slightly below the value of 941 W/m^{2}K calculated by Fallah-Mehrjardi et al. [58]. Several possible causes for the uncertainty in the calculated values were considered:

1) Geometry: the freeze linings are currently modelled as a combination of a cylinder and half a sphere. This configuration was considered an improvement on modelling the freeze lining as a cylinder, but remains an approximation.
2) Metallic copper content: due to the high difference between the thermal conductivities of the oxide system and metallic copper, a small change in metallic copper content has a large effect on the determined thermal conductivity (+ 1% copper → +4 W/mK approximately).
3) Coolant flow rate: the flow rate of the air was controlled within ±5 l/min, resulting in an uncertainty of ±5% in the calculated values for k_{FL} and h_{bath}.
4) Depth probe/bath level: the thermocouples measuring the temperature at the inlet and outlet of the coolant air were positioned at the estimated bath level before the experiment. As the bath level turned out lower than expected, the increase in temperature of the coolant air was partly caused by radiative heat transfer from the environment to the exposed cold probe between the bath level and the thermocouple positions (Figure 7-15).
5) Ridge formation: in the FL3 experiment, a ridge was formed which did not connect to the cold probe. This ridge was not considered part of the freeze lining, but could have influenced the heat transfer in the system (Figure 7-15).
6) Freeze lining temperature profile: due to the limited number of temperature measurements in the freeze lining, the estimated temperature profile could be slightly off. The resulting uncertainty on the thermal conductivity was estimated to be within 10%.

7) Furnace: A significant difference was observed between estimated k_{FL} of the experiments conducted in an electrical furnace (FL1 + preliminary experiments, $k_{FL} \approx$ 6-7 W/m.K) and those conducted in an induction furnace (FL2-4, $k_{FL} \approx$12-23 W/m.K). The reason for these differences is unclear at present.
8) Bath temperature: bath temperature was assumed constant. In reality, temperature gradients could be present in the bath. The uncertainty in bath thermocouple position thus results in an extra uncertainty on the determination of h_{bath}.
9) Interface morphology: differences in deposit interface morphology may result in differences in local fluid flow, and, as a result, rates of heat and mass transfer.
10) Temperature control: constant furnace generator power was used instead of constant bath temperature, resulting in an extra uncertainty in final bath temperature.

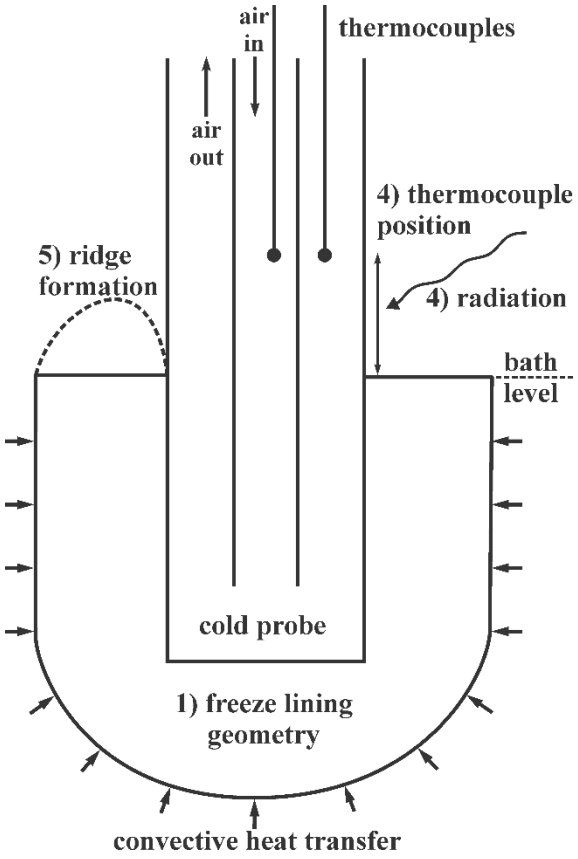

Figure 7-15: Schematic representation of some of the causes of uncertainty in the determination of the thermal conductivity of the freeze lining and the convective heat transfer coefficient between the bath and the freeze lining.

After analysing the possible causes of uncertainty in the calculations, no single cause was found to explain the observed discrepancies. It is recommended that future investigations be undertaken using a thinner freeze lining, a system not forming any metallic particles, a deeper immersion of the probe in the bath and a single furnace while paying particular attention to the position of the bath

thermocouple, and controlling the bath temperature improving the uncertainty caused by issues 1, 2, 4, 7, and 10 respectively.

7.5 Conclusions

In this laboratory based study, slag freeze lining deposits have been created in the 'Cu_2O'-'Fe_2O_3'-MgO-SiO_2 system at copper metal saturation at temperatures between 1180 and 1400 °C. Examination of the deposit microstructures and process parameters have shown that at thermal steady state conditions in this system:

1) Bath-freeze lining interface temperatures are lower than the liquidus temperature
2) Stable freeze linings can be created under subliquidus bath temperatures.
3) Non-planar deposit interface was observed.

It is recognized that after extensive exposure times, the open crystalline layer may evolve into a sealed crystalline layer. Based on the observed microstructures, the classification of layers formed in freeze linings has been modified.

8 Freeze linings in the Al_2O_3–CaO–SiO_2 system

8.1 Introduction

Several processes, such as the iron blast furnace, operate using slags based on the Al_2O_3-CaO-SiO_2 system. There are opportunities to operate the furnaces at different slag compositions. One of the technical issues is that of the design of the freeze lining. Although the phase equilibria and liquidus surface in this system are well established, to date there is no information available on the influence of slag composition on the behaviour of the freeze lining. In addition to providing new information that is relevant to industrial practice, examination of slags in the Al_2O_3-CaO-SiO_2 system also offers an opportunity to explore other physical and chemical factors that may influence the structure and behaviour of freeze linings, as discussed in Chapter 6.

8.2 Methodology

The experimental methodology used in the study is the same as that described in detail in Chapter 7. Essentially, the freeze lining samples are created by immersion of an air-cooled probe into the liquid slag bath. After the desired immersion time, the probe and attached freeze lining are removed from the bath and quenched as fast as possible in water.

The slag bath prepared from a mixture of Al_2O_3 (99.5%, Sigma-Aldrich, USA), CaO (96% (3.5% L.O.I.), Ajax Finechem, Australia) and SiO_2 (99.5% Alfa Aesar, USA).

The bath temperature was continuously measured and controlled using a B-type thermocouple protected by an alumina sheath (ø 8 mm, 1 mm thickness). The temperatures in the freeze lining were measured using 2 B-type thermocouples of which the wires were protected by an alumina sheath (ø 4 mm) and the welded tip by WH 1500 refractory cement (Morgan Thermal Ceramics, USA). These thermocouples were attached to the cooled probe using platinum wire. When possible, positions of the thermocouples within the freeze lining were determined following completion of the experiment by cutting the freeze lining perpendicular to the probe at the position of the thermocouple tips and measuring the distance between probe and thermocouple tips in this cross-section. Due to the brittleness of some of the freeze linings, thermocouple positions were sometimes determined by measuring the distance from the probe to the middle of the alumina sheath instead. The thermocouple positions were determined within ±1 mm.

The temperatures of the in-going and out-going air in the cold probe were measured using K-type thermocouples (ø 1 mm, ECEFAST, Australia) positioned in the inner and outer tube at the estimated bath surface level.

At the start and end of each experiment, a slag sample was taken by submerging a stainless steel rod (ø 6 mm) into the bath for a couple of seconds and quenching this sample in water immediately after removal from the bath. These samples were used to determine the bulk bath composition and the solid crystals present in the bulk bath.

8.2.1 Microstructural analysis

The slag samples and the freeze linings were mounted in epoxy resin and polished cross-sections were prepared for examination using conventional metallographic polishing techniques. An electron-probe X-ray micro-analyser (EPMA), Superprobe JEOL (Japan Electron Optics Ltd., Tokyo) 8200L operated at an accelerating voltage of 15 kV and probe current of 15nA was used to examine the samples using scanning electron microscopy using a backscattered electron imaging (BSE) mode to emphasis the differences in mean atomic weight of the individual phase, and to determine the compositions of the phases present in the freeze lining. $CaSiO_3$, Al_2O_3 and Al_2MgO_4 standards (Charles M. Taylor Co., Stanford, CA) were used for calibration. The standard Duncumb-Philibert atomic number, absorption and fluorescence correction (ZAF-correction) supplied with the probe was used. The concentrations of the oxide components were calculated based on measured cation-concentrations, normalized and reported as Al_2O_3, CaO, MgO and SiO_2. The estimated uncertainty on the measured compositions is ±1 wt.%.

8.2.2 Experimental conditions

Five freeze lining experiments were performed using slags in the Al_2O_3–CaO–SiO_2 system. The bulk compositions of the FL1, 2, 3 and 5 samples were selected such that the liquidus temperature was approximately 1400 °C. The liquidus for the FL4 composition was chosen slightly higher to ensure the presence of gehlenite as primary phase. The samples were chosen such that the viscosity decreased in each subsequent experiment. (Table 8-1). The FL1 bulk composition was chosen in the anorthite primary phase field, which was known to form faceted crystals. The FL2, 3 and 4 bulk compositions were chosen in the gehlenite primary phase field, with a similar slope of the liquidus and % gehlenite formed before forming a secondary phase in order to be able to study the effect of viscosity on freeze lining behaviour. The FL5 experiment was chosen to study the feasibility of using freeze linings in the Al_2O_3-CaO system.

The superheat was chosen as 40 °C for each experiment (i.e. the bath temperature was controlled to be 40 °C above the liquidus). Note that the temperature of the FL5 experiment was set at 1460 °C, based on observations during the experiment. This temperature of 1460 °C turned out to be 40 °C above the estimated liquidus temperature of the bulk bath composition at the end of the experiment (Table 8-2). No rotation was applied to the crucible. The air flow was varied to regulate freeze lining thickness. When the freeze lining thickness was expected to be high, a lower air flow rate was chosen. For a particular composition, this resulted in a higher temperature of the air, a higher temperature at the cold face of the freeze lining and a thinner freeze lining.

The viscosities of the resulting slags were predicted using the model described by Kondratiev et al. [104].

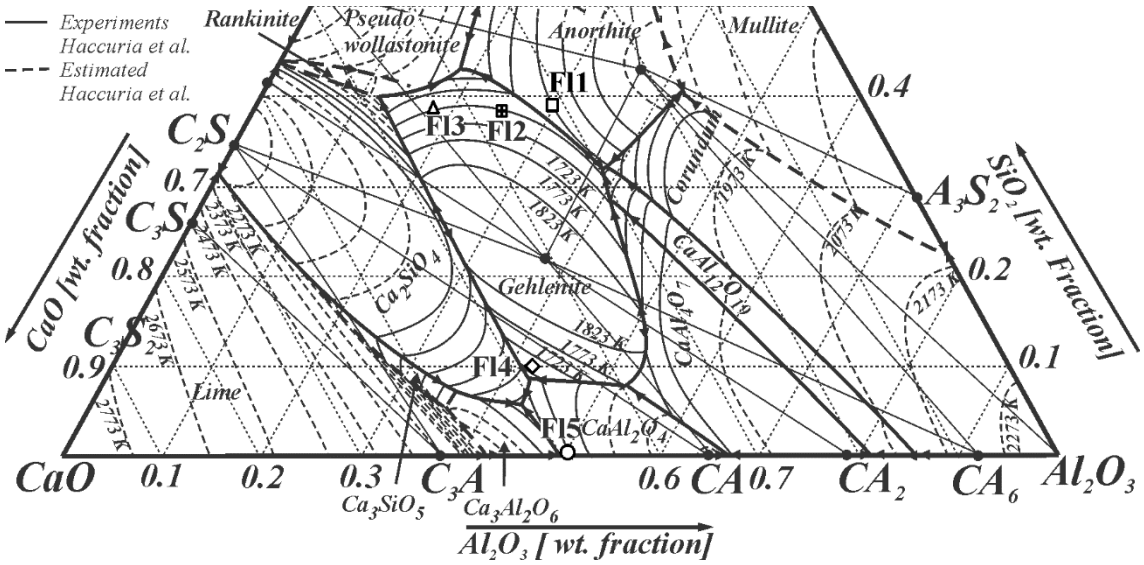

Figure 8-1: Bulk slag compositions investigated in the Al_2O_3-CaO-SiO_2 system.

Table 8-1: Summary of experimental conditions studied in the in the Al_2O_3-CaO-SiO_2 system.

Exp.	Composition (wt. %)			T_{bath}	RPM	Air flow (25 °C, l/min)	Viscosity (T_{bath}, Pa.s)	%solids before 2nd solid phase
	Al_2O_3	CaO	SiO_2	(°C)				
FL1	30.0	31.0	39.0	1440	0	130	2.9	17
FL2	25.0	36.5	38.5	1440	0	130	1.7	16
FL3	18.0	43.5	38.5	1440	0	130	0.86	12
FL4	42.0	48.0	10.0	1460	0	84	0.11	10
FL5	51.0	49.0	0.0	1460	0	84	0.047	6

8.3 Results

8.3.1 Bath compositions

Table 8-2 shows the measured bulk bath compositions of the five experiments. In general, bulk bath compositions and resulting liquidus temperatures were close to the targeted compositions. Between 0.9 and 1.5 wt.% of MgO was measured in the bulk bath, which is thought to have been present in the CaO powder. The predicted liquidus temperatures for these bulk compositions were based on the recent study by Haccuria et al. [67].

In the FL 3 and 4 experiments, solid crystals were present in the subliquidus layer adjacent to the deposit interface and the slag samples taken from the bulk. These crystals have been listed in the 'detached crystals' column.

Table 8-2: Comparison between targeted bath compositions and measured bath compositions at the start and end of each experiment, estimated corresponding liquidus temperature and primary phase and the observed solid phases at the interface and in the subliquidus layer: Anorthite (An), Melilite (Me), Pseudowollastonite (Ps), Dicalcium silicate (C_2S), Monocalcium aluminate (CA). The FL4 freeze lining shattered on quenching, the interface phases were estimated based on the microstructure of the shattered pieces.

Exp.		Al_2O_3 (wt.%)	CaO (wt.%)	SiO_2 (wt.%)	MgO (wt.%)	Fe (ppm)	T_{liq} (°C)	$T_{int.}$ (±10 °C)	Primary phase	Interface phase	Detached crystals
FL1	target	30.0	31.0	39.0	0.0	0	1400		An		
	start	28.7	31.1	39.2	0.9	380	1400	1403	An	An	/
	end	29.2	30.8	38.7	0.9	380	1400	1403	An	An	/
FL2	target	25.0	36.5	38.5	0.0	0	1400		Me		
	start	24.8	36.3	37.3	1.2	290	1410	1397	Me	Me	Me?
	end	24.4	35.9	38.2	1.2	310	1390	1397	Me	Me	Me?
FL3	target	18.0	43.5	38.5	0.0	0	1400		Me		
	start	17.4	42.8	38.4	1.3	390	1380	1317	Me	Me + Ps	Me
	end	17.7	42.9	37.6	1.3	400	1400	1317	Me	Me + Ps	Me
FL4	target	42.0	48.0	10.0	0.0	0	1420		Me		
	start	41.9	46.1	10.3	1.4	300	1440	/	Me	C_2S + CA?	Me
	end	41.9	45.9	10.3	1.5	280	1440	/	Me	C_2S + CA?	Me
FL5	target	51.0	49.0	0.0	0.0	0	1400		CA		
	start	50.1	47.4	0.2	1.4	270	1410	1407	CA	$C_{12}A_7$	/
	end	50.6	47.1	0.3	1.5	300	1420	1407	CA	$C_{12}A_7$	/

8.3.2 Microstructure, temperature logs and phase compositions

Microstructure images of the deposit cross-sections were created by merging several BSE images using the Microsoft ICE software. In some cases, such as for the FL5 freeze lining, this resulted in a

gradual change in brightness over the width of the cross-sections. This brightness gradient is due to the image processing and does not necessarily reflect a change in bulk chemical composition.

In previous research, 7 distinctive freeze lining layers were identified based on deposit microstructure [51, 52]. These layers were redefined in Chapter 7 to allow their use in the current investigation: the quenched layer (1), the devitrified quenched layer (2), the closed crystalline layer (3), the open crystalline layer (4), the sealing crystal layer (5), the subliquidus boundary layer (6) and entrained bulk bath liquid (7). The same subdivision will be used in the current paper.

FL1

Figure 8-2 shows the measured temperatures throughout the FL1 experiment and the estimated temperature profile at thermal steady state. It can be seen that all measured temperatures reach a minimum after approximately 800 s, after which thermal steady state was reached. Further fluctuations after this point in time were due to fluctuations in bath temperature. In later experiments (FL3, 4, 5), the bath temperature was controlled by manually adjusting the power to the furnace, which was found to result in smaller fluctuations in bath temperature.

In FL1, two thermocouples were embedded in the deposit centred at 2.5 and 8 mm from the probe surface. Because of the uncertainties in the positions of the thermocouples, indirect techniques were also used to estimate the temperatures inside the freeze lining at thermal steady state conditions. Using EPMA, the liquid compositions were determined at distances of 6 and 8 mm from the probe and using these data, the liquidus temperatures were derived from the phase diagram of the Al_2O_3–CaO–SiO_2 system [67]. Using the phase diagram to identify the solidification sequence and critical temperatures, it can be seen that for the slag of bulk composition of FL1, the first solid to form on cooling, the primary phase, is anorthite; this is a congruently melting compound. From phase equilibria measurements, the liquidus is estimated to be 1400 °C. As the temperature of the deposit decreased, the next solid to form is melilite at 1340 °C as the liquid meets the univariant line between anorthite and melilite. The appearance of the pseudowollastonite phase occurs with the formation of the ternary eutectic between anorthite, melilite and pseudowollastonite at 1248 °C.

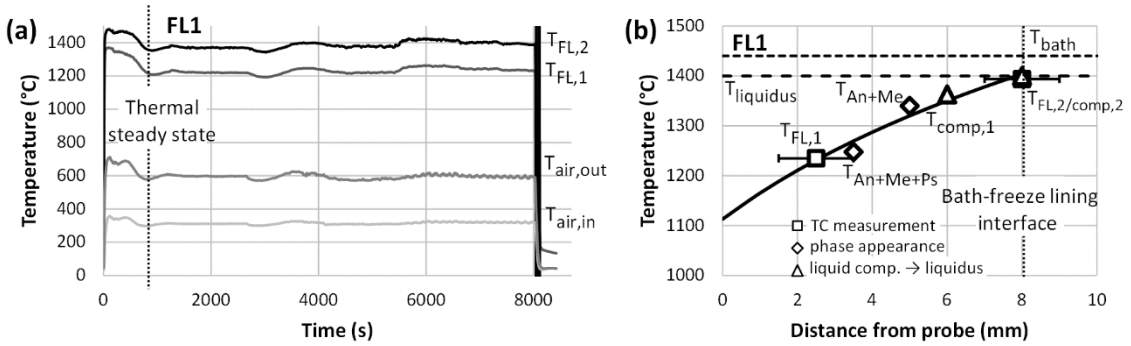

Figure 8-2: (a) Measured temperatures during the experiments and (b) estimated temperature profile inside the freeze lining at thermal steady state in the FL1 experiment. Experiment was carried out using a 30% Al_2O_3, 31 % CaO, 39 % SiO_2 slag at 1440 °C, 0 RPM, 130 lpm air flow.

Figure 8-3 shows the microstructure of the FL1 freeze lining. Closest to the probe, a (1) quenched layer is present. Starting from approximately 0.5 mm from the probe, large plate-like anorthite crystals (An) are present surrounded by partially devitrified quenched liquid (L), forming the devitrified quenched layer (2). The growth directions of the plate-like anorthite crystals, which are several mm in length, appear to be preferentially oriented towards the deposit liquid interface. At a position of approximately 2 mm from the cold probe, the anorthite crystals appear to be more randomly oriented and the quenched liquid is replaced by a ternary eutectic structure (Eu) containing anorthite, melilite and pseudowollastonite, forming the closed crystalline layer (3).

At 3-3.5 mm, the pseudowollastonite phase disappears and the freeze lining microstructure transitions into the open crystalline layer (4). Anorthite crystals are surrounded by a matrix containing melilite (Me) crystals and liquid. The phase assemblage in this open crystalline layer changes with distance from the cold probe. The proportion of melilite gradually decreases with increasing distance and beyond 5 mm, no melilite is present. The number of anorthite crystals decreases and the metallographic evidence suggests that these crystals originate from branching of existing crystals rather than from homogeneous nucleation in the melt. The composition of the liquid phase also changes with distance, e.g. the liquid contains 19 wt.% Al_2O_3 at the layer 3/4 boundary, and 28 wt.% Al_2O_3 at the 4/6 boundary; these agree well with the values expected from equilibrium with the anorthite crystals. At a distance of 7.5-8.5 mm from the cold probe, depending on cross-section, anorthite disappears. This corresponds to the liquidus temperature of 1400 °C. Note that there is no sealing layer of primary crystals despite the fact that the interface is at the liquidus temperature. The composition of the liquid beyond this point is found to be close to that of the bulk bath, but, as can be seen from Figure 8-2, the bulk bath temperature is greater than that at the deposit/liquid interface.

The remainder of the cross-section is taken up by liquid from the bulk bath (7). Several large gas pores are present throughout the freeze lining.

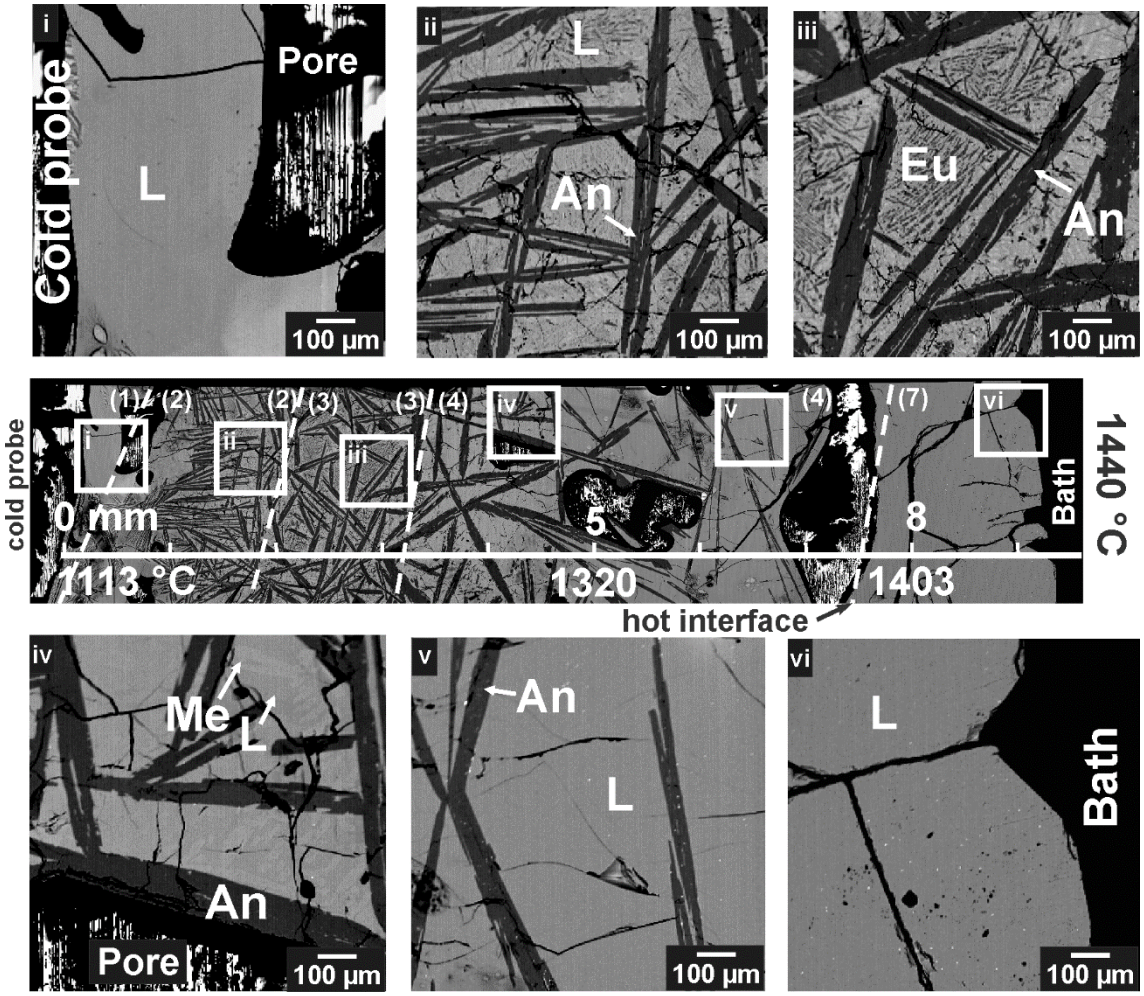

Figure 8-3: BSE image of microstructure of the FL1 freeze lining. Experiment was carried out using a 30% Al_2O_3, 31 % CaO, 39 % SiO_2 slag at 1440 °C, 0 RPM, 130 lpm air flow. Phases present are liquid (L), Anorthite (An), melilite (Me), and a microstructure consisting of a ternary eutectic of anorthite, melilite and pseudowollastonite (Eu).

Table 8-3 shows the measured compositions of the phases observed in the freeze lining. Gehlenite an end member of the melilite group ($(Ca,Na)_2(Al,Mg,Fe)[(Al,Si)SiO_7]$ contained up to 1.5 wt.% MgO, resulting in a higher than expected SiO_2 and lower than expected Al_2O_3 concentration according to reaction (1). Lower temperatures resulted in a higher MgO concentration.

$$2Al^{3+} \rightarrow Mg^{2+} + Si^{4+} \qquad \textbf{(8-1)}$$

Table 8-3: Compositions of solid phases – Melilite, Pseudowollastonite, Anorthite – and liquid in the FL1 freeze lining. Experiment was performed using a rotation speed of 0 RPM, air flow of 130 lpm and bath temperature of 1440 °C

Distance from probe (mm)	T (°C)	Phase	wt.% Al_2O_3	wt.% CaO	wt.% SiO_2	wt.% MgO
0.0	1113	Liquid	28.5	30.3	40.8	1.0
3.0	1251	Melilite	31.7	40.6	26.6	1.5
		Anorthite	36.9	20.3	43.5	0.0
		Pseudowollastonite	/	/	/	/
3.7	1277	Liquid	18.8	35.8	44.6	0.9
		Melilite	30.4	40.1	27.8	1.8
		Anorthite	37.2	20.1	43.1	0.1
4.5	1304	Liquid	23.3	33.5	42.1	1.1
		Melilite	33.2	40.9	25.0	1.2
		Anorthite	36.9	20.3	43.5	0.0
5.5	1336	Liquid	26.7	34.0	38.5	1.2
		Anorthite	37.1	20.2	43.2	0.0
8.0	1404	Liquid	29.1	31.3	38.7	1.0
		Anorthite	36.8	20.5	43.8	0.0
9.0	/	Liquid	29.2	31.5	38.8	0.9

FL2

Figure 8-4 shows the measured temperatures throughout the FL2 experiment and the estimated temperature profile at thermal steady state. Thermal steady state was reached after approximately 600 s.

Again, microstructural evidence was used to estimate the temperatures inside the freeze lining at thermal steady state. The FL2 slag is in the primary phase field of melilite, and the liquidus temperature is estimated from the phase diagram to be 1400 °C. the formation temperature of anorthite (1325 °C) is obtained from the liquidus by determining the intersection of the liquid with the univariant line defining the coexistence of anorthite and melilite. The formation of pseudowollastonite occurs with the appearance of the ternary eutectic structure (Eu) containing anorthite, melilite and pseudowollastonite at 1248 °C. The liquidus temperatures of the slags are estimated knowing the compositions of the liquid phase measured at 5 and 8 mm.

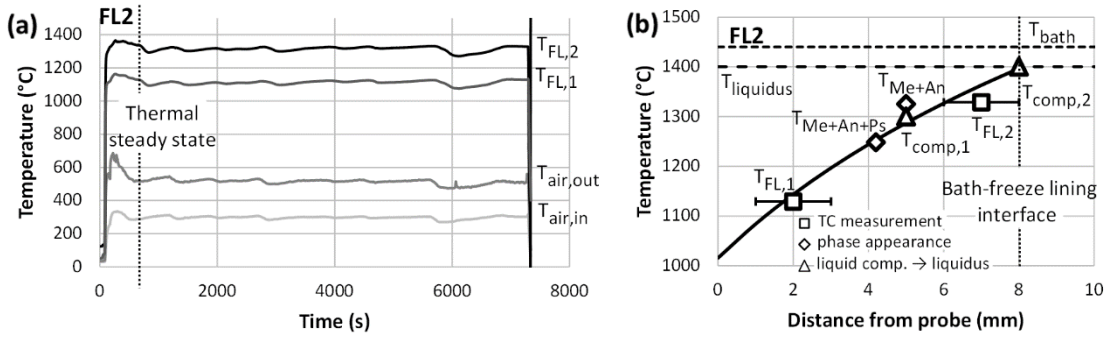

Figure 8-4: (a) Measured temperatures during the experiments and (b) estimated temperature profile inside the freeze lining at thermal steady state in the FL2 experiment. Experiment was carried out using a 25% Al_2O_3, 36.5 % CaO, 38.5 % SiO_2 slag at 1440 °C, 0 RPM, 130 lpm air flow.

Figure 8-5 shows the microstructure of the FL2 freeze lining. Closest to the cold probe, a quenched layer (1) is present, containing a large number of pores. From 1 mm onwards, the liquid is starting to devitrify, forming a devitrified quenched layer (2). Starting from 2 mm, the fully crystalline layer (3), consists of a divorced ternary eutectic containing anorthite (An), melilite (Me) and pseudowollastonite (Ps) crystals. At 4 mm, pseudowollastonite disappears and the anorthite and melilite crystals are surrounded by liquid (L), forming an open crystalline layer (4). Further than 5 mm, no anorthite is present anymore and the freeze lining consists of melilite dendrites surrounded by liquid. The proportion of melilite crystals and the dendrite spacing decreases with increasing distance. Beyond a distance of 9 mm from the probe, there are no melilite crystals. The melilite crystals present between 8-9 mm are considered to be unstable, based on the local temperatures above the liquidus temperature. The remaining microstructure consists of entrained liquid from the bulk bath (7).

Small (1-5 µm diameter) metallic iron droplets were observed throughout the liquid. No iron oxide was detected in the slag.

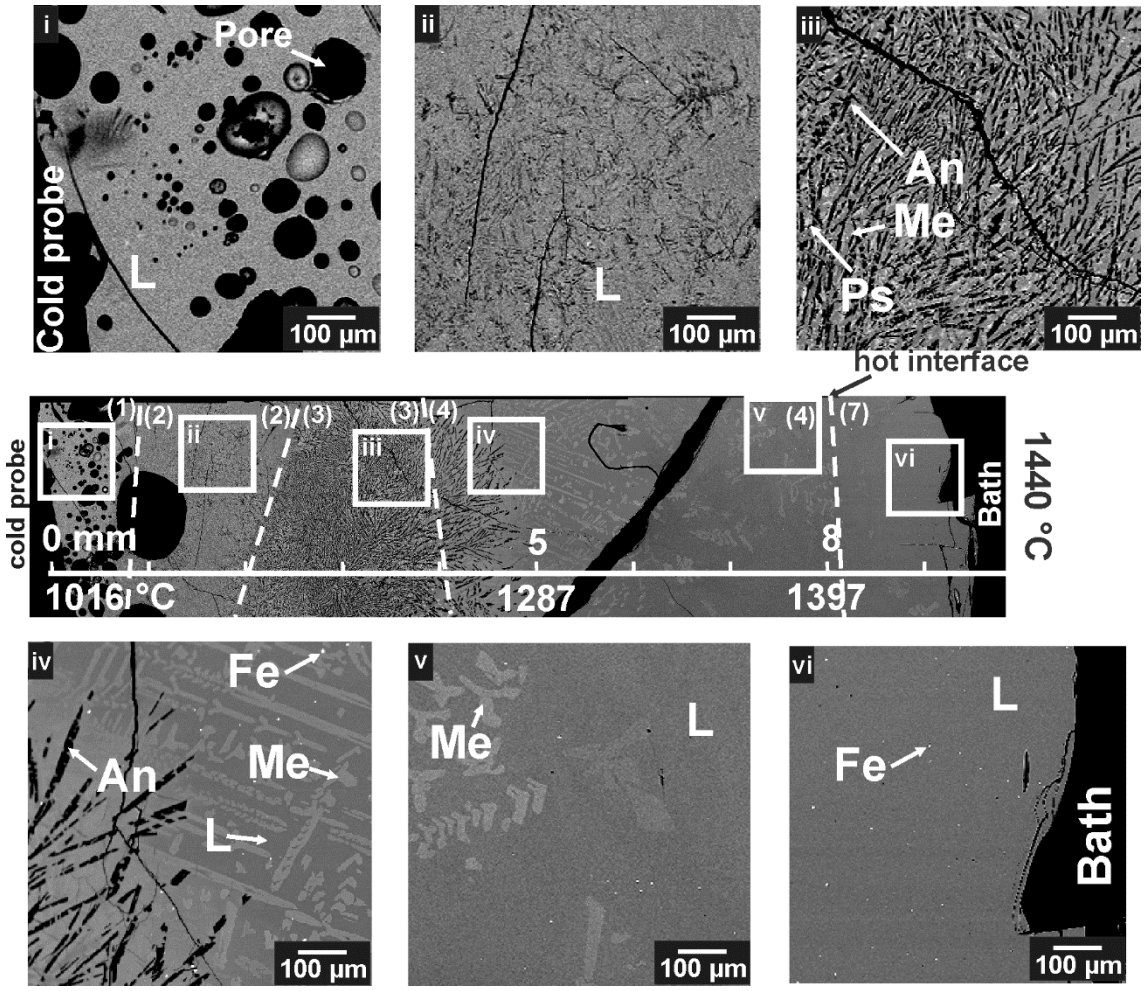

Figure 8-5: BSE image of the microstructure of the FL2 freeze lining. Experiment was carried out using a 25% Al_2O_3, 36.5 % CaO, 38.5 % SiO_2 slag at 1440 °C, 0 RPM, 130 lpm air flow. Phases present are liquid (L), Anorthite (An), Melilite (Me), Pseudowollastonite (Ps) and metallic iron (Fe)

Table 8-4 shows the measured compositions of the non-stoichiometric phases observed in the freeze lining. Melilite contained up to 2.4 wt.% MgO, resulting in a higher SiO_2 and lower Al_2O_3 concentration compared to the stoichiometric gehlenite composition.

Table 8-4: Compositions of solid phases – Melilite, Pseudowollastonite, Anorthite – and liquid in the FL2 freeze lining. Experiment was performed using a rotation speed of 0 RPM, air flow of 130 and bath temperature of 1440 °C

Distance from probe (mm)	T (°C)	Phase	wt.% Al_2O_3	wt.% CaO	wt.% SiO_2	wt.% MgO
0.0	1016	Liquid	25.1	36.3	37.7	1.2
3.0	1197	Melilite	27.5	40.3	29.7	2.4
		Anorthite	35.3	21.2	43.6	0.1
		Pseudowollastonite	0.8	48.5	50.9	0.0
4.2	1253	Liquid	18.8	37.2	43.4	0.9
		Melilite	29.1	40.9	28.5	2.1
		Anorthite	36.1	20.3	43.5	0.1

4.8	1279	Liquid	22.1	35.1	41.9	1.0
		Melilite	29.0	40.6	28.2	2.2
		Anorthite	36.1	20.6	43.5	0.1
5.2	1295	Liquid	22.7	35.0	41.9	1.1
		Melilite	30.0	41.0	27.0	1.9
8.0	1397	Liquid	24.7	35.7	38.7	1.2
		Melilite	32.1	41.4	25.3	1.4
9.0	/	Liquid	24.4	36.7	37.8	1.2

FL3

Figure 8-6 shows the measured temperatures throughout the FL3 experiment and the estimated temperature profile at thermal steady state. Thermal steady state was reached after approximately 600 s.

The FL3 slag is in the melilite primary phase field with a liquidus temperature of 1400 °C. Three additional estimates of the temperatures inside the freeze lining were used to determine the thermal steady state temperature profile.1248 °C marks the anorthite, melilite, pseudowollastonite ternary eutectic temperature; 1325 °C marks the intersection with the univariant line between the melilite and pseudowollastonite phase fields (Figure 8-1); The liquidus temperature of the slag for the composition measured at 3.5 mm is 1320 °C.

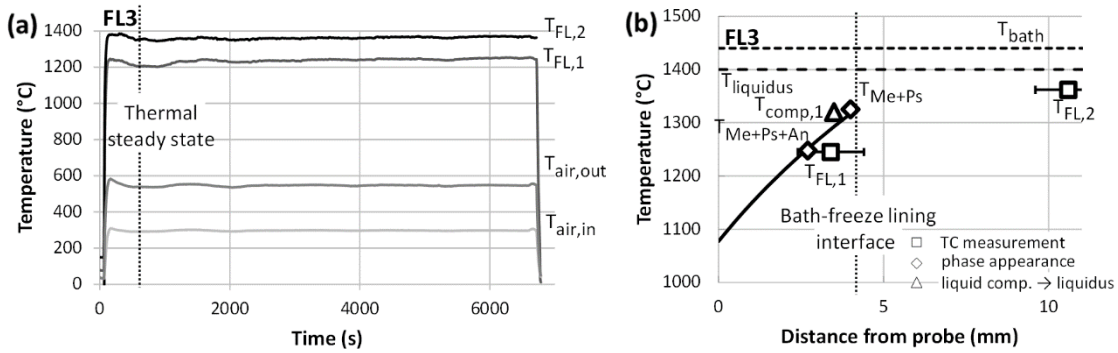

Figure 8-6: (a) Measured temperatures during the experiments and (b) estimated temperature profile inside the freeze lining at thermal steady state in the FL3 experiment. Experiment was carried out using a 25% Al_2O_3, 36.5 % CaO, 38.5 % SiO_2 slag at 1440 °C, 0 RPM, 130 lpm air flow.

Figure 8-7 shows the microstructure of the FL3 freeze lining. Closest to the cold probe, a devitrified quenched layer (2) with anorthite (An), melilite (Me) and pseudowollastonite (Ps) crystals is present. From 0.5 mm, the freeze lining consists of a closed crystalline layer (3), containing anorthite (An), melilite (Me) and pseudowollastonite (Ps) crystals at further distances from the probe, these crystals are surrounded by a matrix of binary pseudowollastonite-melilite eutectic (Eu). At distances greater than 2.7 mm, melilite (Me) and pseudowollastonite (Ps) are present surrounded by a binary pseudowollastonite-melilite eutectic (Eu) and pockets of liquid (L), forming a sealing layer (5).

Beyond 4.3 mm, a subliquidus boundary layer (6) containing detached melilite crystals (Me) surrounded by liquid can be observed.

Throughout the freeze lining, pores are present in a wide variety of sizes.

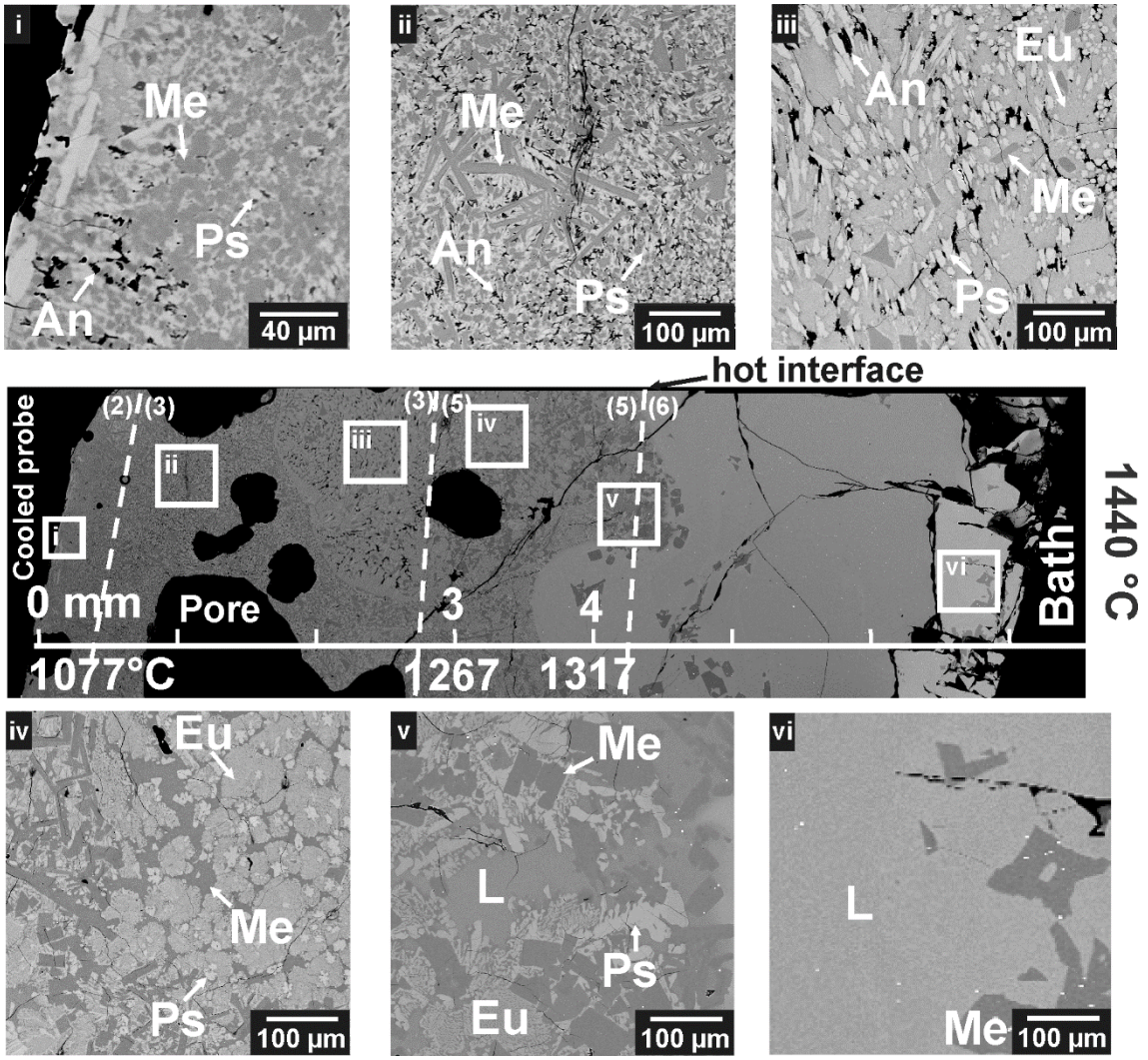

Figure 8-7: BSE image of the microstructure of the FL3 freeze lining. Experiment was carried out using a 18% Al_2O_3, 43.5 % CaO, 38.5 % SiO_2 slag at 1440 °C, 0 RPM, 130 lpm air flow. Phases present are liquid (L), Melilite (Me), Anorthite (An), Pseudowollastonite (Ps) and a eutectic structure (Eu) consisting of pseudowollastonite and melilite. The difference in shading of the close-up given in vi is due to the image stitching process rather than a difference in composition.

Table 8-5 shows the measured composition of the phases observed in the freeze lining. Melilite contained up to 3.0 wt.% MgO.

Table 8-5: Solid phases – Melilite (Me), Pseudowollastonite (Ps), Anorthite (An) – and composition of liquid in the FL3 freeze lining. Experiment was performed using a rotation speed of 0 RPM, air flow of 130 lpm and bath temperature of 1440 °C. *Composition of melilite at a given position in the freeze lining varied strongly, as demonstrated for 2.0 and 3.0 mm.

Distance from	T (°C)	Phase	wt.% Al_2O_3	wt.% CaO	wt.% SiO_2	wt.% MgO

probe (mm)						
0.0	1077	Melilite*	32.8	41.0	25.0	1.6
		Anorthite	/	/	/	/
		Pseudowollastonite	/	/	/	/
2.0	1212	Melilite*	30.9	40.6	24.8	1.7
		Melilite*	29.8	41.0	26.7	2.3
		Melilite*	28.4	40.5	28.2	3.0
		Anorthite	35.1	20.9	44.1	0.2
		Pseudowollastonite	0.9	48.5	0.0	0.1
3.0		Liquid	19.7	36.0	42.1	1.3
		Melilite*	31.8	41.5	24.7	1.5
		Melilite*	33.7	41.5	23.3	1.0
		Pseudowollastonite	0.5	47.9	51.2	0.0
4.0	1317	Liquid	17.8	38.5	42.0	1.2
		Melilite*	31.4	40.6	24.5	1.6
		Pseudowollastonite	0.2	48.4	51.5	0.0
6.5	1423	Liquid	15.9	43.1	40.2	1.3
		Melilite	30.6	40.8	27.0	2.3

FL4

The measured temperatures and the estimated temperature profile at the end of the experiment for FL4 are given in Figure 8-8. Thermocouple measurements were made at 1.8 and 5.8 mm from the cold probe. The freeze lining partially shattered on quenching. Consequently, it was not possible to obtain a complete cross-section of the deposit for microstructural examination, or to determine the phases present at the deposit/liquid interface, or to determine the steady state freeze lining thickness.

The FL4 slag is in the primary phase field of melilite, with an estimated liquidus temperature of 1440 °C. It is anticipated from phase equilibria considerations that the invariant reaction involving melilite (Me) and calcium aluminate (CA) would occur at 1400 °C. The peritectic temperature with the appearance of the dicalcium silicate (C_2S) phase is at 1383 °C.

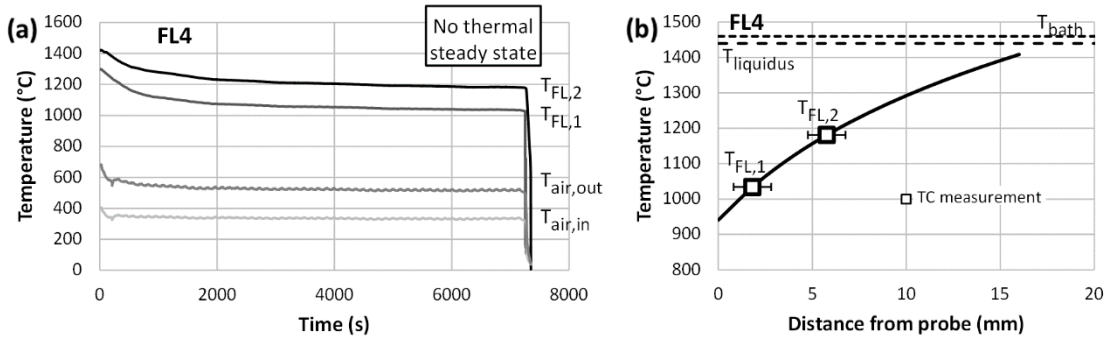

Figure 8-8: (a) Measured temperatures during the experiments and (b) estimated temperature profile inside the freeze lining at thermal steady state in the FL4 experiment. Experiment was carried out using a 42 % Al_2O_3, 48 % CaO, 10 % SiO_2 slag at 1460 °C, 0 RPM, 84 lpm air flow.

Figure 8-9 shows the microstructure of the FL4 freeze lining. Note that this sample was not taken at the height of the thermocouple tips and that the estimated temperature profile may not be representative in this cross-section. Closest to the probe, a quenched layer (1) is present containing blocky melilite (Me) crystals (50-100 µm diameter). At 1.5 mm, this layer transitions into the (2) devitrified quenched layer (2). The crystals in this layer were too small (< 2 µm) for the composition to be determined. At 3.5 mm, the closed crystalline layer (3) starts. This layer contains two separate mixtures of solids: A mixture consisting of dicalcium silicate (C_2S) and lime aluminate (CA), likely formed during the peritectic reaction from melilite to C_2S and CA, and a mixture consisting of mayenite ($C_{12}A_7$) or its hydrate, lime aluminate (CA), melilite (Me) and an undetermined (mixture of) phase(s) with a higher wt.% of MgO. Due to the small size of some crystals and the presence of pores – thought to be caused by the disintegration of dicalcium silicate on quenching – it was not possible to determine the composition of each phase. The same structure is present throughout the recovered piece of freeze lining attached to the cooled probe.

Amongst the particles recovered from the quenching tank is the particle shown in Figure 8-9 (bottom right). The particle contains detached blocky melilite crystals (10-100 µm diameter), surrounded by liquid. Also in this particle were regions consisting of a mixture of dicalcium silicate (C_2S) and lime aluminate (CA). The sample appears to have originated at or near the deposit/liquid interface. Whilst the exact position of the material within the system cannot be categorically identified, it provides important information about the system. Since the bulk bath temperature was held at 1460 °C, the presence of detached melilite crystals confirms the existence of a subliquidus region.

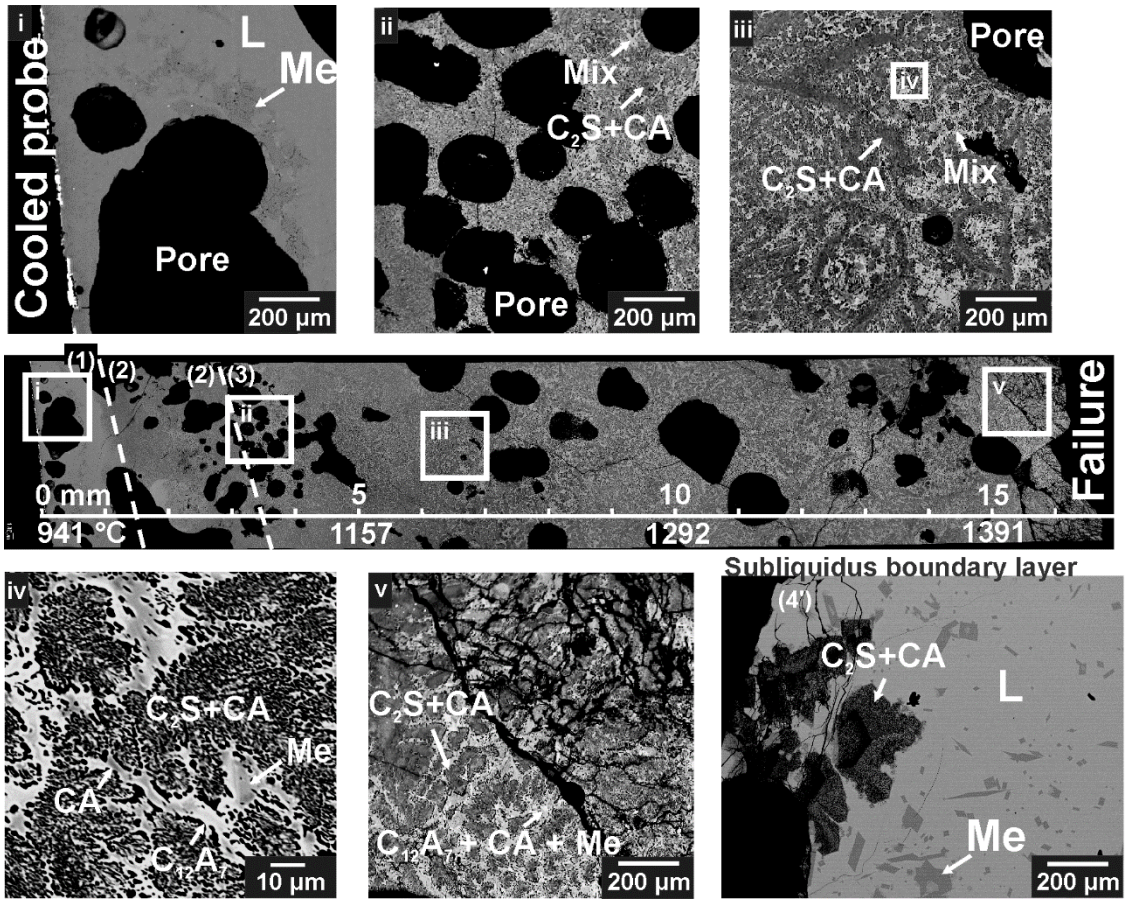

Figure 8-9: BSE image of the microstructure of the FL4 freeze lining. Experiment was carried out using a 42% Al_2O_3, 48 % CaO, 10 % SiO_2 slag at 1460 °C, 0 RPM, 84 lpm air flow. Phases present are liquid (L), Melilite (Me), dicalcium silicate (C_2S), lime aluminate (CA) and a mixture of solids containing melilite, mayenite or its hydrate ($C_{12}A_7$) and an undetermined phase containing approximately 50 wt.% Al_2O_3, 41.2 wt.% CaO, 5.2 wt.% SiO_2 and 3.6 wt.% MgO

Table 8-6 shows the measured composition of the phases observed in the freeze lining.

Table 8-6: Solid phases – Melilite (Me), mayenite ($C_{12}A_7$), dicalcium silicate (C_2S), lime aluminate (CA) and an undetermined phase (Unknown) – and composition of liquid in the FL4 freeze lining. Experiment was performed using a rotation speed of 0 RPM, air flow of 130 and bath temperature of 1440 °C

Distance from probe (mm)	T (°C) (stoichiometric phases present)	Phase	wt.% Al_2O_3	wt.% CaO	wt.% SiO_2	wt.% MgO
0.0	940.8	Liquid	40.9	46.4	10.0	1.7
		Melilite	38.9	41.7	18.1	0.4
5.0	1157	Melilite	40.3	42.3	16.3	0.4
		$C_{12}A_7$	50.3	47.6	0.2	0.8
		CA	63.0	35.7	0.3	0.1
		C_2S	/	/	/	/
10.0	1292	Melilite	39.1	41.9	17.5	0.3
		$C_{12}A_7$	50.5	47.4	0.2	0.5
		CA	62.9	35.7	0.1	0.1
		C_2S	/	/	/	/
		Unknown	49.8	41.0	4.6	3.6

15.0	1391	$C_{12}A_7$	/	/	/	/
		CA	/	/		/
		C_2S	/	/	/	/
		Unknown	50.5	40.9	5.2	3.5
Interface	/	/	/	/	/	/
Subliquidus		Liquid	41.3	46.8	9.2	1.7
		Melilite	38.2	41.4	18.5	0.3

FL5

Figure 8-10 shows the measured temperatures throughout the FL5 experiment and the estimated temperature profile at thermal steady state. Thermal steady state was reached after approximately 1800 s. A temporary power cut to the furnace caused a temporary dip in temperatures around 3000s, however, the experiment was continued until thermal steady state conditions were achieved again. The FL5 slag has bulk composition which should in theory be on the CaO-Al_2O_3 binary, in the CA primary phase field, with a liquidus temperature of 1420 °C. However, microanalysis of the phases present indicates that this is not the case. MgO was found to be present in significant quantities in one of the phases and the presence of the $C_{12}A_7$ phase is consistent with earlier research which demonstrated the significant influence of OH in the melt on the phase equilibria in this region. For these reasons, the binary Al_2O_3-CaO phase diagram reported by Muan and Osborn [105] and still including $C_{12}A_7$ as a stable oxide phase, was used to estimate the melting point of $C_{12}A_7$, and the ternary Al_2O_3-CaO-MgO diagram calculated by FactSage 6.2 [87] was used to estimate the liquidus temperatures of the liquid slag. Note that the $C_{12}A_7$ compound is not present in the FactSage database in this ternary diagram.

Four additional temperature indicators were used to determine the thermal steady state temperature profile. The eutectic temperature between CA, C_3A and C_3MA_2 (1293 °C) from the ternary diagram [87] was taken as the minimum temperature at the furthest position from the cold probe where the unknown solid phase was observed (14 mm), as the $C_{12}A_7$ hydrate phase was not present in the database and the addition of the $C_{12}A_7$ phase to the system can only result in an increase of the eutectic temperature. Similarly, the liquidus temperature of the liquid composition at 15 mm (1368 °C) and 18 mm (1378 °C) were taken as minimum temperatures at these positions. Finally, the melting point of the $C_{12}A_7$ phase, as reported by Muan and Osborn [105] was taken as a maximum temperature at the furthest position from the cold probe this phase was observed (19 mm).

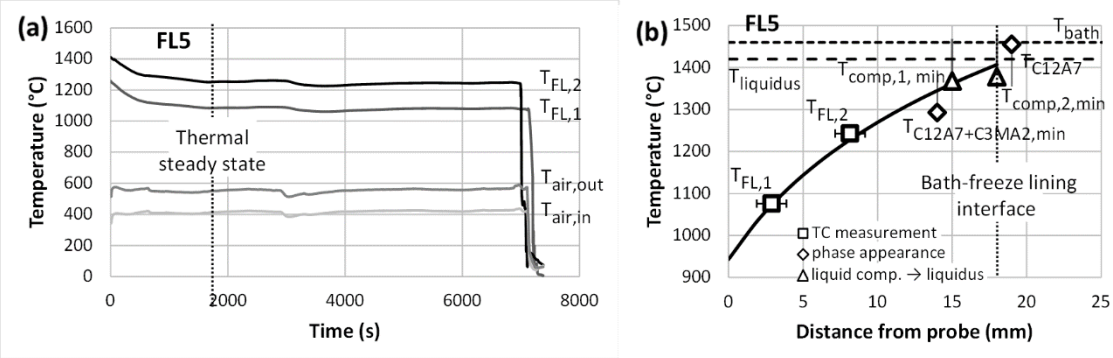

Figure 8-10: Measured temperatures during the experiments and estimated temperature profile inside the freeze lining at thermal steady state in the FL5 experiment. Experiment was carried out using a 51 % Al_2O_3, 49 % CaO, slag at 1460 °C, 0 RPM, 84 lpm air flow.

Figure 8-11 shows the microstructure of the FL5 freeze lining. Closest to the probe, a quenched layer (1) was present. Starting at 1.5 mm, the closed crystalline layer (3) consists of mayenite or its hydrate ($C_{12}A_7$), and an unidentified (mixture) of phase(s). The measured composition of this mixture of phases suggests a 10CaO.2MgO.7Al_2O_3 ($C_{10}M_2A_7$) stoichiometry, though no such compound is mentioned in literature it might form through solid solution of MgO on $C_{12}A_7$. Alternatively, this composition could be formed by a mixture of the 3CaO.MgO.2Al_2O_3 (C_3MA_2) compound and $C_{12}A_7$, however, no separate phases could be observed through optical or electron microscopy.

At 13.5 mm, the unidentified phase disappears and the dendritic $C_{12}A_7$ crystals are surrounded by liquid forming an open crystalline layer (4). At 18 mm, the morphology of the $C_{12}A_7$ crystals changes from dendritic to equiaxed crystals, suggesting these are detached crystals in the subliquidus boundary layer (6). Starting from 19 mm, no crystals are present. The remaining liquid consists of (7) bulk slag.

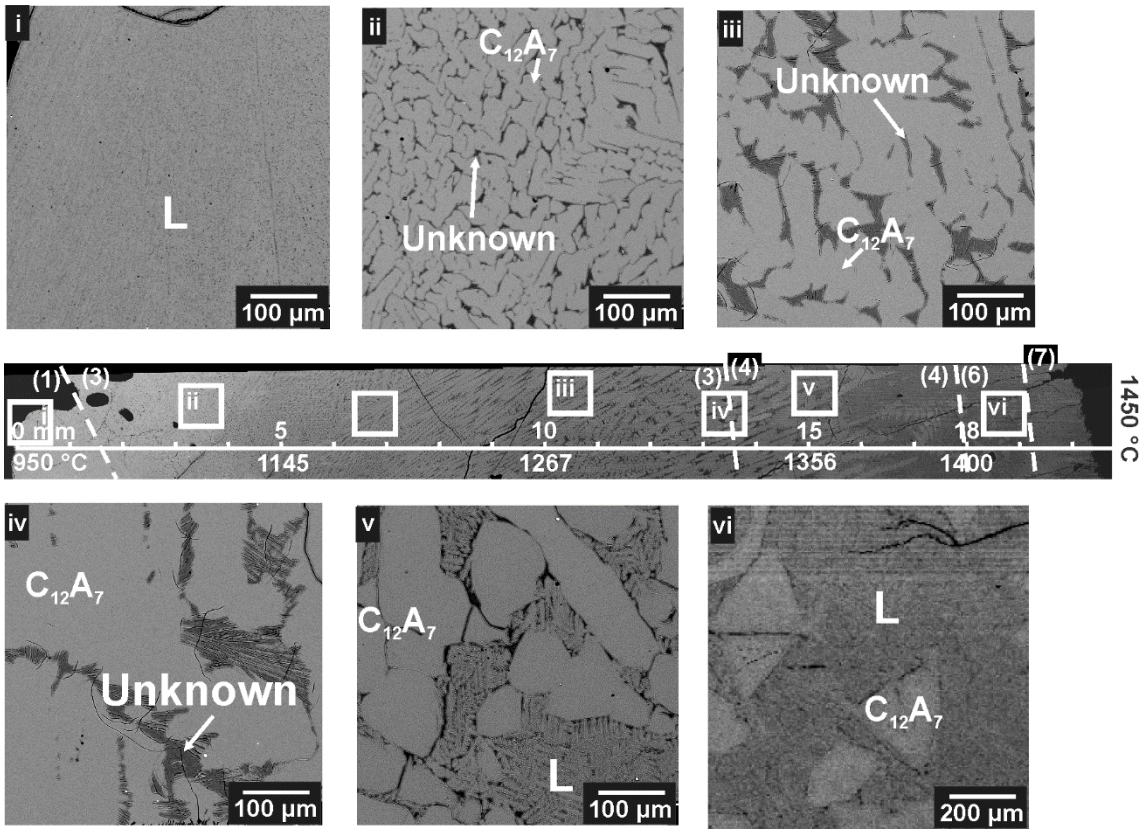

Figure 8-11: Microstructure of the FL5 freeze lining. Experiment was carried out using a 51% Al_2O_3, 49 % CaO, slag at 1460 °C, 0 RPM, 84 lpm air flow. Phases present are (devitrified) liquid (L), mayenite or its hydrate ($C_{12}A_7$) and an unidentified phase (Unknown).

Table 8-7 shows the measured composition of the phases observed in the freeze lining.

Table 8-7: : Solid phases – mayenite or its hydrate ($C_{12}A_7$) and an unidentified phase – and composition of liquid in the FL5 freeze lining. Experiment was performed using a rotation speed of 0 RPM, air flow of 130 lpm and bath temperature of 1440 °C

Distance from probe (mm)	T (°C)	Phase	wt.% Al_2O_3	wt.% CaO	wt.% SiO_2	wt.% MgO
0.0	944	Liquid	50.2	47.2	0.2	1.3
5.0	1144	Unknown	48.8	40.8	1.8	6.8
		$C_{12}A_7$	49.9	48.1	0.0	0.7
10.0	1270	Unknown	51.8	40.6	0.7	6.1
		$C_{12}A_7$	49.4	47.6	0.1	0.6
15.0	1362	Liquid	49.8	46.5	0.4	1.9
		$C_{12}A_7$	50.3	47.6	0.0	0.4
18.0	1407	Liquid	50.1	47.2	0.2	1.2
20.0	/	Liquid	50.2	47.6	0.1	0.8

8.4 Discussion

Experiments in the present study in the Al_2O_3-CaO-SiO_2 system have been designed to identify, explore and illustrate some of the elementary steps, and associated physical and chemical factors influencing the behaviour of freeze linings. Specifically the experiments have been selected for a wide range of different chemical compositions in a number of different primary phase fields of congruently melting compounds, having a similar liquidus temperature, liquidus shape (i.e. decrease in liquidus temperature as a function of composition on the crystallization path), and no bulk stirring (mass transfer only through diffusion and natural convection).

8.4.1 Microstructures

Examination of the microstructures of the freeze lining deposits from FL1-5 samples demonstrates some common features. All samples contain:

1) Primary phase at the deposit interface, and at subliquidus and subsolidus temperatures
2) Local liquid/solid compositions in layer (4) approaching equilibrium values across the respective temperature profiles.

A summary of freeze lining deposit interface structures is given in Table 8-8. It can be seen that detached primary phase crystals in a subliquidus boundary layer (6) are observed in samples FL3-5. No detached crystals are observed in FL1, while the detached crystals in FL2 were considered unstable based on the estimated local temperatures above the liquidus. Examining the microstructures of these crystals in more detail, differences in crystal shape and morphology can be distinguished. In FL1, the primary phase is anorthite; the crystals present at the deposit interface are high aspect ratio, plate-like structures (Figure 8-3); the crystals appear to originate from and are directly connected to the subsolidus anorthite. The microstructural evidence suggests that anorthite nucleation in layer (4) occurs only at the surface of existing crystals, and that there is no homogeneous nucleation.

Melilite is the primary phase in samples 2-4. In FL2 (Figure 8-5), the melilite in the open crystalline layer is in the form of dendrites, which exhibit numerous sidearms. This gives the opportunity for the crystals to grow in any direction in the structure in response to thermal or compositional gradients. There appear to be detached melilite crystals present in the entrained bulk bath liquid (6). These were considered unstable based on the estimated local temperatures. From the microstructural evidence available, it is not possible to identify whether these crystals originated from homogeneous nucleation in the melt at lower temperatures, or by dendrite arm remelting due to thermal and compositional fluctuations in the vicinity of the melilite dendrites. The melilite crystals in FL3 (Figure 8-7) and FL4

(Figure 8-9) are quite different. There is no evidence of dendritic growth of the melilite in these freeze linings, even at lower temperatures. The melilite crystals in these freeze linings are well-defined, angular, and relatively small (less than 100 μm diameter).

$C_{12}A_7$ is the primary phase in samples FL5 (Figure 8-11). The $C_{12}A_7$ in the open crystalline layer is in the form of dendrites which exhibit numerous sidearms. the bulk composition of the liquid is close to the $C_{12}A_7$ stoichiometric composition. Nevertheless, an open crystalline layer (4) and detached crystals are present at the deposit/liquid interface rather than a sealing primary phase layer.

Table 8-8: Summary of freeze lining deposit interface structures the Al_2O_3-CaO-SiO_2 system. (4): open crystalline layer; (5): sealing crystal layer; (6): subliquidus boundary layer; (7): entrained bulk bath liquid

Sample	Primary phases at interface	Deposit Interface solid structure	Interface layers	Interface Temp
FL1	An	plates	(4),(7)	$=T_L$
FL2	Me	Dendrites + detached crystals (unstable?)	(4),(7)	$=T_L$
FL3	Me	Sealing layer + detached crystals	(5),(6)	$< T_L$
FL4	Me	Interface not recovered + Detached crystals	(?),(6)	$< T_L$
FL5	$C_{12}A_7$	Dendrites + detached crystals	(4),(6)	$\leq T_L$

8.4.2 Porosity of the freeze lining

One of the main differences between the freeze linings in the Al_2O_3–CaO–SiO_2 and freeze linings in other systems is the presence of a relatively large number of pores. These pores are thought to form due to the presence of dissolved species, e.g. OH^- [106], in the slag. When the temperature decreases, the solubility of these species decreases (FactSage 6.2 [87]) and gas bubbles are formed. These bubbles subsequently become trapped in between the crystals present in the freeze lining.

Earlier research by Crivits [107] showed, based on numerical calculations using the Abqus program, that for freeze linings with a cold face temperature of 40 °C and a hot face temperature of 1400 °C,

the apparent thermal conductivity, the thickness and the heat flux decrease proportionally to the percentage of pores.

In addition to this, the presence of pores may decrease the mechanical strength of the freeze lining due to an increase in local stresses.

8.4.3 Mechanical stability of freeze linings

In the current study, the FL4 freeze lining was found to shatter on quenching. This is thought to be caused by a combination of the 12 vol.% increase associated with the $\beta \rightarrow \gamma$ transformation of the dicalcium silicate compound [108], and the thermal stresses caused by the high temperature gradients induced during quenching. This is similar to the behaviour of so-called 'self-dusting' or 'falling' slags [109, 110] on cooling.

As Figure 8-8 shows, the minimum temperature in the CAS3 freeze lining during the experiment was approximately 940 °C. This temperature is well above $\alpha' \rightarrow \beta$ and $\beta \rightarrow \gamma$ transformation temperatures of 630-680 and 500 °C respectively [108]. As a result, the freeze lining was stable during the experiment.

In industrial practice, where water is used as cooling medium, the minimum temperature in the freeze lining may be below the $\beta \rightarrow \gamma$ transformation temperature, possibly resulting in mechanical failure of the freeze lining.

A similar phenomenon is observed in the cryolite system, where the rhombic to monoclinic transformation of Cryolite at 563 °C [87] results in shattering of the freeze lining on cooling. For this reason, freeze linings in the Hall Héroult process are operated above this temperature [1].

8.4.4 Effect of viscosity

Changes in chemical composition of the slags lead to not only changes in chemical thermodynamic driving forces for phase transformation, but also to changes in physico-chemical properties. As can be seen in Table 8-1, the viscosities of the FL1-5 slags differ by nearly two orders of magnitude; the FL1 slag having the highest viscosity at 2.9 Pa.s at 1400 °C and FL5 the lowest at 0.047 Pa.s. It is to be expected that there will be related differences in diffusivity, e.g. the mass diffusion coefficient for Ca^{45} at 1500 °C is $10^{-8.6}$ in a 50/50 Al_2O_3 slag, whereas it is $10^{-9.6}$ in a 20/40/40 Al_2O_3/CaO/SiO_2 slag [111].

In the current study, the FL2, 3 and 4 experiments performed in the same primary phase field showed an interface temperature below the liquidus temperature for low viscosities (FL3, 4), and an interface temperature equal to the liquidus at high viscosity (FL2). In previous research, the general consensus was that a decrease in viscosity would result in an interface temperature closer to the liquidus [51, 63].

The reason for the complex influence of viscosity on freeze lining formation is likely to be the dependence of a multitude of parameters on viscosity, such as mass diffusion, boundary layer thickness, convective flow, nucleation, solidification, … All these phenomena play a role in freeze lining behaviour. The interrelations of these factors are not yet established.

8.4.5 Thermal parameters

1.1. Thermal parameters

Using a cylindrical geometry, the convection coefficient of the bath (h_{bath}) and the thermal conductivity of the freeze lining (k_{FL}) can be calculated using the steady state freeze lining thickness (t_{FL}), the submerged length of the probe (L), the air flow rate ($\dot{m_{air}}$), the heat capacity of the air ($c_{p,air}$) [103], the in- and outlet temperature of the air (T_{in} and T_{out}), and two known temperatures ($T_{FL,1}$ and $T_{FL,2}$) at two known positions in the freeze lining ($r_{FL,1}$ and $r_{FL,2}$) using the following equations:

$$Q_{FL} = \dot{m_{air}} \rho_{air} c_{p,air} \left(T_{out,air} - T_{in,air}\right) \quad \textbf{(8-2)}$$

$$Q_{FL} = h_{bath} A_{bath,FL} \left(T_{bath} - T_{bath,FL}\right) \quad \textbf{(8-3)}$$

$$Q_{FL} = \frac{2\pi L k_{FL} \left(T_{FL,2} - T_{FL,1}\right)}{\ln\left(r_{FL,2}/r_{FL,1}\right)} \quad \textbf{(8-4)}$$

Where Q_{FL} is the total rate of heat transfer through the freeze lining and $A_{bath,FL}$ the surface area between the bath and the freeze lining. The results of these calculations can be seen in Table 8-8. The uncertainties related to these calculations were listed in section 7.4.2. Several of the uncertainties were reduced in the freeze lining experiments performed in the Al_2O_3-CaO-SiO_2 system through improved design of the experiment: a deeper immersion of the probe was used, and all experiments were performed in the same furnace while paying particular attention to the position of the bath thermocouple. In addition to this, no ridge formation was observed. Temperature profiles were estimated as discussed in section 8.3.

Table 8-9: Apparent thermal conductivities of the deposit (k_{FL}) and convective heat transfer coefficient between the freeze lining and the bath (h_{bath}) and between the cold probe and the air (h_{air})

Experiment	k_{FL} (W/m.K)	h_{bath} (W/m^2.K)	h_{air} (W/m^2.K)
FL1	5.3	3440	560
FL2	3.1	2180	460
FL3	3.6	1680	530
FL4	2.3	570	310
FL5	2.2	450	330

Based on these results, the apparent thermal conductivities of the freeze linings in the Al_2O_3–CaO–SiO_2 system are approximately 2.1-5.1 W/m.K. The convective heat transfer coefficient between the freeze lining and the bath in the current experiment ranges from 450-2924 W/m^2.K and the convection coefficient between the air and the probe approximately 349-647 W/m^2.K.

The slight decrease of the thermal conductivity of the freeze lining with decreasing SiO_2 concentration (increasing experiment number) was expected based on an earlier study on liquid slags [112].

Based on general heat transfer theory [92] and assuming the heat transfer takes place by thermal diffusion, natural convection and forced convection mechanisms, it is expected that the convective heat transfer coefficient between the bath and the freeze lining would increase with decreasing viscosity. The experimental results given in Table 8-8, however, show the opposite trend. One possible explanation is that there is an additional contribution through radiant heat transfer. This phenomenon is well established in glass melting systems [93]. These systems are sensitive to the presence of impurity elements, such as iron and manganese in solution, and second phase particles, e.g. Fe, and gas bubbles, all of which contribute to a decrease in optical transparency [111-114]. At present it is not possible to accurately predict these effects with the available information.

8.5 Conclusions

Freeze linings were created in the Al_2O_3-CaO-SiO_2 system, starting from five different compositions with similar liquidus temperatures. The temperature profiles in the freeze linings were estimated using a combination of in-situ measurements and temperature estimates based on the phase equilibria of the system. The microstructures and compositions of the phases present in the freeze lining were studied through SEM-EPMA. The following observations were made:

1) For the freeze linings created started from compositions in the gehlenite primary phase field (FL2, 3, 4), lower viscosities resulted in interface temperatures below the liquidus.
2) All observed detached crystals had a blocky morphology, while dendritic or large, plate-like crystals were found to always be attached to the freeze lining.
3) Freeze linings containing dendritic primary phase crystals had a steady state bath-freeze lining interface temperature equal or close to the liquidus temperature.
4) Freeze linings containing dicalcium silicate, undergoing a polymorphic transformation involving a high differential volume, shattered on quenching and might fail mechanically in industrial practice.
5) Freeze linings in the Al_2O_3–CaO–SiO_2 system generally have some degree of porosity, affecting steady state thickness and possibly mechanical stability.
6) The convective heat transfer coefficient was found to decrease with decreasing viscosity. This was attributed to the contribution of radiative heat transfer, however, this hypothesis could not be confirmed based on the current experimental data.

Part V

Conclusions

“By educating one person and sending him into the society of his generation, we make a contribution extending a hundred generations to come. [Jigoro Kano]”

9 Discussion and conclusions

9.1 Introduction

Although initial designs for freeze lining systems assumed that, at thermal steady state, the deposit/bulk liquid interface temperature is the liquidus temperature, it has been confirmed experimentally in the current work that this is not always the case. It is only in recent research that techniques have been established that enable the structure of the deposits formed under controlled process conditions to be subsequently examined and further information regarding these important systems to be obtained. The techniques used and the key findings of this previous research have been reviewed and outlined in Chapter 2. What is clear from the observations is that the processes involved in the formation of freeze linings are complex, involving a number of physical and chemical processes that take place simultaneously. As discussed in Chapter 6, these processes involve not only heat and mass transfer, but also elementary reaction steps, the rates of which are dependent on a range of thermal, physical and chemical factors. Based on these considerations, targeted experimental studies have been undertaken in the present study (Chapters 6-8) to identify the relative importance of these factors and their influence on freeze lining formation. The systems studied, bath temperature, rotation speed of the crucible, formation temperature of the solid compounds, crystal morphology, etc. are listed for ease of comparison in later chapters. Morphology of the phases at the interface has been indicated as follows: equiaxed (E), columnar (C), dendritic (D), faceted (F), non-faceted (NF).

Table 9-1: Summary of experiments in the CaCl2-H2O system (Chapter 6).

Crivits et al. (Chapter 6)						
System	**$CaCl_2$-H_2O**					
	53 wt.% $CaCl_2$					
	Exp. 1	**Exp. 2**	**Exp. 3**	**Exp. 4**	**Exp. 5**	**Exp. 6**
Bath temperature	40 °C	40 °C	40 °C	40 °C	50 °C	50 °C
Solution flow rate (ml/min)	111	328	328	854	328	854
Steady state?	No	No	Yes	Yes	Yes	Yes
	(Based on changes in freeze lining thickness)					
Formation temperatures	$CaCl_2.4H_2O$ (α): 39 °C $CaCl_2.6H_2O$ (β): 29.9 °C (= solidus)					
p.p. stable during cooling?	Yes					
Interface temperature (°C)	35.3	37.0	29.8	36.9	29.5	/
Phases at interface	α	α	β	α	β	α
Comments	No detached crystals observed. Phase at interface depended on the time of transformation of the $CaCl_2.4H_2O$ + liquid layer to a $CaCl_2.4H_2O$ + $CaCl_2.6H_2O$ layer.					
Crivits et al. (Chapter 6)						
System	**$CaCl_2$-H_2O**					
	52 wt.% $CaCl_2$					
	Exp. 7	**Exp. 8**	**Exp. 9**	**Exp. 10**		
Bath temperature	40 °C	40 °C	40 °C	40 °C		
Solution flow rate (ml/min)	111	111	111	854		
Steady state?	Yes	Unclear	Yes	Yes		
	(Based on changes in freeze lining thickness)					
Formation temperatures	$CaCl_2.4H_2O$ (α): 35 °C (approximately) $CaCl_2.6H_2O$ (β): 29.9 °C (= solidus)					
p.p. stable during cooling?	Yes					
Interface temperature (°C)	29.4	34.7	35.9	35.5		
Phases at interface	β	α	α	α		
Comments	No detached crystals observed. Phase at interface depended on the time of transformation of the $CaCl_2.4H_2O$ + liquid layer to a $CaCl_2.4H_2O$ + $CaCl_2.6H_2O$ layer.					

Table 9-2: Summary of experiments in the Cu-Fe-Mg-Si-O system (Chapter 7).

Crivits et al. (Chapter 7)					
System	**Cu-Fe-Mg-Si-O**				
Bath compositions	**Exp.**	**MgO (wt.%)**	**SiO_2 (wt.%)**	**Cu_2O (wt.%)**	**Fe_2O_3 (wt.%)**
	FL1	3.1	19.5	50.6	29.9
	FL2	8.1	25.6	46.0	28.3
	FL3	4.7	25.8	43.0	31.3
	FL4	6.0	26.6	45.3	28.1
	FL1	**FL2**	**FL3**	**FL4**	
Bath temperature	1180 °C	1285 °C	1343 °C	1402 °C	
Rotation speed of crucible	10 rpm	0 rpm	0 rpm	0 rpm	
Steady state?	Yes. (FL1: no change in temperature, FL2-4 changes in temperature inside freeze lining follow changes in bath temperature)				
Formation temperature Olivine	1260 °C	1680 °C	1340 °C	1660 °C	
Formation temperature pyroxene	1200-1210 °C				
p.p. stable during cooling?	No				
Interface temperature (°C)	1132	1207	1198	1203	
Phases at interface	Pyroxene (C, F)				
Comments	Only detached crystals observed in the FL2 experiment. These equiaxed, faceted olivine crystals were present in the whole bath, which was held significantly below the liquidus temperature.				

Table 9-3: Summary of experiments in the Al-Ca-Si-O system (Chapter 8).

Crivits et al. (Chapter 8)				
System	**Al-Ca-Si-O (+ MgO impurity)**			
	FL1: anorthite primary phase field			
Bath composition	**Al_2O_3 (wt.%)**	**CaO (wt.%)**	**SiO_2 (wt.%)**	**MgO (wt.%)**
	29.2	30.8	38.7	0.9
Bath temperature	1440 °C			
Rotation speed of crucible	0 rpm			
Steady state?	Yes (temperature changes inside the freeze lining follow changes in bath temperature)			
Formation temperatures	Anorthite: 1400 °C Melilite: 1340 °C Pseudowollastonite: 1248 °C (solidus)			
p.p. stable during cooling?	yes			
Interface temperature (°C)	1403 °C			
Phases at interface	Anorthite (C, F)			
Comments	No detached crystals			

Crivits et al. (Chapter 8)				
System	**Al-Ca-Si-O (+ MgO impurity)**			
	FL2: melilite primary phase filed: high viscosity			
Bath composition	**Al_2O_3 (wt.%)**	**CaO (wt.%)**	**SiO_2 (wt.%)**	**MgO (wt.%)**
	24.4	35.9	38.2	1.2
Bath temperature	1440 °C			
Rotation speed of crucible	0 rpm			
Steady state?	Yes (temperature changes inside the freeze lining follow changes in bath temperature)			
Formation temperatures	Melilite: 1400 °C Anorthite: 1325 °C Pseudowollastonite: 1248 °C (solidus)			
p.p. stable during cooling?	yes			
Interface temperature (°C)	1397 °C			
Phases at interface	Melilite (D, NF)			
Comments	Some detached melilite crystals present. Comparison of the phase equilibria and the temperature measurements suggests these crystals were not thermodynamically stable.			
Crivits et al. (Chapter 8)				
System	**Al-Ca-Si-O (+ MgO impurity)**			
	FL3: melilite primary phase field: medium viscosity			
Bath composition	**Al_2O_3 (wt.%)**	**CaO (wt.%)**	**SiO_2 (wt.%)**	**MgO (wt.%)**
	17.7	42.9	37.6	1.3
Bath temperature	1440 °C			
Rotation speed of crucible	0 rpm			
Steady state?	Yes (no changes in measured temperatures)			
Formation temperatures	Melilite: 1400 °C Pseudowollastonite: 1325 °C Anorthite: 1248 °C			
p.p. stable during cooling?	yes			
Interface temperature (°C)	1317 °C			
Phases at interface	Melilite (E, F), Pseudowollastonite (D, NF)			
Comments	Detached melilite crystals present.			

Crivits et al. (Chapter 8)				
System	**Al-Ca-Si-O (+ MgO impurity)**			
	FL4: melilite primary phase field: low viscosity			
Bath composition	**Al_2O_3 (wt.%)**	**CaO (wt.%)**	**SiO_2 (wt.%)**	**MgO (wt.%)**
	41.9	45.9	10.3	1.5
Bath temperature	1460 °C			
Rotation speed of crucible	0 rpm			
Steady state?	Yes (no changes in measured temperatures)			
Formation temperatures	Melilite: 1440 °C Calcium aluminate (CA): 1400 °C Dicalcium silicate (C_2S): 1383 °C (melilite disappears)			
p.p. stable during cooling?	no			
Interface temperature (°C)	/ (interface not present in retrieved freeze lining)			
Phases at interface	Estimated to be dicalcium silicate (C_2S) and calcium aluminate (CA)			
Comments	Shattered on quenching due to the presence of dicalcium silicate in the freeze lining. Detached melilite crystals present.			
Crivits et al. (Chapter 8)				
System	**Al-Ca-Si-O (+ MgO impurity)**			
Bath composition	**Al_2O_3 (wt.%)**	**CaO (wt.%)**	**SiO_2 (wt.%)**	**MgO (wt.%)**
	50.6	47.1	0.3	1.5
	FL5: $C_{12}A_7$ primary phase field			
Bath temperature	1460 °C			
Rotation speed of crucible	0 rpm			
Steady state?	Yes (no changes in measured temperatures)			
Formation temperatures	Estimated (presence of $C_{12}A_7$ oxide or hydrate compound could not be modelled) $C_{12}A_7$: 1420 °C			
p.p. stable during cooling?	Yes			
Interface temperature (°C)	1400 °C			
Phases at interface	$C_{12}A_7$ (D,NF)			
Comments	Detached $C_{12}A_7$ crystals present.			

The comments in the following chapter will:

- review the results of previous and current research and highlight the key findings
- analyse the experimental data and their implications for control and selection of freeze linings
- discuss the factors influencing freeze lining systems
- present a summary of phenomenological understanding of freeze linings systems.

9.2 Effect of key process parameters on freeze linings

From a practical perspective, the ability of freeze linings to provide integrity to furnace linings is of paramount importance to avoid loss of charge through breakout, injury to personnel, damage to process plants and loss of production. A finite thickness of freeze lining must therefore be maintained at all times.

The second point is that the rate of heat loss through the freeze lining is also dependent directly on the thickness of the deposit; the thicker the deposit, the lower the rate of heat transfer through the lining.

In practice, a balance must be obtained since increased deposit thickness reduces available working volume of the reactor; too great a freeze lining thickness will result in decreased productivity for a given reactor size.

This discussion is structured around those process parameters that can be changed to influence the stability of the freeze linings: the flow conditions in the reactor, the temperature profiles and the slag composition.

9.2.1 Effects of bulk flow in bath

Deposit interface temperature

For interface temperatures equal to the liquidus temperature, previous research has shown that the bulk flow has no effect on the deposit interface temperature [9]. For interface temperatures below the liquidus temperature, increased bath agitation was found to result in higher interface temperatures at steady state, and a denser (= higher % solid) interface microstructure [58].

Deposit thickness

The effect of the bulk bath flow on the deposit thickness in a planar geometry can be estimated through the following equation, where the effect of bulk flow is integrated in the convective heat transfer coefficient of the bath (h_{bath}) (see also Equations (2-7) and (2-8)).

$$\Delta x_{FL,ss} = \frac{k_{FL}.(T_{bath,FL} - T_{coldface})}{h_{bath}.(T_{bath} - T_{bath,FL})} \quad \textbf{(9-1)}$$

where k_{FL} equals the thermal conductivity of the freeze lining, $T_{bath,FL}$ the bath-freeze lining interface temperature, $T_{coldface}$ the cooling circuit-freeze lining interface, and T_{bath} the bulk bath temperature.

Specifically for molten salt systems, a lot of research focused on estimating the convective heat transfer as function of several process parameters [3, 4, 6, 32, 35, 40]. The majority of this research reported values for the convective heat transfer coefficient of the bath between 250 and 830 W/m^2K. Taylor et al. [6, 35] reported that h_{bath} increased by 34-45 % compared to natural convection for peripheral freeze velocities of 0.09 and 0.12 m/s respectively.

Fallah-Mehrjardi et al. [9] also performed experiments in a cryolite molten salt at notional peripheral velocities of 0 and 0.038 m/s, reporting values for h_{bath} of 3760 and 4059 W/m^2K respectively. These values are much higher than all other values reported in literature, and seem unlikely to be correct.

For the Al-Cu-Fe-Si-O system, values for h_{bath} were reported by Fallah-Mehrjardi et al. [58]. For peripheral velocities of 0, 0.05 and 0.11 m/s, h_{bath} was estimated to be 941, 1345 and 3487 W/m^2K respectively. In the current work, h_{bath} for experiments in the Cu-Fe-Mg-Si-O system at 0 m/s was estimated to be between 530 and 860 W/m^2K depending on the experiment.

In the $CaCl_2$-H_2O system (Chapter 6), the results were found to be dependent on flow conditions. When a primary phase sealing layer formed, the flow rate was found to have no significant effect on the deposit thickness. When a secondary phase sealing layer formed, a higher flow rate was found to decrease the deposit thickness. The latter trend can be extended to the research of Guevera et al. [46] under natural convection conditions. Further research is required to confirm and clarify these trends.

Flow pattern

The flow pattern of the liquid also effects the local freeze lining deposit thickness. This is illustrated perfectly in the cold modelling experiments by Geuvara et al; [46] and in Chapter 6, and has been schematically represented in Figure 9-1a. Under natural convection conditions, the hot liquid flows in from the top. Once it hits the freeze lining, it cools down and flows down due to the increased density, the cooled liquid flows out from the bottom, towards the heating elements. This general flow pattern was kept in the experiments performed in the current study, but was induced through pumping liquid from a separate hot liquid container to the freeze lining bath. As more hot liquid is present at the top part of the container, and the boundary layer is thinner in this area, resulting in a higher local heat transfer coefficient, the freeze lining is thinner in this area (see Section 6.1.4).

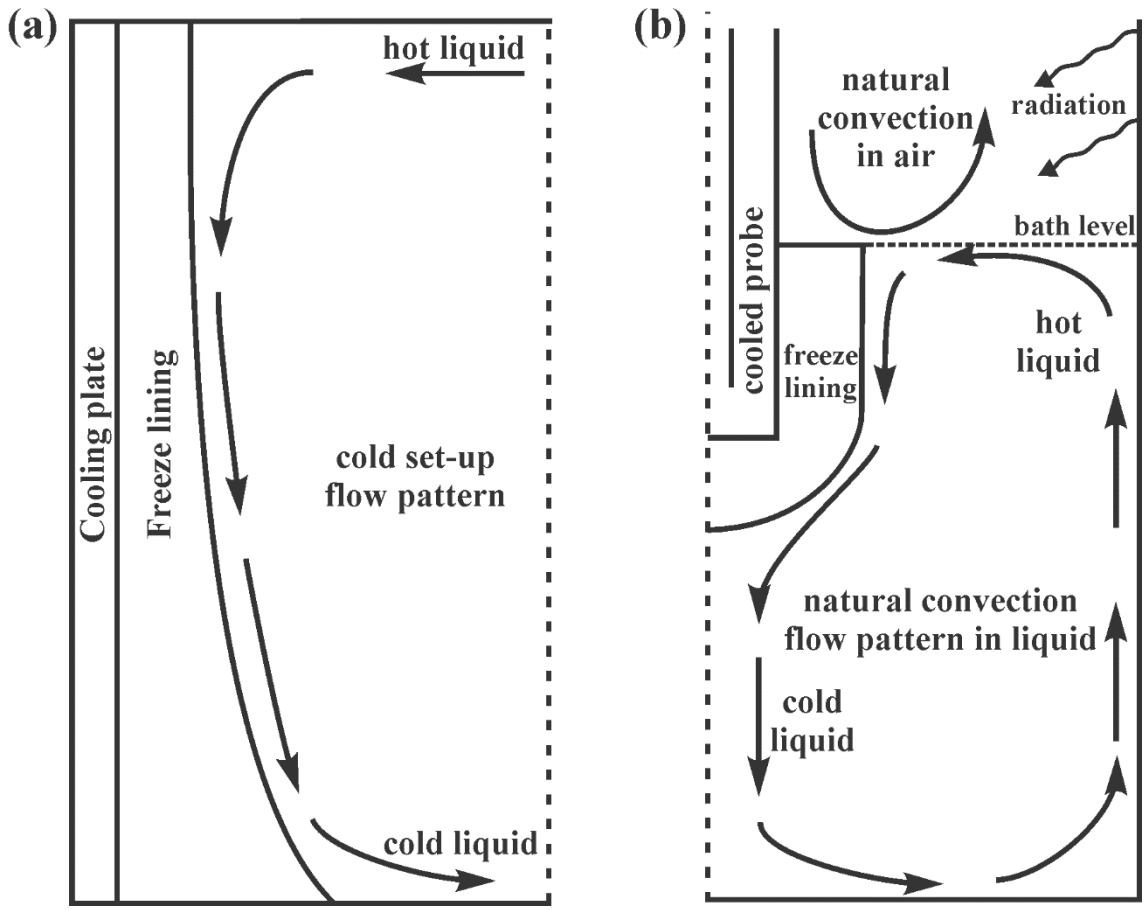

Figure 9-1: Flow patterns in the cold set-up and the cooled probe set-up.

The situation is more complex when considering the cooled probe set-up schematically presented in Figure 9-1b. Under natural convection conditions, the flow pattern in the liquid is similar to that in the cold set-up, with hot liquid flowing towards the freeze lining at the top, and flowing away from the freeze lining at the bottom. From this, it would be expected that the freeze lining is thinner at the top than the bottom. However, due to convective heat transfer from the bath to the air above the furnace, the top layer of the bath cools down, resulting in a thicker freeze lining at the top, which can be observed in the work by Taylor et al. [6]. In addition to this, when the temperature of the furnace is sufficiently high, radiative heat transfer can increase the temperature in the top layer of the bath, resulting in a thinner freeze lining at the top, as can be observed in the FL4 experiment in Chapter 7. Finally, forced convection can be induced through rotation of the crucible or probe, resulting in a more even (equal thickness at the top and bottom) freeze lining thickness ([6]).

In general, areas of higher turbulence in the bath will result in a thinner local freeze lining. This is discussed in the work by Fraser et al. [40], where the most turbulent area and thinnest freeze lining was found at the metal-electrolyte interface.

9.2.2 Bath temperature

Several freeze lining studies have been performed varying the bath temperature while keeping the bath composition constant. The studies selected for comparison in this chapter based on the availability of estimates of the interface temperature at steady state are the studies by Guevara et al. [46] and Fallah-Mehrjardi et al. [9], and Chapters 6 and 7 of the current study.

Deposit interface temperature

In previous studies, no influence of the bath temperature on the interface temperature was observed. In the study by Guevara et al. [46], the interface temperature was equal to the solidus temperature for all of the investigated bath temperatures, while in the study by Fallah-Mehrjardi et al. [9] on Cryolite molten salts, the interface temperature was always found to be equal to the liquidus temperature.

The interface temperatures of the experiments performed in Chapter 6 ($CaCl_2$-H_2O system) did change depending on experiment. However, the steady state interface temperature was found to depend on the nucleation and growth rate of the primary phase, rather than on the bath temperature.

In Chapter 7 (Cu-Fe-Mg-Si-O system), the interface temperature was found in all cases to be below that of the olivine liquidus and to vary depending on bath temperature. In the experiment where the bath temperature was below the formation temperature of pyroxene, the interface temperature was found to be below the formation temperature of pyroxene as well. In the other experiments, where the bath temperature was above the formation temperature of pyroxene, but below the liquidus temperature, the interface temperature was found to equal the formation temperature of pyroxene.

These findings suggest that the interface temperature depends on the bath temperature relative the formation temperature of the solid compounds. In general, a higher bath temperature below the liquidus temperature results in a higher interface temperature, while a higher bath temperature above the liquidus temperature has no influence on the bath-freeze lining interface temperature. Other factors, such as nucleation and growth rate of the solid compounds, may, however be of greater importance.

Deposit thickness

In all of the considered studies, an increase in bath temperature results in a decrease of the deposit thickness. Theoretically, the steady state thickness of a freeze lining in a planar geometry can then be estimated through equation (9-1):

As a result, it should be possible to calculate the thickness of a freeze lining created at different bath temperature (and keeping all other parameters constant) through the relation

$$\frac{\Delta x_{FL,ss,1}}{\Delta x_{FL,ss,2}} = \frac{(T_{bath,FL,1} - T_{coldface,1})}{(T_{bath,1} - T_{bath,FL,1})} \times \frac{(T_{bath,2} - T_{bath,FL,2})}{(T_{bath,FL,2} - T_{coldface,2})} \quad \textbf{(9-2)}$$

In practice, although the trends calculated by equation (9-1) appear to be correct, the errors associated with the differences in deposit geometry, the uncertainties in the convective heat transfer coefficients and on the deposit thickness measurements in any of the considered studies are too high to demonstrate exact correspondence. Take for example the freeze linings created by Guevara et al. [46] at bath temperatures of 40 and 45 °C. In this case, the ratio of the deposit thicknesses observed was 3/2, whereas using equation (9-2):

$$\frac{\Delta x_{FL,ss,40°C}}{\Delta x_{FL,ss,45°C}} = \frac{(30-20)}{(40-30)} \times \frac{(45-30)}{(30-25)} = \frac{150}{50} = \frac{3}{1} \quad \textbf{(9-3)}$$

Where the thickness was measured at 100 mm height on the cold wall.

The equivalent equation for cylindrical geometries can be found by combining equations (7-1)-(7-3).

$$\frac{(T_{bath,1} - T_{bath,FL,1})}{(T_{bath,2} - T_{bath,FL,2})} = \frac{(T_{bath,FL,1} - T_{coldface,1})}{ln(r_{bath,FL,1}/r_{coldface,1})} \times \frac{ln(r_{bath,FL,2}/r_{coldface,2})}{(T_{bath,FL,2} - T_{coldface,2})} \quad \textbf{(9-4)}$$

For experiments FL2 and FL4 in Chapter 7, the left-hand term of this equation gives a value of 0.4. Calculating the right-hand term gives:

$$\frac{(1205-911)}{ln(32.35/6.35)} \times \frac{ln(19.35/6.35)}{(1203-896)} = 0.65 \quad \textbf{(9-5)}$$

It can thus be concluded that, for now, equation (9-1) should be used to determine trends, rather than to get accurate predictions. For example, it can be seen that the thickness will be more sensitive to the bath temperature at low superheat (T_{bath}-$T_{bath,FL}$).

Subliquidus bath temperatures

It has been shown in [64] and Chapter 7 that, under certain conditions, it is possible to create freeze linings at subliquidus bath temperatures. These observations stand in direct contrast with the earlier view on freeze linings that assumed the bath-freeze lining interface to always be equal to the liquidus temperature.

The demonstration plant scale Lead ISASMELT furnace at Mount Isa [115] demonstrates that in industrial practice, maintaining a steady state freeze lining/accretions at subliquidus bath

temperatures requires thorough knowledge of the favourable operating conditions for this to happen. The slag in this furnace was found to contain a high percentage of zinc ferrite crystals. It was observed in the early stages of operation that a freeze lining/accretions consisting of zinc ferrite crystals gradually grew on the furnace walls. After development of empirical approaches to the fluxing and operating temperature, the freeze lining/accretions was maintained at a controlled thickness.

9.2.3 Bath composition

Selection of studies for comparison in this section was based on the availability of information on the microstructure and interface temperature for a variable bath composition. As such, studies performed by Campforts et al. [54], Fallah-Mehrjardi et al. [51] were selected, along with the studies presented in Chapter 6, 7 and 8.

Deposit interface temperature

Campforts et al. [54] studied freeze linings in lead slags and demonstrated that at high SiO_2 concentrations, the crystallization rate of the solid compounds is so low that a fully amorphous freeze lining is formed. As such, the deposit interface temperature would be equal to the glass transition temperature.

Fallah-Mehrjardi et al. [51] observed that a reduction in SiO_2 content within the delafossite primary phase field of the Al-Cu-Fe-Si-O system increased the deposit interface temperature.

From these earlier studies, a preliminary conclusion was made that increasing the SiO_2 content/viscosity results in a decrease of the steady state deposit interface temperature. Experiments performed in the melilite primary phase field in the Al-Ca-Si-O system presented in Chapter 8, however, did not follow this trend. A decrease in viscosity in this primary phase field was found to decrease the interface temperature from the melilite liquidus to the formation temperature of the second solid compound, pseudowollastonite.

Naturally, the bath composition and interface temperature are also linked for those systems where the deposit interface temperature equals the liquidus. This is demonstrated in Chapter 6, where a reduction of the $CaCl_2$ content with 1 wt.% results in significantly thinner freeze linings for a constant bath temperature.

In the previous section (9.2.2, deposit interface temperature), it was concluded that the bath temperature relative to the formation temperature of the solid compounds is an important factor in determining the steady state deposit interface temperature. In Chapter 7, due to the increase in bath

temperature in between experiments, the MgO crucible containing the slag partially dissolves into the bath, increasing the MgO content of the slag and increasing the liquidus temperature. Because of this, the measured bath temperature always stays below the liquidus temperature, resulting in an interface temperature equal to the formation temperature of pyroxene.

Deposit thickness

The influence of the bath composition on the deposit thickness is complex. The bath composition influences several factors in equation (9-1): the thermal conductivity, the convective heat transfer coefficient of the bath, and the interface temperature.

In the study by Campforts et al. [54], a higher SiO_2 content and higher PbO content result in a thinner freeze lining. This could be caused by a decrease in the interface temperature, or a changing thermal conductivity. Note, however, that not all of these freeze linings were at steady state.

Although a reduction of SiO_2 content resulted in an increased interface temperature and reduced superheat ($T_{bath} - T_{bath,FL}$) in the study performed by Fallah-Mehrjardi et al. [51], the thickness of the deposit was still found to decrease. This is likely caused by the decreased viscosity increasing the convective heat transfer coefficient of the bath.

In Chapter 6, it was demonstrated that a change in liquidus temperature caused by a change in bath composition can have a significant effect on the steady state deposit thickness. This can be demonstrated through equation (9-2) for a change in liquidus temperature from 39 to 35 °C, with a constant bath and coldface temperature of 40 and 20 °C respectively. The assumption was made of a freeze lining with an interface temperature equalling the liquidus.

$$\frac{\Delta x_{FL,ss,1}}{\Delta x_{FL,ss,2}} = \frac{(39-20)}{(40-39)} \times \frac{(40-35)}{(35-20)} = \frac{19}{3} \quad \textbf{(9-6)}$$

Chapter 8 again demonstrated the complexity of the relationship between the bath composition and the steady state thickness. In the melilite primary phase field, three freeze linings were created. The freeze lining created in the system with the highest viscosity was found to have the highest interface temperature (lowest superheat), but only the second highest thickness. At intermediate bath viscosities, the interface temperature and the thickness were lowest, while at the lowest bath viscosity, the freeze lining was thickest.

Phase equilibria

Link phase equilibria and interface temperature

As discussed in section 9.2.2, it was observed that the interface temperature often equals the formation temperature of a solid compound. Verscheure [47] reported that for the investigated zinc fuming slag, rather than an interface temperature equalling the liquidus temperature *"…it may be argued that, for the conditions of the experiment, a better assumption for the hot face temperature may be the melilite formation temperature …"*. Based on the presence of both wustite and melilite at the interface.

The majority of experiments performed by Fallah-Mehrjardi et al. [51, 57, 58] in the Al_2O_3-'Cu_2O'-'Fe_2O_3'-SiO_2 system showed the presence of cuprite at the interface, but not in the subliquidus boundary layer, suggesting the interface temperature was approximately the formation temperature of cuprite. (One experiment at high bath agitation resulted in the formation of a delafossite sealing layer, and one experiment showed cuprite in the subliquidus boundary layer, although it isn't clear whether this cuprite was stable at this position during the experiment, or formed at a different position or during cooling.)

Experiments in cryolite melts [9] demonstrated that the interface temperature for this particular system is approximately equal to the liquidus temperature.

Measurements of the interface temperature in $CaCl_2$-H_2O solutions ([46], Chapter 6), showed that, depending on the thermal history, the interface temperature was either equal to the liquidus temperature, or the formation temperature of $CaCl_2.4H_2O$.

Experiments in the 'Cu_2O'-'Fe_2O_3'-MgO-SiO_2 (Chapter 7) system suggested interface temperatures approximately equal to the formation temperature of pyroxene, rather than the primary olivine phase, for a range of bath temperatures.

Experiments in the Al_2O_3-CaO-SiO_2 system suggested interface temperatures equal to the liquidus temperature in the anorthite primary phase field. In the melilite primary phase field, the interface temperature was the liquidus or the formation temperature of pseudowollastonite, depending on the bulk bath composition.

Although some experiments do show interface temperatures that aren't equal to the formation temperature of a particular compound, it seems clear based on the list of examples above that the steady state interface temperature of freeze linings has a high probability to be equal to the formation temperature of a solid compound. This was explained in Chapter 7 as follows: The formation temperature of each compound marks a sudden change in chemical and physical parameters. The difference in nucleation rate, crystallization rate and mass transfer of the components present in different solid compounds could be such that certain compounds are more likely to be deposited on

the freeze lining, while others are more likely to continuously form and dissolve in the subliquidus layer.

Metastability

The phase equilibria of the system influence the freeze lining deposit in other ways as well. Chapter 6 demonstrates that metastability can lead to the formation of a sealing crystal layer consisting solely of a solid different from the primary phase. In fact, any dynamic steady state resulting in a steady state deposit interface temperature below the liquidus is a metastable state. If, through changes in operating conditions, a freeze lining is created that has a sealing layer consisting of the primary phase, and a steady state interface temperature equal to the liquidus temperature, returning to the original operating conditions will not result in the originally observed subliquidus dynamic steady state. The primary phase and the bulk bath would be at equilibrium at the liquidus temperature and no growth or dissolution of the freeze lining would be expected.

Stability of primary phase at low temperatures

Changes to the stability of phases at lower temperatures in the freeze lining affect freeze linings as well. The evidence provided in sections 2.5 and 9.1 appears to show that when the primary phase is not stable at lower temperatures, no sealing crystal layer consisting solely of the primary phase was formed in any of the performed experiments in the previous and current studies.

Deposit interface morphology

The geometry of the freeze lining as visualised and depicted in Figure 2-1 is of a smooth vertical wall with the temperature profile normal to the deposit and reactor wall interfaces. This 1-D representation, whilst useful to provide a general description of the overall process is a significant simplification of what is occurring at the macro- and micro-scale since there will also be heat and mass flow in the second and third dimensions.

A freeze lining is a cooled surface, which will result in all situations in natural convection in the liquid phase adjacent to the deposit interface in addition to forced convection imposed through bulk flow of the fluid in the reactor. The natural convection contribution will lead to downward flow of cooler fluid along the interface. The magnitude of this natural convection contribution to the thermal and mass transfer will depend on not only the orientation of the surface relative to the bulk liquid flow (e.g. vertical or horizontal), the temperature difference between the interface and the bulk fluid and the physical and thermal parameters defining the properties of the liquid phases, but also on the structure of the interface. These differences in the microfluidic conditions at the deposit interface

could be the result of differences in crystal shape (planar, columnar, dendritic), crystal growth morphology (facetted, non-facetted) and crystal strength in addition to the physical properties of the fluid and the driving forces for fluid flow [116].

The potential effect of morphology on freeze lining deposits is supported by the observation that no columnar or dendritic crystals are reported to be present in the subliquidus boundary layer in any previous and current work on freeze linings (see Sections 2.5 and 9.1). As such, columnar and dendritic crystals are always expected to be attached to the freeze lining, resulting in an interface temperature higher or equal to the formation temperature of these crystals. This is demonstrated in particular by the experiments in the Al-Ca-Si-O system (Chapter 8). Three experiments were performed in the melilite primary phase field. In one experiment, dendritic melilite crystals were formed (FL2), which were attached to the freeze lining. In the two other experiments (FL3,4), detached equiaxed melilite crystals were found to be present in the subliquidus boundary layer.

Phase changes in the deposit

Polymorphic transformations

It was also observed through experiments in the Al-Ca-Si-O system that a freeze lining containing dicalcium silicate (C_2S) shattered on quenching (Chapter 8). This was attributed to the combination of thermal stresses during cooling and the significant increase in volume during the polymorphic transformation from β-C_2S to γ-C_2S. A similar phenomenon occurs in the cryolite system, where polymorphic transformation of cryolite at 563 °C results in shattering of the freeze lining on cooling [1]. The freeze linings were stable during the experiments as the steady state temperatures in the freeze lining were well above the β to γ transformation temperature. It is suggested, though, that in industrial applications, where water is usually used as the coolant, such polymorphic transformation could result in regular failure of the freeze lining as the dicalcium silicate is formed and subsequently cooled down. As this would result in an unstable freeze lining, it is recommended to avoid chemical systems forming compounds that undergo large changes in volume during cooling when using freeze lining technology, or to operate the freeze lining above the polymorphic transformation temperature inducing this change in volume.

Liquification of intermediate layers

It was shown in Chapter 6 that under certain conditions, the intermediate layers (more specifically the closed crystalline layer) can liquefy, while the freeze lining interface remains solid, due to

differences in local bulk composition throughout the freeze lining layers. It was demonstrated that this severely reduces the mechanical stability of the freeze lining.

To avoid this in industry, ideally a freeze lining consisting 100% of the primary phase should be created, as the composition of this phase corresponds to the highest achievable melting point of the freeze lining.

Porosity

Due to a decrease in solubility of gases in the liquid, pores can form during formation of the freeze lining. To date, a significant amount of pores has only been observed in the Al-Ca-Si-O system (Chapter 8)

9.3 Phenomenological understanding of freeze lining systems

9.3.1 Deposit microstructure

Based on cooled probe laboratory experiments using silica containing lead slags, Campforts et al. [52] distinguished six different layers in quenched freeze lining deposits, based on microstructure:

(1) The glassy layer
(2) The glassy layer with crystals
(3) The closed crystalline layer
(4) The open crystalline layer
(5) The sealing layer
(6) The entrained slag bath layer

Fallah-mehrjardi et al. [51] added a seventh microstructural layer:

(4')The subliquidus boundary layer

These classifications were based primarily on experiments in high-silica slag systems. From the experiments in the current study, it was found that a minor redefinition of the layers is required to keep this classification applicable to a wide variety of systems. Low-silica systems were found to form a quenched layer, rather than a fully amorphous, glassy layer. Additionally, experiments in the Cu-Fe-Mg-Si-O system reported in the present study (Chapter 7) indicated that the open crystalline layer slowly evolves into a sealing layer, composed of solids, which do not necessarily include the primary phase. This comes about in situations in which continuous mass transfer can take place from

the bulk liquid through the deposit structure via the liquid phase to the low temperature regions of the deposit over long periods of time; the primary phase is not necessarily present in the stable phase assemblage at these low temperatures. Again, in industrial applications, it is expected that the life of the freeze lining or the campaign life of the furnace would be considerable greater than the laboratory-based experiments.

Based on these considerations, the following updated classification is proposed for deposits produced under laboratory conditions:

(1) The quenched layer: this layer is formed adjacent to the cooling apparatus. Due to the fast cooling rate and low temperatures maintained throughout the experiment, limited or no crystallization takes place during cooling and no changes occur in this layer after its formation. The local bulk composition in this layer is equal to that of the bulk bath.

(2) The devitrified quenched layer: similar to layer (1), the fast cooling rate of this layer results in limited crystallization during cooling. Due to the higher steady state temperatures in this layer, devitrification of the quenched material occurs, resulting in the formation of microcrystals over time. The local bulk composition in this layer is equal to that of the bulk bath.

(3) The closed crystalline layer: lower cooling rates in this layer result in the formation of a fully crystalline layer during solidification. The higher steady state temperatures in this layer allow for subsolidus reactions to take place over time. As solid state diffusion is generally slow, the local bulk composition in this layer is approximately equal to that of the bulk bath.

(4) The open crystalline layer: Steady state temperatures in this layer are below the liquidus. As a result, crystals are present in a matrix of liquid, connected to the bath; these open liquid channels enable mass transfer between the bath and the open crystalline layer to take place. As a result, the local bulk composition of this layer changes over time.

(5) The sealing layer: prolonged mass transfer of material from the bath to the open crystalline layer will eventually result in the liquid channels closing up. The solids now form a sealing layer, preventing further significant transfer of chemical components between the bath and the inner freeze lining layers. Note that the sealing of the open crystalline layer will occur at the interface first and that the solids present in this layer are not necessarily the primary phase.

(6) The subliquidus boundary layer: when the steady state interface temperature is below the liquidus, the liquid adjacent to the bath-freeze lining interface will be at subliquidus temperatures. These temperatures allow for the formation of detached crystals, which are

continuously transported to and from the deposit interface through natural and forced convection.

These layers are typically observed on cooled probes that have been immersed in hot slags or melts. In practical systems, where the reactors are more gradually brought to operating temperature, it is to be expected that not all of these layers will be observed. For example, layers (1) and (2), which rely on initial fast cooling for the formation of these structures, would not be formed.

9.3.2 Dynamic steady state framework

To explain the observations by Guevera and Irons [46] and Fallah-Mehrjardi et al. [51, 57, 58, 64], namely the possibility of forming a steady state freeze lining with a bath-freeze lining interface temperature below the liquidus, a dynamic steady state framework has been formulated. It has been proposed [51] that, through natural and forced convection, liquid, possibly with pre-existing solids, continuously flows to and from the bath-freeze lining interface. If the temperatures near this interface are below the liquidus, detached crystals can nucleate or growth can occur on pre-existing crystals; as the detached crystals move towards the deposit interface they can continuously form and grow in this subliquidus layer. If the crystals approach local chemical equilibrium with the surrounding liquid the supersaturation of the fluid with respect to the precipitating solid approaches zero. It is proposed that local fluctuations in temperature and concentration at the interface, caused by turbulent eddies, result in the detached crystals moving back into the bulk bath liquid where, at temperatures above the liquidus, they are dissolved in the bulk bath liquid. The interface temperature then is determined not by the liquidus temperature but by a dynamic steady state condition involving crystallization and dissolution, and heat and mass transfer in the subliquidus boundary layer.

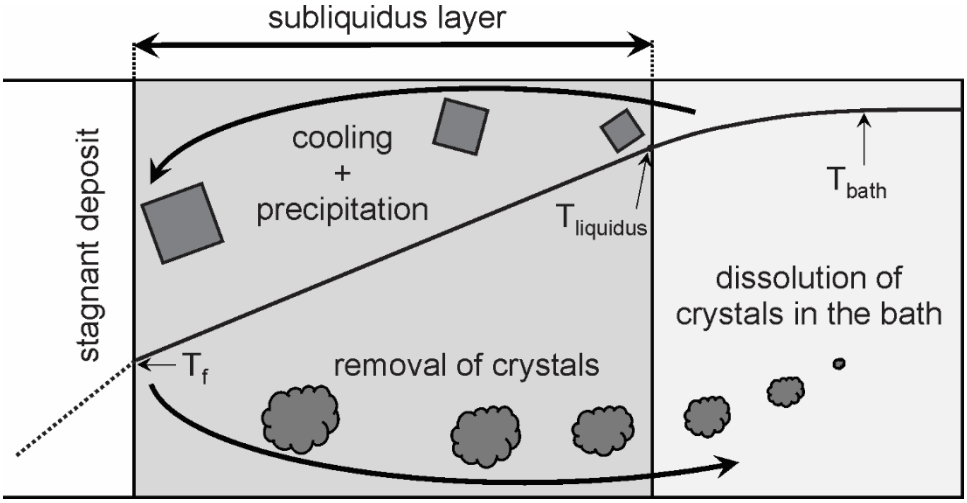

Figure 9-2: Schematic presentation of the dynamic steady state framework for freeze linings proposed by Mehrjardi et al. [51]

The experimental results obtained in Chapter 6 on freeze lining formation in the $CaCl_2$-H_2O system demonstrate that steady state freeze linings can be formed at sub-liquidus temperatures without the presence of detached crystals. In these experiments potential nuclei were redissolved in the flowing re-heated liquid before returning the bulk bath material to the system. This was in contrast to the experimental design used by Guevera and Irons [46] in which detached crystals were allowed to recirculate in the system. The observation that the interface temperature of the freeze lining observed in the present experiments described in Chapter 6 was below the liquidus is explained by the metastability of the solid-liquid system at the deposit liquid interface.

Fallah-Mehrjardi et al. [64] and Chapter 7 observed the formation of steady state freeze linings in the presence of subliquidus bulk bath conditions. In the Al-Ca-Fe-Mg-Si-Zn-O system wustite, melilite and spinel crystals were present at the deposit interface, while melilite and spinel crystals were found to be present in the bulk bath. In the Cu-Fe-Mg-Si-O system (Chapter 7) pyroxene crystals were present at the steady state deposit interface despite the fact that primary phase olivine were observed in the bulk solid /liquid slurry.

The formation of steady state freeze lining with an deposit interface consisting of high silica glass was reported by Campforts et al. [54] with no apparent observation of detached crystals ahead of the deposit interface.

If the crystal interface is below the liquidus temperature there will always be a net driving force for deposition of solute from the liquid phase. Assuming the growth rate of the crystal is mass transfer controlled, the growth rate will be described by the product of the mass diffusion coefficient of the

precipitating component (D_A) and the concentration gradient of this component perpendicular to the bath-freeze lining interface $\left(\frac{dC_A}{dx}\right)_{bath,FL}$ [117] as given by equation (9-7)

$$G_{FL} \sim D_A \left(\frac{dC_A}{dx}\right)_{bath,FL} \quad \textbf{(9-7)}$$

This relationship is valid for the growth of detached crystals and crystals that form as part of the freeze lining interface.

In a positive temperature and concentration gradient there must be a net transfer of species. It has been shown experimentally, however, that a steady state deposit thickness is achieved. There must therefore be a mechanism that prevents material being added at the deposit/liquid interface of the deposit, otherwise it would not be possible to reach a steady state thickness; the freeze lining would continue to grow by diffusional mechanisms.

If it is accepted that local fluctuations in temperature and concentration can occur at the deposit interface as a result of turbulent eddies, then the boundary conditions locally at the deposit interface can be relaxed and indeed reversed. By their very definition these perturbations change with time so that at the interface local dissolution and local growth of the freeze lining is taking place [59]. Through this perturbation mechanism the freeze lining can reach steady state conditions when the net growth rate of the freeze lining equals zero even if macroscopically there is a positive temperature gradient. Importantly, this mechanism is applicable to conditions not only with the presence of detached crystals but also without the detached crystals, as was demonstrated in the present study (Chapter 6). It follows that, provided the turbulent flow at the microfluidics level still takes place at the deposit interface, this concept, inherent in the dynamic steady state framework previously proposed to explain the sub-liquidus temperatures at the freeze lining interface, is still valid. The dynamic steady state framework can in effect be extended and can be regarded as describing the state of the interface over a wide range of conditions. The condition of the interface temperature being equal to the liquidus temperature represents one limit. The conditions necessary at the other low temperature limit of the freeze lining interface are still to be defined. The present study has demonstrated that these are complex reaction systems and that individual process parameters may influence more than one mechanism, the separation of the effects of individual factors is not a trivial exercise.

9.4 Conclusions

The steady state bath-freeze lining interface temperature has a significant effect on both the heat flux through the freeze lining and the steady state thickness. It has been shown through a number of

experimental investigations in several different chemical systems that the steady state bath-freeze lining interface can be equal to, or less than, the liquidus temperature of the bulk material.

To explain the observations of sub-liquidus temperatures at the deposit interface and the microstructural observations made in the previous studies a dynamic steady state framework was proposed. In essence this involves the continuous formation and crystallisation of detached crystals in a sub-liquidus boundary layer as they approach the deposit interface and the dissolution of these crystals as they are returned to bulk liquid through the action of turbulent eddies.

It has been shown in the present study that steady state, sub-liquidus interface temperatures can also be achieved in freeze lining systems despite the absence of detached crystals.

The condition where the deposit interface temperature is equal to the liquidus temperature, which was previously assumed to be valid for all systems, appears as the upper boundary temperature condition to the more general dynamic steady state framework.

10 Summary

In Chapter 6, a list of thermal, chemical and physical factors affecting freeze lining behaviour was introduced. This list provided a guideline for the design of experiments. Each series of experiments in the present study was set up in such a way that one particular factor was singled out for investigation.

Particular focus was paid to the steady state bath-freeze lining interface temperature as this temperature is one of the main factors determining the steady state thickness of, and heat loss through, the freeze lining.

$CaCl_2$-H_2O system

The low-temperature freeze lining experiments carried out in the aqueous $CaCl_2$ system (Chapter 6) were performed to investigate the effect of nucleation and crystallization rate, and the (thermal) history of the freeze lining.

It was found that, depending on the nucleation rate of the primary phase, either a steady state bath-freeze lining interface temperature equalling the liquidus temperature (for high nucleation rates), or an interface temperature equalling the formation temperature of the secondary $CaCl_2.6H_2O$ phase was obtained. These observations were explained through the sealing of the open crystalline layer formed by the secondary $CaCl_2.6H_2O$ phase. When the nucleation of the primary $CaCl_2.4H_2O$ phase is slow compared to the mass transfer of components from the bath to the freeze lining, the secondary phase seals off the open crystalline layer at the interface before any primary phase crystals are formed, creating a metastable freeze lining.

It was observed that a subsequent increase and later decrease of the bath temperature could cause the steady state interface temperature to change from the formation temperature of the secondary phase, to the liquidus temperature, demonstrating the importance of (thermal) history.

'Cu_2O'-'Fe_2O_3'-MgO-SiO_2 system

High temperature freeze lining experiments in the 'Cu_2O'-'Fe_2O_3'-MgO-SiO_2 system (Chapter 7) were used to study the effect of bath temperature on freeze lining behaviour. It was observed that at thermal steady state conditions, the bath-freeze lining interface temperatures were lower than the liquidus temperatures, which were estimated based on the phase equilibria study on this system, reported in Chapters 4 and 5.

This observation, combined with the presence of primary olivine crystals throughout the bath in one of the experiments, clearly demonstrates the possibility of operating freeze linings at subliquidus bath temperatures.

In general, increasing bath temperatures were found to increase the steady state bath-freeze lining interface temperature.

Al_2O_3-CaO-SiO_2 system

Experiments in the melilite primary phase field in the Al_2O_3-CaO-SiO_2 system were designed to investigate the influence of viscosity on freeze lining behaviour. A recent phase equilibria study on this system [67] was used during planning and explanation of the observed phenomena. At higher viscosity, the steady state bath-freeze lining interface temperature was found to equal the liquidus temperature, while at lower viscosities, the interface temperature was found to be below the liquidus temperature. However, it was unclear whether this was caused by the viscosity, or the change in morphology of the melilite primary phase from dendritic to rectangular with a low length/width ratio.

The shattering of a freeze lining containing dicalcium silicate on quenching demonstrated the risks associated with polymorphic transformations. It is advised to always carry out an investigation of the expected solid compounds in freeze linings. Any compounds that are susceptible to reactions inducing large changes in volume should be avoided.

The Al_2O_3-CaO-SiO_2 system is the only system investigated to date in which freeze linings contain a large number of pores. These pores affect the apparent thermal conductivity of the freeze lining and could possibly affect the mechanical stability.

Expansion of conceptual framework

To explain the observations of sub-liquidus temperatures at the deposit interface and the microstructural observations made in the previous studies, a dynamic steady state framework was proposed. In essence, this involves the continuous formation and crystallisation of detached crystals in a sub-liquidus boundary layer as they approach the deposit interface and the dissolution of these crystals as they are returned to bulk liquid through the action of turbulent eddies.

It has been shown in the present study that steady state, sub-liquidus interface temperatures can also be achieved in freeze lining systems in the absence of detached crystals.

The condition where the deposit interface temperature is equal to the liquidus temperature, which was previously assumed to be valid for all systems, appears as the upper boundary temperature condition to the more general dynamic steady state framework.

Final remarks

Traditionally, freeze linings are regarded as a phenomenon dominated by heat transfer. Experiments in the current study have demonstrated that freeze linings are much more complex. When considering the use of freeze linings in operations, heat transfer, thermal, physical and chemical factors should all be considered. In doing so, the optimal freeze lining can be created, allowing for the maximization of freeze lining control and the optimization of the process as a whole.

11 Recommendations for future research

11.1 High temperature experiments

As has been shown in this work, high-temperature experiments can provide information on typical microstructures in certain systems. On top of this, an estimate can be made as to the thermal conductivity of the resulting freeze lining.

Implication and interpretation of these freeze lining experiments tends to be hard and take a long time, with uncertain results. As a result, the main advantage of high-temperature systems seems to be the ability to study (simplified) industrial slag systems. It seems most efficient to use these experiments to gain more specific information on freeze lining behaviour in particular processes.

11.2 Room temperature experiments

Cold modelling of freeze linings provides the unique opportunity to study freeze lining behaviour by visual observation and accurate, in-situ measurements. Even though a relatively small portion of the current work was devoted to these experiments, some interesting new ideas were developed, proving the usefulness of cold modelling in the fundamental research of freeze lining behaviour.

The main difficulty in these experiments is finding room-temperature systems behaving similarly to slag systems at high temperatures. Currently, cold modelling of freeze linings has only been performed in the $CaCl_2$-H_2O system. This system only has peritectics in the viable range for cold modelling (0-90 °C) when using water as a coolant. In order to study eutectic freeze lining behaviour, or to study the effect of crystallization behaviour/viscosity/… on freeze lining behaviour, other systems have to be considered.

Salt-water systems in general seem to be the most promising class of cold model systems. A lot of these systems have been studied before, providing the phase equilibria information needed to plan and interpret freeze lining experiments.

In particular, the $Mg(NO_3)_2$-H_2O system could be used to test eutectic freeze lining behaviour, with a eutectic point present at approximately 50 °C between the $Mg(NO_3)_2.6H_2O$ and the $Mg(NO_3)_2.2H_2O$ compounds, with the melting temperature of $Mg(NO_3)_2.6H_2O$ at approximately 90 °C.

The effect of viscosity could be studied using either a salt-water-glycol solution, although a quick search didn't yield any results as to the phase equilibria of such systems. Another option for this are sucrose solutions. The disadvantage of sucrose solutions is their metastability at low undercoolings.

Naturally, the compatibility of each of these solutions with the acrylic tank, norprene tubing and copper reservoir should be tested and incompatible materials should be replaced in the set-up.

References

[1] K. Grjotheim, B. J. Welch: Aluminium smelter technology: a pure and applied approach, Aluminium-Verlag, Düsseldorf (1988)
[2] M. Campforts: PhD thesis, KU Leuven, Belgium (2009)
[3] A. Solheim, J. Thonstad, in: Adkins, E. M. (Eds.), "Heat transfer coefficients between bath and side ledge in aluminum cells. model experiments" Light Met. (1983) 425-435, TMS, Warrendale
[4] A. Solheim, J. Thonstad: Journal of Metals 36 (1984) 51-55
[5] J. Thonstad, S. Rolseth, in: Adkins, E. M. (Eds.), "Equilibrium between bath and side ledge in aluminium cells. basic principles" Light Met. (1983) 415-424, TMS, Warrendale
[6] M. P. Taylor, B. J. Welch: Metall. Trans. B 18B (1987) 391-398
[7] M. P. Taylor, W. D. Zhang, V. Wills, S. Schmid: Trans. IChemE 74A (1996)
[8] H. Pfundt, D. Vogelsang, U. Gerling, in: Campbell, P. G. (Eds.), "Calculation of the crust profile in aluminium reduction cells by thermal computer modelling." Light Met (1989) 371-377, TMS, Warrendale
[9] A. Fallah-Mehrjardi, P. C. Hayes, E. Jak: Metall. Mater. Trans. B 45 (2014) 1232-1247, doi: 10.1007/s11663-014-0078-z
[10] P. C. Pistorius: J. S. Afr. I. Min. Metall. 104 (2004) 417-422
[11] P. C. Pistorius: J. S. Afr. I. Min. Metall. 103 (2003) 509-14
[12] J. H. Zietsman: PhD thesis, University of Pretoria, South Africa (2004)
[13] J. H. Zietsman, P. C. Pistorius: Miner. Eng. 19 (2006) 262-279
[14] J. H. Zietsman, P. C. Pistorius: J. S. Afr. I. Min. Metall. 104 (2004) 229-235
[15] K. Verscheure, M. Van Camp, B. Blanpain, P. Wollants, P. Hayes, E. Jak, in: Kongoli, F. and Reddy, R. G. (Eds.), "Freeze linings in zinc fuming processes" Sohn International Symposium (2006) 361-374, TMS, Warrendale
[16] K. Verscheure, A. K. Kyllo, A. Filzwieser, B. Blanpain, P. Wollants, in: "Furnace Cooling Technology in Pyrometallurgical Processes" Sohn International Symposium (2006) 139-154, TMS, Warrendale
[17] K. Verscheure, M. Campforts, F. Verhaeghe, E. Boydens, M. Van Camp, B. Blanpain, P. Wollants: Metall. Mater. Trans. B 37B (2006) 929-940, doi: 10.1007/BF02735015
[18] K. Verscheure, M. Van Camp, B. Blanpain, P. Wollants, P. C. Hayes, E. Jak: Metall. Mater. Trans. B 38B (2007) 13-20, doi: 10.1007/s11663-006-9009-y
[19] K. Verscheure, M. Van Camp, B. Blanpain, P. Wollants, P. C. Hayes, E. Jak: Metall. Mater. Trans. B 38B (2007) 21-33, doi: 10.1007/s11663-006-9010-5
[20] J. Liefhebber, R. Hes, J. Stuurwold, J. van der Stel, B. L., in: "Blast furnace hearth grouting at Tata Steel in IJmuiden" METEC & 2nd ESTAD (2015), Steel Institute VDEh, Düsseldorf
[21] P. Sylven, P. L. Duncanson, L. Fontes, in: "Selecting lining materials to achieve long and productive blast furnace hearth campaigns" 6th International Congress on the Science and Technology of Ironmaking (2012), ABM, Rio de janeiro, Brazil
[22] J. Sarvinis, N. Voermann, C. Crowe, J. Bianchini, B. Wasmund, in: "Furnace design for modern, high-intensity pyrometatllurgical processes" Metallurgical Plant Design and Operating Strategies (2002) 318-331, AusIMM, Melbourne, Australia
[23] K. Verscheure, M. Campforts, M. Van Camp: Process for the valorization of metals from hev or ev batteries, Google Patents, (2011)
[24] F. Marx, M. Shapiro, B. Henning, in: "Application of high intensity refractory cooling systems in pyrometallurgical vessel design" 12th Int. Ferroalloys Congr. (2010), SAIMM, Johannesburg
[25] G. Rath, J. Kunze, R. Degel, in: "Status Report on Pyrometallurgical Ferronickel Production" 8th INFACON Conference (2001)

[26] S. Blancher, B., A. Sayasenh, E. Crespo, in: "Follow-up and mineralogical characterization of freeze lining evolution: a record of furnace life" Metal 2015 (2015), Tanger Ltd., Ostrava, Czech Republic
[27] A. M. Hearn, A. S. J. van Rensburg, J. R. Henning, in: ""Freeze" lining on M12 furnace: motivation, installation and operation" Tenth International Ferroalloys Congress (2004) 500-507, SAIMM, Johannesburg, South Africa
[28] L. R. Nelson, R. Sullivan, P. Jacobs, E. Munnik, P. Lewarne, E. Roos, M. J. N. Uys, B. Salt, M. de Vries, K. McKenna, N. Voermann, B. O. Wasmund: J. S. Afr. I. Min. Metall. 104 (2004) 551-561
[29] G. Bisio, G. Rubatto, R. Martini: Energy 25 (2000) 1047-1066
[30] P. Arthur, P. Partington, in: "ISASMELT(tm) - Not Just a Flash in the Pan" Copper 2003 (2003), CIM, Montreal, Quebec
[31] P. Arthur, S. P. Hunt, in: Ranking, W. J. and Nilmani, M. (Eds.), "Isasmelt - 25 Years of Continuous Evolution" John Floyd International Symposium on Sustainable Developments in Metals Processing (2005), AusIMM, Melbourne, Australia
[32] C. B. Solnordal, F. R. A. Jorgensen, R. N. Taylor: Metall. Mater. Trans. B 29 (1998) 485-492
[33] Q. Liang, X. Guo, Z. Dai, H. Liu, X. Gong: Fuel 102 (2012) 491-498, doi: 10.1016/j.fuel.2012.06.092
[34] W. E. Haupin, in: Light Metals (1971) 188-194, AIME, New York
[35] M. P. Taylor: PhD thesis, The University of Auckland, New Zealand (1984)
[36] M. P. Taylor, B. J. Welch, R. McKibbin: AIChE Journal 32 (1986) 1459-1465
[37] J. N. Bruggeman, D. J. Danka, in: Bickert, M. (Eds.), "Two-dimensional thermal modeling of the hall-héroult cell" Light Met. (1990) 203-209, TMS, Warrendale
[38] H. A. Ahmed, S. M. El-Raghy, F. A. Elrefaie, in: Mannweiler, U. (Eds.), "Prediction of the thermal aspects of egyptalum prototype high-amperage pre-baked aluminum reduction cells" Light Met. (1994) 333-338, TMS, Warrendale
[39] A. Valles, V. Lenis, in: Evans, J. (Eds.), "Prediction of ledge profile in hall-héroult cells." Light Met. (1995) 309-313, TMS, Warrendale
[40] K. J. Fraser, M. P. Taylor, A. M. Jenkin, in: "Electrolyte heat and mass transport processes in hall heroult electrolysis cells" Light Metals (1990) 221-226, TMS, Warrendale
[41] C. C. Wei, J. J. J. Chen, B. J. Welch, V. R. Voller, in: Huglen, R. (Eds.), "Modelling of dynamic ledge heat transfer" Light Met. (1997) 309-316, TMS, Warrendale
[42] A. Solheim, L. I. R. Stoen, in: Huglen, R. (Eds.), "On the composition of solid deposits frozen out from cryolitic melts." Light Met. (1997) 325-332, TMS, Warrendale
[43] A. Solheim, in: "Coupled heat and mass transfer during melting or freezing of sideledge in aluminium cells." 12th Aluminium Symposium, Bratislava, Slovakia (2003)
[44] D. G. C. Robertson, S. Kang, in: El-Kaddah, N., Robertson, D. G. C., Johansen, S. T. and Voller, V. R. (Eds.), "Model studies of heat transfer and flow in slag-cleaning furnaces" TMS Annual Meeting, Fluid Flow Phenomena in Minerals Processing (1999) 157-168, TMS, Warrendale
[45] F. J. Guevara, G. A. Irons: Metall. Mater. Trans. B 42B (2011) 664-676
[46] F. J. Guevara, G. A. Irons: Metall. Mater. Trans. B 42B (2011) 652-663
[47] K. Verscheure: PhD Thesis, KU Leuven, Belgium (2007)
[48] T. Crivits: internship report, Ghent University, Ghent (2010)
[49] A. Solheim, in: Lindsay, S. J. (Eds.), "Some aspects of heat transfer between bath and sideledge in aluminium reduction cells" Light Metals (2011) 381-386, TMS, Warrendale
[50] J. Thonstad, S. Rolseth, in: Adkins, E. M. (Eds.), "Equilibrium between bath and side ledge in aluminiium cells. basic principles" Light Met. (1983) 415-424, The Metallurgical Society of AIME,
[51] A. Fallah-Mehrjardi, P. C. Hayes, E. Jak: Metall. Trans. B 44B (2013) 534-548, doi: 10.1007/s11663-013-9807-y
[52] M. Campforts, E. Jak, B. Blanpain, P. Wollants: Metall. Mater. Trans. B 40B (2009) 619-631, doi: 10.1007/s11663-009-9257-8

[53] M. Campforts, E. Jak, B. Blanpain, P. Wollants: Metall. Mater. Trans. B 40 (2009) 632-642, doi: 10.1007/s11663-009-9257-8
[54] M. Campforts, B. Blanpain, P. Wollants: Metall. Mater. Trans. B 40 (2009) 643-655, doi: 10.1007/s11663-009-9258-7
[55] M. Campforts, K. Verscheure, E. Boydens, T. Van Rompaey, B. Blanpain, P. Wollants: Metall. Mater. Trans. B 39 (2008) 408-417, doi: 10.1007/s11663-008-9141-y
[56] M. Campforts, K. Verscheure, E. Boydens, T. Van Rompaey, B. Blanpain, P. Wollants: Metall. Trans. B 38 (2007) 841-851, doi: 10.1007/s11663-007-9099-1
[57] A. Fallah-Mehrjardi, P. C. Hayes, E. Jak: Metall. Trans. B 44B (2013) 534-548
[58] A. Fallah-Mehrjardi, P. C. Hayes, E. Jak: Metall. Mater. B 44B (2013) 1337-1351
[59] A. Fallah-Mehrjardi, P. C. Hayes, E. Jak: JOM 66 (2014) 1654-1663, doi: 10.1007/s11837-014-1127-4
[60] A. Fallah-Mehrjardi: PhD Thesis, University of Queensland, Australia (2013)
[61] S. Nicol: Bachelor Thesis, University of Queensland, Australia (2011)
[62] J. Scheiwe: Bachelor thesis, University of Queensland, Australia (2012)
[63] A. Fallah-Mehrjardi, J. Jansson, P. Taskinen, P. C. Hayes, E. Jak: Metall. Mater. Trans. B 45B (2014) 864-874
[64] A. Fallah-Mehrjardi, P. C. Hayes, S. Vervynckt, E. Jak: Metall. Mater. Trans. B 45 (2014) 850-863, doi: 10.1007/s11663-014-0074-3
[65] J. Jansson, P. Taskinen, M. Kaskiala: Can. Met. Quart. 53 (2014) 11-16
[66] J. Jansson, P. Taskinen, M. Kaskiala: Can. Met. Quart. 53 (2014) 1-10
[67] E. Haccuria, T. Crivits, P. C. Hayes, E. Jak: J. Am. Ceram. Soc. Online (2015), doi: 10.1111/jace.13991
[68] E. Jak, P. C. Hayes, H.-G. Lee: Met. Mater. Int. 1 (1995) 1-8
[69] S. Chen, E. Jak, P. C. Hayes: ISIJ Int. 45 (2005) 791-797
[70] N. L. Bowen, O. Andersen: Am. J. Sci. 37 (1914) 487-500
[71] N. L. Bowen, J. F. Schairer: Am. J. Sci. 29 (1935) 151-217
[72] B. Zhao, P. C. Hayes, E. Jak: Metall. Mater. B 42B (2011) 490-499
[73] A. Muan, E. F. Osborn: J. Am. Ceram. Soc. 39 (1956) 121-140
[74] R. W. Ruddle, B. Taylor, A. P. Bates: Trans. Inst. Min. Metall. 75C (1966) 1-12
[75] T. Oishi, M. Kamuo, K. Ono, J. Moriyama: Metall. Mater. Trans. B 14B (1983) 101-104
[76] S. Nikolic, P. C. Hayes, E. Jak: Metall. Mater. Trans. B 40B (2009) 892-899
[77] T. Hidayat, H. M. Henao, P. C. Hayes, E. Jak: Metall. Mater. Trans. B 43B (2012) 1290-1299, doi: 10.1007/s11663-012-9735-2
[78] T. Hidayat, H. M. Henao, P. C. Hayes, E. Jak: Metall. Mater. Trans. B 43B (2012) 1034-1045
[79] T. Hidayat, E. Jak, in: "A Thermodynamic Optimization of "Cu2O"-Containing Slags systems" Ninth International Conference on Molten Slags, Fluxes and Salts (MOLTEN12) (2012), CSM, Beijing
[80] E. Jak, in: "Integrated experimental and thermodynamic modelling research methodology for metallurgical slags with examples in the copper production field" Ninth International Conference on Molten Slags, Fluxes and Salts (MOLTEN12) (2012), CSM, Beijing
[81] J. Goldstein, D. Newbury, D. Joy, C. Lyman, P. Echlin, E. Lifshin, L. Sawyer, J. Michael: Scanning Electron Microscopy and X-Ray Microanalysis, Kluwer Academic/Plenum Publishers, New York (2003)
[82] H. Jalkanen, J. Vehviläinen, J. Poijärvi: Scand. J. Metall. 32 (2003) 65-70
[83] T. Crivits, P. C. Hayes, E. Jak: Int. J. Mater. Res. 106 (2015) 454-463, doi: 10.3139/146.111201
[84] T. Crivits, P. C. Hayes, E. Jak, in: "Solubility of MgO in high Cu2O slags in equilibrium with Cu metal" COM2014 (2014), CIM, Montreal
[85] A. Ilyushechkin, P. C. Hayes, E. Jak: Metall. Mater. Trans. B 35B (2004) 203-215

[86] E. Jak, P. C. Hayes, in: "Phase equilibria determination in complex slag systems" VII Int. Conf. on Molten Slags, Fluxes and Salts (2004) 85-104, SAIMM, Johannesburg
[87] FactSage ver. 6.2, CRCT-Thermfact Inc. & GTT-Technologies, Montreal, Canada, 2012
[88] T. Hidayat: PhD thesis, University of Queensland, Australia (2013)
[89] S. A. Decterov, I.-H. Jung, A. D. Pelton: J. Am. Ceram. Soc. 85 (2002) 2903-2910
[90] D. Shishin, T. Hidayat, E. Jak, S. A. Decterov: CALPHAD 41 (2013) 160-179
[91] A. Fallah-Mehrjardi, P. C. Hayes, E. Jak: Met. Trans. B 45 (2014) 2040-2049, doi: 10.1007/s11663-014-0149-1
[92] J. R. Welty, C. E. Wicks, R. E. Wilson, G. L. Rorrer: Fundamentals of Momentum, Heat, and Mass Transfer, Wiley, USA (2007)
[93] R. Gardon: J. Am. Ceram. Soc. 44 (1961) 305-312, doi: 10.1111/j.1151-2916.1961.tb15914.x
[94] J. Thonstad, P. Fellner, G. M. Haarberg, J. Hives, H. Kvande, A. Sterten: Aluminium Electrolysis: Fundamentals of the Hall-Héroult Process, Aluminium-Verlag GmbH, Düsseldorf (2001)
[95] J. J. J. Chen, C. C. Wei, S. Thomson, B. J. Welch, M. P. Taylor, in: Mannweiler, U. (Eds.), "A study of cell ledge heat transfer using an analogue ice-water model." Light Met. (1994) 285-293, TMS, Warrendale
[96] W. S. Rasbane, ImageJ, U.S. National Institutes of Health, Bethesda, Maryland, USA, 1997-2015, http://imagej.nih.gov/ij/
[97] M. R. Conde-Petit: Aqeous solutions of lithium and calcium chlorides: property formulations for use in air conditioning equipment design, M. Conde Engineering, Zurich, Switzerland (2014)
[98] D. Chemical: Calcium chloride handbook: a guide to properties, forms, storage and handling, Midland, MI (2002)
[99] T. Crivits, P. C. Hayes, E. Jak: Int. J. Mater. Res. 106 (2015) 587-599, doi: 10.3139/146.111234
[100] Campfort.M, C. Verscheure, E. Boydens, T. Van Rompaey, B. Blanpain, P. Wollants: Metall. Mater. Trans. B 39B (2008) 408-417
[101] M. Campforts, K. Verscheure, F. Verhaeghe, T. Van Rompaey, E. Boydens, B. Blanpain, P. Wollants, in: Kongoli, F. and Reddy, R. G. (Eds.), "Slag Solidification with Water-Cooled Probe Technique" Adv. Process. Met. Mater., Sohn Int. Symp. (2006) 309-321, TMS, Warrendale
[102] T. Crivits, P. C. Hayes, E. Jak, in: "Investigation of freeze linings in magnesia-containing copper slags" COM 2015 (2015), CIM, Montreal
[103] P. T. Tsilingiris: Energ. Convers. Manag. 49 (2008) 1098-1110, doi: 10.1016/j.enconman.2007.09.015
[104] A. Kondratiev, E. Jak: Metall. Mater. Trans. B 32B (2001) 1015-1025
[105] A. Muan, E. F. Osborn: Phase Equilibria among Oxides in Steelmaking, Addison-Wesley Pub. Co., Massachusetts (1965)
[106] E. T. Turkdogan: Physical Chemistry of High Temperature Technology, Academic Press, Inc., London (1980)
[107] T. Crivits: Master Thesis, Ghent University, Belgium (2012)
[108] C. Remy, D. Andrault, M. Madon: J. Am. Ceram. Soc. 80 (1997) 851-60
[109] V. Zalar Serjun, B. Mirtic, A. Mladenovic: Materiali in Tehnologije 47 (2013) 543-550
[110] L. M. Juckes: Trans. Instn Min. Metall. (Sect. C: Mineral Process. Extr. Metall.) 113 (2002) 120-128, doi: 10.1179/037195502766647039
[111] V. D. Eisenhuttenleute: Schlackenatlas/Slag Atlas, Verlag Stahleisen M.B.H., Dusseldorf, Germany (1981)
[112] Y. Kang, K. Morita: ISIJ Int. 46 (2006) 420-426
[113] R. Eriksson, S. Seetharaman: Metall. Mater. Trans. B 35 (2004) 461-469, doi: 10.1007/s11663-004-0047-z
[114] H. Hasegawa, Y. Hoshino, T. Kasamoto, Y. Akaida, T. Kowatari, Y. Shiroki, H. Shibata, H. Ohta, Y. Waseda: Metall. Mater. Trans. B 43B (2012) 1405-1412, doi: 0.1007/s11663-012-9702-y

[115] B. A. Errington, Philip

Wang, Jikun

Dong, Ying, in: "The ISA-YMG lead smelting process" PbZn Conference (2005), Xstrata technology,
[116] M. E. Glicksman, S. R. Coriell, G. B. McFadden: Ann. Rev. Fluid. Mech. 18 (1986) 307-335
[117] D. A. Porter, K. E. Easterling, M. Y. Sherif: Phase transformations in metals and alloys, CRC Press, Boca Raton, USA (2008)
[118] P. Echlin: Low-Temperature Microscopy and Analysis, Springer Science + Business Media, New York (1992), doi: 10.1007/978-1-4899-2302-8
[119] P. Echlin: Handbook of Sample Preparation for Scanning Electron Microscopy and X-ray Microanalysis, Springer Science + Business media, New York (2009), doi: 10.1007/978-0-387-85730-2
[120] F. Habashi: Handbook of Extractive Metallurgy, Volume II: Primary Metals, Secondary Metals and Light Metals, Wiley-VCH, (1997)
[121] J. R. W. Hall, B.F., R. H. Stokes: J. Am. Chem. Soc. 75 (1952) 1556-1560

Appendix A. Microstructure and composition analysis of cold modelling experiments

The following Appendix describes in detail the techniques attempted and the methodology followed for the determination of the microstructure and the composition of the $CaCl_2$-H_2O freeze linings (Chapter 6):

To analyse the differences between the observed layers in the freeze linings, several techniques were utilized. Ideally, a technique should be able to determine the following:

1) Microstructure throughout the freeze lining
2) Composition of the phases

For high-temperature experiments, such an ideal technique is found in the EPMA-SEM analysis. The room temperature experiments, however, pose several challenges regarding the collection and preparation of samples, and regarding the analysis itself:

1) dissolution in water
2) (de)hydration
3) low melting point (down to 30 °C for $CaCl_2.6H_2O$)
4) difficulties in removing samples from experimental set-up

As a result, while in the high temperature experiments obtaining in-situ measurements is an issue, in the room temperature experiments it is the post-experimental analysis that has proven to be problematic.

A.1 Collection of samples

It was found that the attachment of the freeze lining to the copper cooling block and the acrylic tank was too strong to take the freeze lining out as a whole. Samples were taken by emptying the acrylic tank of the liquid solution and shattering the freeze lining. Shattered pieces of each layer were collected and were later broken further until their size was suitable for the respective analysis technique.

It was found that the initially formed grey layer and the white layer (Chapter 6) interlocked with each other. As a result, no separate pieces of the initially formed grey layer were taken, while samples of the white layer were taken from either behind the cooling block or from experiments where no initially

formed grey layer was present. Separation of the grey layer present at steady state and the other layers was generally no issue.

All samples were stored in sealed plastic satchels or cups. Between handling, samples were stored in a freezer at -20 °C to prevent melting and/or hydration. For transport, samples were moved in a container containing $CaCl_2$ to create a dry atmosphere.

A.2 Cryo-SEM

Methodology

Standard SEM measurements are not achievable on the $CaCl_2$-H_2O samples for the following reasons: hydration and melting of the samples prevents polishing – even dry polishing, as samples take up water from the atmosphere and friction would increase temperatures above the melting point; melting of the samples due to interactions with the electron beam would result in destruction of the microstructure and; evaporation of Cl_2 could create a corrosive atmosphere in the electron microscope.

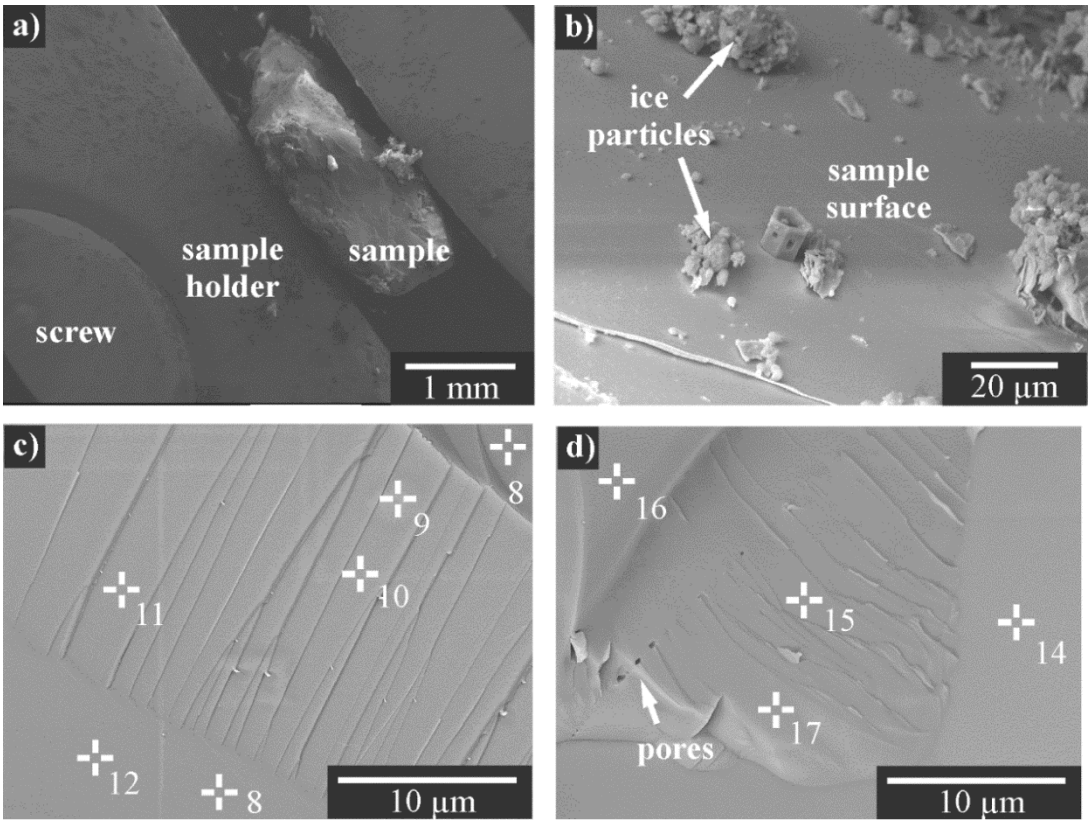

Figure A-1: Cryo-SEM BSE images of (a) sample clamped in sample holder, (b) surface contamination of non-fractured sample in the grey (α) layer, (c) fracture surface of grey (α) layer sample (day 2), (d) fracture surface of grey layer sample (day 2)

To circumvent these issues, it was decided to perform cryo-SEM instead. Cryo-SEM uses liquid nitrogen (-195 °C) to freeze and/or stabilize samples, but retains the advantages of standard SEM such as high resolution, large depth of field and the availability of X-ray microanalysis, and is thus particularly suited for samples containing water [118, 119].

Samples were transported to the Centre for Microscopy and Microanalysis (CMM) and immediately transferred to a cryogenic storage Dewar flask for storage until required. Samples submerged in liquid nitrogen were then cleaved to obtain suitable sizes for SEM analysis. Samples were clamped on a Gatan 118 sample holder (Figure A-1a) and transferred under high vacuum to the cooled pre-chamber (-145 °C) of the Gatan Alto 2500 cryo-preparation and coating station. Samples were then fractured using a Gatan rotary knife to obtain a clean, uncontaminated fracture surface –Figure A-1b and Figure A-1c,d respectively show a contaminated surface and an uncontaminated fracture surface – and then sputter-coated with Pt twice for 120s at 10 mA. Coated samples were then transferred to the SEM chamber for imaging and x-ray analysis.

In the Alto 2500 prep-chamber and the SEM chamber, samples were maintained at circa -145 °C by heating and the respective anti-contaminators were maintained at circa -185 °C by regulated gas flow. This temperature difference ensured that contaminants from the sample were trapped effectively on the anti-contaminators.

Secondary electron (SE) and backscattered electron (BSE) imaging was undertaken using a JEOL Model JSM-7100F SEM system, with an accelerating voltage of 10 kV and probe current of 1.13 nA. The SEM chamber vacuum was maintained at 9.6E-5 Pa (or better – but not indicated).

Energy-dispersive spectroscopy (EDS) analysis was carried out using a JEOL silicon drift detector (Model EX-94300S4L1Q), in combination with an energy-dispersive spectrometer, at 129 eV resolution; silicon drift diode, 10 mm^2 effective area, ultrathin window (UTW) using JEOL Analysis Station JED-2300 Series (v. 3.84) standard software. Microanalysis acquisition conditions were typically 10 keV, 10 mm working distance and 60s live time acquisition with count rates of circa 900 CPS. The low count rates were a result of the small probe current required to reduce specimen charging, which could otherwise compromise the accuracy of the microanalysis.

Results

Two different samples were analysed: The first one originated from the white layer in the cold experiments, and was assumed to consist of two solid phases ($CaCl_2.6H_2O$, β, and $CaCl_2.4H_2O$, α),

and the second originated from the grey layer formed after heating and subsequent cooling of the bath, assumed to consist of a single solid phase ($CaCl_2.4H_2O$).

The fracture surfaces of both samples were similar morphologically. A small difference in porosity can be noted, with samples from the grey (α) layer (Figure A-1) containing a negligible number of pores, while small pockets of porous areas are present in samples from the white (α + β) layer (Figure A-2).

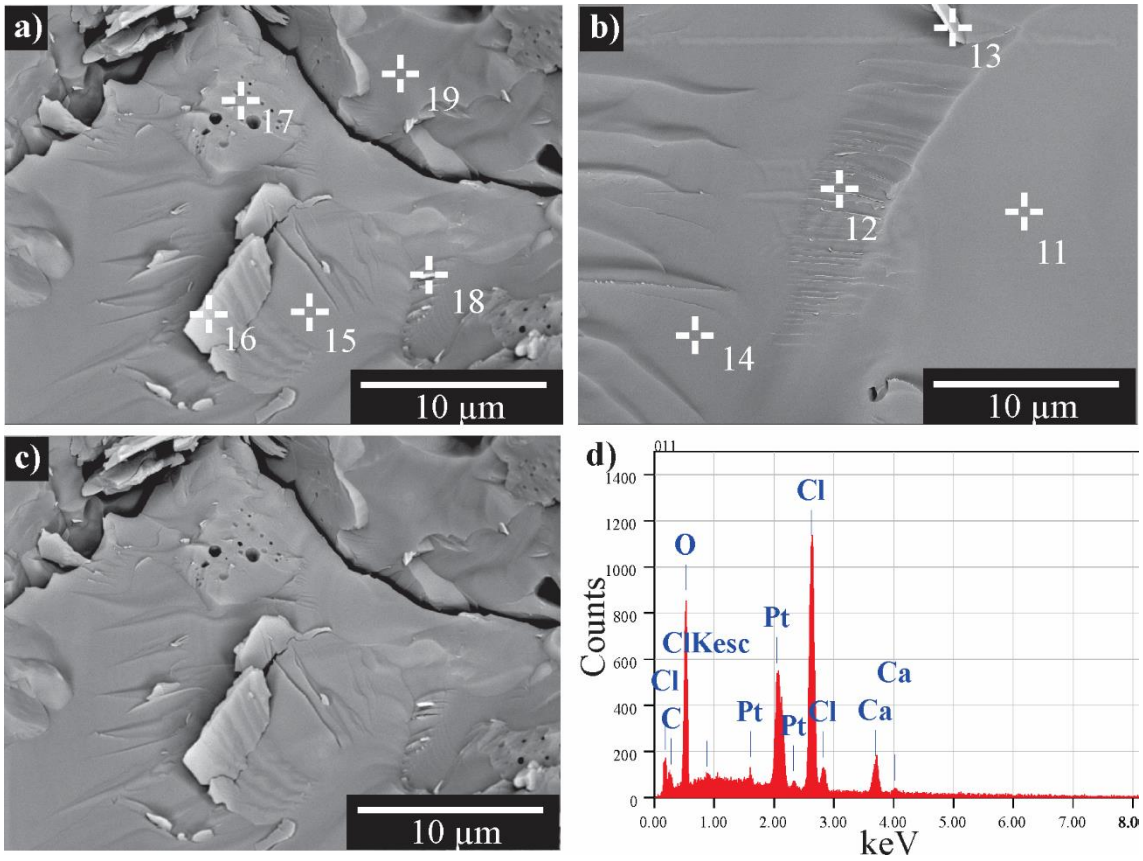

Figure A-2: Cryo-SEM BSE images of day 1 (a) white (α + β) layer, before measurement, (b) white (α + β) layer before measurement, (c) white (α + β) layer after measurement and (d) Example of typical measured counts profile for EDS measurement

Figure A-2a and b show two areas of measurement in samples taken from the white layer of the freeze lining. Figure A-2c shows the area of Figure A-2a after measurement. It can be seen that minimal beam damage was inflicted at the measurement positions. Figure A-2d shows an example of a counts profile obtained by EDS-measurements. The measured elements were O, Cl and Ca, originating from the $CaCl_2$ hydrates, Pt from the platinum coating and C. The presence of C is considered to be related to possible hydrocarbon contamination in the system.

Table A-1 shows the measured compositions in the samples. Platinum and carbon originated from the measurements method and have not been reported, and hydrogen was not measured. Weight percentages of oxygen, chlorine and calcium have been normalized such that their sum equals 100%.

Measurements with a count rate of less than 600 counts per seconds were omitted from the results as these were not regarded as trustworthy.

Table A-1: Measured compositions in $CaCl_2$-H_2O samples. Reported values were normalized such that wt.% O + wt.% Cl + wt.% Ca = 100.

	wt.% O	wt.% Cl	wt.% Ca	O/Cl
Compounds				
$CaCl_2.4H_2O$	36.6	40.5	22.9	0.90
$CaCl_2.6H_2O$	46.3	34.3	19.4	1.35
Measurements				
Day 1, white				
1	34.1	48.6	12.3	0.70
2	27.9	49.2	17.9	0.57
3	39.0	41.0	15.0	0.95
4	43.9	36.2	14.9	1.21
5	43.5	37.7	13.8	1.15
6	30.0	48.4	16.7	0.62
7	39.3	39.4	16.3	1.00
8	39.4	39.0	16.6	1.01
9	37.4	38.5	19.1	0.97
10	38.7	40.5	15.8	0.96
11	37.8	45.6	11.6	0.83
12	49.5	33.9	11.7	1.46
13	44.1	38.8	12.1	1.14
14	40.9	43.8	10.2	0.93
15	41.5	43.3	10.3	0.96
16	53.7	28.3	13.0	1.90
17	38.7	41.4	14.8	0.93
18	52.9	29.7	12.4	1.78
Day 1, grey				
7	72.0	15.6	7.4	4.60
8	46.1	32.8	16.1	1.41

	wt.% O	wt.% Cl	wt.% Ca	O/Cl
9	44.6	34.5	15.9	1.29
10	47.2	32.7	15.1	1.45
Day 2, grey				
1	27.5	51.3	16.2	0.54
2	26.7	53.2	15.1	0.50
3	31.3	46.9	16.8	0.67
4	39.1	40.3	15.6	0.97
5	28.9	51.2	14.9	0.56
6	32.1	48.5	14.3	0.66
7	40.5	39.7	14.8	1.02
8	30.4	51.2	13.4	0.59
9	6.9	71.9	16.2	0.10
10	6.9	72.0	16.1	0.10
11	8.6	72.2	14.2	0.12
12	18.8	60.7	15.4	0.31
13	18.3	60.7	15.9	0.30
14	33.5	49.1	12.3	0.68
15	31.1	50.4	13.5	0.62
16	28.1	53.3	13.6	0.53
17	27.9	53.5	13.6	0.52

From Table A-1, it is clear that the weight percentages of calcium are lower than would be expected from the composition of the present compounds in the $CaCl_2$-H_2O system. To allow for comparison between measurements, it was decided to compare the wt.%O/wt.%Cl ratio. This ratio is 0.90 and 1.35 for $CaCl_2.4H_2O$ and $CaCl_2.6H_2O$ respectively. As these are the only solid compounds present at equilibrium for a bulk composition of 52 wt.%, it was expected that the measured ratios would be in between these two values.

On day 2, most O/Cl ratios were well below 0.90, indicating a dehydrated sample. On day 1, the samples taken from the white layer showed a range of O/Cl ratios from 0.57 to 1.90, once again ranging far beyond the expected range. Measurement 7 was positioned on one of the ice particles shown on Figure A-1b, explaining the high O/Cl ratio of 4.60. The remaining O/Cl ratios for the

samples taken from the grey layer and analysed on day 1 were approximately 1.35, close to that of the compound $CaCl_2.6H_2O$, while this layer was assumed to consist of $CaCl_2.4H_2O$. This was not thought to be representative of the actual composition, but was attributed to uncertainties in the measurement method.

The scatter on the Table A-1 results is quite large for two reasons: (1) (de)hydration of the samples – during sample collection and sample preparation – changes the O/Cl ratio; and (2) differences in coating thickness, surface angle, surface thickness at the position of measurement, … influence the actual measurement and cause a scatter inherent to the measurement method.

It is thus concluded that the composition range of interest is too small to obtain robust quantitative results using cryo-SEM. The use of cryo-SEM may prove useful in future investigations of salt systems where the range of compositions of interest is larger and/or (de)hydration of samples is less likely to occur.

A.3 Analysis by weight loss on heating

The melting points of $CaCl_2$ and its hydrates are 772, 260, 175, 45.5 and 30 °C for $CaCl_2$, $CaCl_2.H_2O$, $CaCl_2.2H_2O$, $CaCl_2.4H_2O$ and $CaCl_2.6H_2O$ respectively. Heating up the obtained hydrate samples to temperatures between 260 and 772 °C thus results in the complete dehydration of $CaCl_2$. By calculating the weight loss on heating, the concentration of $CaCl_2$ and H_2O can be determined.

Methodology

Cylindrical, high-density MgO crucibles (2.5 cm ID, 6.1 cm height) were heated to 400 °C in air using a muffle furnace to remove any volatile components from the crucibles. The crucibles were removed from the furnace and weighed immediately. The samples were weighed inside their plastic storage satchel. The samples (3-5 g) were subsequently removed from the satchels and placed inside the MgO crucibles, after which the satchels were weighed again. The use of the difference between initial weight (containing samples) and empty weight of the satchels prevented hydration of the samples from influencing the measured weights of the samples.

The crucibles and samples were placed inside a muffle furnace and were heated from 50 to 400 °C, increasing the temperature by 50 °C each 10 minutes. The furnace was left at the final temperature of 400 °C for 20 minutes, after which the crucibles were removed and immediately weighed. The difference between the initial weight of the crucible + sample and the final weight of crucible + sample provided the weight loss on heating.

Results

The results of the measurements can be seen in Table A-2. The wt.% of CaCl2 in the white layer is close to that of the bulk (52 wt.% $CaCl_2$), while the wt.% of $CaCl_2$ in the grey layer is close to that of the $CaCl_2.4H_2O$ compound. These results are in line with the hypothesis that the white layer consists of a mixture of $CaCl_2.4H_2O$ and $CaCl_2.6H_2O$, while the grey layer formed at steady state after heating and subsequent cooling of the bath consists of the primary $CaCl_2.4H_2O$ phase.

Table A-2: Weight loss of $CaCl_2$-H_2O samples on heating to 400 °C.

all weights in g	*wt. crucible (initial)*	*wt. sample (initial)*	*wt. crucible + sample (final)*	*wt. sample (final)*	*wt.% $CaCl_2$*
white layer	63.2281	5.0018	65.7906	2.5625	51.2
grey layer	63.2046	3.4214	65.2247	2.0201	59.0

Appendix B. Estimation of slag bath temperature as function of time

The change in bath temperature in Chapter 7 was estimated by determining the convective heat transfer coefficient (h_{bath}) at 1 h and using the determined h_{bath} to calculate the bath temperature at the end of the experiment using the following equation for steady state heat transfer through the freeze lining [16]:

$$Q_{FL} = \dot{m_{air}} \rho_{air} c_{p,air} \left(T_{air,out} - T_{air,in}\right) \quad \textbf{(B-1)}$$

$$Q_{FL} = h_{bath} A_{bath,FL} \left(T_{bath} - T_{bath,FL}\right) \quad \textbf{(B-2)}$$

Where Q_{FL} equals the heat flow through the freeze lining, $\dot{m_{air}}$ the air flow, ρ_{air} the density of the air, $c_{p,air}$ the heat capacity of the air, $A_{bath,FL}$ the surface area of the bath-freeze lining interface and $T_{air,in}$, $T_{air,out}$, T_{bath} and $T_{bath,FL}$ the temperatures at the air inlet, air outlet, the bulk bath and the bath-freeze lining interface respectively.

$T_{bath,FL}$ was estimated through extrapolation of the measured temperatures inside the freeze lining using the equation for the steady state temperature profile in cylindrical coordinates [92].

$$T(r) = T_1 + \frac{T_1 - T_2}{\ln(r_1/r_2)} ln\left(\frac{r}{r_1}\right) \quad \textbf{(B-3)}$$

Where T_1, T_2 and r_1, r_2 are the temperatures and distances from the centre of the cold probe of two points in the freeze lining. This was done considering two different scenarios (a) the thickness of the freeze lining stayed constant during the last hour of the experiment, and (b) the thickness increased by 2 mm in the last hour of the experiment. The combined uncertainty of the estimated bath temperature at the end of the experiment was estimated to be ±15 °C.

Appendix C. Detailed results of high temperature freeze lining experiments

C.1 'Cu_2O'-'Fe_2O_3'-MgO-SiO_2 experiments (Chapter 7)

Settings + measurements

FL4*: lower estimate based on temperatures measured at t = 3600 s

Table C-1: Settings + measured values in copper slag freeze lining experiments at steady state.

Exp.	T_{bath} (°C)	RPM	air flow (lpm)	depth (m)	thickness (mm)	$T_{air,in}$ (°C)	$T_{air,out}$ (°C)
FL1	1180	10	130	0.042	25	390	535
FL2	1285	0	93	0.027	24.8	353	617
FL3	1343	0	93	0.03	24	392	771
FL4	1402	0	130	0.03	13.4	533	801
FL4*	1360	0	130	0.03	13.4	488	749

Freeze lining temperatures at steady state

x_i = distance from probe (mm)

T_i = measured temperature (°C)

T_1 is never taken into account during the calculations, since this temperature was found to consistently be below the estimated profiles (see Chapter 7)

Table C-2: Measured temperatures and positions of thermocouples in copper slag freeze lining experiments at steady state.

Exp.	x_1	x_2	x_3	x_4	x_5	T_1	T_2	T_3	T_4	T_5
FL1	0	6.9	8.9	11.7	18.2	774	938	974	1014	1073
FL2	0	6.9	11.8	18.3	24.8	824	1052	1109	1171	1212
FL3	0	6.8	12.6	19.8	26.5	857	1061	1122	1174	1226
FL4	0	6.0	10.3	/	/	850	1079	1162	/	/
FL4*	0	6.0	10.3	/	/	812	1048	1138	/	/

Calculated values (using the approach outlined in Appendix D)

Note that the contact resistance between the cold probe and the freeze lining was not taken into account in the calculation of h_{air}.

Table C-3: Calculated properties of the bath and freeze lining in copper slag freeze lining experiments at steady state.

Exp.	$q_{interface}$ (kW/m²)	k (W/m.K)	h_{bath} (W/m².K)	h_{air} (W/m².K)	$Ti_{nterface}$ (°C)
FL1	31	6.6	610	895	1129
FL2	53	14.9	750	1356	1213
FL3	76	22.8	530	2250	1199
FL4	146	13.6	760	3913	1210
FL4*	141	12.1	830	3703	1190

C.2 Al_2O_3-CaO-SiO_2 experiments (Chapter 8)

Settings + measurements

Table C-4: Settings + measured values in Al_2O_3-CaO-SiO_2 slag freeze lining experiments at steady state.

Exp.	T_{bath} (°C)	RPM	air flow (lpm)	depth (m)	thickness (mm)	$T_{air,in}$ (°C)	$T_{air,out}$ (°C)
FL1	1440	0	130	0.07	8	316	586
FL2	1440	0	130	0.07	8	302	509
FL3	1440	0	130	0.07	4	304	555
FL4	1460	0	84	0.07	16	338	521
FL5	1460	0	84	0.055	18	436	586

While the depth of the freeze lining was as indicated in the table, the thermocouples measuring the temperature of the ingoing and outgoing air were positioned 6 mm up from the tip of the cooled probe. The 'height of the freeze lining', as indicated in the Matlab code in Appendix D was thus set at 6 mm, unless the depth in Table C-4 was lower than this value.

Freeze lining temperatures at steady state

T_1 and T_2 are thermocouple measurements. The remainder are temperature estimates based on the presence of solid phases or the composition (see Chapter 8).

Table C-5: Measured temperatures and positions of thermocouples in Al_2O_3-CaO-SiO_2 slag freeze lining experiments at steady state.

Exp.	x_1	x_2	x_3	x_4	x_5	x_6	T_1	T_2	T_3	T_4	T_5	T_6
FL1	2.5	8.0	8.0	6.0	5.0	3.5	1235	1394	1400	1363	1340	1248
FL2	2.0	7.0	5.0	4.2	8.0	5.0	1129	1329	1325	1248	1400	1300

FL3	3.4	10.6	3.5	2.5	4.0	/	1245	1362	1320	1248	1325	/
FL4	1.8	5.8	/	/	/	/	1034	1181	/	/	/	/
FL5	2.9	8.2	14.0	19.0	15.0	18.0	1076	1243	1293	1455	1368	1378

Calculated values (using the approach outlined in Appendix D)

Note that the contact resistance between the cold probe and the freeze lining was not taken into account in the calculation of h_{air}.

Table C-6: Calculated properties of the bath and freeze lining in Al_2O_3-CaO-SiO_2 slag freeze lining experiments at steady state.

Exp.	$q_{interface}$ (W/m^2)	k (W/m.K)	h_{bath} ($W/m^2.K$)	h_{air} ($W/m^2.K$)	$Ti_{nterface}$ (°C)
FL1	123	5.3	3439	560	1404
FL2	94	3.1	2183	459	1397
FL3	168	3.6	1681	529	1317
FL4	31	2.3	567	311	1406
FL5	24	2.2	454	330	1400

Appendix D.Determination of thermal parameters

The following MATLAB code was used to determine the thermal parameters of the freeze linings generated in the lab using high-temperature experiments.

```
%This script is used to calculate the thermal parameters of a freeze
%lining based on several (at least 2) thermocouple measurements within the
%freeze lining, the final thickness and height of the freeze lining, and
temperature of in- and outgoing air
%All input is aligned to the left, while calculations are slightly indented
clear
    %measured TC distances from probe
    r = zeros(7,1);
    r(1) = 0; %not used
r(2) = 2.9; %mm
r(3) = 8.2; %mm
r(4) = 14.0; %mm
r(5) = 15; %mm
r(6) = 18; %mm
r(7) = 19; %mm

%probe has radius of 6.35mm
    radius = 0.00635;
    r=r/1000+radius;

%Which thermocouple is last in the freeze lining?
lastTC = 7;

%height freeze lining?
z = 0.055; %m

%thickness freeze lining
thickness = 18.5/1000; %m

%bath temperature
Tbath = 1460+273.15; %K

%temperature profile
    T = zeros(7,1);
    T(1) = 0; %Temperature is not used in the calculation. Only put here to
create a certain symmetry between r and T
T(2) = 1076; %°C
T(3) = 1243; %°C
T(4) = 1293; %°C
T(5) = 1368; %°C
T(6) = 1378; %°C
T(7) = 1455;

    T = T +273.15; %K

Tin = 436+273.15; %K
Tout = 586+273.15; %K
flow = 84; %l/min

    %don't want all to calculate k, only thermocouple data in freeze lining
    rToUse = zeros (lastTC-1,1); %%
```

```
    TToUse = zeros (lastTC-1,1); %%
    for i=1:lastTC-1 %%
        rToUse(i)=r(i+1); %%
        TToUse(i)=T(i+1); %%
    end

    %initial guess
    A = -285;
    B = 1132;

    %curvefitting
    x=zeros(2,1);

    F = @(x,xdata)x(1).*log(rToUse(lastTC-2)./xdata) + x(2); %%
    x0 = [A B];
    [x, resnorm, ~, exitflag, output] = lsqcurvefit(F,x0,rToUse,TToUse);

    %%this is an alternative curvefitting method
    % Fsumsquares = @(x) sum((F(x,rToUse) - TToUse).^2);
    % opts = optimoptions('fminunc','Algorithm','quasi-newton');
    % [xunc,ressquared,eflag,outputu] = fminunc(Fsumsquares,x0,opts)

    %plotting the profile
    axis([0,thickness*100,T(2)-50,F(x,radius+thickness)+50])
    hold on
    plot((r-radius)*100,T,'ro')
    title('Temperature profile')
    xlabel('distance from probe (cm)')
    ylabel('temperature (°C)')
    hold off
    n=20;
    rPlot = zeros(n+1);
    for i=1:n+1
        rPlot(i) = radius+(i-1)*thickness/n;
    end
    hold on
    plot((rPlot-radius)*100,F(x,rPlot))
    hold off

%thermal and measured properties air
TinTop=20+273.15; %K

    a = 1.03409;
    b = -0.284887*10^(-3);
    c = 0.7816818*10^(-6);
    d = -0.4970786*10^(-9);
    e = 0.1077024*10^(-12);
    Cp = @(x)(a + b.*x + c.*x.^2 + d.*x.^3 + e.*x.^4)*28.82; %J/molK (28.82
g/mol air)
    %calculation for Q
    QperMol = quad(Cp,Tin,Tout); %J/mol

    nMol = (flow/1000)/(8.314*TinTop/101325); %mol
    Q = QperMol*nMol/60; %J/s

    %calculate k
    % first step: q at probe-FL interface
    % probe is modeled as cylinder with one closed end (bottom)
    q1 = Q/(pi*z*2*radius+ radius^2*pi); %W/m^2
```

```
    ThermalConductivity = fsolve(@(k)q1*radius/k+x(1),2)

    %estimate interface temperature
    rinterface = thickness+radius; %m
    InterfaceTemperature = F(x,rinterface)-273 %°C

    %calculate hbath
    %freeze lining is modeled as cylinder + half sphere
    Ainterface = (z-radius)*(rinterface)*2*pi+2*pi*rinterface^2;  %m^2 (surface
area cylinder + surface area half sphere)
    hbath = Q/(Ainterface*(Tbath-InterfaceTemperature-273.15))  %W/m^2.K

    %calculate heat flow per interface surface area
    heat_flow_per_interface_area = Q/Ainterface

    %calculate hair
    rinside = radius-0.001; %m
    %probe is modeled as cylinder with one closed end (bottom)
    Ainsideprobe = z*rinside*2*pi +pi*rinside^2; %m^2
 ksteel = 16; %W/m.K
    Tinside = F(x,radius) + Q/(ksteel*2*pi*z)*log(rinside/radius)-273; %C
    %taken average air temperauter
    Tair = (Tin+Tout)/2-273; %C
    hair = Q/(Ainsideprobe*(Tinside-Tair)) %W/m^2.K
```

Appendix E. Development of a numerical model for mass transfer controlled freeze lining growth under quasi steady-state conditions

E.1 Introduction

In section 9.3.2, it was proposed that the growth rate plays an important role in the resulting steady state bath-freeze lining interface temperature. Under the assumption that the proposed conceptual framework is correct, the relative importance of the effect of process parameters on the steady state interface temperatures can be estimated by calculating the effects of these parameters on the growth rates of freeze linings.

Early mathematical modelling of freeze linings involved thermal models assuming a planar interface at the liquidus temperature to calculate freeze lining growth and steady state thickness [5, 16, 22]. Later models incorporated equilibrium solidification, resulting in an interface temperature equal to the solidus temperature [45] or the liquidus temperature [12]. Solheim [49] modelled the interface temperature as function of freeze lining growth in aluminium reduction cells through coupling of heat and mass transfer, finding a slower change in freeze lining thickness over time than predicted through heat transfer models. The steady state interface temperature was not predicted in this latter model.

The current model includes the possible formation of detached crystals in a subliquidus boundary layer ahead of the deposit. The model uses the finite difference method, combined with well-established heat and mass transfer equations and solidification kinetics [92, 117] to calculate freeze lining growth under quasi-steady state conditions for the heat transfer and fluid flow.

E.2 Detached crystals conceptual framework

Fallah-Mehrjardi et al. [51, 57, 58] observed steady state bath-freeze lining interface temperatures between solidus and liquidus under certain conditions. A conceptual framework, describing a dynamic steady state was proposed (Figure E-1): "*As a result of natural and forced convection, fresh portions of liquid move from the bulk bath toward the freeze lining with the temperature decreasing from the bath temperature T_{bath} to the liquidus temperature T_{liq} without crystallization. As the liquid crosses the point with T_{liq} and its temperature decreases below T_{liq}, nucleation and precipitation of*

the primary phase starts. As a result, the composition of the remaining liquid also changes. If the movement of the portion of liquid with the primary phase crystals toward the interface is slow compared to the crystallization rate, then the local equilibrium between the precipitated crystals and the surrounding liquid is maintained during this passage across the 'subliquidus boundary layer'."

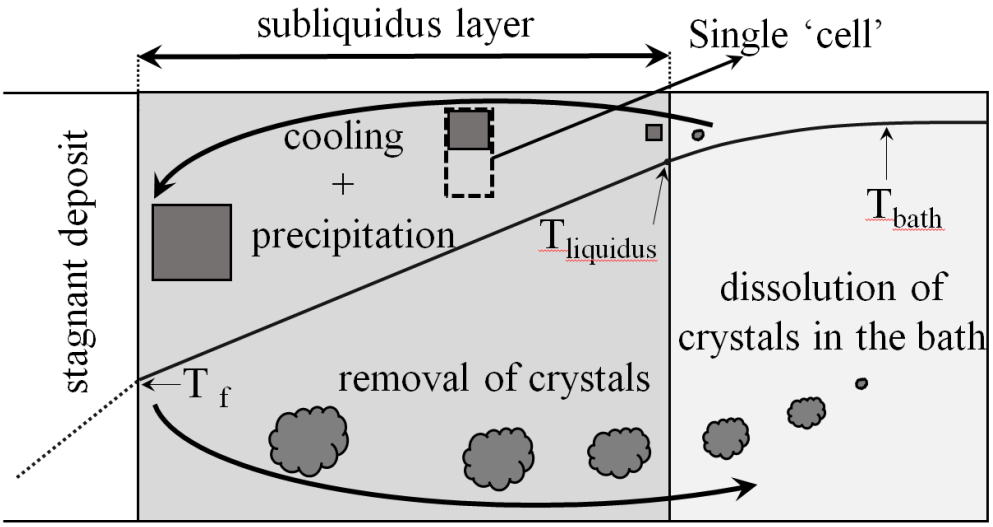

Figure E-1: Schematic representation of the dynamic steady state framework for freeze linings proposed by Mehrjardi et al. [51].

In the earlier mentioned mathematical models, the interface temperature is either assumed or a direct result of the assumptions. As a result, these models can not be used to predict the interface temperature and resulting thickness of and heat flux through the freeze lining. Additionally, the formation of detached crystals in the subliquidus layers hasn't been modelled in earlier studies.

Firstly, this paper will determine those situations in which heat transfer models can be used to predict freeze lining growth. This is done through comparison of modelled freeze lining growth to results obtained through cold modelling using a $CaCl_2$-H_2O solution (Chapter 6).

Additionally, a new, mass transfer controlled freeze lining growth model was developed, including the dynamic steady state proposed in the conceptual framework (Figure E-1). Using this model, it is possible to determine the relative importance of several process and slag parameters on freeze lining growth and the steady state interface temperature.

E.3 Heat transfer controlled freeze lining growth

A cold modelling experiment (set-up and methodology can be found in Chapter 6) was performed using a 52 wt.% $CaCl_2$ in H_2O solution. The measured thickness of the freeze lining was compared to the freeze lining growth predicted by a finite difference, heat transfer controlled freeze lining

growth model, based on the equations given by Verscheure et al. [16] and coded in MATLAB R2013a.

The thermal conductivity of the freeze lining was determined through equation **(E-1)** [16], using measurements from an earlier experiment at steady state

$$Q_{FL} = \dot{m}_{water} c_{p,water} \left(T_{water,out} - T_{water,in}\right) = A.h_{bath}.\left(T_{bath} - T_{bath,FL}\right) = \frac{A.\left(T_{bath,FL} - T_{water}\right)}{\Delta x_{FL}/k_{FL}} \quad \textbf{(E-1)}$$

Where Q_{FL} is the rate of heat transfer through the freeze lining, $\dot{m}_{water}$ the water flow rate, $c_{p,water}$ the heat capacity of the water, $T_{water,out}$ and $T_{water,in}$ the outlet and inlet temperature of the water, A the surface area of the freeze lining, h_{bath} the convective heat transfer coefficient of the bath, T_{bath} the bath temperature, $T_{bath,FL}$ the bath-freeze lining interface temperature, T_{water} the average water temperature, Δx_{FL} the thickness of the freeze lining and k_{FL} the thermal conductivity of the freeze lining.

These measured and calculated parameters can be found in Table E-1.

Table E-1: Measured and calculated parameters for determination of the thermal conductivity of the freeze lining.

$\dot{m}_{water}$ (l/s)	1.8E-3 (measured)
$T_{water,in}$ (°C)	15.9 (measured)
$T_{water,out}$ (°C)	17.5 (measured)
Δx_{FL} (mm)	7 (measured)
T_{bath} (°C)	40 (measured)
$T_{interface}$ (°C)	31 (measured)
A (m^2)	52E-4 (experimental set-up)
Q (W)	12.2 (calculated)
k_{FL} (W/m.K)	1.23 (calculated)

Likewise, the convective heat transfer coefficient of the bath, h_{bath}, was calculated through equation **(E-1)** using the experimentally determined steady state freeze lining thickness.

Table E-2: Properties used in thermal freeze lining growth model.

Heat capacity of freeze lining ($c_{p,FL}$)	1411 [120]
Latent heat of solution (L)	203014 [120]
Density of freeze lining (ρ_{FL})	1726 [120]
Density of solution (ρ_{bath})	1550 [97]

Two different calculations were performed using the thermal model. The first assumes a constant interface temperature equalling the liquidus temperature (35.5 °C). In the second calculation, the interface temperature was taken equal to the measured interface temperature during the first 5000 seconds of the experiment, which was found to be constant. After this, the interface temperature was taken equal to the liquidus temperature again. The results of these calculations are shown in Figure E-2, together with the measured freeze lining thickness and interface temperature.

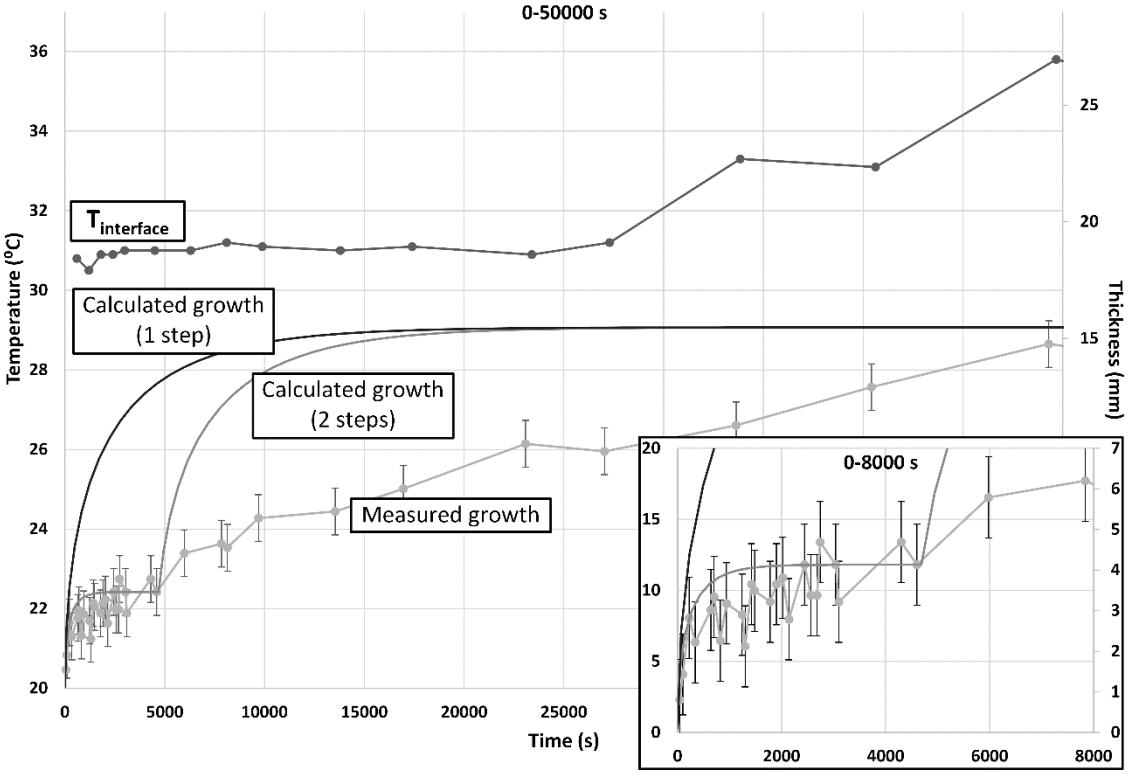

Figure E-2: Measured and calculated thickness of the freeze lining and measured bath-freeze lining interface temperature.

It can be seen that the calculations assuming an interface temperature equalling the liquidus temperature largely overestimate the growth rate of the freeze lining. The results of the initial calculation (up to 5000 s) using an interface temperature of 31 °C, however, are within uncertainty

of the measured data points. This indicates that the initial freeze lining growth was heat transfer controlled, while further growth is controlled by different phenomena.

The same conclusion can be made based on the evolution of the interface temperature. Initially, this interface temperature stays constant at 31 °C, indicating heat transfer controlled growth. When the freeze lining grows further, the interface temperature gradually increases until, within uncertainty of ±1 °C, it reaches the 35 °C liquidus temperature[1] associated with the precipitation of $CaCl_2.4H_2O$ (see Chapter 6). It can thus be concluded that only the initial freeze lining growth is heat transfer controlled.

The only freeze lining growth model including mass transfer reported in the literature to date is that of Solheim et al. [49]. This model, however, can not be used to determine the effect of the detached crystals present in the conceptual framework proposed by Fallah-Mehrjardi et al. [51]. In the next part of this paper, a numerical model for mass transfer controlled freeze lining growth is constructed, including the presence of detached crystals. This model will then be used to calculate the effect of process parameters on mass transfer controlled freeze lining growth and on the steady state bath-freeze lining interface temperature.

E.4 Development of the model

Model geometry

Physically accurate modelling of the proposed dynamic steady state would require modelling nucleation, crystal growth, heat transfer, mass transfer and fluid flow simultaneously. As this was considered out of scope for the current research, a simplified model is proposed.

Considering a single ‘cell’ (Figure E-1) of a detached crystal with adjacent liquid, its growth and trajectory from the bulk bath through the subliquidus layer towards the freeze lining is schematically represented in Figure E-3.

[1] The time lag between the increase in thickness and the increase in interface temperature is due to the uneven growth of the freeze lining (chapter 6). It was observed that as soon as the freeze lining grows locally, the local interface temperature increases.

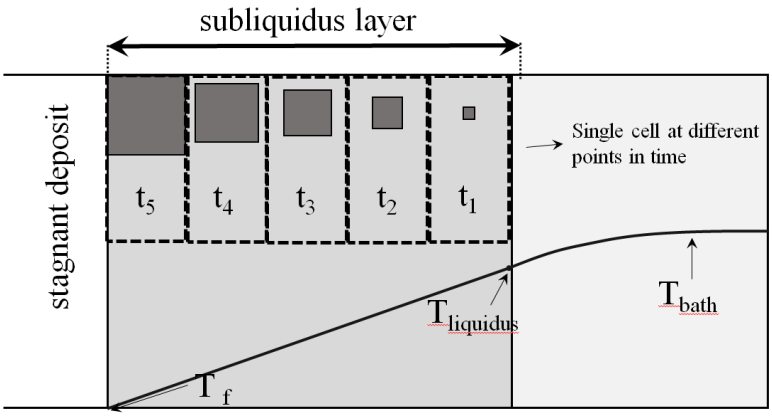

Figure E-3: Schematic representation of single cell moving towards the stagnant deposit

Assuming nucleation is fast, the liquid in the cell always contains a solid crystal. As the crystal is growing, mass diffusion will take place in the liquid, perpendicular to the movement of the cell, in the direction of the solid crystal. Mass transport towards the freeze lining can take place both in the form of mass diffusion and convection.

Assuming that at each point in time, and at all points distant from the interface, detached crystals are present, the system can be modelled as a slab of the precipitating solid at the upper boundary. The other boundaries consist of the stagnant deposit (freeze lining), the bath and a completely isolated/symmetrical boundary. In each cell of the grid, the temperature and the concentration of one of the solutes are calculated using a finite difference method for heat and mass transfer and assuming steady state.

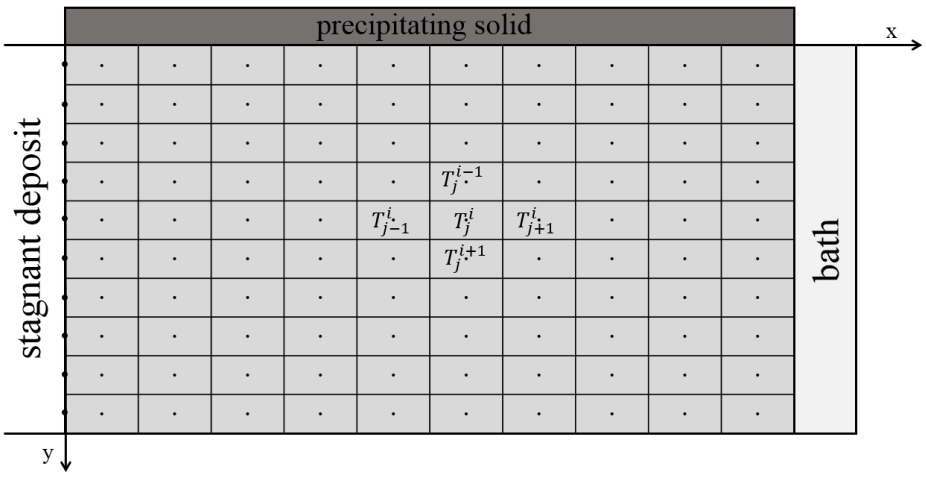

Figure E-4: Schematic representation of the model geometry.

The boundary conditions are thus:

Table E-3: Boundary conditions.

Boundary	Mass transfer boundary condition	Heat transfer boundary condition
Stagnant deposit	Reaction with solid	Constant temperature
Precipitating solid	Reaction with solid	Reaction with solid
Bath	Constant concentration	Constant temperature
Isolated wall	No mass transfer	No heat transfer

The solidification rate was calculated based on solidification under continuous growth conditions (equation **(E-2)** [117]). Although in reality, oxides may grow through spiral growth or surface nucleation (equations **(E-3)** and **(E-4)** [117]), the corresponding equations would result in a non-linear set of equations, requiring a more sophisticated solution method:

$$\text{Continuous growth: } G = R.\Delta T_{undercooling} \quad \textbf{(E-2)}$$

$$\text{Spiral growth: } G = R.\left(\Delta T_{undercooling}\right)^2 \quad \textbf{(E-3)}$$

$$\text{Surface nucleation: } G \sim \exp\left(-\frac{R}{\Delta T_{undercooling}}\right) \quad \textbf{(E-4)}$$

At this stage of the research, mass diffusivity (D), heat capacity (c_p), latent heat (L), density (ρ) and growth rate constant R were chosen constant while liquidus temperature was chosen to depend linearly on the concentration of the liquid.

The velocity of the liquid in the x-direction was chosen as depending linearly on the distance from the stagnant freeze lining deposit with a velocity of 0 at the bath-freeze lining interface and v_{bath} at the position of the bath/subliquidus boundary layer interface.

Solving method

MATLAB R2013a was used to code the finite difference method for this particular problem. To avoid dissolution of the solid slab at temperatures above the liquidus temperature, the set of equations was iterated several times. In the first iteration, dissolution of the solid slab was allowed. In the subsequent iterations, the growth rate constant R was set to zero in each grid cell where the temperature calculated in the first iteration was above the liquidus, preventing interaction between solid slab and liquid in these cells. The resulting effect on calculated temperatures due to the release of heat during solidification was found negligible.

On the freeze lining growth rate

It was found that the freeze lining growth calculated by the model never equals zero. This seemingly contradicts the observation of the existence of a dynamic steady state where freeze lining growth equals zero. The following possible explanations are proposed:

1) At the interface, local fluctuations in temperature and concentration caused by turbulent eddies result in local dissolution and local growth of the freeze lining, eventually cancelling each other out and resulting in a macroscopic steady state.

2) Local phenomena at the interface, similar to the detachment of dendrite arms during casting, occur. Freeze lining stops growing once the growth rate equals the wear rate due to these phenomena.

3) Physical wear of the freeze lining is taking place, eventually cancelling out freeze lining growth and resulting in steady state.

None of these proposed mechanisms has been incorporated in the current model. In order to estimate the effect of parameters on the steady state interface temperature, an arbitrary cut-off value of 1 mm/day (1.16E-8 m/s) was taken for the freeze lining growth rate and interface temperatures were determined such that the calculated growth rate equalled this cut-off value.

E.5 Verification of model

To verify the model, a cold experiment was performed where the evolution of the interface temperature with time was more accurately measured than in the experiment shown in Figure E-2. Figure E-5 shows the measured thickness and interface temperature for the part of this experiment where the interface temperature rose from 29.9 °C (the solidus temperature) to approximately 34.4 °C (the liquidus temperature). The thickness of the freeze lining at the start of this particular segment of the experiment was found to be 0.667 cm. The complete experiment has been described in Chapter 6.

A rational trend line was fitted to the measured deposit interface temperatures. The maximum value of this trend line was set equal to the liquidus temperature. Any predicted temperatures above this value were manually decreased to the liquidus temperature. The resulting fit can be seen in Figure E-5.

The input values for the model were taken from the following sources: eutectic concentration ($C_{eutectic}$), latent heat (H), thermal conductivity (k), solidus temperature ($T_{solidus}$) and liquidus temperature for a solution of 52 wt.% $CaCl_2$ in water (7093 mol/m^3) were taken from [98] and [97]. No values for the mass diffusivity at this concentration were found in literature. Hence, the mass diffusivity at a concentration of 3530 mol/m^3 reported by Hall et al. [121] was used. Boundary layer thickness (L), bath temperature (T_{bath}), concentration in the bath (C_{bath}) and velocity of the liquid were taken from the experimental settings. As no detached crystals were observed in the bath, the distance between detached crystals (W) was chosen high enough to make its influence negligible. The growth rate constant was chosen high such that mass transfer controlled growth was obtained.

Table E-4: Input parameters of numerical model for verification of the model using a 52 wt.% $CaCl_2$ in H_2O solution.

W (m)	L (m)	$T_{interface}$ (°C)	v_{bath} (m/s)	D (m^2/s)	R (mol/K.m^2.s)	H_{latent} (J/mol.K)
5	0.05	variable	0.00074	1.192E-9	1	21000
k (W/m.K)	**$T_{solidus}$ (°C)**	**$T_{liquidus}$ (°C)**	**$C_{eutectic}$ (mol/m^3)**	**T_{bath} (°C)**	**C_{bath} (mol/m^3)**	
0.56	29.9	34.4	7093	40	7288	

It is clear from Figure E-5 that, whereas the heat transfer model largely overestimates the freeze lining growth, the newly developed mass transfer model accurately predicts the growth of the freeze lining over time.

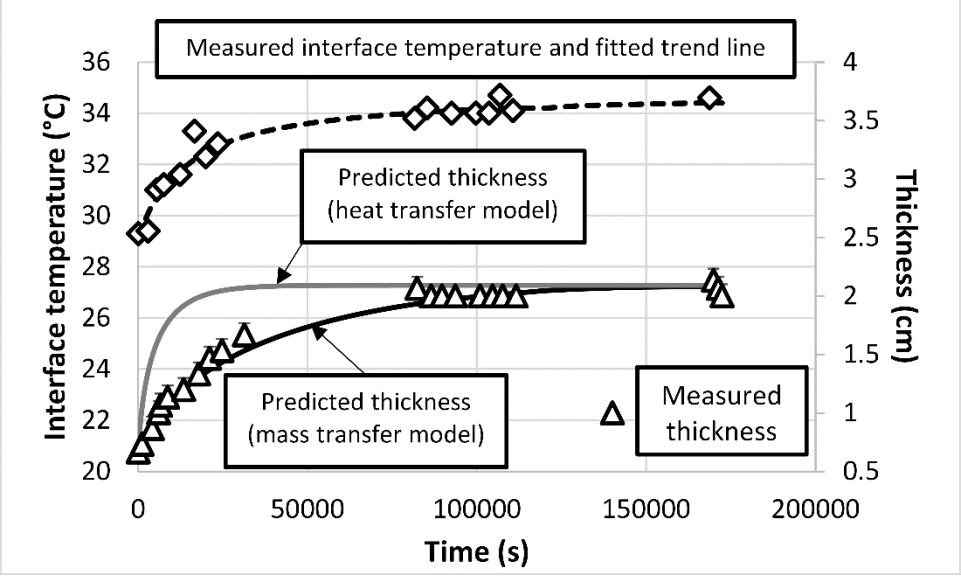

Figure E-5: Measured and calculated thickness and bath-freeze lining interface temperature.

It can be concluded that freeze lining growth consists of two stages:

1) Initial growth stage: in this stage, the interface temperature equals the solidus temperature. As crystallization results in a microstructure with a local bulk composition approximately equal

to the liquid bath bulk composition, limited mass transfer is required. As such, freeze lining growth is heat transfer controlled and occurs rapidly.

2) Growth of open crystalline layer and sealing layer: in this stage, growth of the freeze lining takes place through crystallization of one or a couple of specific solids (for example pyroxene in experiments performed in Chapter 7). As the composition of these solid phases differs from the liquid bath bulk composition, mass transfer of the crystallizing components from the bath to the bulk liquid is required for the freeze lining to grow further. In this stage, freeze lining growth is mass transfer controlled and generally occurs much slower than expected from heat transfer models. The interface temperature in this stage evolves from the solidus temperature to the steady state interface temperature.

E.6 Results

All calculations were performed using the base parameters listed in Table E-5. For each series of calculations, one of the parameters was varied.

Table E-5: Model input parameters, base case values.

W (m)	L (m)	$T_{interface}$ (°C)	v_{bath} (m/s)	D (m^2/s)	R (mol/K.m^2.s)	H_{latent} (J/mol.K)
0.0005	0.05	50	0.001	1.00E-10	1	100000
k (W/m.K)	**$T_{solidus}$ (°C)**	**$T_{liquidus}$ (°C)**	**$C_{eutectic}$ (mol/m^3)**		**T_{bath} (°C)**	**C_{bath} (mol/m^3)**
2	50	100	30000		100	4.00E+04

Effect of bath temperature/superheat

The freeze lining growth rate should decrease with increasing interface temperature and reach zero growth for an interface temperature equalling the liquidus temperature. Without these conditions, the freeze lining would never stop growing.

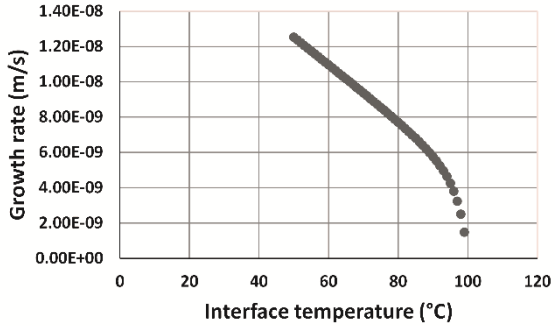

Figure E-6: Calculated effect of the interface temperature on freeze lining growth.

Figure E-6 shows that this is indeed the case. As the interface temperature increases from the solidus to the liquidus temperature, the freeze lining growth rate decreases towards zero.

Effect of fluid velocity

Figure E-7 shows the effect of the velocity of the fluid on freeze lining growth (a) and on the steady state interface temperature of the freeze lining (b). As is expected from general solidification theory, at low velocities freeze lining growth is controlled by diffusion while at very high velocities, growth is controlled by reaction kinetics.

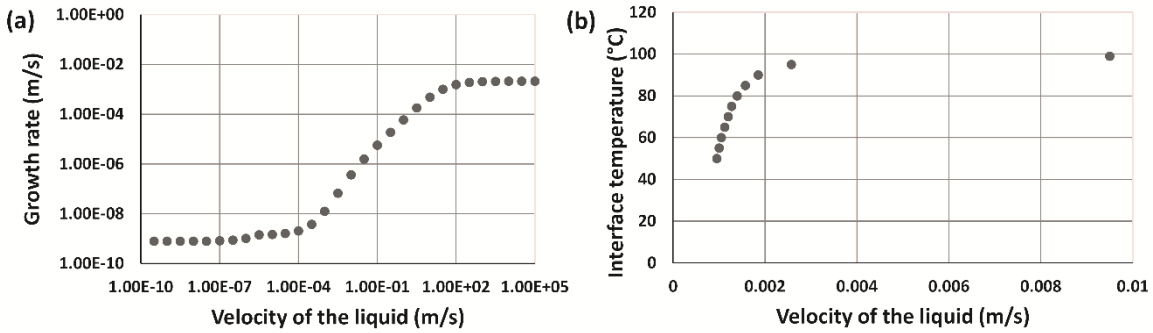

Figure E-7: Calculated effect of velocity of the fluid on freeze lining growth rate and interface temperature.

The velocity of the fluid turns out to be the most impactful factor when it comes to freeze lining growth and interface temperature. A tenfold increase in velocity of the fluid increases the growth rate of the freeze lining by a factor ten or more in the convection controlled regime. As a result, the interface temperature is a near step-like function of the velocity of the liquid. Changing the velocity from 0.001 to 0.002 m/s increases the interface temperature from the solidus temperature to a value within range of uncertainty of measurements of the liquidus temperature in high-temperature processes.

The increase in interface temperature with increasing turbulence is consistent with experimental research by Fallah-Mehrjardi et al. [58] who found that increasing bath agitation in high copper slags resulted in the formation of a sealing crystal layer consisting of the primary phase.

Effect of mass diffusivity

Figure E-8 shows the effect of mass diffusivity on freeze lining growth (a) and on the steady state interface temperature of the freeze lining (b). At very low mass diffusivities, the convective mass transfer is higher than the diffusive mass transfer and the freeze lining growth is convection controlled. At higher mass diffusivities, diffusion becomes more important than convection and the freeze lining growth becomes diffusion controlled. At even higher mass diffusivities, the concentration of the liquid becomes approximately constant throughout the subliquidus layer and the freeze lining growth becomes reaction controlled.

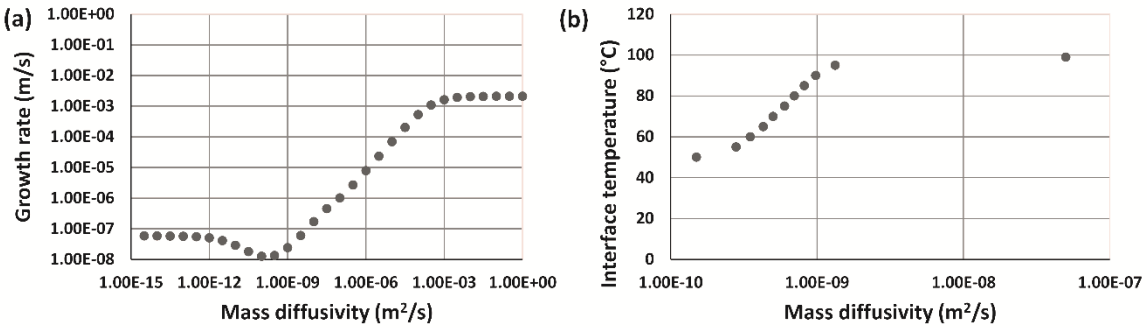

Figure E-8: Calculated effect of mass diffusivity on freeze lining growth rate and interface temperature.

The effect of the detached crystals becomes clear when looking at the slope of the diffusion controlled area. Without precipitates present before the freeze lining, freeze lining growth would increase proportionally with mass diffusivity based on Fick's first law. In this example, as the mass diffusivity increases with a factor of 10000 over the diffusion controlled range, it would be expected that freeze lining growth increases with a factor of 10000 as well. Instead, it can be seen that freeze lining growth only increases with a factor of approximately 3110. It can be demonstrated that this factor depends on the ratio of the distance between crystals (W) on the boundary layer thickness (L).

Also of interest is the small dip in freeze lining growth rate right before the diffusion controlled area. This represents the range of mass diffusivities where diffusion towards the freeze lining is still negligible, but diffusion towards the solid slab is significant. Due to precipitation of material on the precipitating solid, less material can subsequently be deposited on the freeze lining.

Effect of bath temperature/superheat, boundary layer thickness, composition, liquidus temperature and nucleation rate

Figure E-9-Figure E-13 show the effect of several properties on the freeze lining growth rate. Increasing bath temperatures, decreasing boundary layer thicknesses and decreasing liquidus temperatures decrease the time the liquid spends in the subliquidus boundary layer and the amount of material that can precipitate on the detached crystals, thus increasing the concentration at and growth rate of the freeze lining deposit interface.

Increasing the concentration of the precipitating species increases the concentration gradient in the subliquidus boundary layer and at the freeze lining deposit interface, increasing the growth rate.

Increasing nucleation rate lowers the average distance from the liquid to the detached crystals, decreasing the time required for mass diffusion to take place from the liquid to the detached crystals, resulting in more material precipitating on the detached crystals. As a result, the concentration at and growth rate of the freeze lining deposit interface decreases.

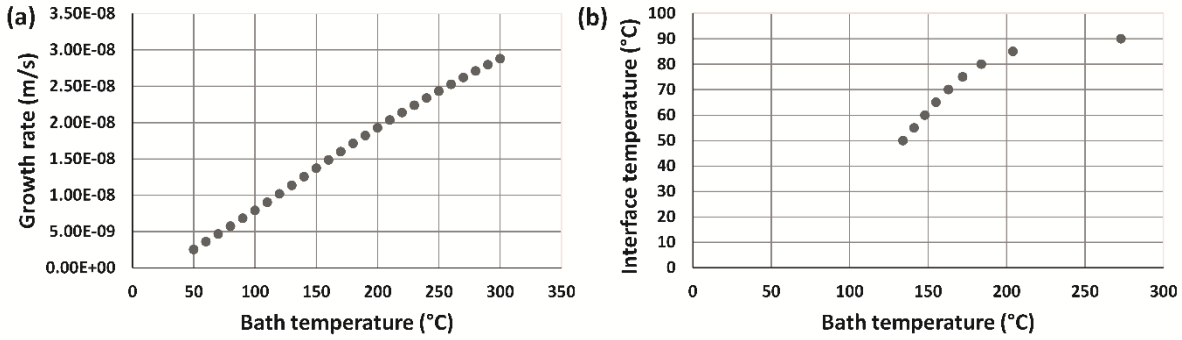

Figure E-9: Calculated effect of bath temperature on freeze lining growth rate and interface temperature.

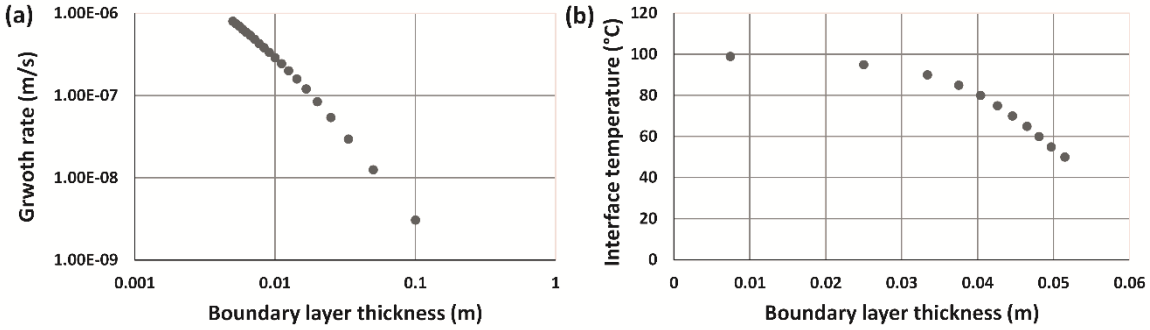

Figure E-10: Calculated effect of boundary layer thickness on freeze lining growth rate and interface temperature.

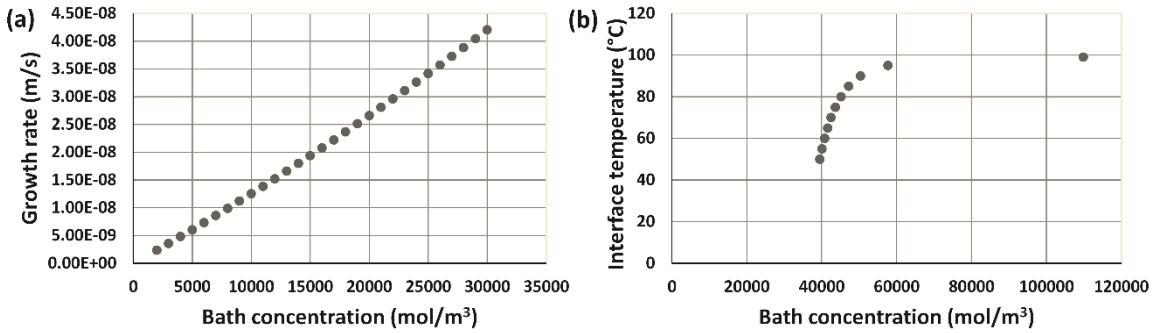

Figure E-11: Calculated effect of concentration of precipitating species in the bulk bath on freeze lining growth rate and interface temperature.

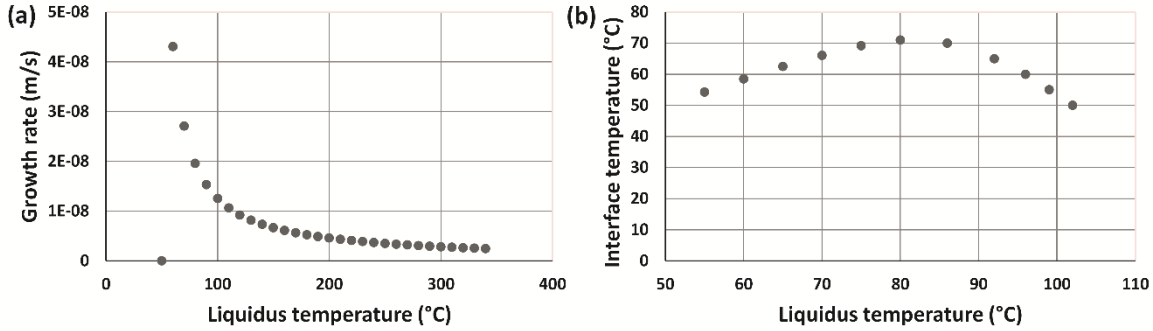

Figure E-12: Calculated effect of liquidus temperature (slope of liquidus) on freeze lining growth rate and interface temperature.

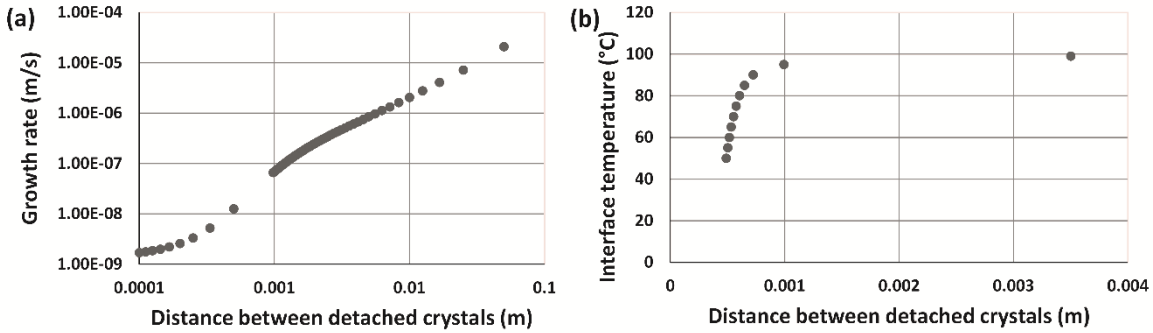

Figure E-13: Calculated effect of distance between detached crystals (nucleation rate) on freeze lining growth rate and interface temperature.

E.7Conclusion

Figure E-14 shows a schematic summary of the effect of properties on freeze lining growth. The effect of parameters will differ depending on whether the growth is heat conduction, convection, diffusion or reaction rate controlled.

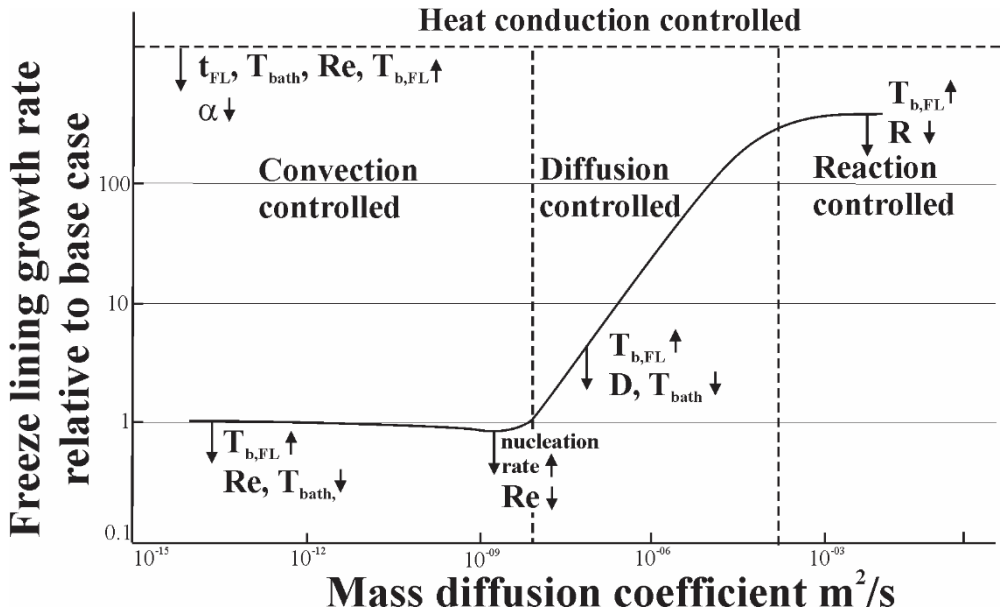

Figure E-14: Effect of mass diffusivity and several other process parameters on freeze lining growth rate

Heat conduction controlled growth would be expected during formation of the glassy layer and the closed crystalline layer, where mass diffusion plays a limited role as no or only short-range mass diffusion is required. Further growth is expected to be either convection or diffusion controlled, depending on the level of turbulence.

The modelled freeze lining growth rate under non-heat conduction controlled conditions shows a remarkable similar behaviour to the steady state interface temperature under changing operating conditions. Higher turbulence increases freeze lining growth rate and steady state interface temperature. Higher bath temperatures only seem to have a minor effect on freeze lining growth rate and steady state interface temperatures.

Although further research is needed to confirm this relation, these results seem to indicate a link between freeze lining growth rate and steady state interface temperature.

Appendix F.Numerical model freeze lining growth

The following MATLAB code describes the numerical model determining mass transfer controlled freeze lining growth. The code allows for precipitation of material onto detached crystals in a so-called subliquidus layer and is based on the conceptual model proposed by Fallah-Mehrjardi et al. The general description of the model can be found in Appendix E of this thesis.

```
% Calculates freeze lining growth under quasi-steady state conditions
% Calculation based on the conceptual framework proposed by
% Fallah-mehrjardi et al.
% Description of method geometry can be found in Appendix E

clear
%this matrix will be used to store results for several calculated
%parameters (the idea is to
%use count1 and count2 to vary two input parameters such as viscosity and
%mass diffusivity, the code then runs the finite difference method each
%iteration, calculating the resulting freeze lining growth for changing
%viscosity and mass diffusivity)

count1max = 1;
count2max = 1;
Results = zeros(count1max*count2max,21);


for count1 = 1:count1max
    for count2 = 1:count2max

count = count2max*(count1-1)+count2;

%input parameters all in SI units, except for Temperatures which can be
%either K or °C, as long as you are consistent
LatentHeat = 100000; %J/mol.K
rho = 1000; %kg/m3
Cp = 500; %J/kg.K
k = 2; %W/m.K
R = 1; %mol/K.m2.s
vbath = 0.001;%m/s
Tliquidus = 100; %K or °C
Tsolidus = 50; %K or °C
EutecticConcentration = 30000; %mol/m3
D = 1.00*10^(-10); %m2/s
Length = 0.05; %m %a high Length will result in long calculation time
Width = 50; %m %a small Width will result in a long calculation time

%boundary conditions all in SI units, except for Temperatures which can be
%either K or °C
Tbath = 100; %°C or K
Tinterface = 50; %°C or K
BathConcentration = 40000; %mol/m3


if Length > Width
    %amount of width nodes
    n = 5; % minimum = 3
```

```
    %%DO NOT CHANGE ANY VALUES FROM HERE ON
    %scale of nodes
    deltaY = Width/(n-1);
    %amount of length nodes (rectangular nodes result in weird results,
    %so nodes are made approximately square)
    m = round(Length/deltaY);
    deltaX = Length/(m-1);
else
    %amount of Length nodes
    m = 20
    %%DO NOT CHANGE ANY VALUES FROM HERE ON
    %scale of nodes
    deltaX = Length/(m-1);
    %amount of width nodes (rectangular nodes result in weird results,
    %so nodes are made approximately square)
    n = round(Width/deltaX);
    deltaY = Width/(n-1);
end
%velocity: taken linearly dependent on distance from interface
v = @(x) vbath/Length*x;

%equilibrium concentration: these are only used to force R = 0 when the
% local temperature is higher than the liquidus (equilibrium) temperature
% and for calculation of supersaturation
Tequilib = @(c) Tsolidus + (Tliquidus-Tsolidus)/(BathConcentration-
EutecticConcentration)*(c-EutecticConcentration);
Cequilib = @(Temperature) EutecticConcentration + (BathConcentration -
EutecticConcentration)/(Tliquidus - Tsolidus)*(Temperature-Tsolidus);


% X = (T11 T12 .. T1m T21 ... T2m ... Tnm  C11 C12 .. C1m C21 ... C2m
% ... Cnm)
%Tij = X(m*(i-1)+j)
%Cij = X(m*n + m*(i-1)+j)


X = zeros (2*m*n,1);
Y = zeros (2*m*n,1);
A = spalloc (2*m*n,2*m*n,6*2*m*n);
Check = 0;

for l = 1:5
%%%define matrix: left is the stagnant freeze lining, upper is the solid
%%%slab, right the bath and lower the isolated boundary
%% define corners
%top left
i = 1;
j = 1;
xplus = (j-0.5)*deltaX;
vplus = v(xplus);
%top left T row 1
A(m*(i-1)+j,m*(i-1)+j) = 1;
A(m*(i-1)+j,m*(i-1)+j+1) = 0;
A(m*(i-1)+j,m*(i)+j) = 0;
Y(m*(i-1)+j) = Tinterface;

%top left C row m*n+1
A(m*n+m*(i-1)+j,m*(i-1)+j) = deltaY/2*R+deltaX/2*R;
```

```
A(m*n+m*(i-1)+j,m*n+m*(i-1)+j) = -D*deltaY/2/deltaX - vplus*deltaY/2/2 -
D*deltaX/2/deltaY  - deltaY/2*R*(Tliquidus-Tsolidus)/(BathConcentration-
EutecticConcentration)- deltaX/2*R*(Tliquidus-Tsolidus)/(BathConcentration-
EutecticConcentration);
A(m*n+m*(i-1)+j,m*n+m*(i-1)+j+1) = D*deltaY/2/deltaX + vplus*deltaY/2/2;
A(m*n+m*(i-1)+j,m*n+m*(i)+j) = D*deltaX/2/deltaY;
Y(m*n+m*(i-1)+j) = deltaY/2*R*Tsolidus - deltaY/2*R*(Tliquidus-
Tsolidus)/(BathConcentration-
EutecticConcentration)*EutecticConcentration+deltaX/2*R*Tsolidus -
deltaX/2*R*(Tliquidus-Tsolidus)/(BathConcentration-
EutecticConcentration)*EutecticConcentration;

%bottom left T row m*(n-1)+1
i = n;
j = 1;
xplus = (j-0.5)*deltaX;
vplus = v(xplus);
A(m*(i-1)+j,m*(i-1)+j) = 1;
A(m*(i-1)+j,m*(i-1)+j+1) = 0;
A(m*(i-1)+j,m*(i-2)+j) = 0;
Y(m*(i-1)+j) = Tinterface;

%bottom left C row m*n+m*(n-1)+1
A(m*n+m*(i-1)+j,m*(i-1)+j) = deltaY/2*R;
A(m*n+m*(i-1)+j,m*n+m*(i-1)+j) = -D*deltaY/2/deltaX - vplus*deltaY/2/2 -
D*deltaX/2/deltaY  - deltaY/2*R*(Tliquidus-Tsolidus)/(BathConcentration-
EutecticConcentration);
A(m*n+m*(i-1)+j,m*n+m*(i-1)+j+1) = D*deltaY/2/deltaX + vplus*deltaY/2/2;
A(m*n+m*(i-1)+j,m*n+m*(i-2)+j) = D*deltaX/2/deltaY;
Y(m*n+m*(i-1)+j) = deltaY/2*R*Tsolidus - deltaY/2*R*(Tliquidus-
Tsolidus)/(BathConcentration-EutecticConcentration)*EutecticConcentration;

%top right T row m
i = 1;
j = m;
A(m*(i-1)+j,m*(i-1)+j) = 1;
A(m*(i-1)+j,m*(i-1)+j-1) = 0;
A(m*(i-1)+j,m*(i)+j) = 0;
Y(m*(i-1)+j) = Tbath;

%top right C row m*n + m
A(m*n+m*(i-1)+j,m*n+m*(i-1)+j) = 1;
A(m*n+m*(i-1)+j,m*n+m*(i-1)+j-1) = 0;
A(m*n+m*(i-1)+j,m*n+m*(i)+j) = 0;
Y(m*n+m*(i-1)+j) = BathConcentration;

%bottom right T row m*n
i = n;
j = m;
A(m*(i-1)+j,m*(i-1)+j) = 1;
A(m*(i-1)+j,m*(i-1)+j-1) = 0;
A(m*(i-1)+j,m*(i-2)+j) = 0;
Y(m*(i-1)+j) = Tbath;

%bottom right C row 2*m*n
A(m*n+m*(i-1)+j,m*n+m*(i-1)+j) = 1;
A(m*n+m*(i-1)+j,m*n+m*(i-1)+j-1) = 0;
A(m*n+m*(i-1)+j,m*n+m*(i-2)+j) = 0;
Y(m*n+m*(i-1)+j) = BathConcentration;
```

```
%%define boundaries
%left
for i = 2:n-1
    j = 1;
    xplus = (j-0.5)*deltaX;
    vplus = v(xplus);
    A(m*(i-1)+j,m*(i-1)+j) = 1;
    A(m*(i-1)+j,m*(i-1)+j+1) = 0;
    A(m*(i-1)+j,m*(i-2)+j) = 0;
    A(m*(i-1)+j,m*(i)+j) = 0;
    Y(m*(i-1)+j) = Tinterface;

    A(m*n+m*(i-1)+j,m*(i-1)+j) = deltaY*R;
    A(m*n+m*(i-1)+j,m*n+m*(i-1)+j) = -D*deltaY/deltaX - vplus*deltaY/2 -
2*D*deltaX/2/deltaY  - deltaY*R*(Tliquidus-Tsolidus)/(BathConcentration-
EutecticConcentration);
    A(m*n+m*(i-1)+j,m*n+m*(i-1)+j+1) = D*deltaY/deltaX + vplus*deltaY/2;
    A(m*n+m*(i-1)+j,m*n+m*(i-2)+j) = D*deltaX/2/deltaY;
    A(m*n+m*(i-1)+j,m*n+m*(i)+j) = D*deltaX/2/deltaY;
    Y(m*n+m*(i-1)+j) = deltaY*R*Tsolidus - deltaY*R*(Tliquidus-
Tsolidus)/(BathConcentration-EutecticConcentration)*EutecticConcentration;
end

%upper
for j = m-1:-1:2
    if Check ==0
        Radapted = 0;
     elseif X(m*(i-1)+j)>Tequilib(X(m*n+m*(i-1)+j))&&Check==1
        Radapted = 0;
    else
        Radapted = R;
    end
    i = 1;
    xminus = (j-1.5)*deltaX;
    xplus = (j-0.5)*deltaX;
    vminus = v(xminus);
    vplus = v(xplus);
    A(m*(i-1)+j,m*n+m*(i-1)+j) =  deltaX*Radapted*LatentHeat*(Tliquidus-
Tsolidus)/(BathConcentration-EutecticConcentration);
    A(m*(i-1)+j,m*(i-1)+j) = -2*k*deltaY/2/deltaX - vplus*deltaY*rho*Cp/2/2 -
k*deltaX/deltaY - vminus*deltaY*rho*Cp/2/2 - deltaX*Radapted*LatentHeat;
    A(m*(i-1)+j,m*(i-1)+j+1) = k*deltaY/2/deltaX + vplus*deltaY/2*rho*Cp/2;
    A(m*(i-1)+j,m*(i-1)+j-1) = k*deltaY/2/deltaX + vminus*deltaY/2*rho*Cp/2;
    A(m*(i-1)+j,m*(i)+j) = k*deltaX/deltaY;
    Y(m*(i-1)+j) = -deltaX*Radapted*LatentHeat*Tsolidus +
deltaX*Radapted*LatentHeat*(Tliquidus-Tsolidus)/(BathConcentration-
EutecticConcentration)*EutecticConcentration;

    A(m*n+m*(i-1)+j,m*(i-1)+j) = deltaX*Radapted;
    A(m*n+m*(i-1)+j,m*n+m*(i-1)+j) = -2*D*deltaY/2/deltaX - vplus*deltaY/2/2 -
D*deltaX/deltaY - vminus*deltaY/2/2  - deltaX*Radapted*(Tliquidus-
Tsolidus)/(BathConcentration-EutecticConcentration);
    A(m*n+m*(i-1)+j,m*n+m*(i-1)+j+1) = D*deltaY/2/deltaX + vplus*deltaY/2/2;
    A(m*n+m*(i-1)+j,m*n+m*(i-1)+j-1) = D*deltaY/2/deltaX + vminus*deltaY/2/2;
    A(m*n+m*(i-1)+j,m*n+m*(i)+j) = D*deltaX/deltaY;
    Y(m*n+m*(i-1)+j) = deltaX*Radapted*Tsolidus - deltaX*Radapted*(Tliquidus-
Tsolidus)/(BathConcentration-EutecticConcentration)*EutecticConcentration;
    if j == 2
       Check=1;
    end
end
```

```
%right
for i = 2:n-1
    j = m;
    A(m*(i-1)+j,m*(i-1)+j) = 1;
    A(m*(i-1)+j,m*(i-1)+j-1) = 0;
    A(m*(i-1)+j,m*(i-2)+j) = 0;
    A(m*(i-1)+j,m*(i)+j) = 0;
    Y(m*(i-1)+j) = Tbath;

    A(m*n+m*(i-1)+j,m*n+m*(i-1)+j) = 1;
    A(m*n+m*(i-1)+j,m*n+m*(i-1)+j-1) = 0;
    A(m*n+m*(i-1)+j,m*n+m*(i-2)+j) = 0;
    A(m*n+m*(i-1)+j,m*n+m*(i)+j) = 0;
    Y(m*n+m*(i-1)+j) = BathConcentration;

end

%lower
for j = 2:m-1
    i = n;
    xminus = (j-1.5)*deltaX;
    xplus = (j-0.5)*deltaX;
    vminus = v(xminus);
    vplus = v(xplus);
    A(m*(i-1)+j,m*(i-1)+j) = -2*k*deltaY/2/deltaX - vplus*deltaY/2*rho*Cp/2 -
k*deltaX/deltaY - vminus*deltaY/2*rho*Cp/2;
    A(m*(i-1)+j,m*(i-1)+j+1) = k*deltaY/2/deltaX + vplus*deltaY/2*rho*Cp/2;
    A(m*(i-1)+j,m*(i-1)+j-1) = k*deltaY/2/deltaX + vminus*deltaY/2*rho*Cp/2;
    A(m*(i-1)+j,m*(i-2)+j) = k*deltaX/deltaY;

    Y(m*(i-1)+j) = 0;

    A(m*n+m*(i-1)+j,m*n+m*(i-1)+j) = -2*D*deltaY/2/deltaX - vplus*deltaY/2/2 -
D*deltaX/deltaY - vminus*deltaY/2/2;
    A(m*n+m*(i-1)+j,m*n+m*(i-1)+j+1) = D*deltaY/2/deltaX + vplus*deltaY/2/2;
    A(m*n+m*(i-1)+j,m*n+m*(i-1)+j-1) = D*deltaY/2/deltaX + vminus*deltaY/2/2;
    A(m*n+m*(i-1)+j,m*n+m*(i-2)+j) = D*deltaX/deltaY;

    Y(m*n+m*(i-1)+j) = 0;

end

%bulk of matrix
for i = 2:n-1
    for j = 2:m-1
        xminus = (j-1.5)*deltaX;
        xplus = (j-0.5)*deltaX;
        vminus = v(xminus);
        vplus = v(xplus);
        %define row m*(i-1)+j
        A(m*(i-1)+j,m*(i-1)+j) = -2*k*deltaY/deltaX - vplus*deltaY*rho*Cp/2 - 2*
k*deltaX/deltaY - vminus*deltaY*rho*Cp/2;
        A(m*(i-1)+j,m*(i-1)+j+1) = k*deltaY/deltaX + vplus*deltaY*rho*Cp/2;
        A(m*(i-1)+j,m*(i-1)+j-1) = k*deltaY/deltaX + vminus*deltaY*rho*Cp/2;
        A(m*(i-1)+j,m*(i-2)+j) = k*deltaX/deltaY;
        A(m*(i-1)+j,m*(i)+j) = k*deltaX/deltaY;
        Y(m*(i-1)+j) = 0;
```

```
        %define row m*n + m*(i-1)+j
        A(m*n+m*(i-1)+j,m*n+m*(i-1)+j) = -2*D*deltaY/deltaX - vplus*deltaY/2 -
2*D*deltaX/deltaY - vminus*deltaY/2;
        A(m*n+m*(i-1)+j,m*n+m*(i-1)+j+1) = D*deltaY/deltaX + vplus*deltaY/2;
        A(m*n+m*(i-1)+j,m*n+m*(i-1)+j-1) = D*deltaY/deltaX + vminus*deltaY/2;
        A(m*n+m*(i-1)+j,m*n+m*(i-2)+j) = D*deltaX/deltaY;
        A(m*n+m*(i-1)+j,m*n+m*(i)+j) = D*deltaX/deltaY;
        Y(m*n+m*(i-1)+j) = 0;

    end
end
X = A\Y;
end

%Transfering values to nice rectangular Temperature and Concentration
%matrices instead of a single column matrix
T = zeros(n,m);
C = zeros(n,m);
for i = 1:n
    for j = 1:m
       T(i,j) = X(m*(i-1)+j);
       C(i,j) = X(m*n + m*(i-1)+j);
    end
end


%getting the results out
%get input
Results(count,1)=Width;
Results(count,2)=Length;
Results(count,3)=Tinterface;
Results(count,4)=vbath;
Results(count,5)=D;
Results(count,6)=R;
Results(count,7)=LatentHeat;
Results(count,8)=k;
Results(count,9)=Tsolidus;
Results(count,10)=Tliquidus;
Results(count,11)=EutecticConcentration;

%Precipitation on freeze lining (= freeze lining growth)
TequilibriumFL = Tequilib(C(:,1));
PrecipitationPerCell = deltaY*R*(TequilibriumFL-T(:,1));
PrecipitationPerCell(1)=PrecipitationPerCell(1)/2;
PrecipitationPerCell(n)=PrecipitationPerCell(n)/2;
PrecipitationFL = sum (PrecipitationPerCell(:));
Results(count,12) = PrecipitationFL;
%Precipitation on detached crystals
TequilibriumDC = Tequilib(C(1,:));
PrecipitationPerCellDC = deltaX*R*(TequilibriumDC-T(1,:));
PrecipitationPerCellDC(PrecipitationPerCellDC<0)=0;
PrecipitationPerCellDC(1)=PrecipitationPerCellDC(1)/2;
PrecipitationPerCellDC(m)=0;
PrecipitationDC = sum(PrecipitationPerCellDC(:));
Results(count,13) = PrecipitationDC;
%Ratio PrecDC/PrecFL
Results(count,14) = PrecipitationDC/PrecipitationFL;
%Supersaturation bottom left
Results(count,15) = C(n,1)-Cequilib(T(n,1));
```

```
%Freeze lining growth rate (molar mass = 147g/mol)
Results(count,16) = PrecipitationFL*0.183/(1830*Width);
%Freeze lining growth in 8 hours
Results(count,17) = Results(count,16)*3600*8;
%Detached crystals growth rate
Results(count,18) = PrecipitationDC*0.183/(1830*Length);
%Detached crystals size
Results(count,19)= Results(count,18)*Length/vbath*2;
%Bath temperature
Results(count,20) = Tbath;
%Bath concentration
Results(count,21) = BathConcentration;

Results(count,16)*3600*24
Results(count,16)

q = (T(n,2)-T(n,1))/deltaX
qdiff = q-220

end
end
```